Precision Nanofibers for Biomedical Applications via Living Crystallization-Driven Self-Assembly

by
Juan Diego García Hernández

Bachelor of Engineering, Instituto Politécnico Nacional, 2015
Master of Research, University of Bristol, 2018

A Dissertation Submitted for Fulfilment of the
Requirements for the Degree of

DOCTOR OF PHILOSOPHY

in the Department of Chemistry

Supervisory Committee

Precision Nanofibers for Biomedical Applications via Living Crystallization-Driven Self-Assembly

by
Juan Diego García Hernández

Bachelor of Engineering, Instituto Politécnico Nacional, Mexico, 2015
Master of Research, University of Bristol, 2018

Supervisory Committee

Prof. Ian Manners, Department of Chemistry
Supervisor

Prof. Jeremy E. Wulff, Department of Chemistry
Departmental Member

Prof. Stephanie Willerth, Department of Biomedical Engineering
Outside Member

Abstract

Nature provides fascinating examples of functional materials with hierarchical structures. Nano and microscale materials have been prepared by synthetic approaches via the self-assembly of discrete building blocks with the aim to mimic nature's materials in complexity and size. The solution-state self-assembly of block copolymers (BCPs) with crystallizable core-forming blocks has enabled access to low curvature morphologies such as 1D and 2D micelles via a spontaneous nucleation method termed crystallization-driven self-assembly (CDSA). Via a seeded growth method known as living CDSA, 1D and 2D micelles of controlled dimensions and low dispersity can easily be prepared. However, due to the challenges associated with the synthesis of high aspect ratio nanoparticles and the low number of noncytotoxic polymers known to undergo CDSA, their use for biomedical applications has been limited. The aim of the work described in this thesis is to develop nanofibers of precise dimensions, with nontoxic materials, for potential biomedical applications such as drug delivery, tissue engineering and materials reinforcement.

Chapter 1 describes how nature makes superb functional hierarchical materials that serve as inspiration for the development of synthetic methods for the preparation of nano and microstructures. The principles regarding the solution-state self-assembly of BCPs with amorphous or crystalline core-forming blocks are discussed. The preparation of length-controlled nanostructures, segmented micelles, and supermicelles via living CDSA and micelle self-assembly are presented. An introduction to nanoparticle drug delivery, materials reinforcement, and tissue engineering with emphasis on the development and advantages of high aspect ratio nanofibers is given. Finally, a brief perspective on the development of nanofiber-based therapeutics is provided.

Chapter 2 discusses the preparation of coaxial-core core nanofibers from the self-assembly of triBCPs. The nanofiber structure is comprised of a crystalline inner core, an amorphous hydrophobic outer core, and a water-soluble corona-forming block. Encapsulation of a model hydrophobic molecule was achieved by the outer amorphous core. This represents the first example of water-soluble, length-controlled, and low length-dispersity (*Đ*) nanofibers loaded via non-covalent interactions. In Chapter 2, preliminary studies suggested cargo uptake by diBCP nanofibers may be possible.

Chapter 3 focusses on investigating the non-covalent loading of length controlled diBCP nanofibers with a hydrophobic cargo. The effect of the chemical identity and the length of the corona-forming blocks was also studied.

Chapter 4 describes the self-assembly of B-A-B triBCPs with crystallizable hydrophobic 'B' terminal segments to yield fiber-like micelle networks and their potential applications. Conditions for the preparation of discrete crystalline core flower-like micelles and intermicellar fiber-like networks of crystalline core nanofibers were investigated. For the first time, crystalline core nanofiber networks are reported.

Chapter 5 focuses on the proof-of-concept development of water-soluble length-controlled nanofibers with corona-forming blocks capable of targeting specific cancer tissue. Additionally, segmented nanofibers for drug delivery applications were prepared. Finally, the association of curcumin with the nanofiber corona-forming block was briefly investigated.

Chapter 6 summarizes the work presented in this thesis which contributes towards the development of length-tunable nanofibers for biomedical applications and outlines future research directions of the work presented.

Table of Contents

List of Figures

List of Supporting Figures

List of Schemes

List of Tables

List of Abbreviations

°C	Degrees centigrade
1D	One-dimensional
^{1}H NMR	Proton nuclear magnetic resonance
2D	Two-dimensional
3D	Three-dimensional
a	Solvophilic head group area
Å	Angstrom
aq	Aqueous
app	apparent
a.u.	Arbitrary units
AFM	Atomic force microscopy
-*b*-	Block
BCP	Block copolymer
brs	Broad singlet
ca.	Circa
CDSA	Crystallization-driven self-assembly
CTA	Chain transfer agent
d	doublet
DBU	1,8-diazabicyclo[5.4.0]undec-7-ene
DCM	Dichloromethane
DLS	Dynamic light scattering
DMAc	Dimethylacetamide
DMF	Dimethyl formamide
DMSO	Dimethyl sulfoxide
DNA	Desoxyribonucleic acid
DP_n	Number average degree of polymerization
E	Energy
EE	Encapsulation efficiency
e.g.	*Exempli gratia:* for example

EtOH	Ethanol
Eq.	Equation
Fr	Fructose monomer or 1-*O*-acryloyl-2,3:4,5-di-*O*-isopropylidene-*β*-D-fructopyranose
FTMC	Fluorenetrimethylenecarbonate
g	Gram
GPC	Gel permeation chromatography
h	Hour
i.e.,	*Id est:* that is
iPrOH	Isopropanol
l	Solvophobic tail length
LC	Loading capacity
LCSM	Laser confocal scanning microscopy
LCST	Lower critical solution temperature
L_n	Number average length
$L_{n(seed)}$	Number average seed length
$L_{n(theory)}$	Number average theoretical length
L_w	Weight average length
$Đ$	Dispersity
-*m*-	Nanofiber or micelle segment
m	Meter
m	multiplet
m/z	Mass over charge
MALDI-TOF MS	Matrix-assisted laser desorption ionization time of flight mass spectrometry
MeOH	Methanol
mg	Milligram
min	Minute
mL	Milliliter
mmol	Millimole
M_n	Number average molecular weight

mol	Mole
mol%	Mole percentage
m_{unimer}/m_{seed}	Unimer-to-seed mass ratio
M_w	Weight average molecular weight
MWCO	Molecular weight cut-off
NF	Nanofiber
nm	Nanometer
NR	Nile Red
p	pentet
P	Packing parameter
P2VP	Poly(2-vinylpyridine)
P3HT	Poly(3-hexylthiophene)
PBMA	Poly(butyl methacrylate)
PBO	Poly(butylene oxide)
PCL	Poly(ε-caprolactone)
PDHF	Poly(di-n-dihexylfluorene)
PDMS	Polydimethylsiloxane
PE	Polyethylene
PEG	Poly(ethylene glycol)
PEO	Poly(ethylene oxide)
PFS	Polyferrocenyldimethylsilane
PFG	Polyferrocenyldimethylgermane
PFr	Poly(fructose)
PPFr	Protected poly(fructose)
PFTMC	Poly(fluorenetrimethylenecarbonate)
PLLA	Poly(*L*-lactide)
PMMA	Poly(methyl methacrylate)
PNIPAM	Poly(*N*-isopropylacrylamide)
PNSL	Preformed nanoparticle solvent-switch
ppm	Parts per million
PS	Polystyrene

q	quartet
RAFT	Reversible addition-fragmentation
Ref	Reference
RI	Refractive index
$R_{h,z}$	Intensity weighted mean hydrodynamic size
s	Second
s	singlet
SARS-CoV-2	Severe acute respiratory syndrome coronavirus 2
t	triplet
TEM	Transmission electron microscopy
TFA	Trifluoroacetic acid
THF	Tetrahydrofuran
TMS	Trimethylsilane
TNBC	Triple negative breast cancer
UV	Ultraviolet
UV/Vis	Ultraviolet/visible
v	Solvophobic tail volume
v/v	Volume by volume
W_n	Number average width
W_w	Weight average width
wt %	Weight percentage
δ	Chemical shift
λ	Wavelength
λ_{abs}	Absorption wavelength
λ_{em}	Emission wavelength
λ_{ex}	Excitation wavelength
μm	Micrometre
σ	Standard deviation
χ	Flory-Huggins parameter

Acknowledgements

I would not have been able to complete my PhD without the support of my family, friends, colleagues, mentors, and supervisor. I would like to thank Professor Ian Manners for the opportunity to do research in his group, for his support, and encouragement to carry on at difficult times. I also like to thank Deborah for helping to keep the group running behind scenes. I am sincerely grateful to the National Council of Science and Technology of Mexico (CONACyT) for the provision of a scholarship (748435).

I would also like to thank all the members of the Manners' group both past and present. It's hard to mention them all but I own special thanks to Alex, Ali, Ayesha, Charlotte E, Chuanqi, Diego R, Etienne, Florian, Hanna, Harvey, Hayley, Horatio, Huda S, Jia, Jiandong, John, Liam, Lei, Marcus, Matt B, Matt W, Mitch, Sam, Steve, Theresa, Tomoya, Vince, Yifan, and Yuetong.

Special thanks must go to few specific people. First, to Diana whose love and support have kept me positive particularly during difficult times and moved to Canada so we were together. I cannot thank all my big family enough for their support, love, and constant encouragement. Specially, I would like to thank my parents Victor and Isabel, my sisters Vicky and Rocio, my brothers-in-law Omar and Ivan, and to my niece Mia. I would also like to thank to my family away from home in both Bristol (UK) and Victoria (Ca): Abril, Alicja, Arca, Carlos, Djen, Esther, Franco, Gary, Gume, Jason, Jess, Marco, Noel, Norma, Rafa, Ron, Siân, and Vicky H. This thesis is dedicated to the memory of my cousins Hector Eduardo, Juan Antonio, and Grandma Rafaela.

Chapter 1

Introduction

1.1 Self-Assembly and Hierarchical Materials: Inspiration from Nature

1.1.1 Nanostructures and Self-Assembly in Nature

Self-assembly, in the context of this thesis, is defined as the transformation of matter from a state of low order to a more ordered state via non-covalent interactions and without external stimuli.[1] The remarkable properties exhibited by biological materials results from hierarchical organization from the molecular level to that of entire biological systems, and life as we know it could not exist without functional self-assembly across several length scales.[2] Nature provides a range of remarkable examples of self-assembled structures such as cells and organelles that serve as source of inspiration for the construction of synthetic systems that aim to act as mimics in terms of function, complexity and size.[3,4] For example, the double-helix structure of human DNA, that stores the entire genome of one individual, results from the self-assembly of complementary DNA strands and has inspired the field of DNA origami.[5,6]

1.1.2 Examples of Order and Hierarchy in Nature

Wood, osseous matter, and tendons are examples from a vast number of fascinating complex materials found in nature whose remarkable macroscopic properties result from the precise and concerted order from the nano and microscale across several hierarchy levels.[7] Tendons are the connective tissue responsible for the transmission of force between bones and muscles to allow locomotion (Figure 1. 1A).[8] The properties of the tendons are fundamentality related to the hierarchical organization of the underlying tissue and the

subunits from which it is constructed. Tendons are comprised of polypeptide fibers (mainly from collagen type 1), proteoglycans, glycoproteins, cells, and water. Proteoglycans and collagen fibers provide viscoelasticity and tensile strength, respectively.[9] Collagen (length ca. 1 – 100 nm) is made from tropocollagen which is formed from three α-peptide strands that self-assemble into a triple helix structure.[10,11] Subsequently, collagen assembles into fibrils (10 – 500 nm. Figure 1. 1C) and then into fibers (> 1 μm. Figure 1. 1B). The fibers self-assemble into primary, secondary, and tertiary bundles of fibers. The fiber bundles are then able to aggregate and bound with endotenons which are enclosed by the epitenon to yield the complex structure of a tendon unit.[9] As shown in Figure 1. 1D, the precise hierarchical order from the nano to microscopic levels of the tendon results in mechanical properties that allow bone-to-tendon-to-muscle transmission of forces, and ultimately in macroscopic movement.[9]

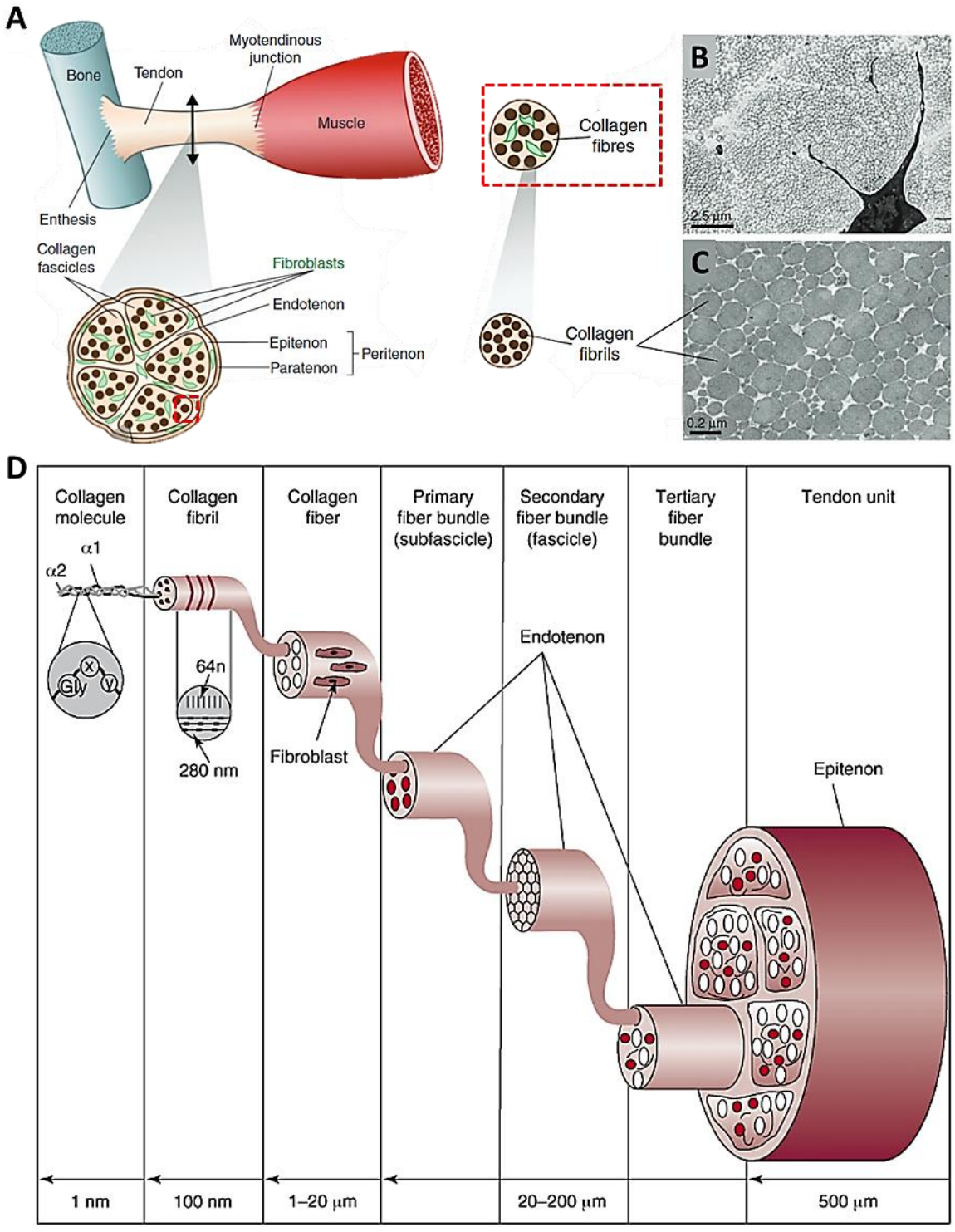

Figure 1. 1. A) Tendon organization for the transmission of mechanical forces between bone and muscle. B-C) Electron microscopy of collagen fibers and fibrils at different scales (scale bars B: 2.5 µm. C: 0.2 µm). D) Hierarchical structure of tendon tissue. Tendons are composed from smaller subunits that are oriented in parallel to the axis of the tendon. The tendon subunits from lower to higher levels of hierarchy are collagen molecules, fibrils, fibers, and fiber bundles (primary, secondary, and tertiary) to give a tendon unit. A-C reproduced and adapted with permission from ref [10]. D reproduced with permission from ref [11].

1.1.3 Top-Down, Bottom-Up Synthesis, and Non-Covalent interactions

Nano and micromaterials are promising and desirable for many applications,[12,13] including biomedical uses,[14,15] as described later in this thesis. Two main strategies for the development of nano and micromaterials have been developed: top-down and bottom-up.[16] The top-down approach aims to produce smaller-sized structures from larger ones until the desired nanomaterial is obtained. This process usually requires energy to break bonds (Figure 1. 2-left).[17] Top-down methods include ball milling or etch lithography, but top-down techniques are generally costly, energetically demanding, and defects may appear as the features of the material become smaller.[16–18] Hence, it is a major challenge to prepare complex and defined structures with high precision on the nano and microscale levels by top-down approaches. The inadequate compatibility of some of the top-down methods with biomolecules led to the integration of top-down methods with self-assembly.[19]

Bottom-up approaches involve the use of small building blocks to create larger nano and microstructures (Figure 1. 2-right).[12] The formation of bonds between atoms and molecules can be regarded as a type of bottom-up approach, however, the synthesis of sequence-defined nano and microstructures with useful functionalities using this approach is challenging and inefficient.[2,20] Self-assembly is a bottom up method that allows access to well-defined structures across a variety of different length scales via non-covalent interactions between molecules or macromolecules.[21–23] As defined by Lehn, self-assembly is ‘chemistry beyond the molecule’.[24]

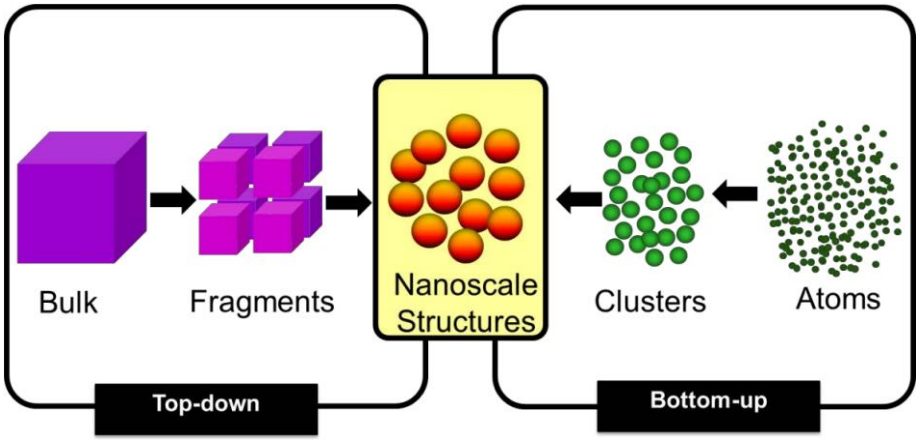

Figure 1. 2. Representation of top-down and bottom-up methods to synthesize nano and microstructures. Reproduced with permission from ref [25].

Non-covalent interactions are individually weak compared to covalent bonds, but when present in sufficient concentration their concerted strength is sufficient to form stable supramolecular assemblies. In the same way that living cells constitute the building blocks of larger ordered organisms, synthetic approaches have been developed to construct complex nanostructures from simpler building blocks via self-assembly.[26] Types of non-covalent interactions of significance for supramolecular chemistry are presented in Table 1. 1.

Table 1. 1. Summary of non-covalent interactions, their relative distances, strengths and examples.[27–30]

Interaction type	Distance (nm)	Strength (kJ/mol)	Example
Ionic	1 – 1000	200 – 300	NaCl lattice
Dipole-dipole	0.1 – 1	5 – 50	Liquid Crystals, CH_3F,
Hydrogen bonding	0.1 – 1	4 – 65	NH_3, CH_3OH, protein folding
$\pi - \pi$	0.1 – 1	0 – 50	Supramolecular polymers
van der Waals	1 – 10	< 5	Molecular crystals, argon
Hydrophobic effect	1 – 100	Specimen specific	Small molecule self-assembly

Two main types of self-assembly exist, static and dynamic self-assembly. Self-assembled systems that are formed at global or local equilibrium are known as static. These may require an initial source of energy, but once the structure is formed it becomes stable. No input of energy is required to maintain stability and there is no continuous dissipation of energy (examples include the cases of self-assembled monolayers, molecular crystals).[2,31] In dynamic self-assembly, also known as fuel-driven self-assembly, systems operate far from equilibrium and require a constant input of energy (either physical or chemical) for the self-assembled structure to be maintained, hence, these systems are transient (e.g. schools of fish). Examples of static self-assemblies will be described in the next sections; however, detailed discussions of dynamic self-assembly are outside the scope of this thesis. Examples and reviews on this topic can be found elsewhere.[32–36]

1.2 Self-Assembly of Small Molecules

Self-assembly of low molecular weight amphiphiles, such as lipids or surfactants, occurs when these molecules are exposed to a selective solvent . A selective solvent is one that only solubilizes the solvophilic part of the molecule but not the solvophobic region. In organic solvents, self-assembly is driven by an unfavorable enthalpy of mixing.[37] In water, self-assembly is driven by an increase in the entropy associated with the expulsion of solvent molecules from the resultant micelles.[38] In addition, exposure to a selective solvent results in unfavorable interactions between the medium and the solvophobic tails, resulting in aggregation, therefore minimizing the enthalpically unfavorable interactions.[39] A range of morphologies can be predicted and accessed with low molecular weight amphiphiles when the critical micelle concentration is reached such as spheres, cylinders, and vesicles, among others.[40,41]

The packing parameter plays a crucial role in predicting the morphology of micelles in solution formed by molecular surfactants. The packing parameter, *P*, is defined as: $P = \frac{v}{a_0 l_c}$ (Figure 1. 3B), where *v* is the volume of the hydrophobic segment, a_o is the contact area of the head group, and l_c is the length of the hydrophobic segment. If $P < 1/3$ spheres, $1/3 < P < 1/2$ cylinders, $1/2 < P < 1$ flexible vesicles or bilayers, and $P = 1$ planar lamella are formed. If $P > 1$ inverted structures can be observed.[40,41]

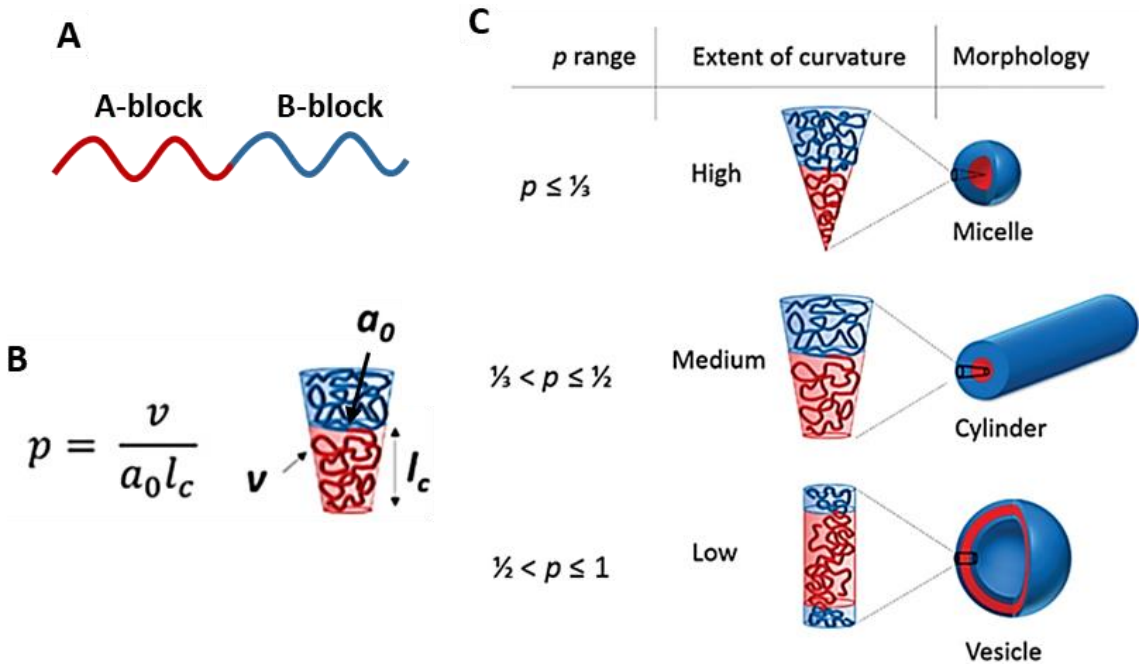

Figure 1. 3. A) Representation of a diblock copolymer with solvophobic (red) and solvophilic (blue) blocks. B) Packing parameter equation. C) Thermodynamic morphologies accessed by targeting different packing parameter values. B-C reproduced and adapted with permission from ref [42].

1.3 Self-Assembly of Block Copolymers

1.3.1 Solid State Self-Assembly of Block Copolymers

Block copolymers (BCPs) are a class of macromolecules with at least two chemically distinct segments covalently linked.[43] Although BCPs are less complex than the building blocks used in nature, supramolecular chemists take inspiration from nature to fabricate functional, diverse, and well-defined BCP-based self-assembled materials.[44,45]

For self-assembly to occur, the individual blocks of the BCP are required to be immiscible with one another to allow for microphase separation. In bulk, for a traditional A-B type diblock copolymer (diBCP. Figure 1. 3A), the phase separation depends on the relative composition of the A and the B blocks, the total degree of polymerization ($DP_n = DP_{n(A)} + DP_{n(B)}$), the volume fraction of the A and B block ($1 = f_A + f_B$), and the degree of incompatibility of each block known as the Flory-Huggins interaction parameter (χ_{AB}).[46] Therefore, phase separation occurs when χ_{AB} exceeds a critical value and the two blocks become immiscible. In addition, different structures based on the volume fraction of each block can be predicted (i.e., f_A and f_B). By tuning the volume fractions of each of the blocks morphological transitions are expected to preserve thermodynamic equilibrium. The resulting morphologies are lamellae, gyroid, hexagonal packed cylinders and body centered cubic structures as represented in the theoretical phase-diagram of diBCPs in the bulk-state.[47–49]

1.3.2 Solution State Self-Assembly of Block Copolymers

Solution state BCP self-assembly is a well-studied field. The work by Eisenberg and coworkers opened up the field to exciting morphologies other than spherical micelles, however, most of the research has focused on the self-assembly of diBCPs with an amorphous core-forming block.[41,50–56] Solution-state BCP self-assembly is generally performed by dispersing the BCP in a selective solvent or a solvent mixture. A selective solvent solubilizes one of the blocks while the other block collapses via solvophobic interactions yielding core-shell morphologies.[57] Formation of thermodynamically stable BCP assemblies with amorphous core-forming blocks is driven by three contributions to the free energy of micellization: i) stretching of the core-forming block to fill the volume

of the micelle core (entropic penalty), to reduce unfavorable core-solvent interactions (enthalpic gain), ii) core-solvent interfacial tension (enthalpic penalty), and iii) repulsive interactions between coronal chains lead to chain stretching (entropic penalty).[39,41] See Table 1. 2 for a summary of the factors influencing the solution state self-assembly of BCPs with amorphous core-forming blocks.

Table 1. 2. Factors influencing the solution state self-assembly of amorphous and crystalline core-forming BCPs.

	Amorphous core BCP self-assembly	**Crystalline core-forming BCP self-assembly**
Contributions	$E_{micellization} = E_{core} + E_{interface} + E_{corona}$	$E_{micellization} = E_{core} + E_{interface} + E_{corona} + E_{crystallization}$
Factors	Core chain stretching, interfacial repulsions, corona swelling and steric repulsions. BCP composition and concentration, additives, solvent mixture, water content.	Core crystallinity, BCP composition, core:corona ratio, temperature, solvent system, and solubility of BCP.
Morphology	Sample specific, hard to predict.	Low core-corona curvatures.

Analogous to small molecule self-assembly, in BCP self-assembly the thermodynamically favored morphology can be predicted by the geometric considerations implicit in the packing parameter, which indicates the favored morphology (i.e. $P \leq 1/3$ for spherical micelles, $1/3 < P \leq 1/2$ 1D for cylindrical (or worm-like) micelles, and $1/2 < P \leq 1$ for vesicles, Figure 1. 3B-C).[42] However, the resulting BCP morphology in solution is also influenced by the presence of additives, temperature, BCP composition (i.e. the DP_n of each block), BCP concentration, the nature of the common and selective solvents, and

the processing method (Figure 1. 4).[58–60] The packing parameter does not account for the aforementioned considerations, which makes this model inadequate as a predictive tool to identify the preferred morphology of BCP self-assemblies in solution. For instance, the affinity of the coronal block towards the selective solvent would affect the surface area value (a_0) of the solvent-swollen corona-forming block (Figure 1. 3B). In selective solvent mixtures, the exchange of BCPs between micelles is very slow unless a high concentration of common solvent for both core- and corona-forming blocks is present.[57,60] This means that self-assembly of BCPs can occur under kinetic control. As a result, far-from-equilibrium morphologies are stable at ambient conditions and present significant variations from the thermodynamically favored morphology.[39,58,61,62] Hence the packing parameter predicts the self-assembly morphology of small surfactants well, but it falls short in predicting the morphology of BCPs in solution. BCPs with more than two segments such as triblock copolymers (triBCPs) can be used for self-assembly, however, this increases the number of variables that determine the morphology of the assembled structure. As a result, more complex structures can be accessed.[63–65]

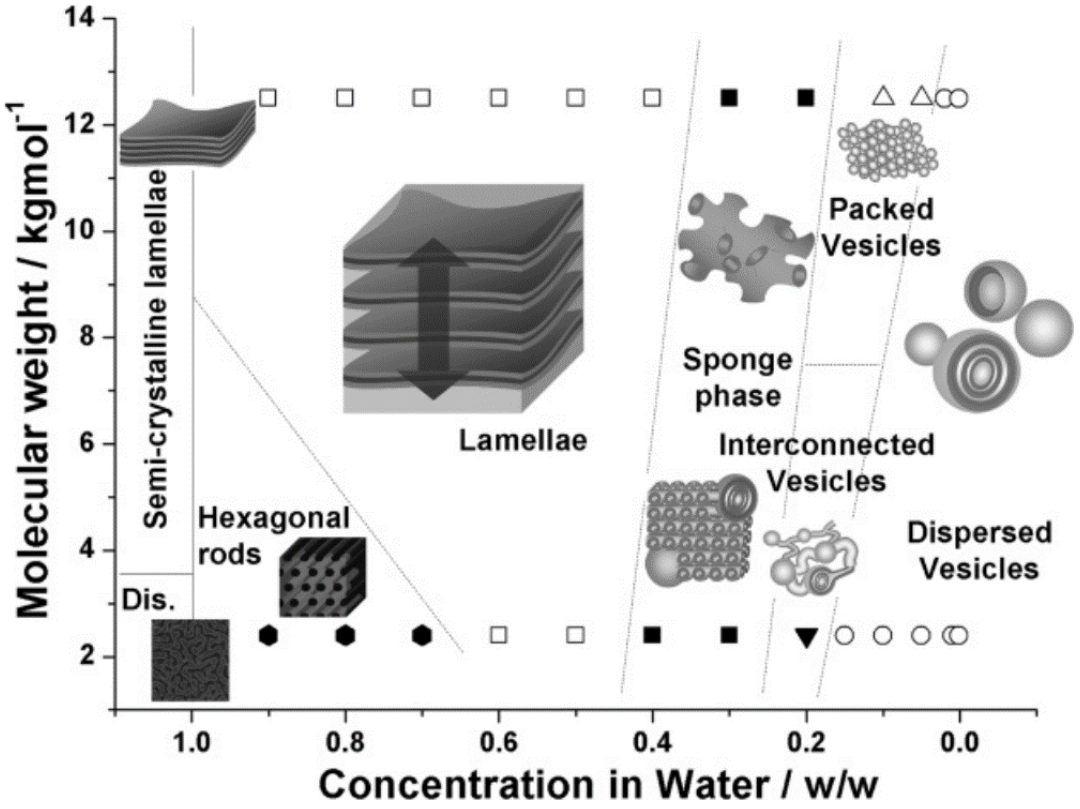

Figure 1. 4. Morphology map of poly(butylene oxide)-*b*-PEO (PBO-*b*-PEO) in water as a function of molecular weight and polymer concentration. The ratio between the hydrophobic:hydrophilic blocks was similar i.e., PBO_{22}-*b*-PEO_{16} (M_n = 2.3 kg/mol) or PBO_{103}-*b*-PEO_{115} (M_n = 12 kg/mol). Reproduced with permission from ref [66].

1.4 Influence of the Core Crystallization on BCP Self-Assembly

Nanofibers present morphological advantages and are desirable for a number of applications such as in nanomedicine,[67–69] composite reinforcement,[70,71] catalysis,[72] and optoelectronics.[13,73] 2D platelets are also good candidates for antibacterial purposes,[74] as emulsifiers,[75] and for enhancing the adhesive and mechanical properties of hydrogels.[76,77] However, preparation of pure morphological micellar assemblies with low curvature of the core-corona interface, such as 1D micelles or nanofibers and 2D platelets, from the solution state self-assembly of diBCPs with an amorphous core forming-block is particularly difficult to achieve, except for spherical micelles which are readily accessible and dominate the phase diagram.[78] In the case of BCPs that possess a crystallizable core-forming block,

the crystallization of the core provides an additional enthalpic contribution to the free energy of micellization and has an important influence on the resultant morphology (Table 1. 2). This drives the formation of morphologies with low core-corona interfacial curvature in order to minimize the free energy of the system.[39]

1.4.1 Crystallization-Driven Self-Assembly

The realization that crystallization of the core-forming block during self-assembly modifies morphological preferences has led to the introduction of the term crystallization-driven self-assembly (CDSA). CDSA of amphiphilic block copolymers with a crystallizable core-forming block has recently emerged as a promising and versatile method to obtain disperse 1D- and 2D-dimensional structures, with the resultant morphology generally being dependent on the core-to-corona block ratio based on the DP_n of each block.[39,79] Poly(ferrocenyldimethylsilane) (PFS) has been extensively used as the crystallizable core-forming block of BCPs for CDSA.[80–84] PFS-based BCPs typically form 2D platelet micelles when the core-to-corona block ratio is close to 1:1 and 1D micelles over a wide range of block ratios between 1:5 and 1:20 (Figure 1. 5).[79] The crystallization increases the thermodynamic stability due to the lattice energy term and the kinetic stability due to kinetic trapping, as unimer exchange becomes even more unfavorable. Furthermore, the critical micelle concentration of BCP with a crystallizable core-forming is effectively zero, allowing access to stable micelles even at very low concentrations.[39,85]

There are many methods to induce self-nucleation of BCPs with a crystallizable core-forming block. The two most relevant and widely used will be discussed. In the first, the diBCP is solubilized in a common solvent for both polymer segments to give molecular dissolved ‘unimers.’ The slow addition of a selective solvent for the corona-forming block

leads to precipitation and usually crystallization of the core-forming block. A second, more common method is to disperse the BCP in a selective solvent mixture for the corona-forming block, then heat the solution such that dissolution of both blocks to form unimers occurs at an elevated temperature. In this case, precipitation and usually crystallization of the core-forming block occurs upon slow cooling. The polymeric nanoparticles formed are generally length-disperse 1D micelles if the corona-forming block is substantially larger than that of the core-forming block, or disperse 2D platelets if this is not the case (Figure 1. 5),[86] although exceptions to this trend exist.[87]

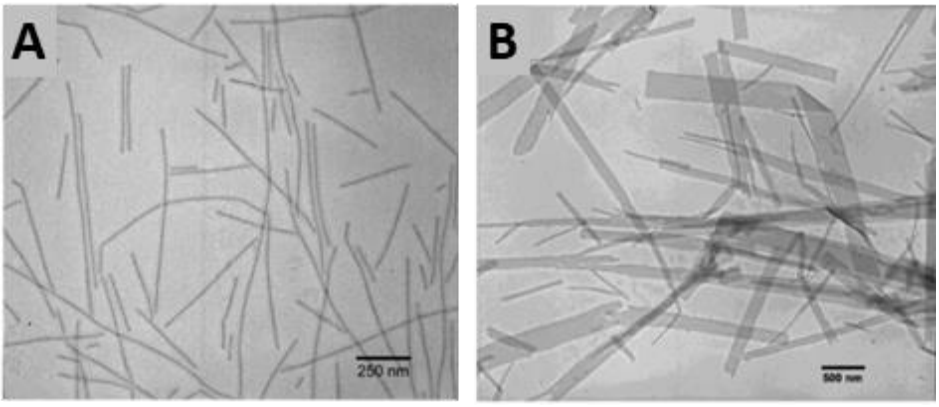

Figure 1. 5. Examples of morphologies accessed via the CDSA of PFS-b-PI BCPs in tetrahydrofuran/hexane mixtures. TEM micrographs of A) 1D micelles made from PFS_{53}-b-PI_{320} and B) 2D micelles made from PFS_{60}-b-PI_{30} (scale bar: 500 nm). PFS: poly(ferrocenyldimethylsilane). PI: polyisoprene. Reproduced and adapted with permission from ref [86].

CDSA is a unique method for the creation of length-disperse pure morphological nanofiber assemblies with increasing relevance. In the last two decades a wide range of BCPs containing a crystallizable core-forming block have shown to assemble via CDSA including: polyacetylene,[88] poly(acrylonitrile),[89] poly(ε-caprolactone) (PCL),[87,90,91] poly(di-n-dihexylfluorene) (PDHF),[73,92,93] poly(ethylene oxide) (PEO),[94,95] poly(ethylenesulfide),[96] poly(ferrocenyldimethylgermane) (PFG),[97,98] poly(fluorenetrimethylenecarbonate) (PFTMC),[99,100] poly(L-lactic acid) (PLLA),[101–103]

poly(3-heptylselenophene),[104,105] poly(3-hexylthiophene) (P3HT),[106–109] poly(2-isopropyl-2-oxazoline),[110,111] poly(3-octylthiophene),[112] poly(perfluoroethyloctyl-methacrylate),[113,114] poly(p-phenylene),[115] poly(p-phenylenevinylene),[116,117] and poly(p-phenyleneethynylene).[118,119]

1.4.2 Living Crystallization-Driven Self-Assembly (Living CDSA)

The dispersity index ($Đ$) is a measure of the nanoparticle size heterogenicity, with $Đ \leq 1.1$ considered of low dispersity, and $Đ > 1.1$ being considered disperse. Low dispersity assemblies of controlled geometries are highly desirable for several applications,[120] but are generally hard to achieve.[42,121] Any conclusion drawn from the effect of a nanoparticle formulation is not reliable when working with disperse samples since the nanoparticle size is largely different and negative or positive results could be an artifact of only a fraction of the nanoparticle population.[121,122] Therefore, CDSA on its own is not a particularly useful technique for such applications.

Living Crystallization-Driven Self-Assembly (living CDSA) is a method that differs from CDSA where nucleation and growth stages of micelle formation do not overlap as the former is avoided by the use of seeds. Living CDSA can therefore be used to grow 1D or 2D BCP micelles with a crystalline core with high precision and low length or area dispersity, respectively ($Đ < 1.1$) (Figure 1. 6). Living CDSA can be thought of as an analogous process to living covalent polymerization of molecular monomers, where the micelle grows proportionally with the addition of more BCP.[123]

To form low dispersity 1D or 2D micelles with length control two methods can be used, self-seeding and seeded growth. The self-seeding approach involves gentle sonication of disperse 1D micelles prepared by CDSA. Next, the smaller fragments are

heated below the annealing temperature enabling partial dissolution of BCPs. Upon slow cooling, the unimers released are able to crystallize at the ends of the remaining micelle fragments and grow epitaxially. The final length of the micelles can then be controlled by the annealing temperature and time (Figure 1. 6, top). A similar process can be achieved by addition and subsequent removal of common solvent from the system under ambient conditions.[124] In seeded growth, ultrasonication is used to cleave the length-disperse nanofibers made via CDSA to yield smaller fragments termed "seeds." When unimer is added to a seed solution, bidirectional epitaxial growth from the crystalline core of the seed termini occurs (Figure 1. 6, bottom).[123] The length of the resulting nanofibers can be predicted and controlled by altering the m_{unimer}/m_{seed} ratio (also known as equivalents), where m_{unimer} is the mass of polymer, and m_{seed} is the mass of the seeds (Figure 1. 6B-F).[39,123]

In self-seeding, the seeds and unimers are generated in situ and the ratio depends on the BCP concentration and sample thermal history. This limits the ability to prepare 1D or 2D micelles of predetermined dimensions and to scale the process. On the contrary, the seeded growth method allows to predict the dimensions of the 1D or 2D micelles in advance as the seeds are preformed rather that generated in situ. Therefore, seeded growth can be conducted at ambient temperature and be scale up as the nanoparticle dimensions are independent of the BCP concentration in solution.[120,125] The seeded growth method is more common than the self-seeding approach. The work described in this thesis utilizes the seeded growth method.

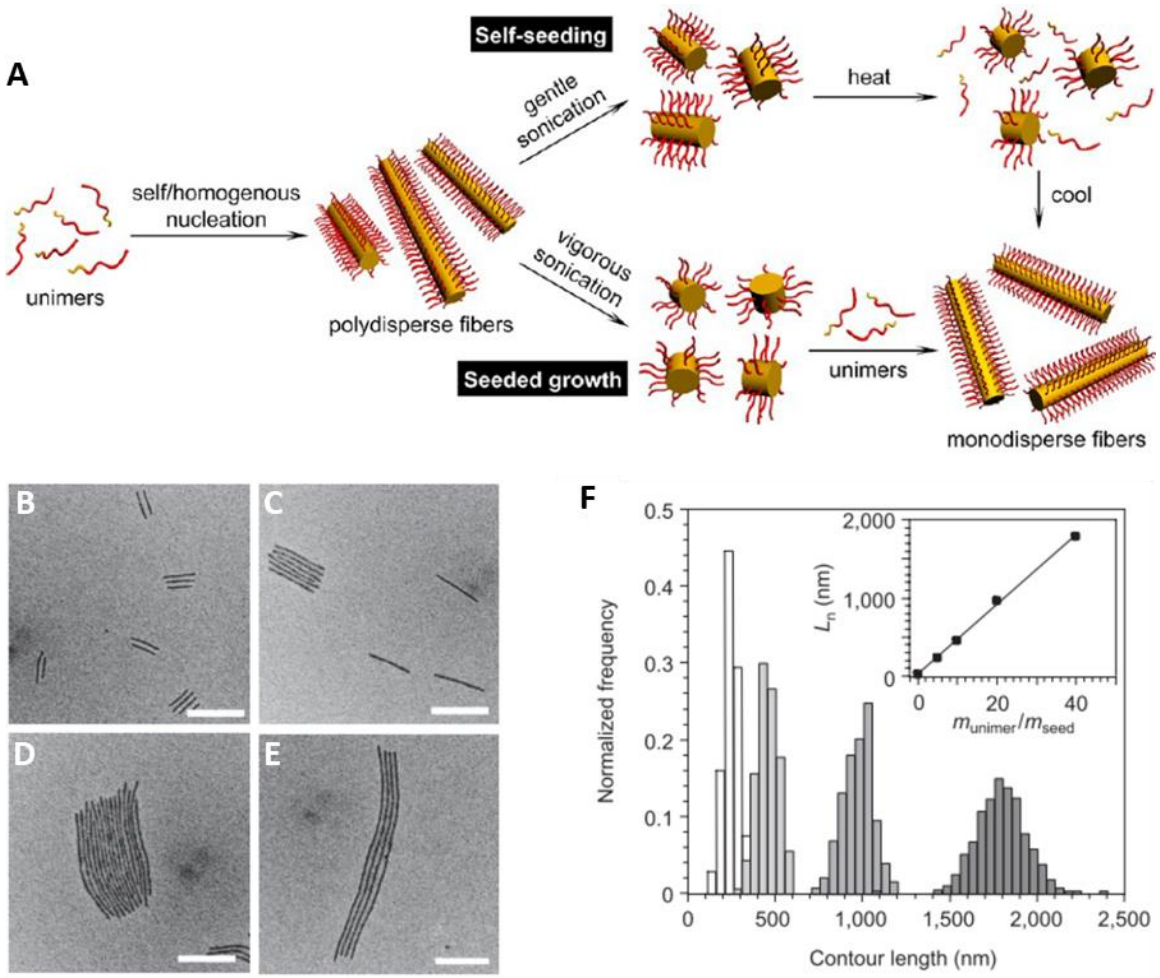

Figure 1. 6. A) Representation of living crystallization driven self-assembly by both self-seeding and seeded growth methods. TEM micrographs of PFS_{50}-*b*-poly(isoprene)$_{550}$ nanofibers prepared via the seeded growth method in *n*-hexane at different m_{unimer}/m_{seed} ratios: B) 5, C) 10, D) 20, and E) 40. F) Contour length histograms and nanofiber length (L_n) vs m_{unimer}/m_{seed} of the nanofibers in B-E. Scale bar: 500 nm. A reproduced with permission from ref [126]. B-F reproduced with permission from ref [123].

Living CDSA is a versatile method from which a range of morphologies can be accessed through the addition of compatible yet distinct BCP unimers to preformed seeds in a sequential fashion to yield segmented micelles.[84,127,128] For instance, 2D micelles were prepared by addition of PLLA BCPs and PLLA homopolymers with charged termini yielding segmented 2D micelles with spatially defined coronal-chemistries (Figure 1. 7A-C).[129] In a similar way, fluorescently-labelled color-coded PFS-based BCPs with core:corona ratios corresponding to 2D micelles were added sequentially to preformed

cylindrical micelles yielding segmented 2D lenticular platelets (Figure 1. 7D-F).[79] Living CDSA has also allowed other kind of morphological self-assemblies such as javelin-like micelles,[126] both centrosymmetric and non-centrosymmetric arrow-like micelles,[79] and branched micelles,[126] usually at low concentrations of solids ca. <0.5% *w/w*.[79,126]

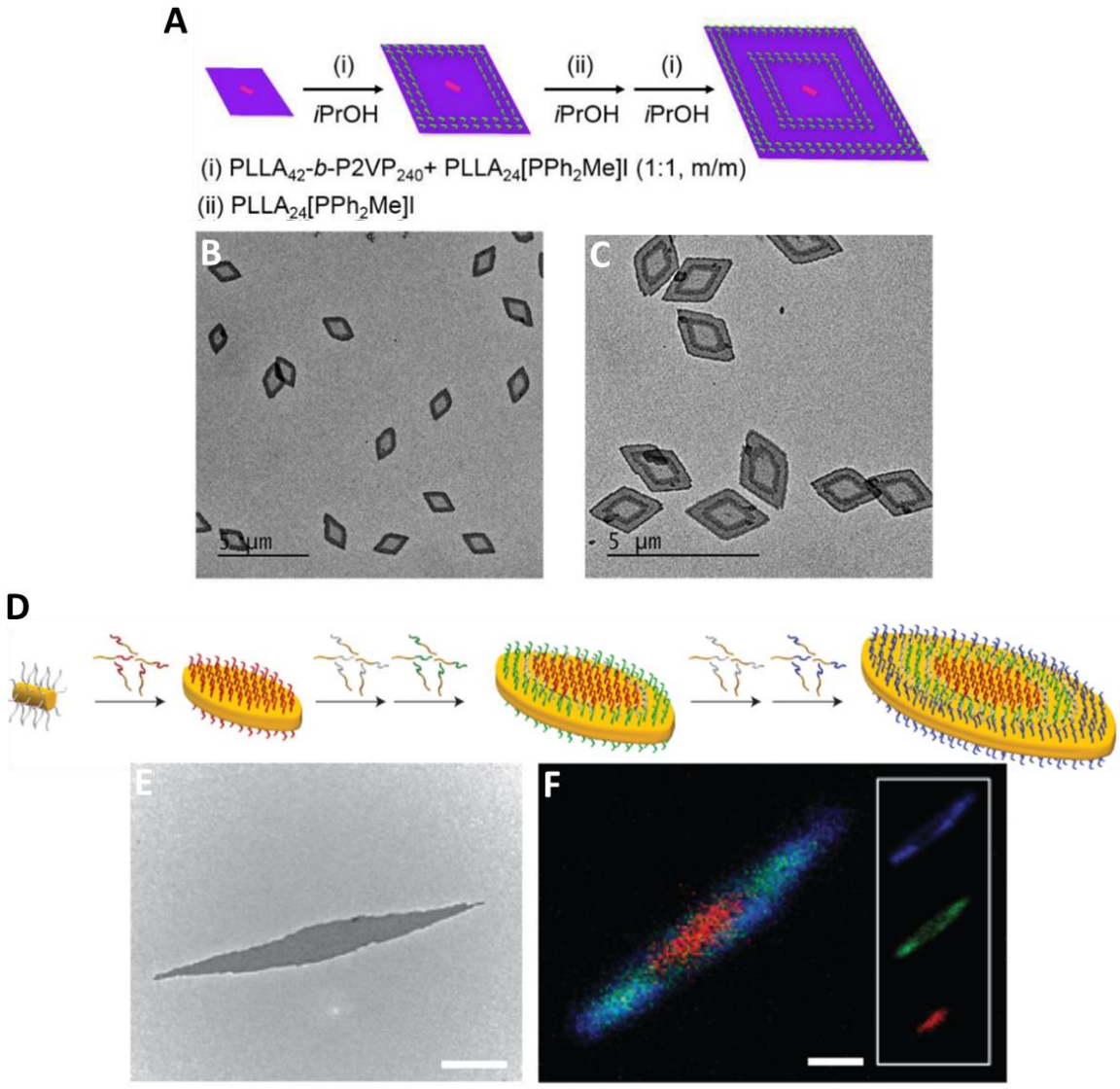

Figure 1. 7. A) Representation of the formation of 2D diamond-shaped segmented micelles with PLLA-based BCPs and homopolymers via living CDSA. TEM micrographs of diamond-shaped micelles: B) after addition of (i), and C) after addition of (ii) and (i) to the micelles in B. D) Representation of the formation of spatially segmented lenticular platelets by the addition of dye-tagged PFS-based BCPs. E) TEM, and F) laser confocal scanning microscopy (LCSM) micrographs of the segmented lenticular platelets. A-C reproduced and adapted with permission from ref [129]. D-F reproduced and adapted with permission from ref [79].

1.4.3 Living CDSA with Molecular Amphiphiles

CDSA and living CDSA are not limited to the use of BCPs with a crystallizable core-forming block. Analogous methods have been applied to small molecular amphiphile systems.[130,131] For instance, thiol-functionalized peptides[130,132] and zinc porphyrin amphiphiles[133,134] have been used in strategies similar to living CDSA to achieve dimensional control. More complex segmented nanofibers with spatially segmented fluorescent dye-tags and organic heterostructures have also recently been prepared from amphiphilic naphthalene diimide derivates (Figure 1. 8).[135–137]

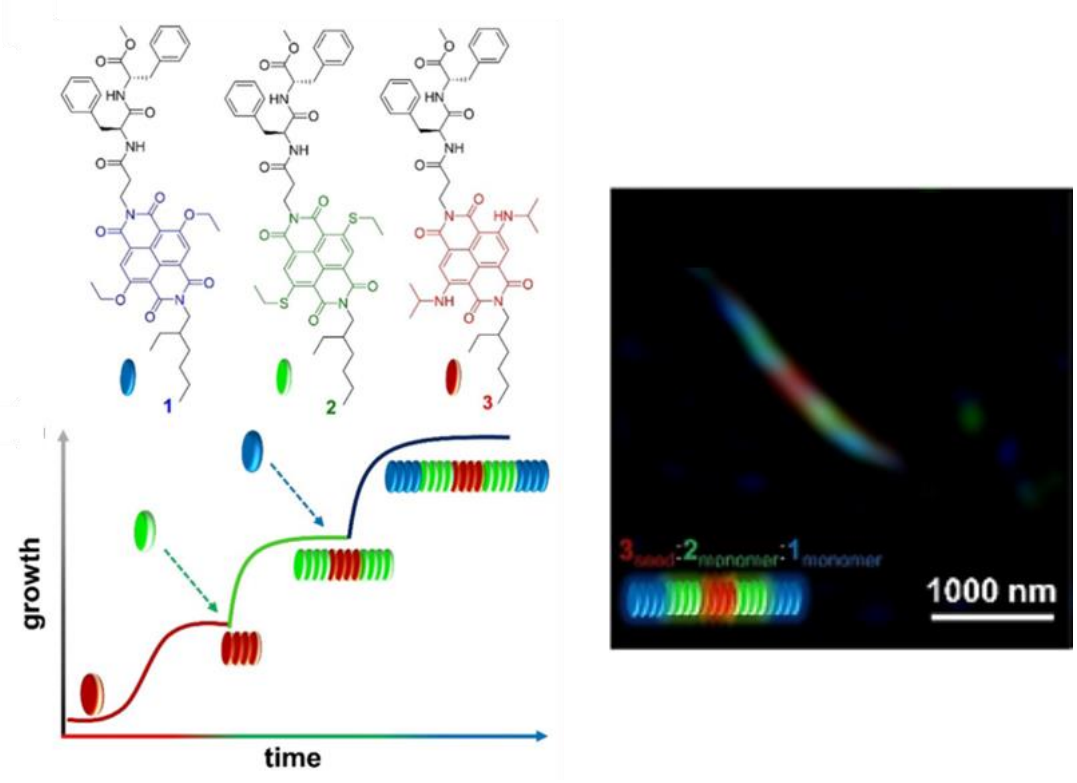

Figure 1. 8. Structure amphiphilic naphthalene diimides derivatives, plot of the sequential seeded growth process, and LCSM of pentablock fibers. Reproduced and adapted with permission from ref [135].

1.4.4 Hierarchical Architectures from Crystalline Core Micelles

Nanostructures with higher degrees of order have been developed from segmented micelles that can further self-assemble. Amphiphilic nanofibers with polar and non-polar

coronal segments will self-assemble when transferred into a solvent that is poor for one of the segments but good for the other. For example, triblock segmented BCP nanofibers made from PFS-*b*-poly(dimethylsiloxane) (PDMS) and two PFS-*b*-poly(2-vinylpyridine) (P2VP) flanking segments were prepared via living CDSA. Transfer of the triblock segmented nanofibers to a poor solvent for the PDMS-block, such as isopropanol, led to aggregation of the nanofibers. By modulating the length of the PFS-*b*-PDMS and PFS-*b*-P2VP nanofiber segments, the morphology of the resulting hierarchical assemblies was controlled from thin and wide train track-like architectures (Figure 1. 9A-B), to 3D superlattices through end-to-end stacking (Figure 1. 9C).[138] Furthermore, hydrogen bonding between the coronal blocks of PFS-based segmented nanofibers has allowed access to other morphologies such as windmill-like supermicelles (Figure 1. 9D).[139] In another example, PFS-based nanofibers functionalized with carboxylic acid moieties were used to stabilize water-in-oil Pickering emulsions yielding colloidosomes which were subsequently crosslinked. Epitaxial growth was observed from the nanofibers surrounding the colloidosomes after sequential addition of functional dye-tagged PFS-based unimers (Figure 1. 9E).[140]

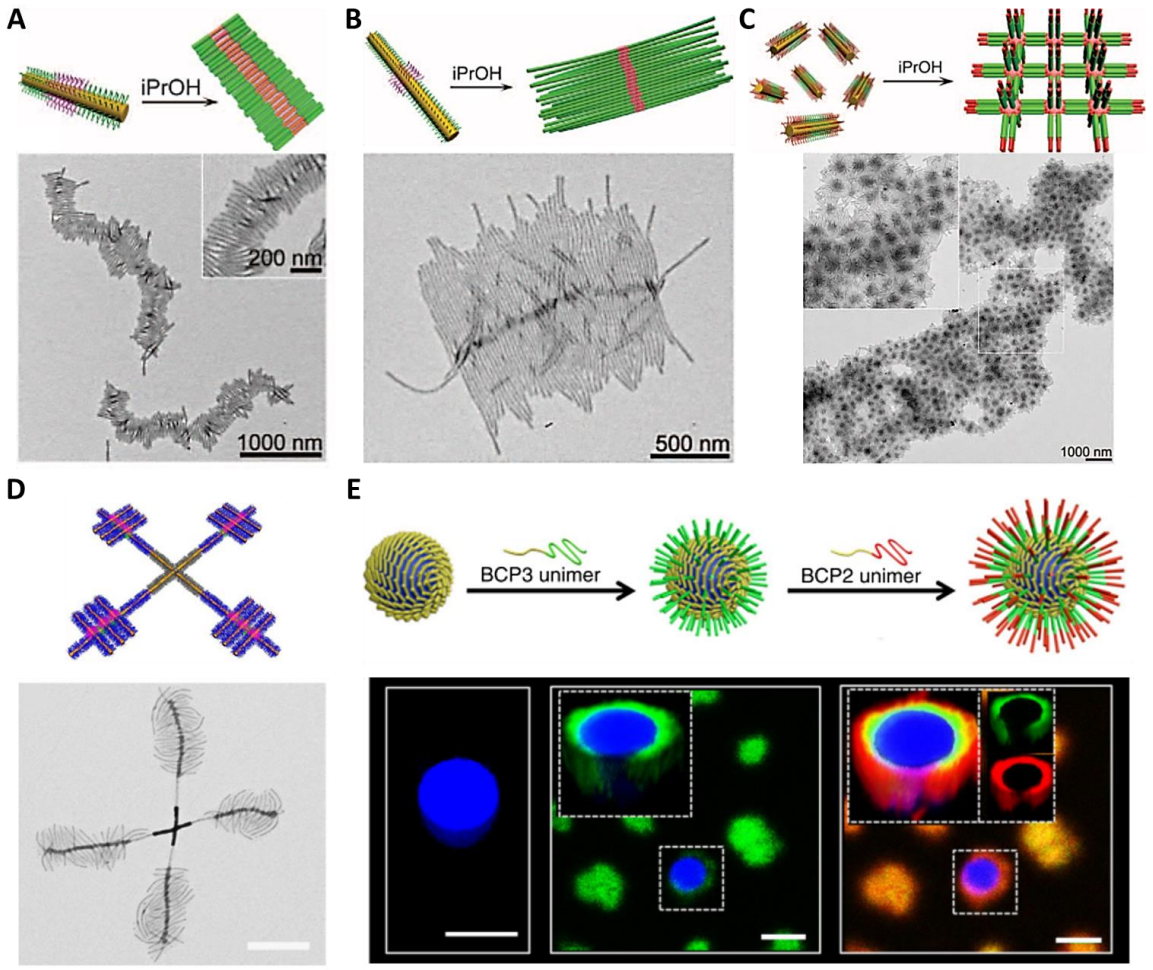

Figure 1. 9. Hierarchical architectures prepared via the self-assembly of PFS-based nanofibers. A-C) Segmented nanofibers made from PFS-*b*-PDMS (green) and PFS-b-P2VP (red) BCPs. A) Schematic and TEM micrograph of hierarchical train track-like micelles prepared from nanofibers with PDMS segments of 35 nm and P2VP segments of 340 nm. B) Schematic and TEM micrograph of hierarchical train track-like micelles prepared from nanofibers with PDMS segments of 55 nm and P2VP segments of 560 nm. C) Schematic and TEM micrograph 3D superlattices formed when short flanking PDMS segments were used (105 nm). D) Schematic and TEM micrograph of a windmill-like supermicelle prepared via hydrogen-bonding interactions between the coronal-blocks of PFS-based segmented fibers, scale bar: 500 nm. E) Schematic and LCSM micrograph of colloidosomes prepared by water-in-oil Pickering emulsions from PFS_{25}-*b*-$PMVS\text{-}COOH_{245}$ nanofibers stabilized by crosslinking and subsequent living CDSA with dye-tagged PFS BCPs, PMVS: poly(methylvinylsiloxane), scale bar: 5µm. A-C reproduced and adapted with permission from ref [138]. D reproduced and adapted with permission from ref [139]. E reproduced and adapted with permission from ref [140].

1.5 Applications of High Aspect Ratio Block Copolymer Micelles for Biomedical Applications

Amorphous and crystalline core-forming BCP nanoparticles offer desirable properties for biomedical applications including low toxicity, biocompatibility, and high functionalization (Figure 1. 11A).[141] Applications of BCP micelles have been extensively reviewed,[142–152] therefore this section focuses on challenges and examples of the use of high aspect ratio nanofibers for biomedical applications, particularly for drug delivery, materials reinforcement, and tissue engineering, in line with the aims of the work presented in this thesis.

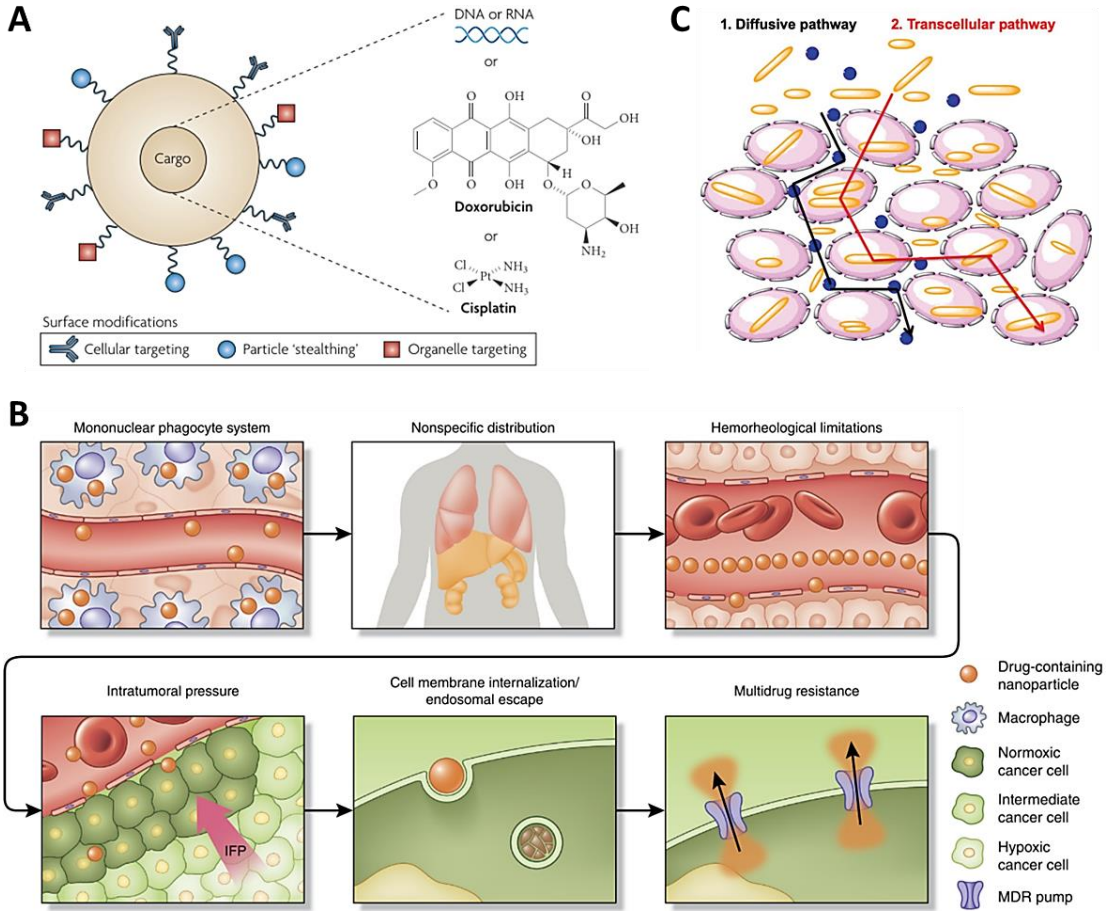

Figure 1. 10. A) Representation of a spherical nanoparticle engineered for cargo loading and targeting. B) Sequential physiological barriers for drug delivery vectors. MDR: multidrug resistance, IFP: interstitial fluid pressure. C). Postulated diffuse (dark arrow) and transcellular (red arrow) pathways for spheres and nanofibers, respectively. A Reproduced with permission from ref [153]. B Reproduced with permission from ref [14]. C Reproduced with permission from ref [154].

1.5.1 Nanoparticle Drug-Delivery Vehicles: Considerations and Examples

One of the biggest challenges of medicine is the delivery of therapeutic agents to specific tissues whilst overcoming many of the physiological barriers present in the human body (Figure 1. 11B).[14] A further complication is that 40% of drugs with market approval and ca. 90% of new drug candidates are poorly soluble in water.[155] Nanoparticle drug-delivery vehicles made from the self-assembly of BCPs have been designed to address these limitations by virtue of the high tunability of the polymeric building blocks and their ability to encapsulate drug molecules.[151,156,157] From the several parameters that will dictate the performance of a drug-delivery vehicle, the most relevant ones for the work described in this thesis are the size, morphology and the dispersity, *Đ*, of the nanoparticles.[158,159] The relevance of *Đ* is discussed in section 1.4.2 . A summary of relevant characteristics to be considered for the design of drug-delivery vectors is presented in Table 1. 3.

Table 1. 3. Summary of relevant parameters for the design of polymeric drug-delivery vectors. Reproduced and adapted with permission from ref [151].

Characteristic	Effect, reason, or description
Shape	Modifies retention times, distribution, toxicity, cellular uptake, intracellular fate, and immune system recognition.
Size	20-200 nm most promising nanoparticle sizes for in vivo applications.
Stability	No drug leakage, dissociation, or detachment.
Stealth	To prevent interaction with plasma proteins, avoid recognition and opsonization. Increase circulation times.
Surface chemistry	Anionic or neutral charges generally have higher circulation times. Positive charges are cleared out of the body faster.
Targeting	Moieties to target specific tissues, and subcellular compartments while avoiding lysosomal degradation. Stimuli-responsive agents.
Administration route	Effect on the barriers faced depending on the entry route.

1.5.1.1 Size

Size-dependent effects have been identified as modifiers of the cell viability, endocytosis rates, and metabolism.[160,161] Furthermore, the size of the delivery vehicle is important as it relates to the mechanism by which it will be cleared from the body and therefore it impacts the circulation times of a nanoparticle system. Nanoparticles <5 nm in diameter will undergo fast renal clearance upon intravenous administration. Nanoparticles >200 nm in size will undergo splenic filtration, and particles from 2 – 5 μm will tend to readily accumulate within the capillaries of the lungs.[14] Most tumor blood vessels have fenestrations of ca. 200 nm. Nanoparticles from 100 – 200 nm have shown ability to extravasate from blood vessels to tumors.[14] However, if the targeted tissue is within the brain the nanoparticle needs to traverse the blood-brain-barrier which has a pore size of ca. 12 nm. In general, dimensions of 20 – 200 nm represents the most promising nanoparticle size range for in vivo applications, however, the pore size of the final targeted tissue also needs to be considered.[151]

1.5.1.2 Shape

The most commonly studied nanoparticle morphology for drug-delivery is spherical.[162] The widespread development of spherical vectors results from the easy access to spherical micelles via amorphous BCP self-assembly.[39,78] However, high aspect ratio nanoparticles termed nanofibers, nanoworms, fiber-like, and rod-like micelles have been the subject of recent investigations and significant advantages for certain applications have been attributed to their inherent morphology.[163,164] For example, PEGylated BCP fiber-like micelles with core-forming blocks of either biodegradable PCL or poly(ethylethylene) with lengths of 1 and 8 μm were shown to circulate ten-times longer than spherical analogues.

This was attributed to the alignment of the fiber-like micelles with the blood flow imparted by hydrodynamic forces. The fiber-like micelles delivery performance of paclitaxel to tumor models was also higher than the studied spheres.[67] Tumor penetration by high aspect ratio nanoparticles also appears to be higher than spherical micelles. For example, the tumor penetration of PEGylated gold-doped nanostructures was higher than with spherical and discoidal analogues in mice models.[165] Recently, PFS-based nanofibers made via living CDSA were shown to internalize more efficiently than spherical micelle counterparts into multicellular tumor spheroids. The authors postulated that the nanofibers followed a more efficient transcellular pathway than the diffusive pathway taken by the spheres (Figure 1. 11C).[154] Antibody-functionalized polystyrene worm-like particles have shown lower uptake rates than spherical analogues by phagocytes.[166] Furthermore, the uptake by RAW 264.7 macrophages of spherical nanoparticles, made from PLLA-based BCPs functionalized with mannose was higher than the cylindrical counterparts prepared via living CDSA.[167]

1.5.1.3 Nanoparticle Surface Functionality

The nanoparticle surface plays a pivotal role as it can affect the hydrophobicity, immunogenicity, surface charge, circulation time, distribution and internalization mechanisms of delivery vectors.[151] For example, PEG has been used widely to increase the circulation times and provide a stealth barrier to nanoparticles.[168,169] To enhance the nanoparticle specificity antibodies and peptides have been conjugated to the nanoparticle surface.[14,151,170,171] Stimuli responsive approaches have also been developed to increase nanoparticle selectivity via pH-sensitive, thermoresponsive, and ultrasound methods.[151,172] Of interest to the research described in this thesis, polysaccharides have been also used for

the targeting of cancer tissues.[173,174] Other molecules such as folic acid have also been employed to target the folate receptors overexpressed in cancer cells.[175,176] Buffering agents can be incorporated into the surface of nanoparticles for endosomal escape to avoid lysosomal degradation.[177] Overall, there are a vast range of tools to decorate the surface of nanoparticles and different considerations that need to be taken into account when designing a drug delivery vector, including the size, the shape, the *Đ*, and the surface chemistry, as there is no universal formula suited for every application.

1.5.1.4 Nanofibers for Drug Delivery Applications: A Brief Perspective

Despite the progress in the field, in 2016 a thorough study of 232 articles from 2005 – 2015 revealed that the overall nanoparticle delivery efficiency towards tumors was of only 0.7%, which means that only 7 out of 1,000 nanoparticles entered a solid tumor in mouse models (Figure 1. 11A).[178] However, the same study underscored that the highest delivery efficiency to tumors was achieved by high aspect ratio nanoparticles (Figure 1. 11B).[178] The higher performance of nanofibers or rod-like structures for some applications is likely related to the morphological advantages of these kind of structures compared to spherical or other shape analogues as mentioned earlier in section 1.5.1.2 . However, nanofibers are the least developed nanoparticle morphology. This may be explained by the difficulty associated to access pure morphological 1D micellar assemblies with precise control on the length and with low length-dispersities.[179] Only a few examples were morphologically pure, non-covalently loaded, fiber-like solutions have been reported.[67,68,180] Morphologically pure, length-controlled, and low dispersity polymeric fiber-like drug loaded formulations, where cargo is non-covalently bound, have not been reported. This drawback results from the processing method were BCP self-assembly and

cargo loading coincide in time and space,[17,180–184] thus limiting the control over the nanoparticle properties. Living CDSA, although a promising method for the preparation of pure 1D micelles of controlled length and low dispersities, is limited by the inability of the crystalline core to encapsulate cargo.[185–187] To address this, covalent corona loading strategies have been developed,[188] but non-covalent loading is desirable to facilitate drug release. Furthermore, this loading method may be unsuitable for drug molecules with poor solubility in aqueous media. Another issue is that a limited number of crystallizable core-forming BCPs potentially suitable for biomedical applications are currently known to undergo living CDSA.[91,102,111,189] Although it appears that nanofiber-based therapeutics have very promising potential for drug-delivery applications, the need of viable nanofiber systems and methods for the non-covalent loading of length-controlled nanofibers have prevented their use. Therefore, an important aim of the research described in this thesis was to bridge the gap between the development of nanofibers made via living CDSA and their non-covalent loading.

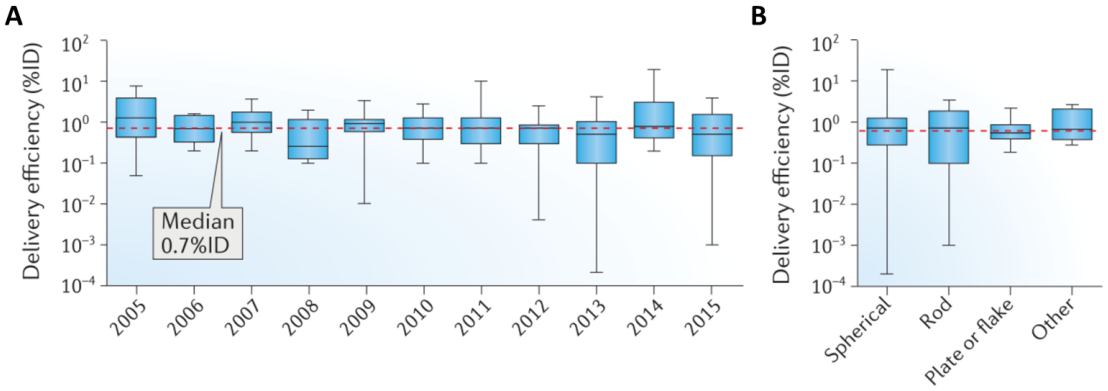

Figure 1. 11. A) Nanoparticle delivery efficiency to solid tumors from 2005 – 2015.B) Delivery efficiency to solid tumors based on the morphology of the nanoparticle vector. Data presented results from 232 data sets published from 2005 – 2015. The blue boxes represent the 25th to 75th percentiles. Black lines the median value, and the red dashes indicate the median of the nanoparticle delivery efficiency. Reproduced and adapted with permission from ref [178].

1.5.2 Nanofibers for Materials Reinforcement and Tissue Engineering

Fiber-like BCP nanoparticles have found applications in the materials reinforcement field. For example, poly(ethylene-*alt*-propylene)-*b*-PEG wormlike micelles were blended within a bisphenol A-based epoxy resin. The fracture toughness of the resulting resin containing wormlike micelles was improved by more than 100% compared to the epoxy resin on its own. Compared to the epoxy resin containing spherical analogues, the wormlike-containing resin performed considerably better.[190] Nanofibers made via CDSA have also been spin-coated onto polystyrene fibers rendering nonwovens catalytically-active.[191] In a recent contribution, the role of nanoparticle shape in the adhesive and mechanical properties of hydrogels was reported, although in this case platelets outperform nanofibers which were shown to outperform spheres.[76] Enhancement of alginate hydrogel mechanical properties has also been evaluated based on the length of nanofibers made via living CDSA. The strain at flow point was enhanced by 37% with nanofibers of ca. 500 nm in length.[70] Since most extracellular matrices (ECMs) are made from hydrogels with fibrous networks,[192,193] it is of significant relevance for the tissue engineering field to develop hydrogel-fiber systems to advance the field as it has been shown that the ECM mechanics plays an important role in stem cell differentiation.[194,195] To further develop the materials reinforcement and the tissue engineering fields nanofiber networks could be utilized to enhance the properties of composites. However, the formation of BCP micellar networks has mainly been achieved with spherical nanoparticles at high concentrations via the self-assembly of associative triblock copolymers (triBCPs),[65,196–199] Figure 1. 12. Chapter 4 of this thesis focuses on the formation of nanofiber micellar networks.

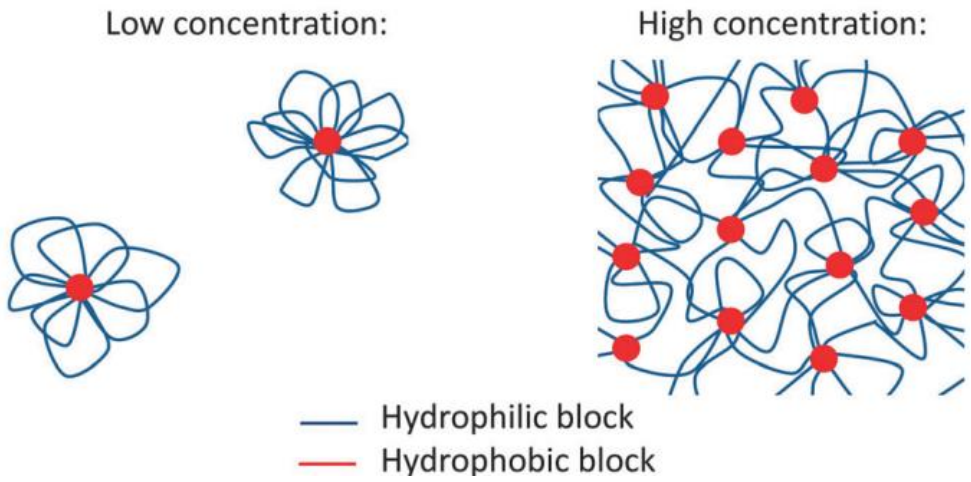

Figure 1. 12. Representation of spherical flower-like micelle networks formed from triBCPs at high concentrations. Reproduced with permission from ref [200].

1.6 Synthesis of Polycarbonate BCPs

Aliphatic polycarbonates are promising biomaterials owing to their degradability, biocompatibility, and low toxicity.[201] It has been shown that aliphatic polycarbonates undergo accelerated enzymatic degradation in vivo and slow hydrolytic degradation in vitro with no harmful degradation products.[202] These materials are relevant for a range of uses, including drug delivery and biomedical applications.[203,204] The ring-opening polymerization (ROP) of cyclic carbonate monomers is one of the best strategies for the control over the molecular weight and polymer architecture. Polycarbonate-based materials can be synthesized by ROP via organocatalytic, anionic, cationic, coordination-insertion, or enzymatic methods.[205] In this thesis, the preparation of polycarbonate materials for the preparation of BCPs is conducted via the organocatalytic method with 1,8-diazabicyclo[5.4.0]undec-7-ene (DBU) as catalyst for the ROP of the cyclic carbonate monomer fluorenetrimethylenecarbonate (FTMC) (Scheme 1. 1). Poly(fluorenetrimethylenecarbonate) (PFTMC) was selected as the crystallizable core-

forming block of the BCPs used in this thesis as the self-assembly of PFTMC-based BCPs in selective solvents have yielded crystalline core-forming nanofibers.[99]

Scheme 1. 1. Synthesis of PFTMC via ROP of the cyclic fluorenetrimethylenecarbonate monomer. Catalyst used 1,8-diazabicyclo[5.4.0]undec-7-ene (DBU).

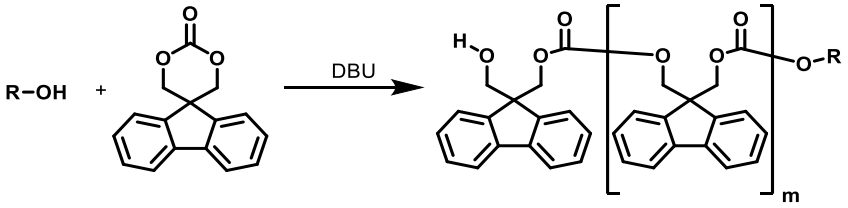

1.7 Thesis Research Objectives

The introduction of this thesis has discussed basic principles and recent advances of supramolecular and BCP self-assembly, with emphasis on specific examples of nanoparticles utilized for biomedical applications. CDSA and living CDSA have been used as convenient methods towards the development of non-spherical micelles with low core-corona interfacial curvatures such as 1D micelles and 2D platelets with controlled dimensions. Sequential living CDSA have also been utilized to generate 1D and 2D micelles with segmented chemistries. Beyond single nanoparticles, hierarchical self-assemblies have been prepared by exploiting the interactions between the corona-forming blocks of 1D fiber-like micelles. However, most of the research regarding nanoparticles with crystalline core-forming blocks has focused on non-biomedical applications, and is mainly based on PFS-containing BCPs. Therefore, the overall aim of the work described in this thesis is to develop high-aspect-ratio crystalline core nanofibers with well-defined dimensions, segmented chemistries, and nanofiber networks for use in biomedical applications based on the self-assembly of PFTMC-containing BCPs.

1.7.1 Exploration of the Non-Covalent loading of Nanofibers with a Crystalline Core

High-aspect ratio nanoparticles have demonstrated advantages for their use as drug-delivery vectors based on their morphological advantages and higher delivery efficiency to tumors, but loading of cargo in nanoparticles with such morphology is a major challenge. The dimensions of most polymeric nanofibers intended to be used for drug-delivery are not well controlled, and there was no study of a drug-loaded polymeric nanofiber system with controlled dimensions reported prior to this work. One of the objectives of the research described in this thesis is to develop water-soluble nanofibers with crystalline cores and of controlled dimensions capable of loading cargo via non-covalent interactions to enable the use of nanofiber-based therapeutics. Therefore, the work described in Chapter 2 focus on the design and cargo loading of triblock copolymer coaxial-core nanofibers with a crystalline inner-core, an amorphous outer-core, and a water-soluble corona-forming block. In Chapter 3, the aim is to study the non-covalent loading of hydrophobic cargo by diBCP nanofibers. In addition, the effect of the chemical nature and the length of corona-forming blocks on the loading was investigated.

1.7.2 Development of Fiber-Like Micelle Networks

Discrete 1D and 2D nanoparticles made via CDSA protocols have proven useful for materials reinforcement and for enhancing the mechanical and adhesion properties of hydrogels. The premise of regenerative medicine is to restore the normal function of cells, tissues, and organs.[206] Tissue engineering uses extracellular matrices or hydrogels for the growth and development of synthetic tissues. Recently, 1D flower-like micelles were prepared from triBCPs via the living CDSA method, but only well-defined flower-like nanofibers were observed.[207] Micellar networks (or bundles) based on nanofibers with a

crystalline core have not been reported yet. Nanofiber networks may find applicability for materials reinforcement and for tissue engineering applications as the mechanical properties of a nanofiber bundle are expected to be higher than a discrete nanofiber and consequently composites may be stronger. The work described in Chapter 4 focus on the self-assembly of triBCP with crystallizable PFTMC terminal segments to yield, for the first time, fiber-like micelle networks.

1.7.3 Preparation of Nanofibers with Targeting Capabilities and Segmented Nanofibers

Chapters 2 and 3 of this thesis, focus on studies regarding the non-covalent cargo loading by coaxial-core and diBCP nanofibers. However, an efficient drug-delivery vector requires a degree of passive, active targeting, or both in the best scenario. The research in Chapter 5 aims to incorporate both passive and active targeting into PFTMC-based nanofibers by precisely controlling the length of the nanofibers and by incorporating a corona-forming block with known targeting capabilities. Finally, one of the objectives of the work described in Chapter 5 is to develop segmented nanofibers with sections suited for the multiple barriers and stages of the drug delivery process.

1.8 Thesis Structure and Collaborator Acknowledgements

1.8.1 Thesis Structure

This thesis is comprised of different research projects based on the self-assembly of PFTMC-containing block copolymers. One introduction chapter, four results chapters, and a final chapter is provided with a summary, future directions, and outlook. In line with the research group policy of Prof. Ian Manners, each result chapter of this thesis is self-contained with individual introduction, results, discussion, and summary sections in a

format that is suitable for publication and peer-review. The contents of each subsequent chapter are as follows:

Chapter 2: Cargo Encapsulation in Uniform, Length-Tunable Aqueous Nanofibers with a Coaxial Crystalline and Amorphous Core.

Chapter 3: Hydrophobic Cargo Loading of Uniform, Length-Tunable Aqueous Diblock Copolymer Nanofibers with a Crystalline Core at the Core-Corona Interface.

Chapter 4: Fiber-Like Micelle Networks from the Solution Self-Assembly of B-A-B Triblock Copolymers with Crystallizable Terminal Polycarbonate Segments

Chapter 5: Length-Tunable Water-Soluble Block Copolymer Nanofibers and Segmented Nanofibers with a Crystalline Core and a Polyfructose Corona for Cancer Targeting and Drug-Loading.

Chapter 6: Summary, Future Directions, and Outlook

1.8.2 Collaborator Acknowledgments

As part of a large research group, projects are generally conducted with collaboration of colleagues and credit for their contributions are acknowledged below.

Chapter 2: Reproduced from *Macromolecules* **2021**, *54* (12), 5784–5796. Synthesis of polymers, self-assembly, loading of nanofibers, and characterization conducted by Juan Diego Garcia Hernandez. Energy minimization calculations were conducted by Dr. Steven Street. AFM was conducted by Dr. Yuetong Kang. Laser confocal scanning microscopy was conducted in collaboration with Dr. Yifan Zhang. Initial scientific design of the experiments was conducted in collaboration with Dr. Steven Street and Prof. Ian Manners. Research was conducted at the University of Victoria.

Chapter 3: Contains unpublished results. Synthesis of polymers, characterization, and self-assembly were conducted by Juan Diego Garcia Hernandez. Loading of nanofibers were conducted in collaboration with Hayley Parkin. Initial scientific design of the experiments was conducted by Juan Diego Garcia Hernandez. Research was conducted at the University of Victoria.

Chapter 4: Contains unpublished results. Synthesis of polymers, and characterization were conducted by Juan Diego Garcia Hernandez. Self-assembly experiments were conducted in collaboration with Dr. Yuetong Kang and Dr. Tomoya Fukui. AFM was conducted by Dr. Yuetong Kang. Initial scientific design of the project conducted by Juan Diego Garcia Hernandez with input from Dr. John Finnegan. Research was conducted at the University of Victoria.

Chapter 5: Contains unpublished results. This research was conducted by Juan Diego Garcia Hernandez. Helpful discussions were provided by Dr. Chuanqi Zhao. Research was conducted at the University of Victoria.

Chapter 6: This work was conducted by Juan Diego Garcia Hernandez.

1.9 References

(1) Halley, J. D.; Winkler, D. A. Consistent Concepts of Self-Organization and Self-Assembly. *Complexity* **2008**, *14* (2), 10–17.

(2) Whitesides, G. M.; Grzybowski, B. Self-Assembly at All Scales. *Science* **2002**, *295* (5564), 2418–2421.

(3) Mendes, A. C.; Baran, E. T.; Reis, R. L.; Azevedo, H. S. Self-Assembly in Nature: Using the Principles of Nature to Create Complex Nanobiomaterials. *Nanomedicine and Nanobiotechnology* **2013**, *5* (6), 582–612.

(4) Zhang, F.; Yan, H. DNA Self-Assembly Scaled Up. *Nature* **2017**, *552* (7683), 34–35.

(5) Wang, P.; Meyer, T. A.; Pan, V.; Dutta, P. K.; Ke, Y. The Beauty and Utility of DNA Origami. *Chem* **2017**, *2* (3), 359–382.

(6) Dey, S.; Fan, C.; Gothelf, K. V.; Li, J.; Lin, C.; Liu, L.; Liu, N.; Nijenhuis, M. A. D.; Sacca, B.; Simmel, F. C.; Yan, H.; Zhan, P. DNA Origami. *Nat. Rev. Methods Prim.* **2021**, *1* (13), 1–38.

(7) Fratzl, P.; Weinkamer, R. Nature's Hierarchical Materials. *Prog. Mater. Sci.* **2007**, *52* (8), 1263–1334.

(8) Provenzano, P. P.; Vanderby, R. Collagen Fibril Morphology and Organization: Implications for Force Transmission in Ligament and Tendon. *Matrix Biol.* **2006**, *25* (2), 71–84.

(9) Wang, J. H. C. Mechanobiology of Tendon. *J. Biomech.* **2006**, *39* (9), 1563–1582.

(10) Gaut, L.; Duprez, D. Tendon Development and Diseases. *Wiley Interdiscip. Rev. Dev. Biol.* **2016**, *5* (1), 5–23.

(11) Liu, Y.; Ramanath, H. S.; Wang, D.-A. Tendon Tissue Engineering Using Scaffold Enhancing Strategies. *Trends Biotechnol.* **2008**, *26* (4), 201–209.

(12) Lu, W.; Lieber, C. M. Nanoelectronics From the Bottom Up. *Nat. Mater.* **2007**, *6* (11), 841–850.

(13) MacFarlane, L. R.; Shaikh, H.; Garcia-Hernandez, J. D.; Vespa, M.; Fukui, T.; Manners, I. Functional Nanoparticles through π-Conjugated Polymer Self-Assembly. *Nat. Rev. Mater.* **2021**, *6* (1), 7–26.

(14) Blanco, E.; Shen, H.; Ferrari, M. Principles of Nanoparticle Design for Overcoming Biological Barriers to Drug Delivery. *Nat. Biotechnol.* **2015**, *33* (9), 941–951.

(15) Stupp, S. I.; Palmer, L. C. Supramolecular Chemistry and Self-Assembly in Organic Materials Design. *Chem. Mater.* **2013**, *26* (1), 507–518.

(16) Iqbal, P.; Preece, J. A.; Mendes, P. M. Nanotechnology: The "Top-Down" and "Bottom-Up" Approaches. *Supramol. Chem. From Mol. to Nanomater.* **2012**, 1–14.

(17) Kumar, R.; Dalvi, S. V.; Siril, P. F. Nanoparticle-Based Drugs and Formulations: Current Status and Emerging Applications. *ACS Appl. Nano Mater.* **2020**, *3* (6), 4944–4961.

(18) Takahashi, S.; Suzuki, K.; Okano, M.; Imada, M.; Nakamori, T.; Ota, Y.; Ishizaki, K.; Noda, S. Direct Creation of Three-Dimensional Photonic Crystals by a Top-down Approach. *Nat. Mater.* **2009**, *8* (9), 721–725.

(19) H. Smith, K.; Montes, E. T.; Poch, M.; Mata, A. Integrating Top-down and Self-Assembly in the Fabrication of Peptide and Protein -Based Biomedical Materials. *Chem. Soc. Rev.* **2011**, *40* (9), 4563–4577.

(20) Lutz, J. F.; Ouchi, M.; Liu, D. R.; Sawamoto, M. Sequence-Controlled Polymers. *Science* **2013**, *341* (6146), 1238149–1238157.

(21) Thorkelsson, K.; Bai, P.; Xu, T. Self-Assembly and Applications of Anisotropic Nanomaterials: A Review. *Nano Today* **2015**, *10* (1), 48–66.

(22) Wang, L.; Gong, C.; Yuan, X.; Wei, G. Controlling the Self-Assembly of Biomolecules into Functional Nanomaterials through Internal Interactions and External Stimulations: A Review. *Nanomaterials* **2019**, *9* (2), 285–312.

(23) Aida, T.; Meijer, E. W.; Stupp, S. I. Functional Supramolecular Polymers. *Science* **2012**, *335* (6070), 813–817.

(24) Lehn, J. Perspectives in Supramolecular Chemistry—From Molecular Recognition towards Molecular Information Processing and Self-Organization. *Angew. Chemie Int. Ed. English* **1990**, *29* (11), 1304–1319.

(25) Rawat, R. S. Dense Plasma Focus - From Alternative Fusion Source to Versatile High Energy Density Plasma Source for Plasma Nanotechnology. *J. Phys. Conf. Ser.* **2015**, *591* (1), 012021.

(26) Grzelczak, M.; Vermant, J.; Furst, E. M.; Liz-Marzán, L. M. Directed Self-Assembly of Nanoparticles. *ACS Nano* **2010**, *4* (7), 3591–3605.

(27) Steed, J. W.; Turner, D. R.; Wallace, K. J. *Core Concepts in Supramolecular Chemistry and Nanochemistry*, 2nd ed.; John Wiley, 2007.

(28) Hoeben, F. J. M.; Jonkheijm, P.; Meijer, E. W.; Schenning, A. P. H. J. About Supramolecular Assemblies of π-Conjugated Systems. *Chem. Rev.* **2005**, *105* (4), 1491–1546.

(29) Grzybowski, B. A.; Wilmer, C. E.; Kim, J.; Browne, K. P.; Bishop, K. J. M. Self-Assembly: From Crystals to Cells. *Soft Matter* **2009**, *5* (6), 1110–1128.

(30) Wahl, M. C.; Sundaralingam, M. C-H…O Hydrogen Bonding in Biology. *Trends Biochem. Sci.* **1997**, *22* (3), 97–102.

(31) Wang, G.; Liu, S. Strategies to Construct a Chemical-Fuel-Driven Self-Assembly. *ChemSystemsChem* **2020**, *2* (4), 1–8.

(32) Leng, Z.; Peng, F.; Hao, X. Chemical-Fuel-Driven Assembly in Macromolecular Science: Recent Advances and Challenges. *Chempluschem* **2020**, *85* (6), 1190–1199.

(33) Ragazzon, G.; Prins, L. J. Energy Consumption in Chemical Fuel-Driven Self-Assembly. *Nat. Nanotechnol.* **2018**, *13*, 882–889.

(34) Hao, X.; Sang, W.; Hu, J.; Yan, Q. Pulsating Polymer Micelles via ATP-Fueled Dissipative Self-Assembly. *ACS Macro Lett.* **2017**, *6* (10), 1151–1155.

(35) Safdar, M.; Khan, S. U.; Jänis, J. Progress toward Catalytic Micro- and Nanomotors for Biomedical and Environmental Applications. *Adv. Mater.* **2018**, *30* (24), 1–27.

(36) Shao, J.; Abdelghani, M.; Shen, G.; Cao, S.; Williams, D. S.; Van Hest, J. C. M. Erythrocyte Membrane Modified Janus Polymeric Motors for Thrombus Therapy. *ACS Nano* **2018**, *12* (5), 4877–4885.

(37) Lombardo, D.; Kiselev, M. A.; Magazù, S.; Calandra, P. Amphiphiles Self-Assembly: Basic Concepts and Future Perspectives of Supramolecular Approaches. *Adv. Condens. Matter Phys.* **2015**, *2015* (151683), 1–22.

(38) Greaves, T. L.; Drummond, C. J. Solvent Nanostructure, the Solvophobic Effect and Amphiphile Self-Assembly in Ionic Liquids. *Chem. Soc. Rev.* **2013**, *42* (3), 1096–1120.

(39) Tritschler, U.; Pearce, S.; Gwyther, J.; Whittell, G. R.; Manners, I. 50th Anniversary Perspective: Functional Nanoparticles from the Solution Self-Assembly of Block Copolymers. *Macromolecules.* **2017**, *50* (9), 3439–3463.

(40) Blanazs, A.; Armes, S. P.; Ryan, A. J. Self-Assembled Block Copolymer Aggregates: From Micelles to Vesicles and Their Biological Applications. *Macromol. Rapid Commun.* **2009**, *30* (4–5), 267–277.

(41) Mai, Y.; Eisenberg, A. Self-Assembly of Block Copolymers. *Chem. Soc. Rev.* **2012**, *41* (18), 5969–5985.

(42) Doncom, K. E. B.; Blackman, L. D.; Wright, D. B.; Gibson Ab, M. I.; O'Reilly, R. K. Dispersity Effects in Polymer Self-Assemblies: A Matter of Hierarchical Control. *Chem. Soc. Rev* **2017**, *46* (14), 4119–4134.

(43) Jenkins, A. D.; Kratochvíl, P.; Stepto, R. F. T.; Suter, U. W. Glossary of Basic Terms in Polymer Science. *Pure Appl. Chem.* **1996**, *68* (12), 2287–2311.

(44) Brendel, J. C.; Schacher, F. H. Block Copolymer Self-Assembly in Solution—Quo Vadis? *Chem. – An Asian J.* **2018**, *13* (3), 230–239.

(45) Epps, T. H.; O'Reilly, R. K. Block Copolymers: Controlling Nanostructure to Generate Functional Materials – Synthesis, Characterization, and Engineering. *Chem. Sci.* **2016**, *7* (3), 1674–1689.

(46) Hadjichristidis, N.; Pispas, S.; Floudas, G. *Block Copolymers: Synthetic Strategies, Physical Properties, and Applications*; John Wiley & Sons, Inc.: Hoboken, USA, 2003.

(47) Bates, F. S.; Fredrickson, G. H. Block Copolymers - Designer Soft Materials. *Phys. Today* **1999**, *52* (2), 38.

(48) Matsen, M. W.; Bates, F. S. Unifying Weak- and Strong-Segregation Block Copolymer Theories. *Macromolecules* **1996**, *29* (4), 1091–1098.

(49) Swann, J. M. G.; Topham, P. D. Design and Application of Nanoscale Actuators Using Block-Copolymers. *Polym. 2010, Vol. 2, Pages 454-469* **2010**, *2* (4), 454–469.

(50) Cameron, N. S.; Corbierre, M. K.; Eisenberg, A. 1998 E.W.R. Steacie Award Lecture Asymmetric Amphiphilic Block Copolymers in Solution: A Morphological Wonderland. *Can. J. Chem.* **1999**, *77* (8), 1311–1326.

(51) Zhang, L.; Eisenberg, A. Multiple Morphologies and Characteristics of "Crew-Cut" Micelle-like Aggregates of Polystyrene-b-Poly(Acrylic Acid) Diblock Copolymers in Aqueous Solutions. *J. Am. Chem. Soc.* **1996**, *118* (13), 3168–3181.

(52) Discher, D. E.; Eisenberg, A. Polymer Vesicles. *Science* **2002**, *297* (5583), 967–973.

(53) Zhang, L.; Eisenberg, A. Multiple Morphologies of "Crew-Cut" Aggregates of Polystyrene-b-Poly(Acrylic Acid) Block Copolymers. *Science* **1995**, *268* (5218), 1728–1731.

(54) Gao, Z.; Varshney, S. K.; Wong, S.; Eisenberg, A. Block Copolymer "Crew-Cut" Micelles in Water. *Macromolecules* **1994**, *27* (26), 7927.

(55) Zhang, L.; Yu, K.; Eisenberg, A. Ion-Induced Morphological Changes in "Crew-Cut" Aggregates of Amphiphilic Block Copolymers. *Science* **1996**, *272* (5269), 1777–1779.

(56) Gao, Z. J.; Nguyen, D.; Williams, C. E. Adi Eisenberg. *Macromolecules* **2000**, *33* (21), 7673–7674.

(57) Hayward, R. C.; Pochan, D. J. Tailored Assemblies of Block Copolymers in Solution: It Is All about the Process. *Macromolecules* **2010**, *43* (8), 3577–3584.

(58) Cui, H.; Chen, Z.; Zhong, S.; Wooley, K. L.; Pochan, D. J. Block Copolymer Assembly via Kinetic Control. *Science* **2007**, *317* (5838), 647–650.

(59) Zhong, S.; Cui, H.; Chen, Z.; Wooley, K. L.; Pochan, D. J. Helix Self-Assembly through the Coiling of Cylindrical Micelles. *Soft Matter* **2008**, *4* (1), 90–93.

(60) Choucair, A.; Eisenberg, A. Control of Amphiphilic Block Copolymer Morphologies Using Solution Conditions. *Eur. Phys. J. E* **2003**, *10* (1), 37–44.

(61) Busseron, E.; Ruff, Y.; Moulin, E.; Giuseppone, N. Supramolecular Self-Assemblies as Functional Nanomaterials. *Nanoscale* **2013**, *5* (16), 7098–7140.

(62) Riess, G. Micellization of Block Copolymers. *Prog. Polym. Sci.* **2003**, *28* (7), 1107–1170.

(63) Gröschel, A. H.; Schacher, F. H.; Schmalz, H.; Borisov, O. V.; Zhulina, E. B.; Walther, A.; Müller, A. H. E. Precise Hierarchical Self-Assembly of Multicompartment Micelles. *Nat. Commun.* **2012**, *3* (710), 1–10.

(64) Gröschel, A. H.; Müller, A. H. E. Self-Assembly Concepts for Multicompartment Nanostructures. *Nanoscale* **2015**, *7* (28), 11841–11876.

(65) Winnik, M. A.; Yekta, A. Associative Polymers in Aqueous Solution. *Curr. Opin. Colloid Interface Sci.* **1997**, *2* (4), 424–436.

(66) Battaglia, G.; Ryan, A. J. Effect of Amphiphile Size on the Transformation from a Lyotropic Gel to a Vesicular Dispersion. *Macromolecules* **2005**, *39* (2), 798–805.

(67) Geng, Y.; Dalhaimer, P.; Cai, S.; Tsai, R.; Tewari, M.; Minko, T.; Discher, D. E. Shape Effects of Filaments versus Spherical Particles in Flow and Drug Delivery. *Nat. Nanotechnol.* **2007**, *2* (4), 249–255.

(68) Ridolfo, R.; Arends, J. J.; M van Hest, J. C.; Williams, D. S. Wormlike Nanovector with Enhanced Drug Loading Using Blends of Biodegradable Block Copolymers. *Biomacromolecules* **2020**, *21* (6), 2199–2207.

(69) Kim, Y.; Dalhaimer, P.; Christian, D. A.; Discher, D. E. Polymeric Worm Micelles as Nano-Carriers for Drug Delivery. *Nanotechnology* **2005**, *16* (7), S491.

(70) Li, Z.; Pearce, A. K.; Dove, A. P.; O'Reilly, R. K. Precise Tuning of Polymeric Fiber Dimensions to Enhance the Mechanical Properties of Alginate Hydrogel Matrices. *Polymers (Basel).* **2021**, *13* (13), 22014.

(71) Thio, Y. S.; Wu, J.; Bates, F. S. Epoxy Toughening Using Low Molecular Weight Poly(Hexylene Oxide)−Poly(Ethylene Oxide) Diblock Copolymers. *Macromolecules* **2006**, *39* (21), 7187–7189.

(72) Tian, J.; Zhang, Y.; Du, L.; He, Y.; Jin, X.-H.; Pearce, S.; Eloi, J.-C.; Harniman, R. L.; Alibhai, D.; Ye, R.; Phillips, D. L.; Manners, I. Tailored Self-Assembled Photocatalytic Nanofibres for Visible-Light-Driven Hydrogen Production. *Nat. Chem.* **2020**, *12* (12), 1150–1156.

(73) Shaikh, H.; Jin, X. H.; Harniman, R. L.; Richardson, R. M.; Whittell, G. R.; Manners, I. Solid-State Donor-Acceptor Coaxial Heterojunction Nanowires via Living Crystallization-Driven Self-Assembly. *J. Am. Chem. Soc.* **2020**, *142* (31), 13469–13480.

(74) Inam, M.; Foster, J. C.; Gao, J.; Hong, Y.; Du, J.; Dove, A. P.; O'Reilly, R. K. Size and Shape Affects the Antimicrobial Activity of Quaternized Nanoparticles. *J. Polym. Sci. Part A Polym. Chem.* **2019**, *57* (3), 255–259.

(75) Inam, M.; Jones, J. R.; Pérez-Madrigal, M. M.; Arno, M. C.; Dove, A. P.; O'Reilly, R. K. Controlling the Size of Two-Dimensional Polymer Platelets for Water-in-Water Emulsifiers. *ACS Cent. Sci.* **2018**, *4* (1), 63–70.

(76) Arno, M. C.; Inam, M.; Weems, A. C.; Li, Z.; Binch, A. L. A.; Platt, C. I.; Richardson, S. M.; Hoyland, J. A.; Dove, A. P.; O'Reilly, R. K. Exploiting the Role of Nanoparticle Shape in Enhancing Hydrogel Adhesive and Mechanical Properties. *Nat. Commun.* **2020**, *11* (1), 1–9.

(77) Pearce, A. K.; Wilks, T. R.; Arno, M. C.; O'Reilly, R. K. Synthesis and Applications of Anisotropic Nanoparticles with Precisely Defined Dimensions. *Nat. Rev. Chem.* **2021**, *5* (1), 21–45.

(78) Blanazs, A.; Ryan, A. J.; Armes, S. P. Predictive Phase Diagrams for RAFT Aqueous Dispersion Polymerization: Effect of Block Copolymer Composition, Molecular Weight, and Copolymer Concentration. *Macromolecules* **2012**, *45* (12), 5099–5107.

(79) Hudson, Z. M.; Boott, C. E.; Robinson, M. E.; Rupar, P. A.; Winnik, M. A.; Manners, I. Tailored Hierarchical Micelle Architectures Using Living Crystallization-Driven Self-Assembly in Two Dimensions. *Nat. Chem.* **2014**, *6* (10), 893–898.

(80) Zhou, H.; Lu, Y.; Zhang, M.; Guerin, G.; Manners, I.; Winnik, M. A. PFS-b-PNIPAM: A First Step toward Polymeric Nanofibrillar Hydrogels Based on Uniform Fiber-Like Micelles. *Macromolecules* **2016**, *49* (11), 4265–4276.

(81) Nazemi, A.; Boott, C. E.; Lunn, D. J.; Gwyther, J.; Hayward, D. W.; Richardson, R. M.; Winnik, M. A.; Manners, I. Monodisperse Cylindrical Micelles and Block Comicelles of Controlled Length in Aqueous Media. *J. Am. Chem. Soc.* **2016**, *138* (13), 4484–4493.

(82) Shen, L.; Wang, H.; Guerin, G.; Wu, C.; Manners, I.; Winnik, M. A. A Micellar Sphere-to-Cylinder Transition of Poly(Ferrocenyldimethylsilane-b-2-Vinylpyridine) in a Selective Solvent Driven by Crystallization. *Macromolecules* **2008**, *41* (12), 4380–4389.

(83) Wang, H.; Lin, W.; Fritz, K. P.; Scholes, G. D.; Winnik, M. A.; Manners, I. Cylindrical Block Co-Micelles with Spatially Selective Functionalization by Nanoparticles. *J. Am. Chem. Soc.* **2007**, No. 43, 12924–12925.

(84) Wang, X.; Guerin, G.; Wang, H.; Wang, Y.; Manners, I.; Winnik, M. A. Cylindrical Block Copolymer Micelles and Co-Micelles of Controlled Length and Architecture. *Science* **2007**, *317* (5838), 644–647.

(85) Ganda, S.; Stenzel, M. H. Concepts, Fabrication Methods and Applications of Living Crystallization-Driven Self-Assembly of Block Copolymers. *Prog. Polym. Sci.* **2020**, *101* (101195), 1–33.

(86) Cao, L.; Manners, I.; Winnik, M. A. Influence of the Interplay of Crystallization and Chain Stretching on Micellar Morphologies: Solution Self-Assembly of Coil−Crystalline Poly(Isoprene-Block-Ferrocenylsilane). *Macromolecules* **2002**, *35* (22), 8258–8260.

(87) Yu, W.; Inam, M.; Jones, J. R.; Dove, A. P.; O'Reilly, R. K. Understanding the CDSA of Poly(Lactide) Containing Triblock Copolymers. *Polym. Chem.* **2017**, *8* (36), 5504–5512.

(88) Thakellapalli, H.; Li, S.; Farajidizaji, B.; Baughman, N. N.; Akhmedov, N. G.; Popp, B. V.; Wang, K. K. Synthesis and Properties of Conjugated Macrocycles Containing 2,7-Bis(2-Thienyl)-9H-Fluoren-9-One Units. *Org. Lett.* **2017**, *19* (10), 2674–2677.

(89) Lazzari, M.; Scalarone, D.; Vazquez-Vazquez, C.; López-Quintela, M. A. Cylindrical Micelles from the Self-Assembly of Polyacrylonitrile-Based Diblock Copolymers in Nonpolar Selective Solvents. *Macromol. Rapid Commun.* **2008**, *29* (4), 352–357.

(90) Du, Z. X.; Xu, J. T.; Fan, Z. Q. Micellar Morphologies of Poly(ε-Caprolactone)-b-Poly(Ethylene Oxide) Block Copolymers in Water with a Crystalline Core. *Macromolecules* **2007**, *40* (21), 7633–7637.

(91) Arno, M. C.; Inam, M.; Coe, Z.; Cambridge, G.; Macdougall, L. J.; Keogh, R.; Dove, A. P.; O'Reilly, R. K. Precision Epitaxy for Aqueous 1D and 2D Poly(ϵ-Caprolactone) Assemblies. *J. Am. Chem. Soc.* **2017**, *139* (46), 16980–16985.

(92) Jin, X. H.; Price, M. B.; Finnegan, J. R.; Boott, C. E.; Richter, J. M.; Rao, A.; Matthew Menke, S.; Friend, R. H.; Whittell, G. R.; Manners, I. Long-Range Exciton Transport in Conjugated Polymer Nanofibers Prepared by Seeded Growth. *Science* **2018**, *360* (6391), 897–900.

(93) Zhang, Y.; Shaikh, H.; Sneyd, A. J.; Tian, J.; Xiao, J.; Blackburn, A.; Rao, A.; Friend, R. H.; Manners, I. Efficient Energy Funneling in Spatially Tailored Segmented Conjugated Block Copolymer Nanofiber-Quantum Dot or Rod Conjugates. *J. Am. Chem. Soc.* **2021**, *143* (18), 7032–7041.

(94) Schmelz, J.; Schedl, A. E.; Steinlein, C.; Manners, I.; Schmalz, H. Length Control and Block-Type Architectures in Worm-like Micelles with Polyethylene Cores. *J. Am. Chem. Soc.* **2012**, *134* (34), 14217–14225.

(95) Hils, C.; Schmelz, J.; Drechsler, M.; Schmalz, H. Janus Micelles by Crystallization-Driven Self-Assembly of an Amphiphilic, Double-Crystalline Triblock Terpolymer. *J. Am. Chem. Soc.* **2021**, *143* (38), 15582–15586.

(96) Brubaker, C. E.; Velluto, D.; Demurtas, D.; Phelps, E. A.; Hubbell, J. A. Crystalline Oligo(Ethylene Sulfide) Domains Define Highly Stable Supramolecular Block Copolymer Assemblies. *ACS Nano* **2015**, *9* (7), 6872–6881.

(97) Gädt, T.; Ieong, N. S.; Cambridge, G.; Winnik, M. A.; Manners, I. Complex and Hierarchical Micelle Architectures from Diblock Copolymers Using Living, Crystallization-Driven Polymerizations. *Nat. Mater.* **2009**, *8* (2), 144–150.

(98) Zhang, Y.; Pearce, S.; Eloi, J.-C.; Harniman, R. L.; Tian, J.; Cordoba, C.; Kang, Y.; Fukui, T.; Qiu, H.; Blackburn, A.; Richardson, R. M.; Manners, I. Dendritic

Micelles with Controlled Branching and Sensor Applications. *Cite This J. Am. Chem. Soc* **2021**, *143* (15), 5805–5814.

(99) Finnegan, J. R.; He, X.; Street, S. T. G.; Garcia-Hernandez, J. D.; Hayward, D. W.; Harniman, R. L.; Richardson, R. M.; Whittell, G. R.; Manners, I. Extending the Scope of "Living" Crystallization-Driven Self-Assembly: Well-Defined 1D Micelles and Block Comicelles from Crystallizable Polycarbonate Block Copolymers. *J. Am. Chem. Soc.* **2018**, *140* (49), 17127–17140.

(100) He, X.; Finnegan, J. R.; Hayward, D. W.; Macfarlane, L. R.; Harniman, R. L.; Manners, I. Living Crystallization-Driven Self-Assembly of Polymeric Amphiphiles: Low-Dispersity Fiber-like Micelles from Crystallizable Phosphonium-Capped Polycarbonate Homopolymers. *Macromolecules* **2020**, *53* (23), 10591–10600.

(101) Sun, L.; Petzetakis, N.; Pitto-barry, A.; Schiller, T. L.; Kirby, N.; Keddie, D. J.; Boyd, B. J.; Reilly, R. K. O.; Dove, A. P. Tuning the Size of Cylindrical Micelles from Poly(L-Lactide)-b-poly(Acrylic Acid) Diblock Copolymers Based on Crystallization-Driven Self-Assembly. *Macromolecules* **2013**, *46* (22), 9074–9082.

(102) He, Y.; Eloi, J. C.; Harniman, R. L.; Richardson, R. M.; Whittell, G. R.; Mathers, R. T.; Dove, A. P.; O'Reilly, R. K.; Manners, I. Uniform Biodegradable Fiber-Like Micelles and Block Comicelles via "Living" Crystallization-Driven Self-Assembly of Poly(l -Lactide) Block Copolymers: The Importance of Reducing Unimer Self-Nucleation via Hydrogen Bond Disruption. *J. Am. Chem. Soc.* **2019**, *141* (48), 19088–19098.

(103) Petzetakis, N.; Dove, A. P.; O'Reilly, R. K. Cylindrical Micelles from the Living Crystallization-Driven Self-Assembly of Poly(Lactide)-Containing Block Copolymers. *Chem. Sci.* **2011**, *2* (5), 955–960.

(104) Kynaston, E. L.; Gould, O. E. C.; Gwyther, J.; Whittell, G. R.; Winnik, M. A.; Manners, I. Fiber-like Micelles from the Crystallization-Driven Self-Assembly of Poly(3-Heptylselenophene)-Block-Polystyrene. *Macromol. Chem. Phys.* **2015**, *216* (6), 685–695.

(105) Kynaston, E. L.; Nazemi, A.; MacFarlane, L. R.; Whittell, G. R.; Faul, C. F. J.; Manners, I. Uniform Polyselenophene Block Copolymer Fiberlike Micelles and Block Co-Micelles via Living Crystallization-Driven Self-Assembly. *Macromolecules* **2018**, *51* (3), 1002–1010.

(106) Li, X.; Wolanin, P. J.; MacFarlane, L. R.; Harniman, R. L.; Qian, J.; Gould, O. E. C.; Dane, T. G.; Rudin, J.; Cryan, M. J.; Schmaltz, T.; Frauenrath, H.; Winnik, M. A.; Faul, C. F. J.; Manners, I. Uniform Electroactive Fibre-like Micelle Nanowires for Organic Electronics. *Nat. Commun.* **2017**, *8* (15909), 1–9.

(107) Gilroy, J. B.; Lunn, D. J.; Patra, S. K.; Whittell, G. R.; Winnik, M. A.; Manners, I. Fiber-like Micelles via the Crystallization-Driven Solution Self-Assembly of Poly(3-Hexylthiophene)-Block-Poly(Methyl Methacrylate) Copolymers. *Macromolecules* **2012**, *45* (14), 5806–5815.

(108) Gwyther, J.; Gilroy, J. B.; Rupar, P. A.; Lunn, D. J.; Kynaston, E.; Patra, S. K.; Whittell, G. R.; Winnik, M. A.; Manners, I. Dimensional Control of Block Copolymer Nanofibers with a π-Conjugated Core: Crystallization-Driven Solution Self-Assembly of Amphiphilic Poly(3-Hexylthiophene)-b-Poly(2-Vinylpyridine). *Chem. – A Eur. J.* **2013**, *19* (28), 9186–9197.

(109) Fukui, T.; Garcia-Hernandez, J. D.; MacFarlane, L. R.; Lei, S.; Whittell, G. R.; Manners, I. Seeded Self-Assembly of Charge-Terminated Poly(3-Hexylthiophene) Amphiphiles Based on the Energy Landscape. *J. Am. Chem. Soc.* **2020**, *142* (35), 15038–15048.

(110) Legros, C.; De Pauw-Gillet, M. C.; Tam, K. C.; Taton, D.; Lecommandoux, S. Crystallisation-Driven Self-Assembly of Poly(2-Isopropyl-2-Oxazoline)-Block-Poly(2-Methyl-2-Oxazoline) above the LCST. *Soft Matter* **2015**, *11* (17), 3354–3359.

(111) Finnegan, J.; Pilkington, E.; Alt, K.; Rahim, M. A.; Kent, S. J.; Davis, T. P.; Kempe, K. Stealth Nanorods via the Aqueous Living Crystallisation-Driven Self-Assembly of Poly(2-Oxazoline)S. *Chem. Sci.* **2021**, *12* (21), 7350–7360.

(112) Tritschler, U.; Gwyther, J.; Harniman, R. L.; Whittell, G. R.; Winnik, M. A.; Manners, I. Toward Uniform Nanofibers with a π-Conjugated Core: Optimizing the "Living" Crystallization-Driven Self-Assembly of Diblock Copolymers with a Poly(3-Octylthiophene) Core-Forming Block. *Macromolecules* **2018**, *51* (14), 5101–5113.

(113) Li, X.; Jin, B.; Gao, Y.; Hayward, D. W.; Winnik, M. A.; Luo, Y.; Manners, I. Monodisperse Cylindrical Micelles of Controlled Length with a Liquid-Crystalline Perfluorinated Core by 1D "Self-Seeding." *Angew. Chemie - Int. Ed.* **2016**, *55* (38), 11392–11396.

(114) Gao, Y.; Li, X.; Hong, L.; Liu, G. Mesogen-Driven Formation of Triblock Copolymer Cylindrical Micelles. *Macromolecules* **2012**, *45* (3), 1321–1330.

(115) Lee, I. H.; Amaladass, P.; Choi, T. L. One-Pot Synthesis of Nanocaterpillar Structures via in Situ Nanoparticlization of Fully Conjugated Poly(p-Phenylene)-Block-Polythiophene. *Chem. Commun.* **2014**, *50* (59), 7945–7948.

(116) Mori, T.; Watanabe, T.; Minagawa, K.; Tanaka, M. Self-Assembly of Oligo(p-Phenylenevinylene)-Block-Poly(Ethylene Oxide) in Polar Media and Solubilization of an Oligo(p-Phenylenevinylene) Homooligomer inside the Assembly. *J. Polym. Sci. Part A Polym. Chem.* **2005**, *43* (8), 1569–1578.

(117) Tao, D.; Feng, C.; Cui, Y.; Yang, X.; Manners, I.; Winnik, M. A.; Huang, X. Monodisperse Fiber-like Micelles of Controlled Length and Composition with an Oligo(p-Phenylenevinylene) Core via "Living" Crystallization-Driven Self-Assembly. *J. Am. Chem. Soc.* **2017**, *139* (21), 7136–7139.

(118) Li, K.; Wang, Q. Multiple Self-Assembled Nanostructures from an Oligo(p-Phenyleneethynylene) Containing Rod–Coil–Rod Triblock Copolymer. *Chem. Commun.* **2005**, No. 38, 4786–4788.

(119) Samorí, P.; Francke, V.; Müllen, K.; Rabe, J. P. Self-Assembly of a Conjugated Polymer: From Molecular Rods to a Nanoribbon Architecture with Molecular Dimensions. *Chem. - A Eur. J.* **1999**, *5* (8), 2312–2317.

(120) Macfarlane, L.; Zhao, C.; Cai, J.; Qiu, H.; Manners, I. Emerging Applications for Living Crystallization-Driven Self-Assembly. *Chem. Sci.* **2021**, *12* (13), 4661–4682.

(121) Gaumet, M.; Vargas, A.; Gurny, R.; Delie, F. Nanoparticles for Drug Delivery: The Need for Precision in Reporting Particle Size Parameters. *Eur. J. Pharm. Biopharm.* **2008**, *69* (1), 1–9.

(122) Danaei, M.; Dehghankhold, M.; Ataei, S.; Hasanzadeh Davarani, F.; Javanmard, R.; Dokhani, A.; Khorasani, S.; Mozafari, M. R. Impact of Particle Size and Polydispersity Index on the Clinical Applications of Lipidic Nanocarrier Systems. *Pharmaceutics* **2018**, *10* (2), 1–17.

(123) Gilroy, J. B.; Gädt, T.; Whittell, G. R.; Chabanne, L.; Mitchels, J. M.; Richardson, R. M.; Winnik, M. A.; Manners, I. Monodisperse Cylindrical Micelles by Crystallization-Driven Living Self-Assembly. *Nat. Chem.* **2010**, *2* (7), 566–570.

(124) Qian, J.; Lu, Y.; Chia, A.; Zhang, M.; Rupar, P. A.; Gunari, N.; Walker, G. C.; Cambridge, G.; He, F.; Guerin, G.; Manners, I.; Winnik, M. A. Self-Seeding in One Dimension: A Route to Uniform Fiber-like Nanostructures from Block Copolymers with a Crystallizable Core-Forming Block. *ACS Nano* **2013**, *7* (5), 3754–3766.

(125) MacFarlane, L. R.; Li, X.; Faul, C. F. J.; Manners, I. Efficient and Controlled Seeded Growth of Poly(3-Hexylthiophene) Block Copolymer Nanofibers through Suppression of Homogeneous Nucleation. *Macromolecules* **2021**, *54* (24), 11269–11280.

(126) Qiu, H.; Gao, Y.; Du, V. A.; Harniman, R.; Winnik, M. A.; Manners, I. Branched Micelles by Living Crystallization-Driven Block Copolymer Self-Assembly under Kinetic Control. *J. Am. Chem. Soc.* **2015**, *137* (6), 2375–2385.

(127) He, X.; Hsiao, M. S.; Boott, C. E.; Harniman, R. L.; Nazemi, A.; Li, X.; Winnik, M. A.; Manners, I. Two-Dimensional Assemblies from Crystallizable Homopolymers with Charged Termini. *Nat. Mater.* **2017**, *16* (4), 481–488.

(128) Qian, J.; Li, X.; Lunn, D. J.; Gwyther, J.; Hudson, Z. M.; Kynaston, E.; Rupar, P. A.; Winnik, M. A.; Manners, I. Uniform, High Aspect Ratio Fiber-like Micelles and Block Co-Micelles with a Crystalline π-Conjugated Polythiophene Core by Self-Seeding. *J. Am. Chem. Soc.* **2014**, *136* (11), 4121–4124.

(129) He, X.; He, Y.; Hsiao, M. S.; Harniman, R. L.; Pearce, S.; Winnik, M. A.; Manners, I. Complex and Hierarchical 2D Assemblies via Crystallization-Driven Self-Assembly of Poly(l-Lactide) Homopolymers with Charged Termini. *J. Am. Chem. Soc.* **2017**, *139* (27), 9221–9228.

(130) Mattia, E.; Otto, S. Supramolecular Systems Chemistry. *Nat. Nanotechnol.* **2015**, *10* (2), 111–119.

(131) Aida, T.; Meijer, E. W. Supramolecular Polymers – We've Come Full Circle. *Isr. J. Chem.* **2020**, *60* (1–2), 33–47.

(132) Pal, A.; Malakoutikhah, M.; Leonetti, G.; Tezcan, M.; Colomb-Delsuc, M.; Nguyen, V. D.; Van Der Gucht, J.; Otto, S. Controlling the Structure and Length of Self-Synthesizing Supramolecular Polymers through Nucleated Growth and Disassembly. *Angew. Chemie - Int. Ed.* **2015**, *54* (27), 7852–7856.

(133) Fukui, T.; Kawai, S.; Fujinuma, S.; Matsushita, Y.; Yasuda, T.; Sakurai, T.; Seki, S.; Takeuchi, M.; Sugiyasu, K. Control over Differentiation of a Metastable Supramolecular Assembly in One and Two Dimensions. *Nat. Chem.* **2017**, *9*, 493.

(134) Ogi, S.; Sugiyasu, K.; Manna, S.; Samitsu, S.; Takeuchi, M. Living Supramolecular Polymerization Realized through a Biomimetic Approach. *Nat. Chem.* **2014**, *6* (3), 188–195.

(135) Sarkar, A.; Sasmal, R.; Das, A.; Venugopal, A.; Agasti, S. S.; George, S. J. Tricomponent Supramolecular Multiblock Copolymers with Tunable Composition via Sequential Seeded Growth. *Angew. Chemie Int. Ed.* **2021**, *60* (33), 18209–18216.

(136) Sarkar, A.; Sasmal, R.; Das, A.; Agasti, S. S.; George, S. J. Kinetically Controlled Synthesis of Supramolecular Block Copolymers with Narrow Dispersity and Tunable Block Lengths. *Chem. Commun.* **2021**, *57* (32), 3937–3940.

(137) Sarkar, A.; Behera, T.; Sasmal, R.; Capelli, R.; Empereur-Mot, C.; Mahato, J.; Agasti, S. S.; Pavan, G. M.; Chowdhury, A.; George, S. J. Cooperative Supramolecular Block Copolymerization for the Synthesis of Functional Axial Organic Heterostructures. *J. Am. Chem. Soc.* **2020**, *142* (26), 11528–11539.

(138) Qiu, H.; Hudson, Z. M.; Winnik, M. A.; Manners, I. Multidimensional Hierarchical Self-Assembly of Amphiphilic Cylindrical Block Comicelles. *Science* **2015**, *347* (6228), 1329–1332.

(139) Li, X.; Gao, Y.; Boott, C. E.; Winnik, M. A.; Manners, I. Non-Covalent Synthesis of Supermicelles with Complex Architectures Using Spatially Confined Hydrogen-Bonding Interactions. *Nat. Commun.* **2015**, *6* (1), 1–8.

(140) Dou, H.; Li, M.; Qiao, Y.; Harniman, R.; Li, X.; Boott, C. E.; Mann, S.; Manners, I. Higher-Order Assembly of Crystalline Cylindrical Micelles into Membrane-Extendable Colloidosomes. *Nat. Commun.* **2017**, *8*, 1–8.

(141) Feng, L.; Zhu, C.; Yuan, H.; Liu, L.; Lv, F.; Wang, S. Conjugated Polymer Nanoparticles: Preparation, Properties, Functionalization and Biological Applications. *Chem. Soc. Rev.* **2013**, *42* (16), 6620–6633.

(142) Aflori, M.; Poni, P. Smart Nanomaterials for Biomedical Applications—A Review. *Nanomater. 2021* **2021**, *11* (2), 396–429.

(143) Lin, M.; Dai, Y.; Xia, F.; Zhang, X. Advances in Non-Covalent Crosslinked Polymer Micelles for Biomedical Applications. *Mater. Sci. Eng. C* **2021**, *119* (111626), 1–9.

(144) Samaddar, P.; Deep, A.; Kim, K. H. An Engineering Insight into Block Copolymer Self-Assembly: Contemporary Application from Biomedical Research to Nanotechnology. *Chem. Eng. J.* **2018**, *342*, 71–89.

(145) Zarrintaj, P.; Ramsey, J. D.; Samadi, A.; Atoufi, Z.; Yazdi, M. K.; Ganjali, M. R.; Amirabad, L. M.; Zangene, E.; Farokhi, M.; Formela, K.; Saeb, M. R.; Mozafari, M.; Thomas, S. Poloxamer: A Versatile Tri-Block Copolymer for Biomedical Applications. *Acta Biomater.* **2020**, *110*, 37–67.

(146) Gohy, J. F.; Zhao, Y. Photo-Responsive Block Copolymer Micelles: Design and Behavior. *Chem. Soc. Rev.* **2013**, *42* (17), 7117–7129.

(147) Thévenot, J.; Oliveira, H.; Sandre, O.; Lecommandoux, S. Magnetic Responsive Polymer Composite Materials. *Chem. Soc. Rev.* **2013**, *42* (17), 7099–7116.

(148) Walther, A.; Müller, A. H. E. Janus Particles: Synthesis, Self-Assembly, Physical Properties, and Applications. *Chem. Rev.* **2013**, *113* (7), 5194–5261.

(149) Bakshi, M. S. Colloidal Micelles of Block Copolymers as Nanoreactors, Templates for Gold Nanoparticles, and Vehicles for Biomedical Applications. *Adv. Colloid Interface Sci.* **2014**, *213*, 1–20.

(150) Truong, N. P.; Quinn, J. F.; Whittaker, M. R.; Davis, T. P.; And, F. Polymeric Filomicelles and Nanoworms: Two Decades of Synthesis and Application. *Polym. Chem* **2016**, *7* (26), 4295–4312.

(151) Elsabahy, M.; Wooley, K. L. Design of Polymeric Nanoparticles for Biomedical Delivery Applications. *Chem. Soc. Rev.* **2012**, *41* (7), 2545–2561.

(152) Oltra, N. S.; Nair, P.; Discher, D. E. From Stealthy Polymersomes and Filomicelles to "Self" Peptide-Nanoparticles for Cancer Therapy. *Annu. Rev. Chem. Biomol. Eng.* **2014**, *5* (1), 281–299.

(153) Petros, R. A.; DeSimone, J. M. Strategies in the Design of Nanoparticles for Therapeutic Applications. *Nat. Rev. Drug Discov.* **2010**, *9* (8), 615–627.

(154) Yu, Q.; Roberts, M. G.; Houdaihed, L.; Liu, Y.; Ho, K.; Walker, G.; Allen, C.; Reilly, R. M.; Manners, I.; Winnik, M. A. Investigating the Influence of Block Copolymer Micelle Length on Cellular Uptake and Penetration in a Multicellular Tumor Spheroid Model. *Nanoscale* **2021**, *13* (1), 280–291.

(155) Kalepu, S.; Nekkanti, V. Insoluble Drug Delivery Strategies: Review of Recent Advances and Business Prospects. *Acta Pharm. Sin. B* **2015**, *5* (5), 442–453.

(156) Mitragotri, S.; Lahann, J. Materials for Drug Delivery: Innovative Solutions to Address Complex Biological Hurdles. *Adv. Mater.* **2012**, *24* (28), 3717–3723.

(157) Owen, S. C.; Chan, D. P. Y.; Shoichet, M. S. Polymeric Micelle Stability. *Nano Today* **2012**, *7* (1), 53–65.

(158) Venkataraman, S.; Hedrick, J. L.; Ong, Z. Y.; Yang, C.; Ee, P. L. R.; Hammond, P. T.; Yang, Y. Y. The Effects of Polymeric Nanostructure Shape on Drug Delivery. *Adv. Drug Deliv. Rev.* **2011**, *63* (14–15), 1228–1246.

(159) Banerjee, A.; Qi, J.; Gogoi, R.; Wong, J.; Mitragotri, S. Role of Nanoparticle Size, Shape and Surface Chemistry in Oral Drug Delivery. *J. Control. Release* **2016**, *238* (1), 176–185.

(160) Chithrani, B. D.; Ghazani, A. A.; Chan, W. C. W. Determining the Size and Shape Dependence of Gold Nanoparticle Uptake into Mammalian Cells. *Nano Lett.* **2006**, *6* (4), 662–668.

(161) Karlsson, H. L.; Gustafsson, J.; Cronholm, P.; Möller, L. Size-Dependent Toxicity of Metal Oxide Particles-A Comparison between Nano- and Micrometer Size. *Toxicol. Lett.* **2009**, *188* (2), 112–118.

(162) Cabral, H.; Miyata, K.; Osada, K.; Kataoka, K. Block Copolymer Micelles in Nanomedicine Applications. *Chem. Rev.* **2018**, *118* (14), 6844–6892.

(163) Kinnear, C.; Moore, T. L.; Rodriguez-Lorenzo, L.; Rothen-Rutishauser, B.; Petri-Fink, A. Form Follows Function: Nanoparticle Shape and Its Implications for Nanomedicine. *Chem. Rev.* **2017**, *117* (17), 11476–11521.

(164) Zhao, Y.; Wang, Y.; Ran, F.; Cui, Y.; Liu, C.; Zhao, Q.; Gao, Y.; Wang, D.; Wang, S. A Comparison between Sphere and Rod Nanoparticles Regarding Their in Vivo Biological Behavior and Pharmacokinetics. *Sci. Rep.* **2017**, *7* (1), 1–11.

(165) Black, K. C. L.; Wang, Y.; Luehmann, H. P.; Cai, X.; Xing, W.; Pang, B.; Zhao, Y.; Cutler, C. S.; Wang, L. V.; Liu, Y.; Xia, Y. Radioactive 198Au-Doped Nanostructures with Different Shapes for in Vivo Analyses of Their Biodistribution, Tumor Uptake, and Intratumoral Distribution. *ACS Nano* **2014**, *8* (5), 4385–4394.

(166) Champion, J. A.; Mitragotri, S. Shape Induced Inhibition of Phagocytosis of Polymer Particles. *Pharm. Res.* **2009**, *26* (1), 244–249.

(167) Li, Z.; Sun, L.; Zhang, Y.; Dove, A. P.; O'Reilly, R. K.; Chen, G. Shape Effect of Glyco-Nanoparticles on Macrophage Cellular Uptake and Immune Response. *ACS Macro Lett.* **2016**, *5* (9), 1059–1064.

(168) Milton Harris, J.; Chess, R. B. Effect of Pegylation on Pharmaceuticals. *Nat. Rev. Drug Discov.* **2003**, *2* (3), 214–221.

(169) Duncan, R. Polymer Conjugates as Anticancer Nanomedicines. *Nat. Rev. Cancer* **2006**, *6* (9), 688–701.

(170) Logie, J.; Ganesh, A. N.; Aman, A. M.; Al-awar, R. S.; Shoichet, M. S. Preclinical Evaluation of Taxane-Binding Peptide-Modified Polymeric Micelles Loaded with Docetaxel in an Orthotopic Breast Cancer Mouse Model. *Biomaterials* **2017**, *123*, 39–47.

(171) Chan, D. P. Y.; Owen, S. C.; Shoichet, M. S. Double Click: Dual Functionalized Polymeric Micelles with Antibodies and Peptides. *Bioconjug. Chem.* **2013**, *24* (1), 105–113.

(172) Mura, S.; Nicolas, J.; Couvreur, P. Stimuli-Responsive Nanocarriers for Drug Delivery. *Nat. Mater.* **2013**, *12* (11), 991–1003.

(173) Zhao, J.; Babiuch, K.; Lu, H.; Dag, A.; Gottschaldt, M.; Stenzel, M. H. Fructose-Coated Nanoparticles: A Promising Drug Nanocarrier for Triple-Negative Breast Cancer Therapy. *Chem. Commun.* **2014**, *50* (100), 15928–15931.

(174) Lu, M.; Chen, F.; Cao, C.; Garvey, C. J.; Fletcher, N. L.; Houston, Z. H.; Lu, H.; Lord, M. S.; Thurecht, K. J.; Stenzel, M. H. Importance of Polymer Length in

Fructose-Based Polymeric Micelles for an Enhanced Biological Activity. *Macromolecules* **2019**, *52* (2), 477–486.

(175) Bahrami, B.; Mohammadnia-Afrouzi, M.; Bakhshaei, P.; Yazdani, Y.; Ghalamfarsa, G.; Yousefi, M.; Sadreddini, S.; Jadidi-Niaragh, F.; Hojjat-Farsangi, M. Folate-Conjugated Nanoparticles as a Potent Therapeutic Approach in Targeted Cancer Therapy. *Tumor Biol.* **2015**, *36* (8), 5727–5742.

(176) Street, S. T. G.; He, Y.; Jin, X.-H.; Hodgson, L.; Verkade, P.; Manners, I. Cellular Uptake and Targeting of Low Dispersity, Dual Emissive, Segmented Block Copolymer Nanofibers. *Chem. Sci.* **2020**, *11* (32), 8394–8408.

(177) Guo, S.; Huang, L. Nanoparticles Escaping RES and Endosome: Challenges for SiRNA Delivery for Cancer Therapy. *J. Nanomater.* **2011**, *2011*, 1–12.

(178) Wilhelm, S.; Tavares, A. J.; Dai, Q.; Ohta, S.; Audet, J.; Harold, F.; Chan, W. C. W. Analysis of Nanoparticle Delivery to Tumours. *Nat. Rev. Mater.* **2016**, *1* (5), 1–138.

(179) Tritschler, U.; Gwyther, J.; Harniman, R. L.; Whittell, G. R.; Winnik, M. A.; Manners, I. Toward Uniform Nanofibers with a π-Conjugated Core: Optimizing the "Living" Crystallization-Driven Self-Assembly of Diblock Copolymers with a Poly(3-Octylthiophene) Core-Forming Block. *Macromolecules* **2018**, *51* (14), 5101–5113.

(180) Wan, X.; Min, Y.; Bludau, H.; Keith, A.; Sheiko, S. S.; Jordan, R.; Wang, A. Z.; Sokolsky-Papkov, M.; Kabanov, A. V. Drug Combination Synergy in Worm-like Polymeric Micelles Improves Treatment Outcome for Small Cell and Non-Small Cell Lung Cancer. *ACS Nano* **2018**, *12* (3), 2426–2439.

(181) Pathak, C.; Vaidya, F. U.; Pandey, S. M. Mechanism for Development of Nanobased Drug Delivery System. In *Applications of Targeted Nano Drugs and Delivery Systems: Nanoscience and Nanotechnology in Drug Delivery*; Mohapatra, S. S., Ranjan, S., Dasgupta, N., Kumar Mishra, R., Thomas, S., Eds.; Elsevier: Online, 2019; pp 35–67.

(182) Pinto Reis, C.; Neufeld, R. J.; Ribeiro, A. J.; Veiga, F. Nanoencapsulation I. Methods for Preparation of Drug-Loaded Polymeric Nanoparticles. *Nanomedicine Nanotechnology, Biol. Med.* **2006**, *2* (1), 8–21.

(183) Ridolfo, R.; Ede, B. C.; Diamanti, P.; White, P. B.; Perriman, A. W.; van Hest, J. C. M.; Blair, A.; Williams, D. S. Biodegradable, Drug-Loaded Nanovectors via Direct Hydration as a New Platform for Cancer Therapeutics. *Small* **2018**, *14* (32), 1703774–1703784.

(184) Doane, T.; Burda, C. Nanoparticle Mediated Non-Covalent Drug Delivery. *Adv. Drug Deliv. Rev.* **2013**, *65* (5), 607–621.

(185) Bains, A.; Cao, Y.; Moffitt, M. G. Multiscale Control of Hierarchical Structure in Crystalline Block Copolymer Nanoparticles Using Microfluidics. *Macromol. Rapid Commun.* **2015**, *36* (22), 2000–2005.

(186) Bains, A.; Wulff, J. E.; Moffitt, M. G. Microfluidic Synthesis of Dye-Loaded Polycaprolactone-Block-Poly(Ethylene Oxide) Nanoparticles: Insights into Flow-Directed Loading and in Vitro Release for Drug Delivery. *J. Colloid Interface Sci.* **2016**, *475* (1), 136–148.

(187) Gou, J.; Feng, S.; Xu, H.; Fang, G.; Chao, Y.; Zhang, Y.; Xu, H.; Tang, X. Decreased Core Crystallinity Facilitated Drug Loading in Polymeric Micelles without Affecting Their Biological Performances. *Biomacromolecules* **2015**, *16* (9), 2920–2929.

(188) Ganda, S.; Wong, C. K.; Stenzel, M. H. Corona-Loading Strategies for Crystalline Particles Made by Living Crystallization-Driven Self-Assembly. *Macromolecules* **2021**, *54* (14), 6662–6669.

(189) Garcia-Hernandez, J. D.; Street, S. T. G.; Kang, Y.; Zhang, Y.; Manners, I. Cargo Encapsulation in Uniform, Length-Tunable Aqueous Nanofibers with a Coaxial Crystalline and Amorphous Core. *Macromolecules* **2021**, *54* (12), 5784–5796.

(190) Liu, J.; Thompson, Z. J.; Sue, H. J.; Bates, F. S.; Hillmyer, M. A.; Dettloff, M.; Jacob, G.; Verghese, N.; Pham, H. Toughening of Epoxies with Block Copolymer Micelles of Wormlike Morphology. *Macromolecules* **2010**, *43* (17), 7238–7243.

(191) Schöbel, J.; Burgard, M.; Hils, C.; Dersch, R.; Dulle, M.; Volk, K.; Karg, M.; Greiner, A.; Schmalz, H. Bottom-Up Meets Top-Down: Patchy Hybrid Nonwovens as an Efficient Catalysis Platform. *Angew. Chemie - Int. Ed.* **2017**, *56* (1), 405–408.

(192) Theocharis, A. D.; Skandalis, S. S.; Gialeli, C.; Karamanos, N. K. Extracellular Matrix Structure. *Adv. Drug Deliv. Rev.* **2016**, *97*, 4–27.

(193) Bosman, F. T.; Stamenkovic, I. Functional Structure and Composition of the Extracellular Matrix. *J. Pathol.* **2003**, *200* (4), 423–428.

(194) Smith, L. R.; Cho, S.; Discher, D. E. Stem Cell Differentiation Is Regulated by Extracellular Matrix Mechanics. *Physiology* **2018**, *33* (1), 16–25.

(195) Steinmetz, N. J.; Aisenbrey, E. A.; Westbrook, K. K.; Qi, H. J.; Bryant, S. J. Mechanical Loading Regulates Human MSC Differentiation in a Multi-Layer Hydrogel for Osteochondral Tissue Engineering. *Acta Biomater.* **2015**, *21*, 142–153.

(196) Kim, H.-J.; Kim, T.; Lee, M. Responsive Nanostructures from Aqueous Assembly of Rigid-Flexible Block Molecules. *Acc. Chem. Res.* **2011**, *44* (1), 72–82.

(197) Tsitsilianis, C.; Serras, G.; Ko, C.-H.; Jung, F.; Papadakis, C. M.; Rikkou-Kalourkoti, M.; Patrickios, C. S.; Schweins, R.; Chassenieux, C. Thermoresponsive Hydrogels Based on Telechelic Polyelectrolytes: From Dynamic to "Frozen" Networks. *Macromolecules* **2018**, *51* (6), 2169–2179.

(198) Nielsen, J. E.; Zhu, K.; Sande, S. A.; Kováčik, L.; Cmarko, D.; Knudsen, K. D.; Nyström, B. Structural and Rheological Properties of Temperature-Responsive Amphiphilic Triblock Copolymers in Aqueous Media. *J. Phys. Chem. B* **2017**, *121* (18), 4885–4899.

(199) Najafi, M.; Kordalivand, N.; Moradi, M.-A.; Dikkenberg, J. van den; Fokkink, R.; Friedrich, H.; Sommerdijk, N. A. J. M.; Hembury, M.; Vermonden, T. Native

Chemical Ligation for Cross-Linking of Flower-Like Micelles. *Biomacromolecules* **2018**, *19* (9), 3766–3775.

(200) Voorhaar, L.; Hoogenboom, R. Supramolecular Polymer Networks: Hydrogels and Bulk Materials. *Chem. Soc. Rev.* **2016**, *45* (14), 4013–4031.

(201) Zhu, K. J.; Hendren, R. W.; Jensen, K.; Pitt, C. G. Synthesis, Properties, and Biodegradation of Poly(1,3-Trimethylene Carbonate). *Macromolecules* **1991**, *24* (8), 1736–1740.

(202) Watanabe, J.; Kotera, H.; Akashi, M. Reflexive Interfaces of Poly(Trimethylene Carbonate)-Based Polymers: Enzymatic Degradation and Selective Adsorption. *Macromolecules* **2007**, *40* (24), 8731–8736.

(203) Fukushima, K. Poly(Trimethylene Carbonate)-Based Polymers Engineered for Biodegradable Functional Biomaterials. *Biomater. Sci.* **2016**, *4* (1), 9–24.

(204) Feng, J.; Zhuo, R. X.; Zhang, X. Z. Construction of Functional Aliphatic Polycarbonates for Biomedical Applications. *Prog. Polym. Sci.* **2012**, *37* (2), 211–236.

(205) Chan, J. M. W.; Zhang, X.; Brennan, M. K.; Sardon, H.; Engler, A. C.; Fox, C. H.; Frank, C. W.; Waymouth, R. M.; Hedrick, J. L. Organocatalytic Ring-Opening Polymerization of Trimethylene Carbonate to Yield a Biodegradable Polycarbonate. *J. Chem. Educ.* **2015**, *92* (4), 708–713.

(206) Langer, R.; Vacanti, J. P. Tissue Engineering. *Science* **1993**, *260* (5110), 920–926.

(207) Zhang, Q.; He, Y.; Oliver, A. M.; Pearce, S.; Harniman, R. L.; Whittell, G. R.; Liu, Y.; Du, S.; Leng, J.; Manners, I. Low Length Dispersity Fiber-like Micelles from an A–B–A Triblock Copolymer with Terminal Crystallizable Poly(Ferrocenyldimethylsilane) Segments via Living Crystallization-Driven Self-Assembly. *Polym. Chem.* **2019**, *10* (29), 3973–3982.

Chapter 2

Cargo Encapsulation in Uniform, Length-Tunable Aqueous Nanofibers with a Coaxial Crystalline and Amorphous Core

This chapter has been adapted from:

Garcia-Hernandez, J. D.; Street, S. T. G.; Kang, Y.; Zhang, Y.; Manners, I. Cargo Encapsulation in Uniform, Length-Tunable Aqueous Nanofibers with a Coaxial Crystalline and Amorphous Core. *Macromolecules* **2021**, *54* (12), 5784–5796.

Contributions:

Synthesis of polymers, self-assembly, loading of nanofibers, and characterization conducted by Juan Diego Garcia Hernandez. Energy minimization calculations were conducted by Dr. Steven Street. AFM was conducted by Dr. Yuetong Kang. Laser confocal scanning microscopy was conducted in collaboration with Dr. Yifan Zhang. Initial scientific design of the experiments was conducted in collaboration with Dr. Steven Street and Prof. Ian Manners. Research was conducted at the University of Victoria.

2.1 Abstract

Low dispersity, length-tunable, water-dispersable block copolymer nanofibers with spatially-controlled functionalization and a crystalline core have recently become accessible using the living crystallization-driven self-assembly (CDSA) seeded-growth method. Unfortunately, a potential obstacle to their use as delivery vectors is that encapsulation within the ordered, crystalline core is expected to be highly problematic. Herein, we address this problem through the design of an ABC triblock copolymer (triBCP) with a crystallizable poly(fluorenetrimethylenecarbonate) (PFTMC) core-forming block (A), a hydrophobic amorphous poly(butyl methacrylate) (PBMA) central block (B), and a hydrophilic poly(N-isopropylacrylamide) (PNIPAM) corona-forming block (C). Living CDSA of the triBCP in polar organic media yielded nanofibers of predetermined and uniform length, with a crystalline PFTMC core and a solvated PBMA-*b*-PNIPAM corona. Transfer to aqueous media led to the collapse of the PBMA block to yield nanofibers comprised of an inner crystalline PFTMC core surrounded coaxially by an outer amorphous PBMA core with a solubilizing PNIPAM corona. Performing a solvent switch from organic to aqueous media in the presence of a model hydrophobic cargo, Nile Red (NR), led to efficient encapsulation of the dye in the outer PBMA core, while the reverse solvent switch facilitated NR release. We estimate that only ca. 14% of the core volume is occupied by the crystalline PFTMC leaving 86% available for encapsulation. The results suggest that nanofibers with a coaxial crystalline and amorphous core are promising for the development of tailored, nanoparticle-based drug delivery systems with low dispersity and precise dimensions.

2.2 Introduction

Nanoparticle-based drug delivery vectors hold major potential for the treatment of a variety of diseases, including cancer.[1–3] Nanoparticles help minimize issues in "free" drug therapies such as poor solubility, non-specific tissue damage, degradation, poor biodistribution, side effects, and unfavorable pharmacokinetics.[4,5] To be used as delivery vectors, nanoparticles must address critical requirements prior to clinical use.[6] The ideal nanoparticle vector would be non-toxic and biocompatible,[7] degradable,[8] able to release cargo in a controlled manner,[9] and capable of exhibiting a high cargo loading capacity.[10] The effectiveness of a treatment is related to the ability of the system to facilitate drug accumulation at particular tissue or organelle; therefore nanoparticle engineering is of fundamental importance.[11–13] Essential properties such as surface chemistry,[14] targeting ability,[15,16] morphology,[17,18] size,[19] shape,[19] and dispersity ($Đ$)[20,21] dictate cellular uptake, biodistribution, clearance, and ultimately the success of nanoparticle-based therapeutics.[11,22–26]

Nanoparticle vectors can be synthesized from a range of materials.[2] However, polymeric nanoparticles are of broad interest as the macromolecular components can be easily modulated to yield delivery vehicles with different characteristics such as surface chemistry, size, and shape.[27] Non-spherical morphologies have exhibited significant advantages over conventional spherical geometries, particularly those with high aspect ratios.[28] For example, high-aspect ratio 1D nanoparticles often benefit from improved retention times,[29] pharmacokinetics,[30] tumor penetration,[31,32] and specificity,[33] as well as reduced phagocytosis,[34,35] and renal clearance.[30] Despite evidence of the substantial

advantages of high aspect ratio materials, access to low dispersity and morphologically pure nanofibers of controlled length remains a considerable challenge.[36,37]

Recent research has focused on the self-assembly and loading of amphiphilic block copolymer nanoparticles that contain an amorphous, hydrophobic core-forming block, and a solubilizing, hydrophilic corona-forming block. These assemblies can form high aspect ratio core-shell nanoparticles, termed nanoworms, that are capable of encapsulating hydrophobic cargo.[29,38,39] They are however generally difficult to access in morphologically pure form and length control is a major obstacle.[36] Crystallization-driven self-assembly (CDSA) has recently emerged as a versatile method that utilizes amphiphilic block copolymers with a crystallizable core-forming block to drive self-assembly into morphologies with a low curvature core-corona interface, such as 1D nanofibers and 2D platelets.[36] Living CDSA, a seeded growth method, enables access to low dispersity 1D and 2D nanoparticles with control over the size and surface chemistry.[40–45] Nanofibers and nanoplatelets with tailored coronal chemistries (including segmentation) are of interest as modular, multifunctional nanoparticles that can possess targeting or tracking capability.[32,46–49] Whilst the use of a crystalline core brings important advantages, it also inhibits the non-covalent loading of hydrophobic cargo into the core,[50–52] limiting potential drug delivery applications. A further complication is that, to date, only a limited number of crystallizable polymers that are potentially suitable for biomedical applications are currently known to undergo living CDSA.[42,47,53,54]

Recently, we reported a noncytotoxic, poly(fluorenetrimethylenecarbonate) (PFTMC) block copolymer that was able to yield low dispersity aqueous nanofibers of controlled length via living CDSA.[55] Building on this previous work, herein we provide

proof of concept studies which demonstrate that aqueous polymer nanofibers of controlled length are capable of non-covalently binding valuable cargo for use as delivery vehicles. This was achieved by using a coaxial-core approach, where the crystalline PFTMC core is surrounded by an amorphous core that can encapsulate hydrophobic cargo, with aqueous colloidal stability maintained through a hydrophilic corona.

2.3 Results

2.3.1 Design of the triBCP Coaxial-Core Nanofibers

Although crystalline materials have been used previously for the encapsulation of small molecules and gases,[10,56,57] we rationalized that the crystalline core of PFTMC nanofibers was unlikely to be capable of efficiently encapsulating hydrophobic cargo without disrupting the crystallization process and inducing crystal defects. We envisaged that a hybrid system should provide the advantages of both amorphous- and crystalline-core materials, namely in terms of encapsulation and controlled self-assembly, without any of the disadvantages. We therefore designed a coaxial-core nanofiber system comprised of a crystalline ‘inner core,’ a hydrophobic amorphous ‘outer core,’ and a water-soluble corona.

The crystalline and hydrophobic PFTMC was selected for the ‘inner core’ as it has been previously shown to yield colloidally stable aqueous nanofibers via living CDSA.[55,58] An amorphous, hydrophobic central block was required as an ‘outer core’ to encapsulate cargo. This block must remain soluble under the living CDSA conditions to avoid potential interference with the formation of the crystalline PFTMC inner core by epitaxial growth. Poly(butyl methacrylate) PBMA meets these requirements as it is an amorphous and hydrophobic polymer that has been previously used to encapsulate hydrophobic drugs,[59]

and it presents a moderate solubility in alcoholic solvents.[60] Finally, to provide colloidal stability in water and further protect the cargo, a hydrophilic corona-forming block was required. For this segment, PNIPAM was selected as it is a water- and alcohol-soluble, thermoresponsive material that has been previously used in drug delivery formulations, and may be of utility in triggering the release of cargo upon external stimuli.[61] Therefore, through careful design, we envisaged that a PFTMC-*b*-PBMA-*b*-PNIPAM triBCP would fulfill our requirements: namely, (i) by enabling living CDSA to yield low dispersity nanofibers which in aqueous media possess a coaxial crystalline-amorphous (PFTMC-*b*-PBMA) core, and (ii) by possessing the ability to encapsulate cargo through hydrophobic interactions[62] by means of the PBMA block (Figure 2. 1).

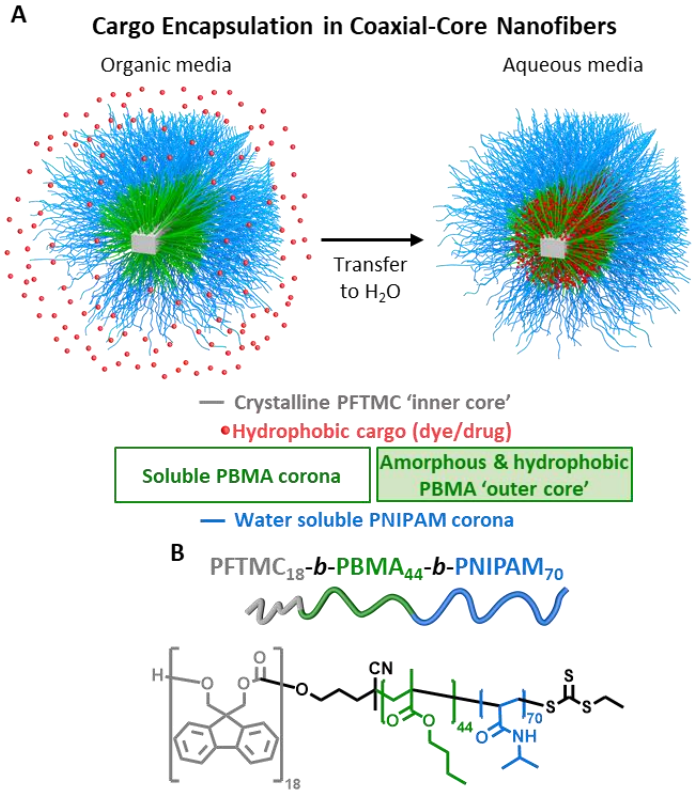

Figure 2. 1. Concept for loading hydrophobic cargo into coaxial-core nanofibers formed from PFTMC-*b*-PBMA-*b*-PNIPAM. A) Process for encapsulating hydrophobic cargo (red) in the hydrophobic amorphous PBMA 'outer core' (green) of preformed nanofibers upon transfer to H_2O, with the role of each component of the system described. B) Structure of color-coded $PFTMC_{18}$-*b*-$PBMA_{44}$-*b*-$PNIPAM_{70}$ triBCP used in this work.

The degree of polymerization (DP_n) of each block in the PFTMC-*b*-PBMA-*b*-PNIPAM triBCP was designed based on previous reports that core:corona DP_n ratios of ca. 1:5 to 1:20 are generally required to yield nanofibers.[63,64] Here, the triBCP core to corona ratio was 1:7 to meet such requirements and the DP_n of the PFTMC block (18) was consistent with previous work.[55] However, the DP_n of the PBMA segment (44) was designed as large as possible to maximize the potential cargo loading capacity whilst retaining colloidal stability under aqueous conditions, and good solubility under the alcoholic conditions used for self-assembly. Thus, our selected core to corona ratio includes the PBMA segment as part of the corona. The DP_n of the corona-forming PNIPAM block (70) was selected to ensure adequate water solubility combined with an efficient rate of growth via living CDSA.[65]

2.3.2 Synthesis and Characterization of PFTMC-*b*-PBMA-*b*-PNIPAM triBCP

The $PFTMC_{18}$-*b*-$PBMA_{44}$-*b*-$PNIPAM_{70}$ triBCP was prepared using a combination of ring-opening polymerization (ROP) and reversible addition-fragmentation chain-transfer (RAFT) polymerization. First, the chain transfer agent (CTA) functionalized $PFTMC_{18}$ homopolymer was obtained by ROP of the cyclic carbonate spiro[fluorene-9,5′-[1,3]-dioxan]-2′-one (FTMC) monomer using 2-cyano-5-hydroxypentan-2-yl ethyl carbonotrithioate as an initiator to yield $PFTMC_{18}$-CTA. This was characterized using matrix-assisted laser desorption/ionization-time of flight (MALDI-TOF) mass spectrometry (M_n = 4,800 g/mol, Figure S2. 1), gel permeation chromatography (GPC, $Đ_M$ = 1.17, polystyrene standards, Figure S2. 2) and NMR spectroscopy (Figure S2. 3). RAFT polymerization of the $PFTMC_{18}$-CTA with butyl methacrylate in dioxane yielded the intermediate diblock copolymer, $PFTMC_{18}$-*b*-$PBMA_{44}$ (M_n = 13,200 g/mol, $Đ_M$ = 1.12 by

GPC, Figure S2. 2) with the DP_n values determined via ^{1}H NMR integration (Figure S2. 4). Subsequent RAFT polymerization of the isolated intermediate with *N*-isopropylacrylamide monomer yielded the triBCP, which was precipitated from MeOH and then purified by flash chromatography to remove homopolymer impurities from the first reaction (water-initiated ROP of FTMC). The $PFTMC_{18}$-*b*-$PBMA_{44}$-*b*-$PNIPAM_{70}$ triBCP was characterized by ^{1}H NMR, 2D ^{1}H COSY NMR and GPC (M_n = 21,200 g/mol, $Đ_M$ = 1.32. Figure S2. 2, 5, 6). The interaction of the amino-group containing PNIPAM block with the GPC column likely contributes towards the broadening of the peak observed in the refractive index traces. Such issues have been previously noted for the analysis of PNIPAM-based materials.[66] Tailing to the low molar mass was also detected in the GPC traces of other PNIPAM -containing materials prepared in this study (Figure S2. 2, 7B, 15), resulting in an overestimation of the dispersities reported.[67] The homopolymers $PBMA_{130}$ and $PNIPAM_{178}$ homopolymers were also synthesized via RAFT for solubility experiments (DP_n determined via ^{1}H NMR integration, Figure S2. 8, 9). Polymer characterization data is summarized in Table S2. 1.

2.3.3 Self-Assembly and Seeded Growth of PFTMC-*b*-PBMA-*b*-PNIPAM to Form Nanofibers

To produce nanofibers of controlled length and low dispersity, a combination of CDSA (self-nucleation) and living CDSA (seeded growth) was used in sequence. First, the solution state self-assembly of $PFTMC_{18}$-*b*-$PBMA_{44}$-*b*-$PNIPAM_{70}$ was investigated (Figure 2. 2A). THF and DMSO were preselected as common solvents, the triBCP exhibited excellent solubility in both THF and DMSO (Figure S2. 10). Since PNIPAM and PBMA possess moderate-to-good solubility in alcoholic solvents[59,60,68] whilst PFTMC is insoluble,[55] we selected H_2O, MeOH, EtOH, and iPrOH as selective solvents for the

PNIPAM corona (Table S2. 2). Our first attempts at forming disperse nanofibers via spontaneous nucleation in mixtures of the above solvents at 1:9 common:selective solvent ratio (*v/v*) yielded exclusive nanofiber formation in THF:MeOH, THF:EtOH, DMSO:MeOH, and DMSO:EtOH mixtures as evidenced by TEM (Figure S2. 11D-G). Solvent mixtures with either H_2O or iPrOH yielded a mixture of spheres and nanofibers (Figure S2. 11B-C, H-I). The formation of spheres is a likely consequence of the rapid precipitation of the PFTMC block under these conditions due to the existence of insufficient time for crystallization leading to an amorphous core.[69,70] Optimized conditions for spontaneous nucleation involved annealing the triBCP (1.5 mg/mL) in a 15:85 THF:MeOH (*v/v*) solution at 70 °C for 3 h, followed by cooling to 20 °C and a 48 h ageing period. TEM analysis revealed morphologically pure nanofibers that were uniform in width (W_n = 12.6 nm, $Đ$ = 1.03, σ = 2 nm, Figure S2. 12) but disperse in length (> 3 μm, Figure 2. 2B). All TEM samples in this work were negatively stained with uranyl acetate solution (3 wt% in EtOH), the good interaction of the staining solution with the nanofiber-corona (PNIPAM-*b*-PBMA) but not the crystalline-core (PFTMC), results in a bright nanofiber-core against a dark background.

Seed nanofibers were prepared by sonication of the diluted length disperse nanofibers (0.5 mg/mL in a 15:85 THF:MeOH solution) for 3 h at 10 °C. TEM analysis revealed short nanofibers of 22 nm in length ($Đ$ = 1.12, σ = 7.7 nm, Figure 2. 2C). Low dispersity nanofibers of controlled length were then prepared via the living CDSA method. Briefly, unimeric $PFTMC_{18}$-*b*-$PBMA_{44}$-*b*-$PNIPAM_{70}$ in THF (10 mg/mL) was added to solutions of seed nanofibers in 15:85 THF:MeOH mixtures (0.1 mg/mL) followed by a 48 h aging period. By tuning the unimer to seed ratio (m_{unimer}/m_{seed}) from 0:1 to 50:1, we were

able to achieve length control from 22 nm ($Đ$ = 1.12, σ = 7.7 nm) to 818 nm ($Đ$ = 1.06, σ = 192 nm), as evidenced by TEM (Figure 2. 2D-G, S2.13). The width of the crystalline-core of the nanofibers prepared via living CDSA was found to be ~12.3 nm by TEM ($Đ$ = 1.03, σ = 2 nm, Figure S2. 12), which was consistent across assemblies of all lengths and with previous work where $PFTMC_{18}$ was found to undergo one chain fold.[55] Low length and width dispersity nanofibers were obtained in all seeded growth experiments, and a linear dependency of the final length vs m_{unimer}/m_{seed} ratio was observed (Figure 2. 2H-J, S2. 12, 13, Table S2. 3, and section 2.6.7 2.6). Moreover, the lengths of the nanofibers were unchanged upon leaving the samples for 4 months which suggested that all of the added unimer had been consumed.

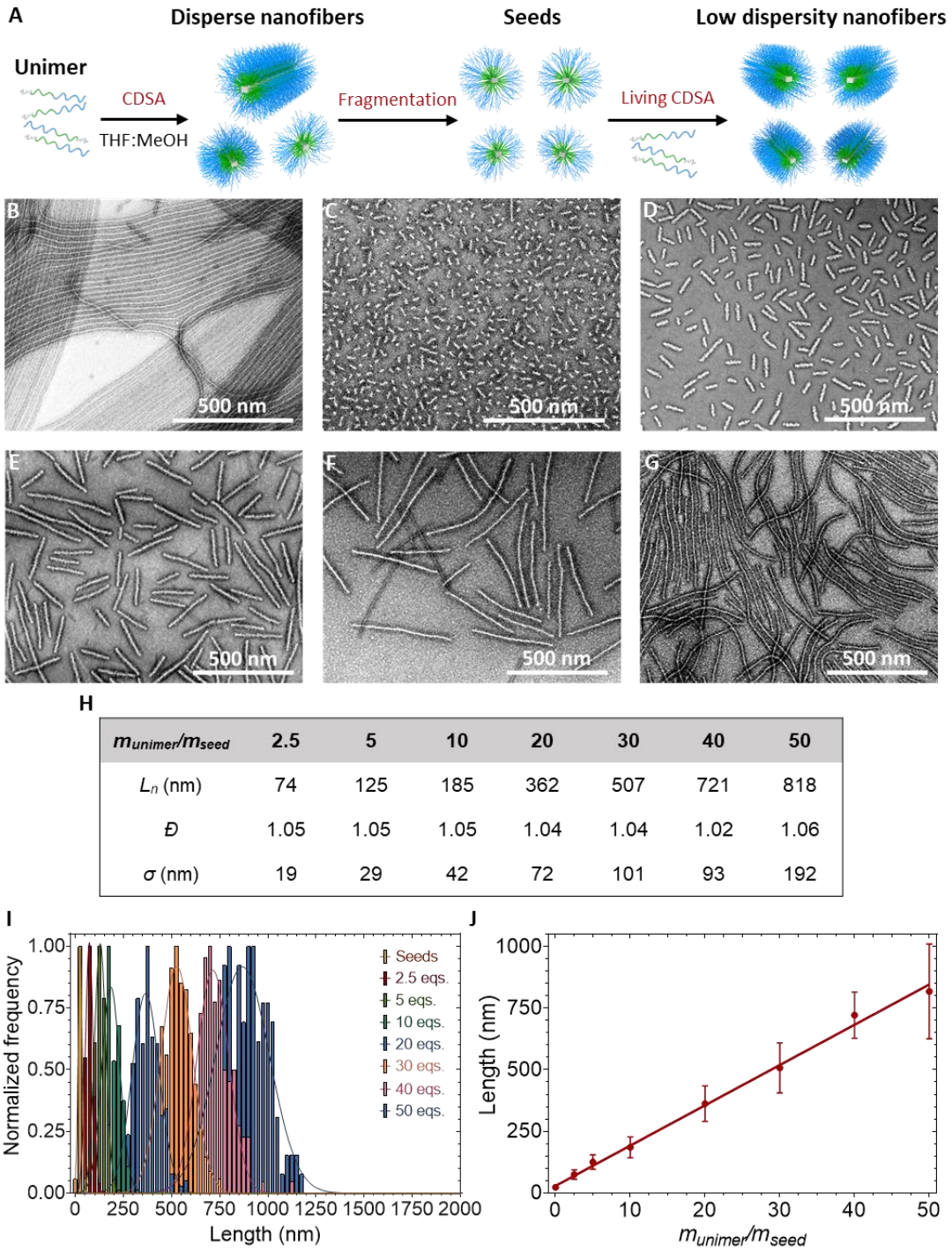

H

m_{unimer}/m_{seed}	2.5	5	10	20	30	40	50
L_n (nm)	74	125	185	362	507	721	818
$Đ$	1.05	1.05	1.05	1.04	1.04	1.02	1.06
σ (nm)	19	29	42	72	101	93	192

Figure 2. 2. Preparation of low dispersity nanofibers of controlled length. A) Schematic representation of the generation of low dispersity PFTMC$_{18}$-*b*-PBMA$_{44}$-*b*-PNIPAM$_{70}$ nanofibers through the living CDSA method. B) TEM of disperse PFTMC$_{18}$-*b*-PBMA$_{44}$-*b*-PNIPAM$_{70}$ nanofibers (0.5 mg/mL) prepared in THF:MeOH (15:85 *v/v*), after annealing at 70 °C for 3 h, and aged for 48 h. C) TEM of seed nanofibers (22 nm, $Đ = 1.12$, $\sigma = 7.7$ nm) prepared through sonication of the disperse nanofibers (from B, in THF:MeOH) for 3h at 0 °C. D-G) TEM images of low dispersity nanofibers prepared through seeded-growth by addition of unimer in THF to the nanofiber seed solution at: D) 2.5:1 E) 10:1 F) 20:1 and G) 30:1 m_{unimer}/m_{seed} ratios. H) nanofiber length summary. I) Contour length histograms of seeds and low dispersity nanofibers J) Plot of m_{unimer}/m_{seed} against L_n. TEM images were stained with uranyl acetate (3 wt% in EtOH).

2.3.4 Characterization of the PBMA Coaxial 'Outer Core' in Segmented A-B-A Triblock Nanofibers.

The living CDSA method allows for the preparation of segmented nanofibers with spatially localized coronal chemistries, thus enabling direct comparisons of the dimensions of the constituent nanofiber blocks. Therefore, to investigate if segmented nanofibers can be produced from PFTMC$_{18}$-*b*-PBMA$_{44}$-*b*-PNIPAM$_{70}$ seeds, and to gather evidence of the formation of the PBMA coaxial-outer-core, segmented A-B-A PFTMC$_{18}$-*b*-PNIPAM$_{425}$-***m***-PFTMC$_{18}$-*b*-PBMA$_{44}$-*b*-PNIPAM$_{70}$-***m***-PFTMC$_{18}$-*b*-PNIPAM$_{425}$ nanofibers were prepared by utilizing a PFTMC$_{18}$-*b*-PNIPAM$_{425}$ diBCP as the flanking 'A' segment (Figure 2. 3). Briefly, PFTMC$_{18}$-*b*-PNIPAM$_{425}$ was synthesized via RAFT polymerization with *N*-isopropylacrylamide from the intermediate PFTMC$_{18}$-CTA, and purified using flash chromatography to remove traces of residual homopolymer (Figure S2. 14, 15). Then, to a solution of 412 nm ($Đ$ = 1.04, σ = 78 nm) PFTMC$_{18}$-*b*-PBMA$_{44}$-*b*-PNIPAM$_{70}$ nanofibers (in THF:MeOH 15:85), 1 equivalent (m_{unimer}/m_{seed}) of the unimeric PFTMC$_{18}$-*b*-PNIPAM$_{425}$ diBCP (in THF) was added, and aged for 48 h. TEM analysis revealed an increase in length of the nanofibers from 412 nm to 701 nm ($Đ$ = 1.03, σ = 112 nm), however it was not possible to convincingly distinguish the 'A' and 'B' segments via TEM due to similar uranyl acetate staining interactions with the corona-blocks (Figure 2. 3B). Atomic Force Microscopy (AFM), however, enabled differentiation of the nanofiber segments (Figure 2. 3C). AFM analysis revealed that the core dimensions of the PFTMC$_{18}$-*b*-PBMA$_{44}$-*b*-PNIPAM$_{70}$ nanofiber (B) segment were significantly greater than that of the terminal PFTMC$_{18}$-*b*-PNIPAM$_{425}$ (A) segments. The larger height (ca. 13 nm) and width (ca. 48 nm) dimensions of the 'B' segment were observed despite the larger DP$_n$ of the PNIPAM corona in the terminal segments (A, DP$_n$ = 425) when compared to the central

segment (B, DP_n = 70, Figure 2. 3C-E). This indicated that the PNIPAM corona makes a minimal contribution towards the topological analysis of either segment. This demonstrates that the increase in core-size results from the presence of PBMA that coaxially surrounds the crystalline PFTMC inner core as the DP_n of the PFTMC inner core is identical in both segments. The cross-section of the crystalline PFTMC core is presumably rectangular based on the TEM analysis of the width (12.3 nm, Figure S2. 12), and the AFM analysis of the height (8.5 nm, Figure 2. 3. See supplementary discussion in section 2.6.7 on multifunctional segmented A-B-A nanofibers, Figure S2. 16, 17, 18).

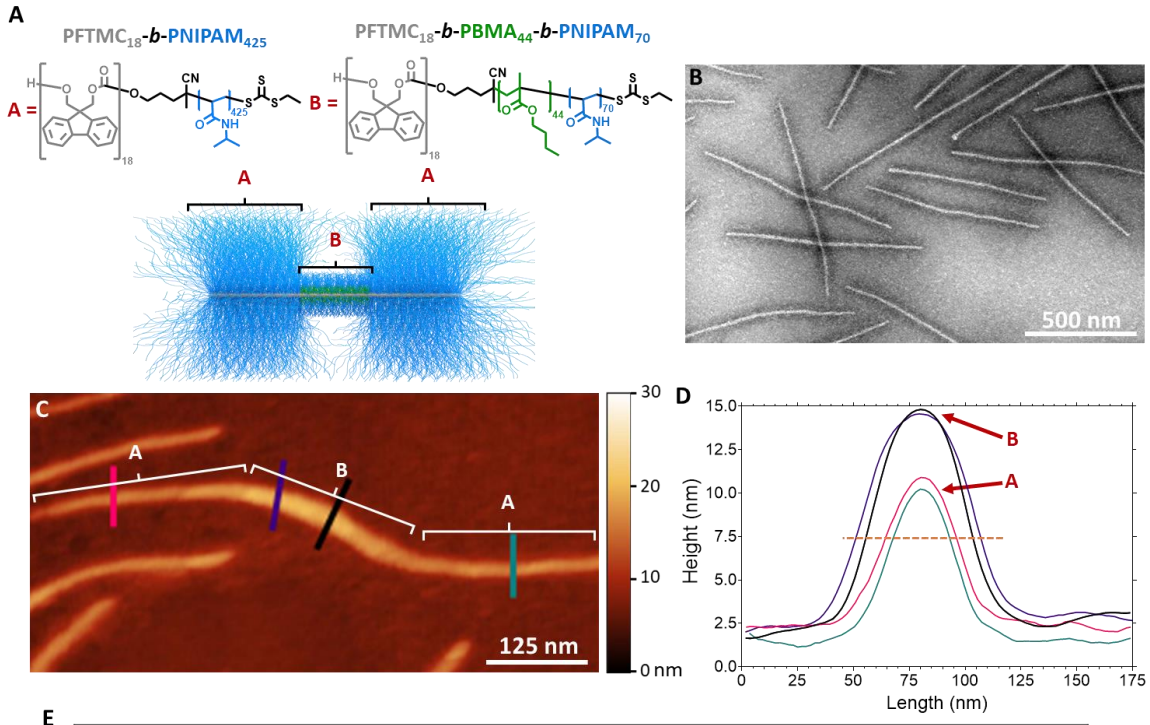

A trace B trace	A segment height (nm)	B segment height (nm)	A & B segments Δ height (nm)	A segment width (nm)	B segment width (nm)	A & B segments Δ width (nm)
AFM	8.5	12.5	4	25	48	23 nm

Figure 2. 3. A) Structure of segmented PFTMC$_{18}$-*b*-PNIPAM$_{425}$-***m***-PFTMC$_{18}$-*b*-PBMA$_{44}$-*b*-PNIPAM$_{70}$-***m***-PFTMC$_{18}$-*b*-PNIPAM$_{425}$ nanofibers (*m* = micelle segment), analyzed by: B) TEM (L_n = 701 nm, $Đ$ = 1.03, σ = 112 nm) and C) AFM. D) Height profiles of the segmented nanofibers. The pink and green traces correspond to the terminal PFTMC$_{18}$-*b*-PNIPAM$_{425}$ segment, and the purple and black traces correspond to the PFTMC$_{18}$-*b*-PBMA$_{44}$-*b*-PNIPAM$_{70}$ segment. Orange dashed line traced to get L_n values at the intersections. E) Summary of AFM dimensional analysis of the segmented nanofibers.

2.3.5 Loading of Length Disperse Coaxial Nanofibers with NR via Dialysis

Having demonstrated control over nanofiber length and achieving basic insight into the nature of the coaxial core, we investigated the solubility of PFTMC$_{18}$-*b*-PBMA$_{44}$-*b*-PNIPAM$_{70}$ nanofibers in deionized water before attempting to load the nanofibers with cargo. Nanofiber solutions were placed in dialysis membranes (MWCO 12 – 14 kDa), and the solvent was exchanged from THF:MeOH 15:85 to water. The nanofibers exhibited good solubility and colloidal stability in organic and aqueous media for at least one year. However, significant nanofiber fragmentation occurred upon dialysis into water as observed via TEM analysis (Figure S2. 19). Such behavior has been previously observed for other polymeric micelles with a crystalline core,[47,71] and is believed to occur due to the induced stress to the core from the corona swelling upon solvent exchange.[72,73]

Nanofiber loading was explored with a fluorescent dye, Nile Red (NR), as an example of a model hydrophobic cargo. The fluorescence emission spectra of NR is affected by the nature of the local solvent environment.[74] The emission wavelength of NR undergoes a red-shift with an increase in polarity of the surrounding molecular species until its fluorescence is fully quenched in water, making it an excellent probe to assess the encapsulation process.[75] First, we aimed to investigate if the presence of the hydrophobic NR is detrimental for the crystallization of the PFTMC core-forming block during the spontaneous nucleation step, as external molecules are known to interfere with crystallization processes.[76] Briefly, after heating unimeric PFTMC$_{18}$-*b*-PBMA$_{44}$-*b*-PNIPAM$_{70}$ in the presence of NR in 15:85 THF:MeOH (*v/v*) at 70 °C, followed by cooling to 20 °C and a 48 h ageing period, the resulting nanofibers were examined by both TEM and laser confocal scanning microscopy (LCSM). TEM revealed nanofibers that were several μm long (> 3 μm) which indicated that CDSA proceeded successfully in the

presence of NR. LCSM exhibited a red background with no distinguishable morphological features (Figure S2. 20A-C). Subsequent dialysis of the nanofibers and NR into water revealed length disperse nanofibers by TEM (length > 1 μm) and short nanofiber fragments (Figure S2. 20D), with widths found to be similar both before (W_n = 12.6 nm, $Đ$ = 1.03, σ = 2 nm) and after loading in H_2O (W_n = 13.1 nm, $Đ$ = 1.02, σ = 2 nm, Figure S2. 12). LCSM revealed discernible anisotropic fluorescence of NR along the nanofiber axis (Figure S2. 20E-F). Analysis of the fluorescence emission spectra of the NR loaded coaxial nanofibers in water revealed a peak emission at ca. 610 nm (Figure S2. 21), which is comparable to the emission of NR in polymethyl methacrylate (PMMA) and PBMA thin films reported elsewhere.[77,78] Since the NR emission is quenched in water, the observed emission must result from complexation of NR with the PFTMC$_{18}$-*b*-PBMA$_{44}$-*b*-PNIPAM$_{70}$ nanofibers. The inclusion of NR during the self-assembly process does not appear to interfere with the crystallization of the PFTMC core-forming block or nanofiber formation. It also appears that the NR remains in solution until it is encapsulated, likely by the PBMA, during the dialysis into H_2O. To confirm that NR was encapsulated in the PBMA outer core and not in the crystalline PFTMC inner core, we studied the loading of NR into preformed low dispersity nanofibers produced via living CDSA.

2.3.6 Loading NR into Low Dispersity Coaxial Nanofibers via Dialysis

While the shape of a nanoparticle drives the initial interaction with cells, controlling the length of the loaded nanofibers is highly desirable as the size can determine its effective uptake.[1,11,12] Although low dispersity nanoparticles ranging from 20 – 200 nm in size are the most viable for nanomedicine,[11,22] we selected ca. 400 nm nanofibers to further evaluate NR encapsulation due to the resolution limits of LCSM.[79] Therefore, 412 nm nanofibers

were prepared prior to the loading ($Đ$ = 1.04, σ = 78 nm, via TEM, Figure S2. 22B, H) in a mixture of MeOH:THF (85:15). Then, NR (12.5 µL, from a 1 mg/mL MeOH stock solution) was added to obtain a mixture of the nanofibers (1 mL, 0.1 mg/mL) with NR (0.025 mg/mL, 25 wt%), and the resulting solution was dialyzed against water. TEM analysis revealed that nanofiber fragmentation had occurred, leading to a substantial decrease of the length and an increase in the dispersity of the nanofibers (before dialysis: L_n = 412 nm, $Đ$ = 1.04, σ = 78 nm; after dialysis: L_n = 159 nm, $Đ$ = 1.41, σ = 101 nm, Figure S2. 22C, H). LCSM analysis revealed NR loaded nanofibers as evidenced by the anisotropic NR fluorescence observed (Figure S2. 22D), with a peak emission at ca. 610 nm (Figure S2. 23), similar to that observed for the length-disperse NR loaded nanofibers (Figure S2. 22I).

Control experiments where a sample containing NR (0.025 mg/mL) in 15:85 THF:MeOH (*v/v*, 1.5 mL) was dialyzed into water in the absence of any nanofibers revealed no fibrillar self-assembled structures by LCSM and TEM (Figure S2. 24A-B). LCSM analysis of the NR in water confirmed that the emission is quenched in water, and that the emission observed during the loading of both disperse and low dispersity nanofibers is due to interaction between NR and either the PBMA outer core or the PNIPAM corona of the polymer nanofibers. Dialysis into water was not sufficient to remove unencapsulated NR (Figure S2. 24C-D), and since nanofiber fragmentation negates the length control obtained from living CDSA (Figure S2. 22H), a revised loading procedure was developed.

2.3.7 Improved Loading Method for Low Dispersity Nanofibers: Preformed-Nanoparticle Solvent-Switch Loading (PNSL)

We attempted to minimize fragmentation by slowing the solvent exchange rate to better facilitate corona swelling during transfer from MeOH:THF to H_2O. Although dialysis is an efficient tool for solvent-switches, control over the rate of solvent diffusion cannot be obtained. A rapid change in solvent composition, evidenced by the quenching and precipitation of NR, was observed to occur within the first 10 minutes of the dialysis of NR from MeOH to H_2O (Figure S2. 24C). This is thought to contribute to the fragmentation of the nanofibers by inducing a sudden swelling of the coronal chains, imparting a considerable and rapid increase in stress to the crystalline core that ultimately results in cleavage.

To overcome these limitations, we developed a new approach, the Preformed-Nanoparticle Solvent-Switch Loading (PNSL) method (Figure 2. 4A). This allows for precise control over the solvent exchange rate. PNSL represents a two-step process involving, firstly the preparation, and secondly the loading, of nanoparticles with cargo via a solvent-switch process. Briefly, the nanofiber solutions (0.1 mg/mL, in THF:MeOH) were placed in a vial together with the NR (in MeOH) under constant homogenization using an orbital shaker. Then, H_2O was very slowly added via a syringe-pump at 100 µL/min until the water content reached 50%. The organic solvents were left to evaporate in the dark during homogenization at room temperature for 12 h, and this was followed by the introduction of a gentle flow of air into the vials (30 min). Finally, the loaded nanofibers in H_2O were filtered through a 0.45 µm syringe filter to remove any non-encapsulated NR, and the resulting solutions were diluted to their original volume through the gravimetric addition of water. The degree of fragmentation of the pristine 412 nm ($Đ$ = 1.04, σ = 78 nm) NR loaded nanofibers was found to be reduced by almost 50% using the PNSL method

compared to that of the dialysis approach, as evidenced by TEM (after PNSL: L_n = 339 nm, $Đ$ = 1.29, σ = 185 nm; after dialysis: L_n = 159 nm, $Đ$ = 1.41, σ = 101 nm, Figure S2. 22E,H). However, as a consequence of the shear forces involved, the filtration process after PNSL also led to some further fragmentation of the nanofibers with a consequential length reduction from L_n = 339 nm to L_n = 251 nm by TEM ($Đ$ = 1.50, σ = 178 nm, Figure S2. 22F, H). LCSM revealed that the nanofibers were loaded with NR after the filtration process (Figure S2. 22G). Control experiments revealed efficient NR removal via syringe filtration (0.45 µm, nylon filter), as evidenced by the minimal fluorescence detected from the NR in MeOH (Figure S2. 24E).

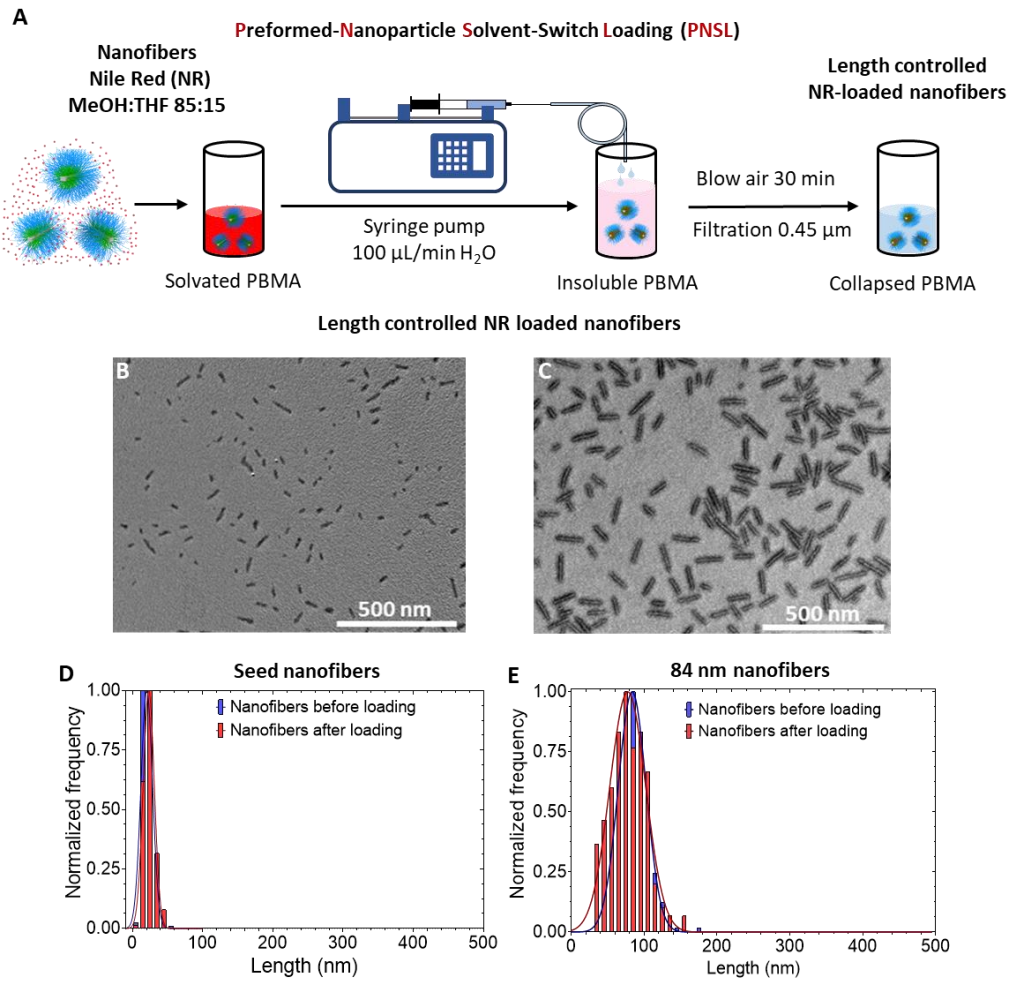

Figure 2. 4. Loading of model hydrophobic cargo Nile Red (NR) into low dispersity preformed nanofibers of controlled length (0.1 mg/mL, 1.5 mL, in MeOH:THF 85:15) with NR (10 wt%, in MeOH). 1.5 mL of H2O added at 100 µL/min. A) Schematic process for loading NR into low dispersity PFTMC$_{18}$-*b*-PBMA$_{44}$-*b*-PNIPAM$_{70}$ nanofibers via the PNSL method. B-C) TEM images of the low dispersity NR loaded nanofibers in H_2O; B) L_n = 25 nm, $Đ$ = 1.08, σ = 7.0 nm; C) L_n = 78 nm, $Đ$ = 1.09, σ = 24 nm. (D-E) Contour length histograms of the low dispersity NR loaded nanofibers in H_2O before and after loading.

The decrease in fragmentation of the 412 nm triBCP nanofibers associated with the use of the PNSL protocol prompted us study the analogous cleavage of PFTMC$_{18}$-*b*-PBMA$_{44}$-*b*-PNIPAM$_{70}$ nanofibers with lengths more relevant to drug delivery (20 – 200 nm).[11,22,25] Thus, very short seed nanofibers (L_n = 22 nm, $Đ$ = 1.12, σ = 7.7 nm, Figure S2. 25A) and 84 nm long nanofibers formed from the seeds by living CDSA ($Đ$ = 1.05, σ = 20 nm, Figure S2. 25B) were loaded with NR via the PNSL method, followed by filtration. No significant change was observed in the length of the resulting

seeds (L_n = 25 nm, $Đ$ = 1.08, σ = 7.0 nm) or of the 84 nm loaded nanofibers (L_n = 78 nm, $Đ$ = 1.09, σ = 24 nm) as evidenced by TEM (Figure 2. 4B-E). Interestingly, in the analogous experiment with the same 84 nm nanofibers loaded with NR via dialysis, the dispersity and σ increased considerably based on TEM analysis (L_n = 86 nm, $Đ$ = 1.26, σ = 44 nm, Figure S2. 26), representing a loss of control and uniformity obtained through the living CDSA method. As discussed below minimal fragmentation of nanofibers was detected using the PNSL method for lengths up to 125 nm.

2.3.8 Optimization and Quantification of NR Loading in Coaxial Nanofibers

With the fragmentation issue effectively addressed for nanofiber lengths relevant to drug delivery using the PNSL method, optimization and quantification of the encapsulation of NR, the encapsulation efficiency (EE) and loading capacity (LC) was studied. As an initial step, the loading conditions were optimized by varying the amount of NR added between 0.1 and 25 wt % of the nanofiber. The nanofiber concentration was kept constant at 0.1 mg/mL for all experiments. For simplicity, short nanofibers of PFTMC$_{18}$-*b*-PBMA$_{44}$-*b*-PNIPAM$_{70}$ were examined (L_n = 25 nm, $Đ$ = 1.08, σ = 7.0 nm, Figure 2. 4B). Our findings indicate that the maximum loading (and loading capacity, LC %) of NR in the triBCP nanofiber system is achieved when the NR is loaded at 1 wt% (with respect to the nanofiber concentration, Figure S2. 27, 28, 29). The triBCP nanofibers (of 25 nm) were able to encapsulate ca. 600 ng NR per mg of polymer (4.0 mol%, Figure S2. 29A). Interestingly, the EE % of NR into the triBCP nanofibers increased as the NR wt% loading decreased, with a maximum EE of 25% at a 0.01 wt% loading (Figure S2. 29B).

To further evaluate and to compare the loading of NR in nanofibers with relevant lengths for drug delivery PFTMC$_{18}$-*b*-PBMA$_{44}$-*b*-PNIPAM$_{70}$ L_n = 125 nm ($Đ$ = 1.08,

σ = 35 nm) nanofibers were prepared and examined by TEM (Figure 2. 5A). Then, the nanofibers were loaded via the PNSL method at the optimal loading concentration of NR (1 wt%) determined previously (Figure S2. 29A). No significant change in the nanofiber length was observed after the PNSL process (L_n = 121 nm, $Đ$ = 1.09, σ = 37 nm, Figure 2. 5B), and after filtration (L_n = 119 nm, $Đ$ = 1.09, σ = 36 nm, Figure 2. 5C). Analysis of the contour length of the triBCP nanofibers revealed that fragmentation was virtually non-existent after the PNSL process (Figure 2. 5D), and that fragmentation by filtration is likely avoided because of the lower aspect ratio of the nanofibers of length L_n = 125 nm compared to those with L_n = ca. 400 nm (Figure S2. 22H).

Fluorometry experiments revealed that the triBCP nanofibers (L_n = 125 nm) were able to encapsulate ca. 667 ng of NR per mg of polymer (4.2 mol%), with 6.7% EE (Figure 2. 5E). The LC % of the 25 nm and the 125 nm triBCP nanofibers was similar at both nanofiber lengths (ca. 0.06%, Figure S2. 29C-D). Furthermore, to assess the emission of NR in a different system, a sample of PFTMC$_{18}$-*b*-PEG$_{530}$ nanofibers was prepared via living CDSA (L_n = 108 nm, $Đ$ = 1.08, σ = 30 nm, Figure S2. 30A) and analyzed by TEM through the NR loading process at 1 wt% of NR (Figure S2. 30B-C). Fluorescence measurements of the nanofibers in H_2O revealed that the NR was present in both BCP systems, but in different polar environments (Figure 2. 5F). The NR emission from triBCP PFTMC$_{18}$-*b*-PBMA$_{44}$-*b*-PNIPAM$_{70}$ nanofibers (λ_{max} = 610 nm) was consistent with the PBMA environment observed for both the disperse and the low length dispersity nanofibers previously loaded with NR (Figure S2. 22I). In contrast, the emission from NR loaded into PFTMC$_{18}$-*b*-PEG$_{530}$ nanofibers was red-shifted (λ_{max} = 625 nm) which is indicative of a more polar local environment, likely arising from the adsorption of NR at the core-corona

interface of PFTMC$_{18}$-*b*-PEG$_{530}$ nanofibers, where unfavorable interactions with the polar solvent would still be present but minimized (Figure 2. 5F). Detailed studies of the hydrophobic adsorption of NR into diBCP nanofibers with a crystalline core are in progress and will be published elsewhere.

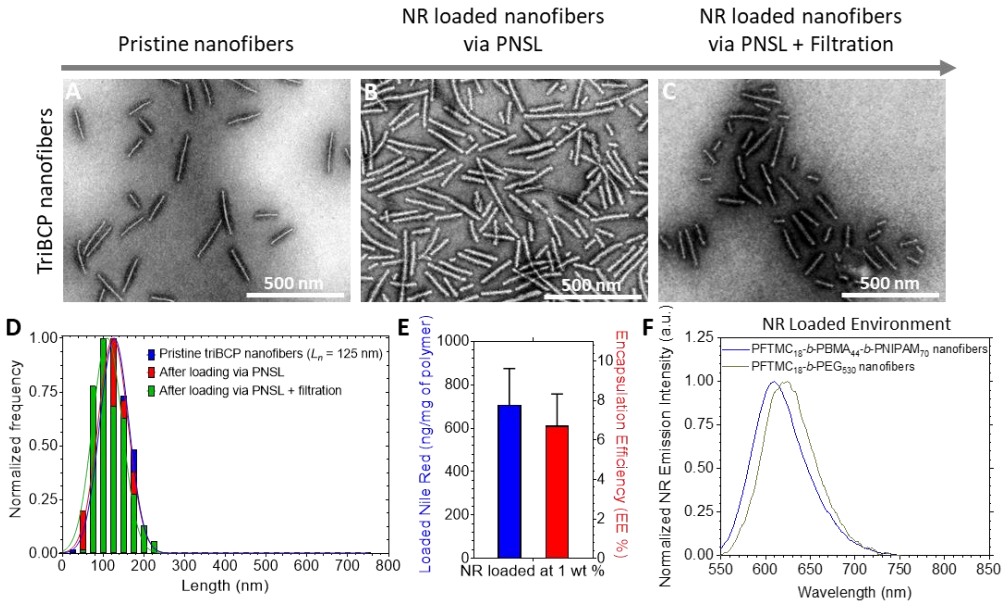

Figure 2. 5. Loading and quantification of NR into preformed (triBCP and diBCP) nanofibers of controlled length and low length dispersity. TEM images of the loading process of the PFTMC$_{18}$-*b*-PBMA$_{44}$-*b*-PNIPAM$_{70}$ nanofibers A) before loading (L_n = 125 nm, $Đ$ = 1.08, σ = 35 nm), B) after loading via PNSL (L_n = 121 nm, $Đ$ = 1.09, σ = 37 nm), C) after syringe filtration (L_n = 119 nm, $Đ$ = 1.09, σ = 36 nm). D) Contour length histograms of the nanofiber loading process; before loading, after PNSL loading, and after filtration. E) Encapsulated NR (in ng/mg of polymer), and encapsulation efficiency (EE %) determined by fluorometry of the triBCP nanofibers in 'C' with respect to the initial NR concentration (1 wt%). F) Emission spectra of the NR loaded in both PFTMC$_{18}$-*b*-PBMA$_{44}$-*b*-PNIPAM$_{70}$, and PFTMC$_{18}$-*b*-PEG$_{530}$ diBCP nanofibers in water (nanofiber concentration = 0.1 mg/mL).

2.3.9 Investigating NR Release from PFTMC$_{18}$-*b*-PBMA$_{44}$-*b*-PNIPAM$_{70}$ Coaxial Nanofibers

Based on the proposed encapsulation mechanism of the triBCP coaxial nanofibers, we envisage that the encapsulated NR should be released upon increasing the solubility of the PBMA 'outer core' (Figure 2. 6A, S2. 31A). Therefore, to examine whether the cargo loading is a reversible process, the release of NR was examined by preparing both uniform 412 nm ($Đ$ = 1.04, σ = 78, Figure S2. 22F) and disperse nanofibers (> 3 μm, Figure S2. 31B) at 0.1 mg/mL, loaded with NR (0.05 mg/mL) via the PNSL process. Both the uniform and disperse nanofiber samples exhibited anisotropic fluorescence by LCSM after the PNSL consistent with NR loading (Figure 2. 6B-C, S2.31C). The NR loaded nanofibers were then dialyzed from H_2O back to MeOH. TEM revealed that the nanofibers remained in the MeOH solution (Figure S2. 31D, 32). However, LCSM analysis of the samples in MeOH revealed minimal residual NR fluorescence emission from both the anisotropic nanofibers and from the solution, indicating that NR was successfully removed through dialysis into MeOH (Figure 2. 6D, S2. 31F-G). This result confirmed that that cargo release can be driven by a change in the solvent environment, with the soluble NR removed into the dialysate. The lack of observable NR emission from the sample after dialysis into MeOH also provided evidence that the NR is encapsulated in the PBMA outer core with release occurring due to an increase in the solubility of the PBMA block and NR. Release of NR from within the crystalline PFTMC inner core would not be expected as it remains insoluble in both MeOH and water.

The thermo-responsive properties of the PNIPAM block could also potentially be utilized for the release of NR from the coaxial nanofibers. An increase in temperature above the lower critical solution temperature (LCST) of the PNIPAM would be expected to

dehydrate the PNIPAM-corona, resulting in the loss of aqueous colloidal stability, and possibly facilitating NR release.[59,80]

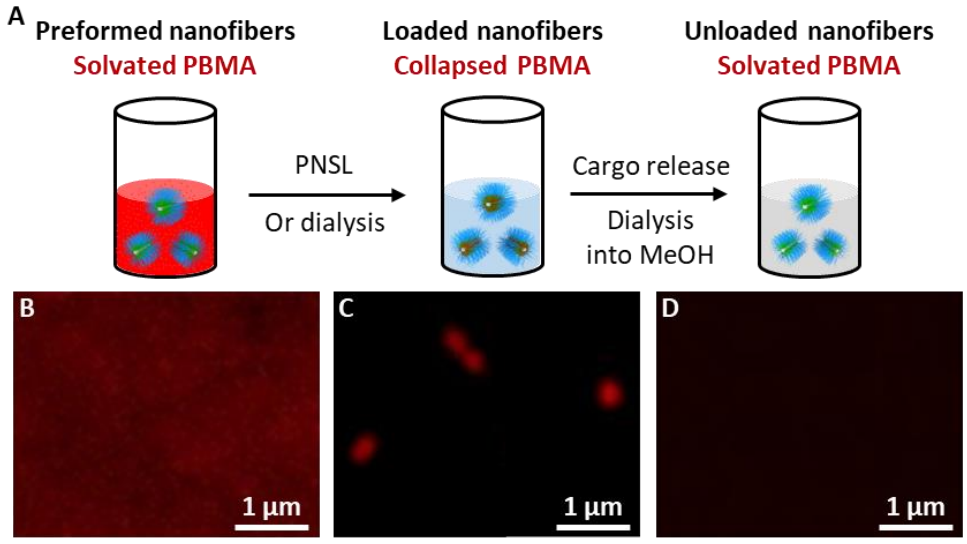

Figure 2. 6. A) Schematic representation of the NR loading and unloading of preformed PFTMC$_{18}$-*b*-PBMA$_{44}$-*b*-PNIPAM$_{70}$ nanofibers of controlled length. LCSM images of the 412 nm ($Đ$ = 1.04, σ = 78 nm, by TEM) NR loaded nanofibers: B) before loading in MeOH, C) after loading in H_2O, and D) after dialysis into MeOH.

2.3.10 Assessment of the Encapsulation Volume Lost Due to the Presence of the Crystalline PFTMC 'Inner Core'

Although the crystalline PFTMC inner core of the triBCP nanofibers allows for length control through the living CDSA approach, its presence also reduces the volume available for cargo encapsulation. To estimate how significant the impact of this is likely to be, we calculated the volume of the PFTMC$_{18}$-*b*-PBMA$_{44}$ core, and compared it to the volume of the PFTMC$_{18}$ inner core, to arrive at the % of the core occupied by the PFTMC and therefore unavailable for cargo encapsulation. We utilized a rectangular-cross section model[55] for the calculation of the PFTMC$_{18}$ volume, which had a width of 12.3 nm (obtained via TEM, Figure S2. 12) and a height of 8.5 nm (obtained via AFM, Figure 2. 3E), which led to the a volume of ca. 105 nm^3 per unit length for the PFTMC$_{18}$ inner core. According to energy minimization calculations (Figure S2. 33), the length of the PBMA$_{44}$

chain is ca. 10.1 nm. Thus, the geometric dimensions of a rectangular PFTMC crystalline core-cross-section with an ellipsoidal PBMA amorphous outer core yield a calculated volume of the $PFTMC_{18}$-*b*-$PBMA_{44}$ coaxial core of ca. 732 nm^3 per unit length. This equates to the $PFTMC_{18}$ inner core occupying ca. 14% of the total volume of the core. See section 2.6.7 for details.

2.4 Discussion

To our knowledge, there are no reports to date of a drug delivery platform that is able to encapsulate cargo into preformed, low dispersity polymeric nanofibers of controlled length, driven through hydrophobic interactions.[38,62,81–85] The manufacture of nanoparticle-based therapeutics via methods such as nanoprecipitation often involve cargo loading and self-assembly occurring synchronously,[86] utilizing processes such as mechanical stirring, temperature or solvent changes, and hydration/dehydration, amongst others, to drive encapsulation.[86–89] An inherent disadvantage of these approaches is that the resulting nanoparticle properties are intrinsically linked to the cargo loading process as well as the self-assembly process. In this manner, changes to the type or amount of cargo, the temperature, and the quantities of carrier or solvents used will affect the size, shape, dispersity, and surface chemistry of the resulting particles. These processes are unsuitable for nanoparticles that possess a crystalline core, as the conditions used (frequently addition to water) are unlikely to allow core-crystallization to occur, resulting in amorphous nanoparticles with limited control over particle size and shape.[90,91] Separating the nanoparticle self-assembly process from the cargo loading process may add an additional level of complexity into polymer and nanoparticle engineering, but it enables significantly more control over both steps than the multivariable process of simultaneously forming and

loading nanoparticles in a single step. Preforming the nanoparticles has the additional advantage of facilitating access to nanoparticles that would be unobtainable through synchronous cargo loading and self-assembly.[91] This can be used to generate nanoparticles of uniform size, shape, and dimensions independent of the cargo to be loaded. For these reasons, the concept of a two-step loading procedure, and of polymer nanoparticles with a coaxial amorphous/crystalline core are both beneficial for the future development of precision polymer nanoparticles for drug delivery applications, and are especially pertinent to the challenge of creating precision non-spherical polymer delivery systems.

In this work, the good solubility of NR in MeOH simplified the loading process, MeOH:THF (85:15) was the solvent mixture where morphologically pure PFTMC$_{18}$-*b*-PBMA$_{44}$-*b*-PNIPAM$_{70}$ nanofibers were obtained, allowing for polymer self-assembly and cargo solubilization to occur in one solvent system. Nonetheless, solvent transfer to other organic solvents, prior to the solvent switch to H_2O, should be possible to meet different cargo solubility requirements in order to expand the scope of the cargo species available for loading. Slow solvent exchange of the nanofiber and NR solution from MeOH:THF (85:15) to H_2O via the PNSL method reduced the solubility of both the cargo and the PBMA block, allowing for the NR cargo to associate with the hydrophobic PBMA coaxial 'outer core', as a result of the decreased solubility of the PBMA block. One advantage of this process is the use of minimal hydrophobic cargo due to the separation of the cargo loading step from the self-assembly step. Reducing the quantities of drug needed for a nanoparticle formulation is of high importance, as drugs are often among the most valuable and expensive component of the delivery systems.[92] Additionally, the PNSL loading procedure developed here minimizes nanofiber fragmentation, which is essentially

eliminated for nanofibers of lengths < 125 nm. It also facilitated the complete removal of non-encapsulated NR through syringe filtration.

PFTMC$_{18}$-*b*-PBMA$_{44}$-*b*-PNIPAM$_{70}$ nanofibers up to 125 nm (Figure 2. 5) were successfully loaded with hydrophobic cargo (NR) through the PNSL method, and the length remained unchanged through the process. The NR peak emission (ca. 610 nm, Figure 2. 5F, S2. 22I) from the loaded PFTMC$_{18}$-*b*-PBMA$_{44}$-*b*-PNIPAM$_{70}$ nanofibers was consistent regardless of whether NR was present during self-assembly, or added post-assembly, suggesting that NR is associated with the same environment: the PBMA outer core. An evident mismatch of the encapsulated NR emission spectra would be apparent if NR was encapsulated in a different environment, such as inside, or adsorbed to the PFTMC core (see Figure 2. 5F).

The optimal loading of NR into the 25 nm ($Đ$ = 1.08, σ = 7.0 nm) coaxial core triBCP nanofibers occurred at 1 wt%, with loadings of ca. 600 ng/mg of polymer (Figure S2. 29A). The 125 nm ($Đ$ = 1.08, σ = 35 nm) PFTMC$_{18}$-*b*-PBMA$_{44}$-*b*-PNIPAM$_{70}$ coaxial core nanofibers were loaded with ca. 667 ng of NR/mg of polymer at the same loading concentration (1 wt%, Figure 2. 5E). The resulting amount of NR loaded is, within error, similar at both nanofiber lengths. Furthermore, the EE % and LC % (at 1 wt% NR loading) of both the 25 nm and 125 nm triBCP nanofibers were also comparable, with values of ca. 6% (EE), and 0.06% (LC), regardless of the nanofiber length (Figure 2. 5E, S2. 29B-D).

The volume of the coaxial core was estimated using a combination of experimental TEM and AFM analysis, alongside energy minimization calculations (Figure 2. 3, S2. 12, 33), thereby providing an estimation of the volume occupied by the crystalline PFTMC core (105 nm^3) per nm of nanofiber. This represents ca. 14% of the core that is unavailable

for encapsulation, based on a crystalline core with a rectangular cross-section of $PFTMC_{18}$,[55] surrounded coaxially by an elliptical, amorphous $PBMA_{44}$ outer core. The small reduction in encapsulation space caused by the presence of the crystalline inner core appears to be a modest tradeoff for the ability to control the nanoparticle morphology and dimensions due to the importance of controlling nanoparticle size, shape, and dispersity in biomedical applications.[32]

Release of the encapsulated NR was achieved via an increase on the solubility of the PBMA block through dialysis from water back into organic media (MeOH). This suggests that NR is associated with the PBMA outer core, with encapsulation and release both occurring primarily due to changes in the solubility of PBMA and NR. The change in solubility of the PBMA was achieved via a second solvent switch to MeOH. Thus, the association of NR and the PBMA coaxial core only occurs during the transfer from organic media to water. In this manner, the design of the coaxial-core nanofibers resembles a traditional solvent-switch loading process, with the exception that self-assembly has been removed to a preceding step.

2.5 Summary and Conclusions

In summary, we have developed a novel approach for loading hydrophobic cargo into anisotropic polymer nanoparticles via nanoparticle and polymer engineering of triBCP nanofibers that contain a coaxial-core design. The nanofibers were composed of a crystalline inner core and an amorphous outer core, that provided the morphology and size control of crystalline systems with the cargo loading capabilities of amorphous systems, in one nanoparticle. Rational design led to the development of $PFTMC_{18}$-*b*-$PBMA_{44}$-*b*-$PNIPAM_{70}$ coaxial-core nanofibers. The cargo-loaded nanofibers were prepared in a two-

stage process, which consisted of self-assembly in organic media, followed by aqueous dispersion and encapsulation of a model hydrophobic dye, NR, via a process termed PNSL.

Nanofiber loading was studied via dialysis as well as via the PNSL process. In general, dialysis was found to be inefficient, expensive and time consuming, leading to nanofiber fragmentation and the ineffective removal of non-loaded hydrophobic components. We found that nanofiber fragmentation was minimal for short nanofibers (<125 nm) loaded and transferred to H_2O via the PNSL method, and that syringe filtration was an effective method for removal of non-encapsulated material. Low dispersity nanofibers were used to optimize the NR loading process. The optimal loading concentration of NR was obtained at 1 wt% (NR:polymer). The amount of NR encapsulated in triBCP nanofibers of length 25 nm and 125 nm was ca. 600-667 ng of NR loaded per mg of nanofiber (4-4.2 mol%).

Nanofiber loading was found to occur at the water-transfer stage on both micrometer length disperse and low dispersity nanofibers of controlled length. Confirmation of the coaxial core and the role of the PBMA outer core in facilitating NR association was demonstrated through a combination of fluorimetry, LCSM, TEM, and AFM. Our results suggest that the PFTMC crystalline inner core cannot load hydrophobic cargo, and that NR release is facilitated by an increase in solubility of the PBMA block and the NR, which can be mediated through a solvent switch.

Two examples of segmented nanofibers were prepared, which provided evidence of the coaxial core via AFM analysis, and provided evidence for the feasibility of smart multicomponent nanofibers that may be of utility for enhanced precision nanomedicines. A combination of computation, and TEM / AFM analysis allowed us to estimate the

volume of the PFTMC inner core, which was found to be ca. 14%. In principle, the volume fraction occupied by the PFTMC inner core can be further minimized by either decreasing the DP_n of the PFTMC and/or by increasing the DP_n of the PBMA block and further optimization of this type is currently being explored.

The combination of amorphous and crystalline polymeric materials into coaxial-core nanofibers, as well as the two stage PNSL loading method are both new concepts for loading hydrophobic material into polymeric nanoparticles, with significant potential advantages over previous 'assembly-stage' loading processes. Future work will investigate the release profiles and biological activity in detail, leading to the development of stimuli-responsive materials for drug delivery and nanomedicine applications.

2.6 Supporting Information

2.6.1 General Considerations and Instrumentation

Methoxy PEG (19 kDa) was purchased from Polymer Source. All other reagents and solvents were purchased from Sigma-Aldrich (Canada), Combi-Blocks (USA), VWR (Canada), or Fisher Scientific (Canada) and used as received unless otherwise noted. Solvents for self-assembly were of HPLC grade and were filtered through PTFE, nylon or cellulose membranes with a pore size of 200 nm before use. All reactions were carried out in an MBraun 200B glove box under a nitrogen atmosphere or using standard Schlenk line techniques. RAFT polymerizations were performed in custom-made Schlenk-vials to fit dry heating blocks. 1,8-Diazabicyclo[5.4.0]undec-7-ene (DBU) was dried over CaH_2, and purified by distillation under reduced pressure. Anhydrous solvents were dried and purified using an MBraun Grubbs/Dow solvent purification system.[93] Spiro[fluorene-9,5′-[1,3]-dioxan]-2′-one (FTMC) was synthesized according to the procedure reported by Finnegan et al.[55] Synthesis of 2-cyano-5-hydroxypentan-2-yl ethyl carbonotrithioate was prepared according to the procedure reported by Arno et al.[42] The PEG and RAFT-CTAs were dried via vacuum desiccation over phosphorus pentoxide prior to use.

Ultrasonication

Micelle sonication was carried out using a Fisherbrand 112xx series advanced ultrasonic cleaner (FB-11203). The instrument was operated in sweep mode for seeds at 80 % power and 37 MHz at 10 °C.

NMR Spectroscopy

^{1}H and COSY NMR spectra were obtained using a Bruker 500 MHz spectrometer with CD_2Cl_2 (^{1}H NMR: δ = 5.32 ppm), or DMSO-d_6 (^{1}H NMR: δ = 2.50 ppm) used as the

solvents. Chemical shifts are quoted in parts per million, with spectra referenced to the residual solvent peak. Multiplicities are abbreviated as brs (broad singlet), s (singlet), d (doublet), t (triplet), q (quartet), p (pentet), m (multiplet) and *app.* (apparent) or combinations thereof.

Gel permeation chromatography (GPC)

GPC was conducted on a Malvern OMNISEC chromatograph equipped with a refractive index (RI), UV/Vis photodiode detector array, light scattering detector and viscometer. Triethylamine/THF (1% *v/v*) was used as the eluent, with the flow rate set at 1 mL/min. The columns used were T3000, followed by T5000 (Viscotek) at a constant temperature of 35 °C. The calibration (universal) of the RI detector was carried out using polystyrene standards (Viscotek). Samples were prepared at 1 mg/mL in eluent and filtered through a polytetrafluorethylene membrane filter, pore size = 0.2 µm.

Matrix-assisted laser desorption/ionization-time of flight mass spectrometry (MALDI-TOF MS)

MALDI-TOF MS measurements performed using a Bruker Ultraflextreme running in linear mode. The samples were prepared using a *trans*-2-[3-(4-*tert*-butylphenyl)-2-methyl-2-propenylidene]malononitrile matrix (20 mg/mL in THF) and the polymer sample (2 mg/mL in THF), mixed in a 10:1 (*v*/*v*) ratio. Approximately 3 µL of the mixed solution was deposited onto a stainless-steel sample plate and allowed to dry in air.

Transmission electron microscopy (TEM)

TEM images were obtained on a JEOL 1011 microscope with an 11 Megapixel CCD camera, operated at 80 kV. Samples were prepared by drop-casting 7.5 µL of the micelle solution onto a carbon-coated copper grid, followed by drop-casting 10 µL of

uranyl acetate in EtOH (3 wt %). Sample concentration for TEM analysis was either 0.5 or 0.1 mg/mL based on nanofiber concentration. Copper grids (400 mesh) were purchased from Ted Pella, and carbon films (ca. 6 nm) were prepared on mica sheets by carbon sputtering with a Leica ACE 600 carbon coater. The carbon films were deposited onto the copper grids by floatation on water and the carbon-coated grids allowed to dry in air.

For micelle contour length and width analysis, a minimum of 150 nanofibers in several images were traced manually using the ImageJ software package developed at the US National Institute of Health. The number average micelle length (L_n) or width (W_n) and weight average micelle length (L_w) or width (W_w) were calculated using eqs. S2. 1-2 from measurements of the contour lengths (L_i) of individual micelles, where N_i is the number of micelles of length L_i, and n is the number of micelles examined in each sample. The distribution of micelle lengths is characterized by $Đ = L_w/L_n$.

$$L_n = \frac{\sum_{i=1}^{n} N_i L_i}{\sum_{i=1}^{n} Ni} \qquad L_w = \frac{\sum_{i=1}^{n} N_i L_i^2}{\sum_{i=1}^{n} NiLi} \quad \text{(Eq. S2. 1-2)}$$

Atomic Force Microscopy

AFM analysis was obtained using a 5500 Atomic Force Microscope (Agilent Technologies). The images were recorded in AC mode with a scanning speed of 1.0 μm/s in an area of 4.0 μm^2 at 1024 × 1024 resolution. The tips employed (Tap150Al-G, Budget Sensors) consisted of a conical silicon tip with aluminum reflective coating and a resonance frequency and force constant of 150 kHz and 5N/m, respectively. The samples for AFM were prepared on a silicon wafer by casting the nanofiber solution (in ~ 100% MeOH, 20 μL, 0.05 mg/mL) onto the clean silicon wafer. The silicon wafer was gently dried from the sides with a filter paper and dried via vacuum desiccation.

Laser confocal scanning microscopy (LCSM)

LCSM images were obtained using a ZEISS LSM 880 Axio Observer or Leica TCS SP 8 3X. Images were recorded using a HC PL APO CS2 100x/1.40 or HC PL APO 63x/1.4 oil immersion objectives. Samples were excited using a either 543 or 561 laser lines, with the fluorescence emission monitored between ca. 560 - 640 nm in channel mode or from 550 - 700 nm with 10 nm intervals in "lambda mode." The resulting images were obtained as digital false-color images and then color-coded as red. Analysis of the fluorescence emission spectra experiments were performed using the software Zen 3.1, blue edition, from Zeiss, or using the software ImageJ, from the National Institute of Health (USA). The subsequent data treatment was performed in GraphPad Prism 7 (GraphPad Software LLC) with Gaussian fit and smoothing curve functions, with backgrounds subtracted where applicable. The micrographs of the 412 nm nanofibers loaded with NR where deconvoluted using the Iterative Deconvolve 3D function in ImageJ.[94] The nanofiber samples (10 µL, 0.01 mg/mL) were prepared by placing diluted micelle solutions (in water, MeOH, or water:glycerol 50:50) on a glass slide. A coverslip was then placed on top of the solution and sealed in place with clear nail polish.

Spectroscopic Experiments

UV-Vis spectra were recorded by using a Varian Cary 100 Bio spectrophotometer at 25°C, unless otherwise indicated. Fluorescence measurements were obtained by using a PTI QM40 fluorometer at 25°C. The slits were set to 2 nm bandpass. All measurements were corrected for the fluctuations of the lamp intensity and transmission of the optics. The samples were excited at 540 nm for the emission scans, and the emission was recorded from 550 - 750 nm. For determining excitation wavelength to use, excitation scans were

recorded with the emission detected at 665 nm, with excitation wavelengths scanned from 400 - 650 nm. The emission of NR from the loaded nanofibers was studied in H_2O and in MeOH. Analysis of the NR content in the nanofibers (from loading and release studies) was determined by measuring the fluorescence of NR in MeOH or H_2O after either dialysis or the PNSL process, and analyzed with the calibration curves (Figure S2. 28) prepared prior to the measurements, where applicable. The loaded nanofibers or non-encapsulated NR, in water, were freeze dried and resuspended in MeOH (1.5 mL) for spectroscopic analysis.

Dynamic Light Scattering (DLS)

Dynamic light scattering (DLS) experiments were carried out using a Zetasizer Pro. Samples of different polymer concentrations were prepared in filtered solvents by passing through a 0.45 μm membrane filter into an optical quartz glass cuvette (PCS8501 type, 10.0 mm light path). The correlation function was acquired in real time and analyzed with a function capable of modelling multiple exponentials (Cumulant analysis). This process enabled the diffusion coefficients for the component particles to be extracted, and these were subsequently expressed as the intensity weighted mean hydrodynamic size ($R_{h,z}$) using the Stokes-Einstein relationship for coated spheres in H_2O, THF, and DMSO with core properties of polystyrene latex (RI = 1.590, Absorption = 0.010).

2.6.2 Synthetic Procedures

2.6.2.1 Synthesis of PFTMC$_{18}$-CTA

Scheme S2. 1. Synthesis of PFTMC$_{18}$-CTA by ring-opening polymerization of FTMC

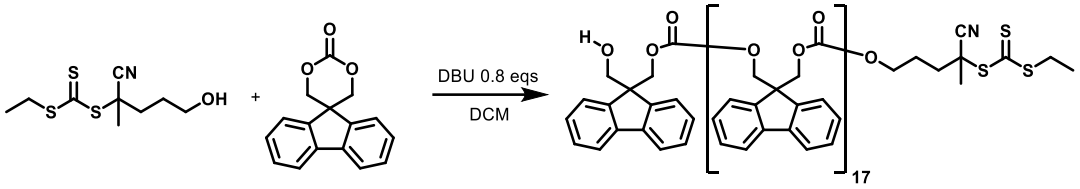

To a solution of 2-cyano-5-hydroxypentan-2-yl ethyl carbonotrithioate[42] in anhydrous CH_2Cl_2 (500 µL, 100 mg/mL, 0.2 mmol, 1.0 eq), DBU (24 µL, 24.4 mg, 0.16 mmol, 0.8 eq) was added in an oven-dried round bottom flask equipped with a magnetic stirring bar. To the stirring solution, FTMC (1.01 g, 4.0 mmol, 20 eq) in anhydrous CH_2Cl_2 (6 mL) was added, and the reaction mixture was stirred at room temperature for 1 h, before the reaction mixture was quenched by the addition of benzoic acid (100 mg). The crude product was purified by precipitation into ice-cold diethyl ether three times, followed by precipitation into ice-cold MeOH three times, and drying *in vacuo* to yield PFTMC$_{18}$-CTA as a yellow solid (1.0 g, 95%).

MALDI-TOF MS $[M]^+$ found: 4729.3, DP_n: 18.

GPC: M_n = 4,800, $Đ_M$ = 1.17.

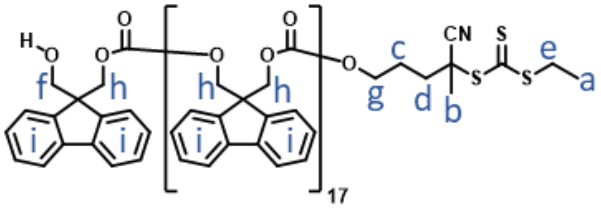

^{1}H NMR (500 MHz, CD_2Cl_2) δ 7.78 – 7.69 (36H, m, Hi), 7.61 – 7.47 (36H, m, Hi), 7.44 – 7.34 (36H, m, Hi), 7.32 – 7.19 (36H, m, Hi), 4.50 – 4.27 (70H, m, Hh), 4.07 (2H, t, *J* = 5.2 Hz, Hg), 3.70 (2H, d, *J* = 6.4 Hz, Hf), 3.31 (2H, dd, *J* = 7.4 Hz, He), 2.22 – 2.13

(1H, m, Hd), 2.06 – 1.98 (1H, m, Hd), 1.87 (2H, h, Hc), 1.80 (3H, s, Hb), 1.31 (3H, t, J = 7.4 Hz, Ha). The ^{1}H ratio of g/f indicates the CTA capping effiency. ^{1}H integration is based on 'f' (HOCH_2).

2.6.2.2 Synthesis of PFTMC$_{18}$-*b*-PBMA$_{44}$

Scheme S2. 2. Synthesis of PFTMC$_{18}$-*b*-PBMA$_{44}$ by reversible addition-fragmentation chain-transfer (RAFT) polymerization.

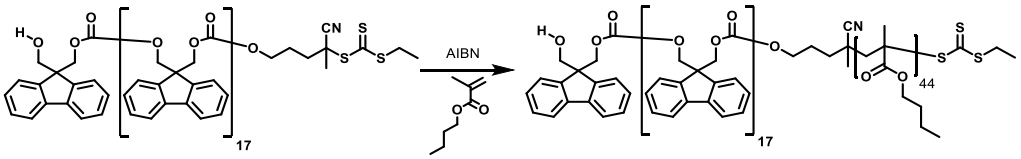

PFTMC$_{18}$-CTA (150 mg, 0.03 mmol, 1 eq), *n*-butyl methacrylate (338 mg, 2.4 mmol, 75 eq), and AIBN (1.6 mg, 0.009 mmol, 0.3 eq) were dissolved in dioxane (9 mL) in a custom-made shlenk-vial. The reaction mixture was homogenized by stirring for 0.5 h at 37 °C followed by four freeze-pump-thaw cycles. The vial with the reaction mixture was placed in a preheated dry heating block and heated to 70 °C for 18 h. The reaction was quenched by submersion in liquid nitrogen. The product was precipitated three times in ice-cold MeOH and dried *in vacuo* to yield PFTMC$_{18}$-*b*-PBMA$_{44}$ as yellow solid (325 mg, 67%). GPC analysis indicated the presence of PFTMC homopolymer as evidenced by the UV/Vis trace. The product was used without further purification in the next reaction.

GPC: M_n = 13,200, $Đ_M$ = 1.12.

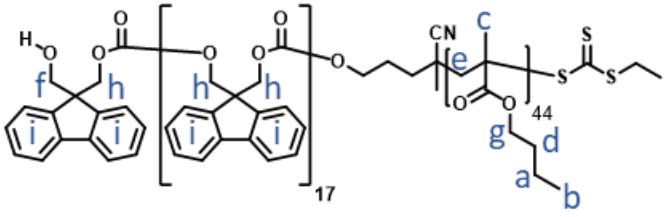

^{1}H NMR (500 MHz, CD_2Cl_2) δ δ 7.81 – 7.67 (36H, m, Hi), 7.58 – 7.45 (36H, m, Hi), 7.45 – 7.33 (36H, m, Hi), 7.31 – 7.15 (36H, m, Hi), 4.48 – 4.26 (70H, m, Hh), 3.98 –

3.89 (89H, b, Hg), 3.69 (2H, t, J = 5.8 Hz, Hf), 2.04 – 1.67 (78H, m, He), 1.67 – 1.55 (89H, m, Hd), 1.40 – 1.32 (97H, m, Ha), 1.07 – 0.73 (256H, m, Hc + Hb). ^{1}H integration is based on 'f' (HOCH_2).

2.6.2.3 Synthesis of PFTMC$_{18}$-*b*-PBMA$_{44}$-*b*-PNIPAM$_{70}$

Scheme S2. 3. Synthesis of PFTMC$_{18}$-*b*-PBMA$_{44}$-*b*-PNIPAM$_{70}$ by RAFT polymerization.

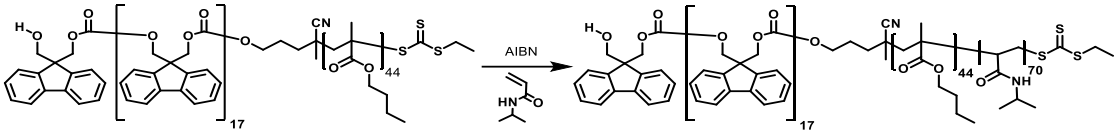

PFTMC$_{18}$-*b*-PBMA$_{44}$ (75 mg, 0.006 mmol, 1 eq), *N*-isopropylacrylamide (287 mg, 2.5 mmol, 400 eq), and AIBN (0.3 mg, 0.001 mmol, 0.3 eq) were dissolved in dioxane (9 mL) in a custom-made shlek-vial. The reaction mixture was stirred for 0.5 h at 37 °C followed by four freeze-pump-thaw cycles. The vial with the reaction mixture was placed in a preheated dry heating block and heated to 70 °C for 18 h. The reaction was quenched by submersion in liquid nitrogen. The product was precipitated three times in ice-cold diethyl ether and three times in ice-cold MeOH. The product was dried *in vacuo* to yield PFTMC$_{18}$-*b*-PBMA$_{44}$-*b*-PNIPAM$_{70}$ as a white-yellow solid (257 mg, 71%, before flash chromatography). The color of this material arises from the sulfur-containing CTA. GPC analysis indicated the presence of water initiated PFTMC homopolymer (as evidenced by a lower M_w shoulder with increased absorbance at 268 nm via UV/Vis).

The PFTMC homopolymer was removed from the triBCP (141 mg of triBCP) via flash chromatography (hexane/ethyl acetate, 40:60 to ethyl acetate / TEA 99:1 to remove homopolymer, then CH_2Cl_2:MeOH:H_2O, 65:35:2 to elute the triblock copolymer). The residual silica-gel was removed via dissolution in THF (50 mL), followed by centrifugation (4500 rpm, 10 mins) and decantation five times. The resulting polymer was dried and

precipitated in ice-cold diethyl ether to yield PFTMC$_{18}$-*b*-PBMA$_{44}$-*b*-PNIPAM$_{70}$ as a white-yellow solid (116 mg, 82%). GPC and TLC analysis confirmed the removal of the homopolymer.

TLC: (hexane/ethyl acetate 1:1): PFTMC Homopolymer R_f ~ 0.9, PFTMC$_{18}$-*b*-PBMA$_{44}$-*b*-PNIPAM$_{70}$ R_f ~ 0.0.

TLC: (CH_2Cl_2:MeOH:H_2O, 64:34:2): PFTMC$_{18}$-*b*-PBMA$_{44}$-*b*-PNIPAM$_{70}$ R_f ~ >0.9.

GPC: M_n = 21,200, $Đ_M$ = 1.32.

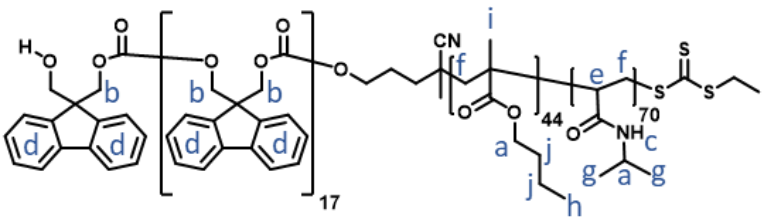

^{1}H NMR (500 MHz, DMSO-d_6) δ 8.00 – 6.65 (308H, m, Hd + Hc), 4.50 – 4.19 (70H, m, Hb), 4.95 – 3.76 (165H, m, Ha), 2.20 – 0.90 (1669H, m, Hf + He + Hj + Hg + Hh + Hi). ^{1}H integration is based on 'b' (OCH_2C) from the PFTMC, matching the value from the homopolymer.

2.6.2.4 Synthesis of PBMA$_{130}$ homopolymer

Scheme S2. 4. Synthesis of PBMA$_{130}$ by RAFT polymerization.

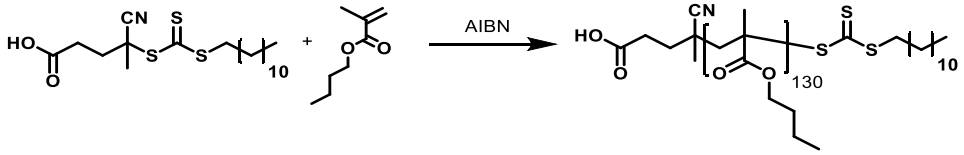

To a solution of 4-cyano-4-[(dodecylsulfanylthiocarbonyl)sulfanyl]pentanoic acid (20 mg, 0.05 mmol, 1 eq), *n*-butyl methacrylate (529 mg, 3.76 mmol, 75 eq), and AIBN (2.4 mg, 0.015 mmol, 0.3 eq) were dissolved in dioxane (4 mL) in a custom-made shlenk-vial, equipped with a stir bar, followed by four freeze-pump-thaw cycles. The vial with the reaction mixture was placed in a preheated dry heating block and heated to 70 °C for 18 h.

The reaction was quenched by submersion in liquid nitrogen. The product was precipitated three times in ice-cold MeOH and dried *in vacuo* to yield $PBMA_{130}$ as yellow gummy solid (332 mg, 63%).

GPC: M_n = 10,300 $Đ_M$ = 1.03.

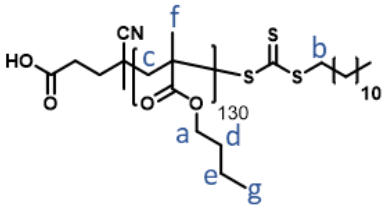

^{1}H NMR (500 MHz, CD_2Cl_2) δ 4.27 – 3.55 (257H, m, Ha), 3.24 (2H, dd, *J* = 7.6 Hz, Hb), 2.13 – 1.69 (239H, m, Hc), 1.68 – 1.52 (286H, m, Hd), 1.51 – 1.32 (286H, m, He), 1.14 – 0.64 (752H, m, Hf + Hg).). ^{1}H integration is based on 'b' (SCH_2CH_2) from the CTA.

2.6.2.5 Synthesis of $PNIPAM_{178}$ homopolymer

Scheme S2. 5. Synthesis of $PNIPAM_{178}$ by RAFT polymerization.

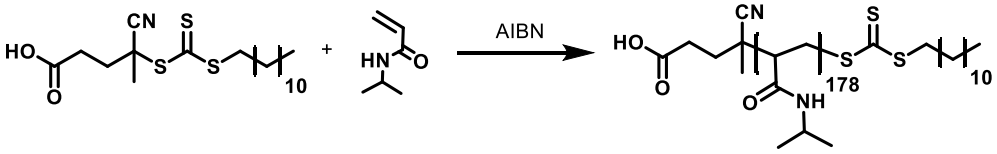

To a solution of 4-cyano-4-[(dodecylsulfanylthiocarbonyl)sulfanyl]pentanoic acid (20 mg, 0.05 mmol, 1 eq), n-isopropylacrylamide (561 mg, 4.95 mmol, 100 eq), and AIBN (2.4 mg, 0.015 mmol, 0.3 eq) were dissolved in dioxane (5 mL) in a custom-made shlenk-vial, equipped with a stir bar, followed by four freeze-pump-thaw cycles. The vial with the reaction mixture was placed in a preheated dry heating block and heated to 70 °C for 18 h. The reaction was quenched by submersion in liquid nitrogen. The product was precipitated

three times in ice-cold diethyl ether and dried in vacuo to yield $PNIPAM_{178}$ as white-yellow solid (497 mg, 94%).

GPC: M_n = 13,300 $Đ_M$ = 1.13 (for main peak, see Table S2. 1).

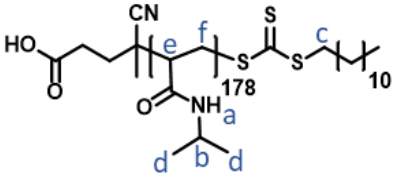

^{1}H NMR (500 MHz, CD_2Cl_2) δ 6.62 (166H, brs, Ha), 4.01 (178H, brs, Hb), 3.39 (2H, brs, Hc), 3.02 – 0.81 (913H, m, Hf + He + Hd + H_2O). ^{1}H integration is based on 'c' (SCH_2CH_2) from the CTA.

2.6.2.6 Synthesis of $PFTMC_{18}$-*b*-$PNIPAM_{425}$

Scheme S2. 6. Synthesis of $PFTMC_{18}$-*b*-$PNIPAM_{425}$ by RAFT polymerization.

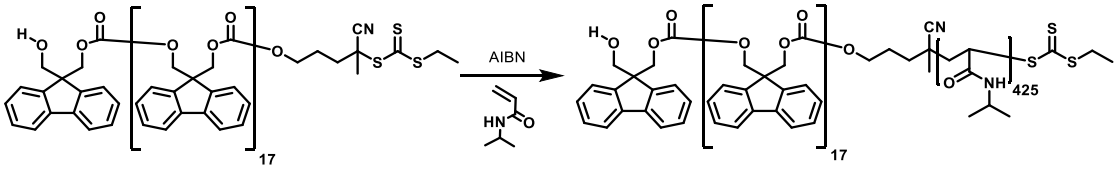

$PFTMC_{18}$-CTA (50 mg, 0.004 mmol, 1 eq), *N*-isopropylacrylamide (192 mg, 1.7 mmol, 400 eq), and AIBN (0.2 mg, 0.001 mmol, 0.3 eq) were dissolved in dioxane (4 mL) in a custom-made shlek-vial followed by four freeze-pump-thaw cycles. The vial with the reaction mixture was placed in a preheated dry heating block and heated to 70 °C for 18 h. The reaction was quenched by submersion in liquid nitrogen. The product was precipitated three times in ice-cold diethyl ether. The product was dried *in vacuo* to yield PFTMC-*b*-PNIPAM as a white-yellow solid. GPC analysis indicated the presence of PFTMC homopolymer (as evidenced by a lower M_w shoulder with increased absorbance at 268 nm via UV/Vis). The PFTMC homopolymer was removed via flash chromatography (hexane/ethyl acetate, 40:60 to ethyl acetate, then CH_2Cl_2:MeOH:H_2O, 65:35:2 to elute the

diblock copolymer). The residual silica-gel was removed via dissolution in THF (50 mL), followed by centrifugation (4500 rpm, 10 mins) and decantation five times. The resulting polymer was dried and precipitated in ice-cold diethyl ether to yield PFTMC$_{18}$-*b*-PNIPAM$_{425}$ as a white-yellow solid (175 mg, 91%).

GPC: M_n = 31,800, $Đ_M$ = 1.76. This value is likely overestimated due to GPC column absorption effects (see main text).

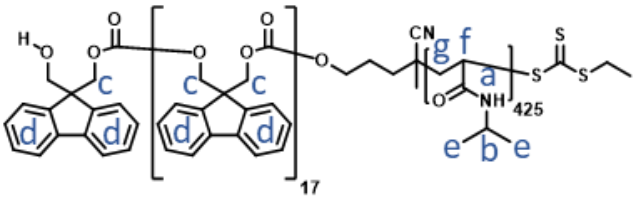

^{1}H NMR (500 MHz, DMSO-d_6) δ 7.99 – 6.72 (556H, m, Ha + Hd), 4.44 – 4.17 (70H, m, Hc), 4.06 – 3.58 (425H, m, Hb), 2.43 – 0.67 (m, 3735H). ^{1}H integration is based on 'c' (OC*H*$_2$C) from the PFTMC, matching the value on the homopolymer.

2.6.2.7 Synthesis of PFTMC$_{18}$-*b*-PEG$_{530}$

Scheme S2. 7. Synthesis of PFTMC$_{18}$-*b*-PEG$_{530}$ by organocatalytic ring-opening polymerization.

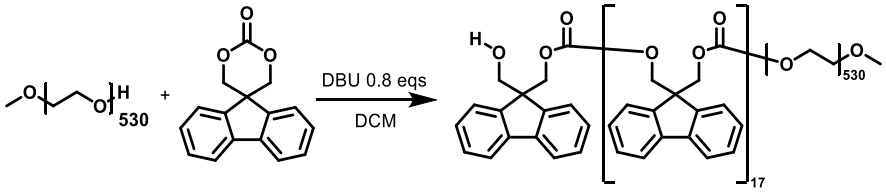

PEG$_{530}$ (500 mg, 0.02 mmol, 1 eq) and DBU (2.9 µL, 2.9 mg, 0.02 mmol, 0.8 eq) were dissolved in the minimum volume of anhydrous CH_2Cl_2 in a round bottom flask equipped with a magnetic stirring bar. To the stirring solution, FTMC (122 mg, 0.49 mmol, 20 eq) in anhydrous CH_2Cl_2 (1 mL) was added, and the reaction mixture was stirred at room temperature for 3 h, before the reaction mixture was quenched by the addition of benzoic acid (10 mg). The crude product was purified by precipitation into ice-cold diethyl

ether three times and dried *in vacuo* (515 mg, 83%). 300 mg of the collected white solid was then dissolved in 20 mL of THF in a 50 mL centrifuge with a stir bar. 10 mL of hexane was added to the stirring solution and centrifuged. To the supernatant an extra 6 mL of hexanes was added, stirred and centrifuged. The resulting solid was dried *in vacuo* to yield $PFTMC_{18}$-PEG_{530} as a white solid (210 mg, 70%).

GPC: M_n = 26,600, $Đ_M$ = 1.14.

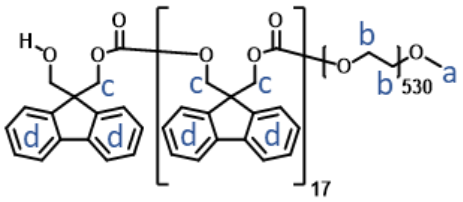

^{1}H NMR (500 MHz, CD_2Cl_2) δ 7.84 – 7.68 (37H, m, Hd), 7.63 – 7.47 (37H, m, Hd), 7.46 – 7.32 (38H, m, Hd), 7.32 – 7.20 (37H, m, Hd), 4.47 – 4.17 (73H, m, Hc), 3.77 – 3.42 (2120H, m, Hb), 3.34 (3H, s, Ha). ^{1}H integration is based on 'a' (CH_2OCH_3) from the terminal methyl group of the PEG.

2.6.3 Self-Assembly Procedures

Composition of all solvents given in *v:v*

Self-nucleation of PFTMC$_{18}$-*b*-PBMA$_{44}$-*b*-PNIPAM$_{70}$. PFTMC$_{18}$-*b*-PBMA$_{44}$-*b*-PNIPAM$_{70}$ (675 µL, 10 mg/mL solution in THF) was added to MeOH (3.825 mL) in a vial. The resulting solution (1.5 mg/mL in 15:85 THF:MeOH) was manually shaken for ~15 s and annealed for 3 h at 70 °C. The solution was cooled to 20 °C over 3 h, and aged for 48 h. The resulting solution contained morphologically pure nanofibers with disperse lengths and uniform widths, as analysed via TEM.

Preparation of PFTMC$_{18}$-*b*-PBMA$_{44}$-*b*-PNIPAM$_{70}$ seed nanofibers. PFTMC$_{18}$-*b*-PBMA$_{44}$-*b*-PNIPAM$_{70}$ disperse nanofibers (4 mL, 1.5 mg/mL) were fragmented by ultrasonication for 3 h at 10 °C. The resulting nanofibers were analysed by TEM (L_n = 22 nm, $Đ$ = 1.11, σ = 7.8 nm).

Preparation PFTMC$_{18}$-*b*-PBMA$_{44}$-*b*-PNIPAM$_{70}$ nanofibers of controlled length and low dispersity by seeded growth (living CDSA). For seeded growth assemblies with $m_{unimer}/m_{seed} \leq 10$: aliquots of PFTMC$_{18}$-*b*-PBMA$_{44}$-*b*-PNIPAM$_{70}$ unimer (10 mg/mL in THF), equivalent to corresponding m_{unimer}/m_{seed}, were added to diluted seed nanofiber solutions in MeOH (200 µL). The self-assembly solutions (0.1 mg/mL, THF/MeOH 15:85) were manually shaken for ~15 s and aged for 48 h at 20 ºC.

For seeded growth assemblies with m_{unimer}/m_{seed} 20, 30, and 50: aliquots of PFTMC$_{18}$-*b*-PBMA$_{44}$-*b*-PNIPAM$_{70}$ unimer (10 mg/mL in THF), equivalent to corresponding m_{unimer}/m_{seed}, were added to diluted seed nanofiber solution in MeOH (100 µL). The unimer was added in intervals of 10 m_{unimer}/m_{seed} every 24 h. The self-assembly solutions (0.1 mg/mL, THF/MeOH 10:90) were manually shaken for ~15 s and aged 48 h at 20 ºC. TEM analysis was conducted after 48 h and also after 4 months. The length of the

nanofibers remained constant, indicating that there was no unimer present in solution that could undergo epitaxial growth after 48 h.

Preparation of 412 nm long PFTMC$_{18}$-*b*-PBMA$_{44}$-*b*-PNIPAM$_{70}$ nanofibers of controlled length and low dispersity by seeded growth (living CDSA). To a diluted seed solution (2 mL, 0.072 mg/mL, in MeOH), PFTMC$_{18}$-*b*-PBMA$_{44}$-*b*-PNIPAM$_{70}$ unimer (10 mg/mL in THF, final m_{unimer}/m_{seed} equivalent to 23.5) was added in two portions (2 × 169 µL), 24 h apart. The self-assembly solution (2.3 mL, 1.5 mg/mL, THF/MeOH 15:85) was manually shaken for ~15 s after each addition, and then aged for 48 h at 20 ºC.

Preparation of PFTMC$_{18}$-*b*-PBMA$_{44}$-*b*-PNIPAM$_{70}$ or PFTMC$_{18}$-*b*-PEG$_{530}$ nanofibers of controlled length and low dispersity by seeded growth (living CDSA). To diluted seed solutions of either PFTMC$_{18}$-*b*-PBMA$_{44}$-*b*-PNIPAM$_{70}$ or PFTMC$_{18}$-*b*-PEG$_{530}$, respective unimeric solution in THF (10 mg/mL), was added in one portion to yield nanofibers of different, but controlled lengths (by tuning the final m_{unimer}/m_{seed} added). The resulting self-assembly solutions were manually shaken for ~15 s and aged for 48 h at 20 ºC.

Preparation of segmented A-B-A nanofibers of controlled length by seeded growth (living CDSA).

A solution of 412 nm nanofibers prepared via seeded growth (Table S2. 3) was diluted in MeOH (0.5 ml, 0.1 mg/mL). Either unimeric PFTMC$_{18}$-*b*-PNIPAM$_{425}$ or PFTMC$_{18}$-*b*-PEG$_{530}$ (5 or 2.5 µL, 10 mg/mL in THF) was added in one portion to the vial containing the 412 nm nanofibers and solution was manually shaken for ~15 s and aged for 48 h at 20 ºC.

2.6.4 Nile Red (NR) Loading Procedures.

Method 1: Self-Assembly in the presence of NR

Preparation of disperse nanofibers via CDSA loaded with NR. In a vial, MeOH (435 µL), THF (60 µL), PFTMC$_{18}$-*b*-PBMA$_{44}$-*b*-PNIPAM$_{70}$ unimer (30 µL, 10 mg/mL in THF), and NR solution (75 µL, 1 mg/mL in MeOH) were added. The self-assembly solution (0.5 mg/mL nanofiber, 0.125 mg/mL NR) was manually shaken for ~15 s and annealed for 3 h at 70 °C. The solution was cooled to 20 °C over 3 h and aged for 48 h. The resulting solution was analysed by TEM, and then dialysed into water. Dialysis was performed by placing aliquots (150 µL minimum) inside a dialysis bag (Sigma Aldrich, MWCO = 12,000 – 14,000 Da) that was clip-sealed. The dialysis bag containing the solution was placed inside a beaker filled with deionized water (500 mL) and the media was changed four times over 18 - 24 h. The sample was retrieved and stored in the dark.

Method 2: Post-assembly loading of preformed, low dispersity nanofibers via dialysis

Preparation of 412 nm preformed nanofibers loaded with NR. A solution of 412 nm nanofibers ($Đ$ = 1.04, σ = 78, 33.3 µL, 1.5 mg/mL) in THF:MeOH (15:85) was diluted in THF:MeOH (15:85, 454.2 µL) and a solution of NR in MeOH (12.5 µL, 1 mg/mL) was added. The resulting solution was homogenized by shaking for 10 s, and then dialysed into water. Dialysis was performed by placing aliquots (150 µL, minimum) inside a dialysis bag (Sigma Aldrich, MWCO = 12,000 – 14,000 Da) that was clip-sealed. The dialysis bag containing the solution was placed inside a beaker filled with deionized water (500 mL) and the media was changed four times over 18 - 24 h. The sample was retrieved and stored in the dark.

Method 3: Post-assembly loading of low dispersity nanofibers via PNSL

Preparation of low dispersity nanofibers loaded with NR. Vials containing either triBCP or diBCP nanofiber solutions of a given length (i.e. 412, 125, 108, 84, 25 nm nanofibers) were prepared by adding THF, MeOH and NR to obtain final solutions containing nanofibers (0.1 mg/mL) and NR (25, 10, 1, 0.1, or 0.01 *w*/*w*) in MeOH:THF (15:85, 1-2 mL). The resulting solutions were placed in an orbital shaker (300 rpm), and H_2O (same volume as prepared nanofiber solution e.g. 1.5 mL) was infused into the vials via syringe pump at a rate of 100 µL/min. The vials were left uncapped but protected from light in the orbital shaker for 12 h, before residual organic solvent was evaporated by introduction of a gentle flow of air into the vials (30 min). Finally, the solutions were passed through a Nylon syringe-filter (0.45 µm pore size) and made up to a final volume in H_2O equal to the originally prepared nanofiber solution (e.g. 1.5 mL, as measured by weight, using the densitiy of water).

Control experiments with NR. Control experiments to investigate NR removal via dialysis or via filtration were carried out with the same procedures and concentrations as for the loading of nanofibers, but without the nanofibers, unless otherwise noted.

2.6.5 NR release from Coaxial-Core Nanofibers

Solvent-switch release of NR from disperse nanofibers. An aliquot of disperse nanofibers (200 µL) loaded with NR in water (0.5 mg/mL nanofiber, 0.125 mg/mL NR) using 'Method 3' was placed inside a dialysis bag (Sigma Aldrich, MWCO = 12,000 – 14,000 Da). The dialysis bag containing the solution was placed inside a beaker filled with MeOH (500 mL) and the media was changed four times over 18 - 24 h. The sample was retrieved and stored in the dark.

Solvent-switch release of NR from low dispersity nanofibers. An aliquot of 412 nm nanofibers (200 µL) loaded with NR in water (0.1 mg/mL nanofiber, 1 wt % NR) using 'Method 3' was placed inside a dialysis bag (Sigma Aldrich, MWCO = 12,000 – 14,000 Da). The dialysis bag containing the solution was placed inside a beaker filled with MeOH (500 mL) and the media was changed four times over 18 - 24 h. The sample was retrieved and stored in the dark.

2.6.6 Volume calculations of the PFTMC 'inner core' and PBMA 'outer core.'

To estimate the approximate percentage of the cross-sectional volume occupied by the crystalline $PFTMC_{18}$ inner-core and therefore unavailiable for encapsulation, we computationally estimated the length of the $PBMA_{44}$ block, and then compared the volume occupied by $PFTMC_{18}$-*b*-$PBMA_{44}$ to the volume occupied by $PFTMC_{18}$ using the volume of the crystalline PFTMC 'inner core'.The volume of the $PBMA_{44}$ 'outer core' was estimated using an energy minimization of $PFTMC_9$-*b*-$PBMA_{22}$-*b*-$PNIPAM_{35}$ (DP of each block divided by two for computational efficiency), using the energy minimization function in Chem3D (PerkinElmer Informatics) with the MM2 force field, set to a minimum RMS gradient of 0.01. The length of $PBMA_{44}$ (10.1 nm) was obtained by measuring the end-to-end distance of the $PBMA_{22}$ block (5.04 nm) in USCF Chimera (University of California, San Francisco),[95] and multiplying it by two.

The volume of the $PFTMC_{18}$ (105 nm^3) was calculated with the following formula:

$$V_{PFTMC} = width \times height \times depth \quad \text{(Eq. S2. 3)}$$

V is the volume, the width is 12.3 nm (obtained via TEM, Figure S2. 12) and the height is 8.5 nm (obtained via AFM, Figure 2. 3). The depth for both PFTMC and PBMA was considered to be 1 nm.

The volume of the $PFTMC_{18}$-*b*-$PBMA_{44}$ (733 nm^3) segment was calculated with the following formula:

$$V_{PFTMC-b-PBMA} = \pi \times a \times b \times depth \quad \text{(Eq. S2. 4)}$$

Where *V* is the volume of a cylindrical ellipse, *a* is the distance from the center to the '*a*' vertex, and *b* is the distance from the center to the '*b*' co-vertex, and depth was considered to be 1 nm. According to the energy minimization simulation (Figure S2. 33), the PBMA chain has a length of ca. 10.1 nm. Thus a nanofiber with an ellipsoidal amorphous outer core and a rectangular core-cross-section will have geometric values of *a* = 14.35 nm (0.5 x height of $PFTMC_{18}$ + length of $PBMA_{44}$), and *b* = 16.25 nm (0.5 x width of $PFTMC_{18}$ + length of $PBMA_{44}$).

The % volume occupied by the crystalline $PFTMC_{18}$ inner-core and therefore unavailiable for encapsulation is given by:

$$\frac{V_{PFTMC}}{V_{PFTMC-b-PBMA}} \times 100\% \quad \text{(Eq. S2. 5)}$$

$$i.e. \frac{105\ nm^3}{733\ nm^3} \times 100\% = 14\%$$

In principle, the AFM data obtained on the nanofibers used in this study should allow a calculation of the % PFTMC core volume in the coaxial core. However, AFM analysis likely underestimates the PBMA dimensions as the PBMA outer core that lies above and below the PFTMC inner core may collapse upon drying. Another consideration is the T_g of PBMA near room-temperature (20 – 25 °C)[96] might affect the width and height data obtained by the tip-based AFM method when compared to a crystalline material such as PFTMC.[96] As discussed above, our approach therefore uses TEM and AFM data to estimate the width and height dimensions of the crystalline PFTMC core and the volume of the PBMA outer core was estimated using a computational approach.

2.6.7 Supplementary Discussion

Self-Assembly

The linear regression of the m_{unimer}/m_{seed} ratio plot (Figure 2. 2J) allows for alternate measurements of seed length, namely the gradient of the line (L_n = 16 nm) and the Y-intercept (L_n = 28 nm). For an idealized system, the Y intercept, gradient of the line, and the length of the seeds measured via TEM should all be equal. For this system, the Y-intercept (28 nm ± 5 nm) and gradient (16 nm ± 0.2 nm) are within error of the measured length via TEM (22nm ± 8 nm), hence any discrepancy is not statistically significant.

AFM Considerations

In principle, the AFM data obtained on the nanofibers used in this study should allow a calculation of the % core volume. However, AFM analysis likely underestimates the PBMA dimensions as the PBMA outer core that lies above and below the PFTMC inner core likely collapses upon drying. Another consideration is the T_g of PBMA near room-temperature (20 – 25 °C)[96] might affect the width and height data when compared to a crystalline material such as PFTMC.[96] Our approach used TEM and AFM data to estimate the dimensions of the crystalline PFTMC core and the volume of the PBMA outer core was estimated via energy minimization simulation (see section 2.6.6 , and Figure S2. 33).

Segmented and Multifunctional A-B-A Nanofibers

To investigate the potential utility of triBCP coaxial nanofibers in drug delivery, and to highlight the easy modularity of segmented nanofibers made by Living CDSA, we prepared multifunctional A-B-A nanofibers with terminal $PFTMC_{18}$-*b*-PEG_{530} (A) segments. $PFTMC_{18}$-*b*-PEG_{530} (DP calculated by ^{1}H NMR; M_n = 26,600, $Đ_M$ =1.14 by GPC, Figure S2. 15, 16) was synthesized following a previously reported procedure.[55] The A segments should improve the solubility and stealth properties of the resulting segmented

nanofibers, as PEG is known for minimizing protein binding and increasing the circulation times.[97] Thus, segmented PFTMC$_{18}$-*b*-PEG$_{530}$-***m***-PFTMC$_{18}$-*b*-PBMA$_{44}$-*b*-PNIPAM$_{70}$-***m***-PFTMC$_{18}$-*b*-PEG$_{530}$ nanofibers were prepared from a solution of 412 nm ($Đ$ = 1.04, σ = 78 nm) PFTMC$_{18}$-*b*-PBMA$_{44}$-*b*-PNIPAM$_{70}$ seed nanofibers (in MeOH:THF 85:15), by addition of PFTMC$_{18}$-*b*-PEG$_{530}$ (0.5 equivalents, in THF) followed by aging the solution for 48 h before characterization. TEM analysis revealed the formation of 584 nm nanofibers ($Đ$ = 1.14, σ = 216 nm, n = 101), with clearly distinguishable segments (Figure S2. 18). Differences in penetration of the uranyl acetate staining solution within the coronal-block of each segment allowed us to identify the flanking 'B' PFTMC$_{18}$-*b*-PEG$_{530}$ segment, as well as the central cargo-carrying PFTMC$_{18}$-*b*-PBMA$_{44}$-*b*-PNIPAM$_{70}$ 'A' segment. The simple and versatile construction of the segmented nanofibers described here pave the way towards the development of modular, customizable, and multi-stage nanofiber drug delivery systems that contain individual segments tailored towards specific functions.

2.6.8 Supplementary Tables

Table S2. 1. Summary of molecular weight data for $PFTMC_{18}$-CTA, $PBMA_{130}$, $PNIPAM_{178}$, $PFTMC_{18}$-*b*-$PBMA_{44}$ and $PFTMC_{18}$-*b*-$PBMA_{44}$-*b*-$PNIPAM_{70}$ polymers.

Polymer	M_n (g/mol) GPC	M_w (g/mol) GPC	$Đ_M$ GPC	DP_n NMR	DP_n MALDI-TOF
$PFTMC_m$	4,800	5,600	1.17	m =18	18
$PBMA_n$	16,000	18,200	1.14	n = 130	-
$PNIPAM_l$	13,300	15,00	1.13[a]	l = 178	-
$PFTMC_{18}$-*b*-$PBMA_o$	13,200	14,700	1.12	o = 44	-
$PFTMC_{18}$-*b*-$PBMA_{44}$-*b*-$PNIPAM_p$	21,200	28,000	1.32[b]	p = 70	-
$PFTMC_{18}$-*b*-$PNIPAM_q$	31,800	55,900	1.76[b]	q = 425	-
$PFTMC_r$-*b*-PEG_s	26,600	30,300	1.14	r = 18 s = 530	-

[a] Column adsorption and possibly aggregation effects were detected during GPC analysis leading to small additional peaks (Figure S2. 7B). The data given is for the main peak.
[b] Column adsorption effects were detected during GPC analysis leading to a broadening of the peak. The dispersity is likely overestimated in these cases.

Table S2. 2. Solubility chart of PBMA, PNIPAM, and PFTMC-containing polymers, and FTMC, BMA, and NIPAM monomers with different solvents at 20 °C (~ 10 mg sample, in 500 µL of solvent).

Solvent	Polymer or monomer							
	$PFTMC_{18}$	$PBMA_{130}$	$PNIPAM_{178}$	$PFTMC_{18}$-*b*-$PBMA_{44}$	$PFTMC_{18}$-*b*-$PBMA_{44}$-*b*-$PNIPAM_{70}$	FTMC	BMA	NIPAM
Diethyl ether	X	S	X	X	X	X	S	S
MeOH	X	SCA*	S	X	SCA	X	S	S
EtOH	X	S	S	X	SCA	X	S	S
iPrOH	X	S	S	X	SCA	X	S	S
H_2O	X	X	S	X	SCA	X	E	S
Acetonitrile	X	S	S	X	SCA	X	X	S
Hexanes	X	S	X	X	X	X	S	X

X = not soluble, SCA = soluble with colloidal aggregates (*< 10-20% THF), S = soluble, and E = emulsion.

Table S2. 3. Statistical analysis of contour length measurements for PFTMC$_{18}$-*b*-PBMA$_{44}$-*b*-PNIPAM$_{70}$ nanofibers prepared via seeded growth at 20 °C, in MeOH:THF solvent mixtures (THF = 10 – 20%), measured via. The number of nanofibers measured is represented by *n*, *σ* represents the standard deviation of the measured length, and L_n/*eq* corresponds to the L_n of the nanofibers per mass equivalent of triBCP in the sample.

	Seeds	m_{unimer}/m_{seed}								
		2.5	3.5	5	10	20	23.5	30	40	50
n	487	204	276	215	217	221	203	275	210	181
L_n (nm)	22	74	84	125	185	362	412	507	721	818
L_w (nm)	25	79	89	132	194	377	427	527	734	863
Đ	1.12	1.06	1.05	1.05	1.05	1.04	1.04	1.04	1.02	1.06
L_n/*eq* (nm)	22	21	19	21	18	18	18	17	18	16
σ (nm)	7.7	19	20	29	42	72	78	101	93	192
σ / L_n	0.35	0.26	0.23	0.23	0.23	0.19	0.19	0.20	0.13	0.23

2.6.9 Supplementary Figures

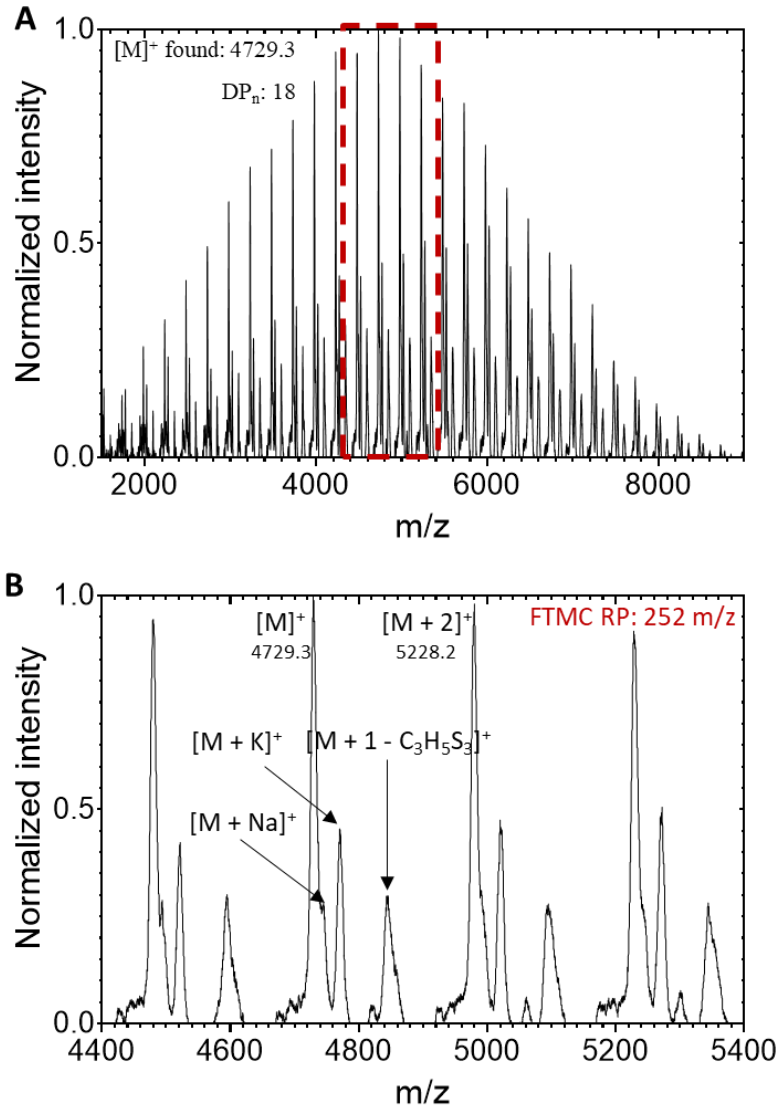

Figure S2. 1. A) MALDI-TOF MS spectra of $PFTMC_{18}$. The red square represents the area expanded in B. RP: repeating unit.

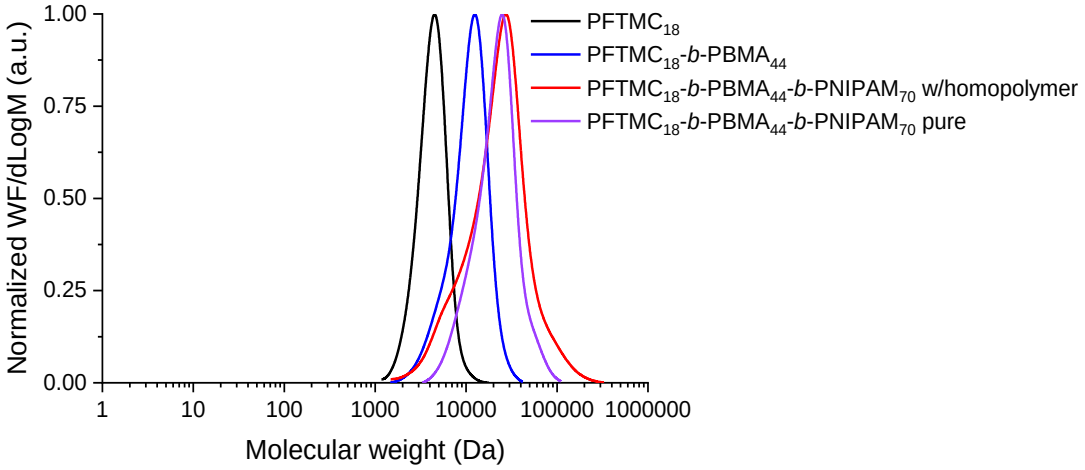

Figure S2. 2. GPC (refractive index) traces eluted in triethylamine/THF (1% *v/v*), 1 mL min^{-1}, 35 °C of PFTMC-CTA homopolymer (black trace), $PFTMC_{18}$-*b*-$PBMA_{44}$ diBCP (blue trace), $PFTMC_{18}$-*b*-$PBMA_{44}$-*b*-$PNIPAM_{70}$ triBCP with homopolymer impurities (red trace), and $PFTMC_{18}$-*b*-$PBMA_{44}$-*b*-$PNIPAM_{70}$ purified by flash column chromatography (purple trace). The y-axis reflects the distribution of weight fractions by molecular weight.

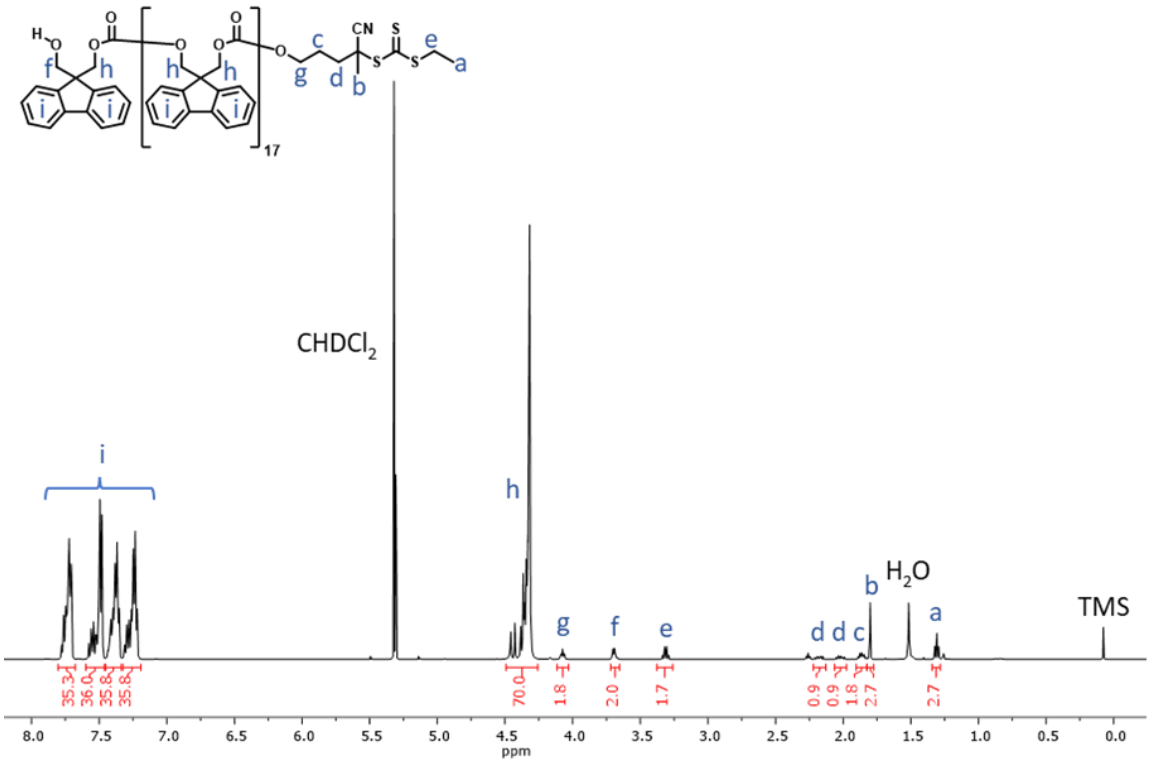

Figure S2. 3. ^{1}H NMR spectra (in CD_2Cl_2) of $PFTMC_{18}$-CTA.

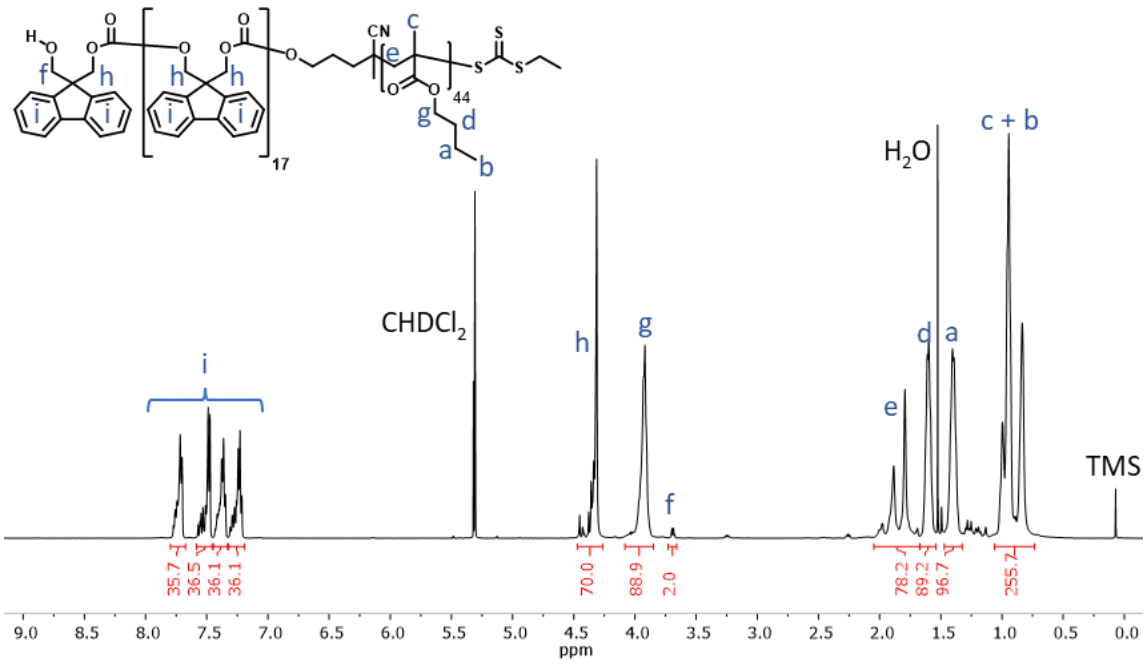

Figure S2. 4. ^{1}H NMR spectra (in CD_2Cl_2) of $PFTMC_{18}$-*b*-$PBMA_{44}$.

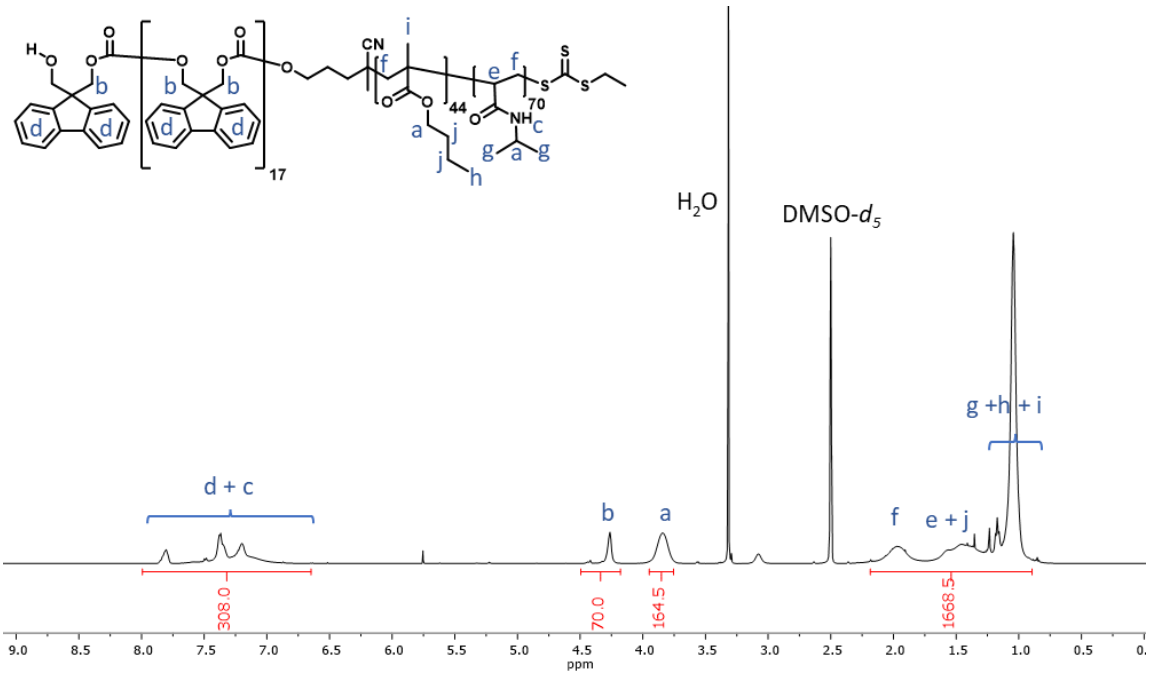

Figure S2. 5. ^{1}H NMR spectra (in DMSO-d_6) of $PFTMC_{18}$-*b*-$PBMA_{44}$-*b*-$PNIPAM_{70}$.

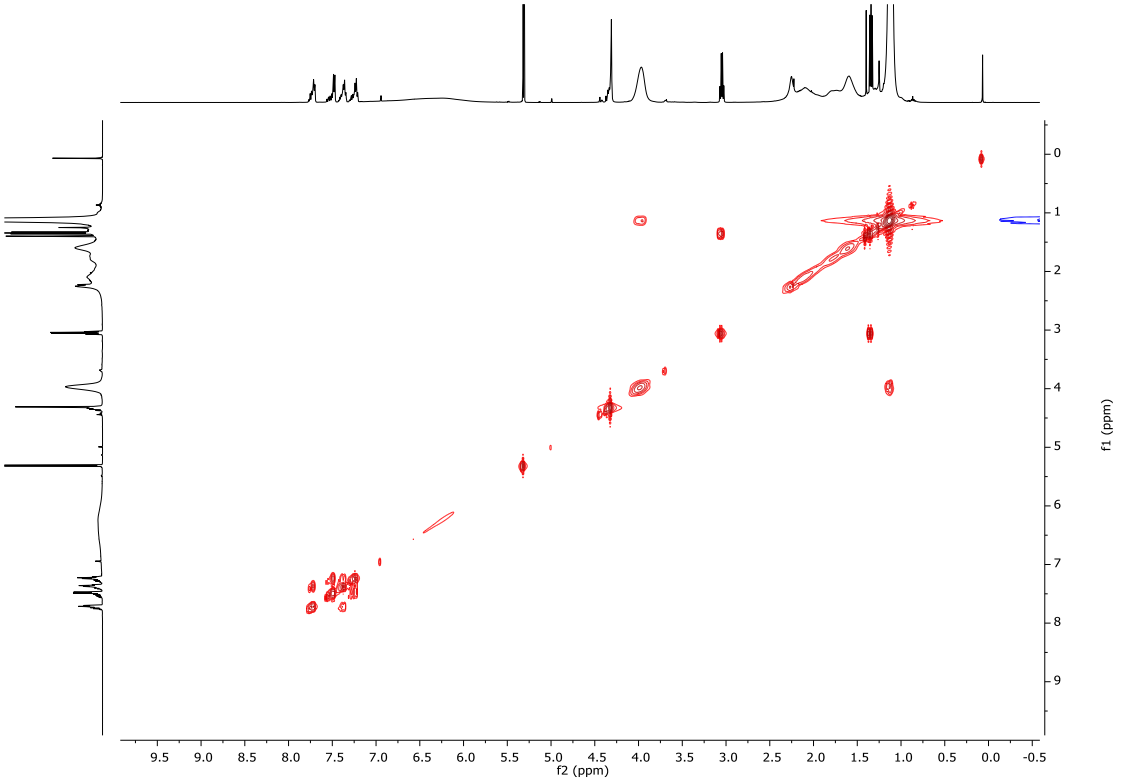

Figure S2. 6. 2D ^{1}H COSY NMR spectra (in CD_2Cl_2) of $PFTMC_{18}$-*b*-$PBMA_{44}$-*b*-$PNIPAM_{70}$. The peak at 1.12 ppm represents the protons labelled as g, h, and i in Figure S2. 5. Additionally, characteristic ether impurity (quartet) is observed at 3.06 ppm, hence, the ether impurity is thought to contribute to the signal at 1.12 ppm.

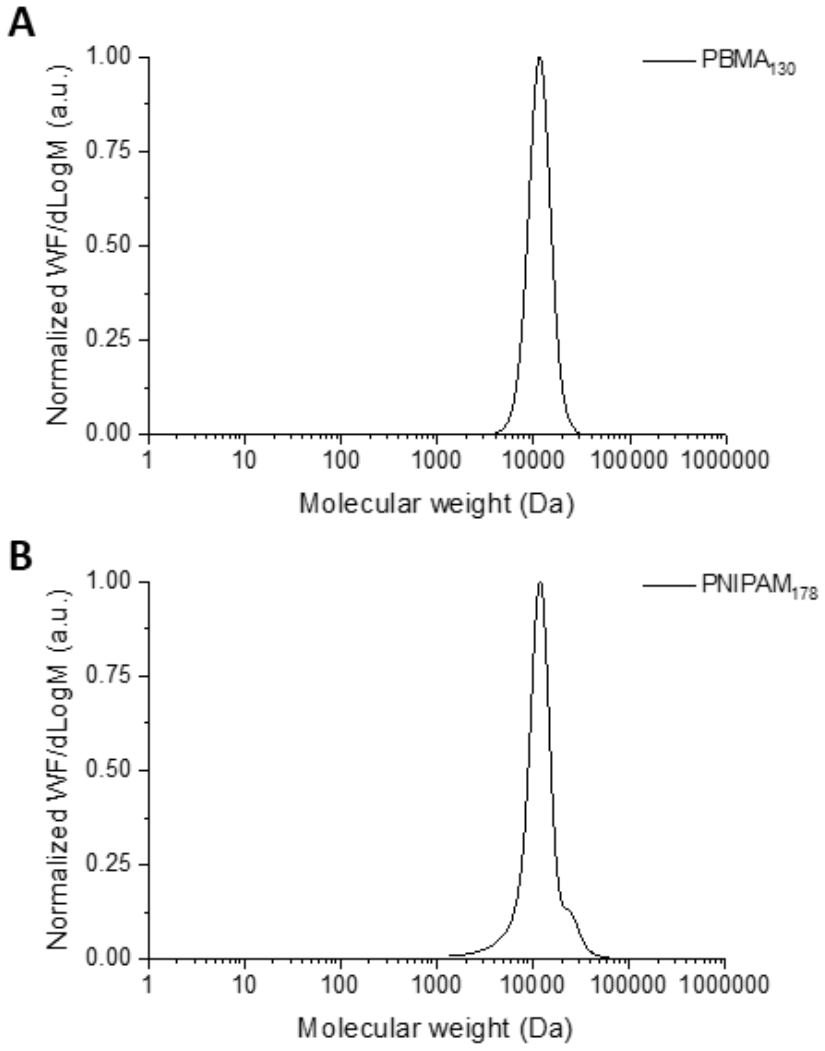

Figure S2. 7. GPC (refractive index) traces eluted in triethylamine/THF (1% *v/v*), 1 mL min^{-1}, 35 °C of A) $PBMA_{130}$ homopolymer, and B) $PNIPAM_{178}$ homopolymer. The y-axis reflects the distribution of weight fractions by molecular weight.

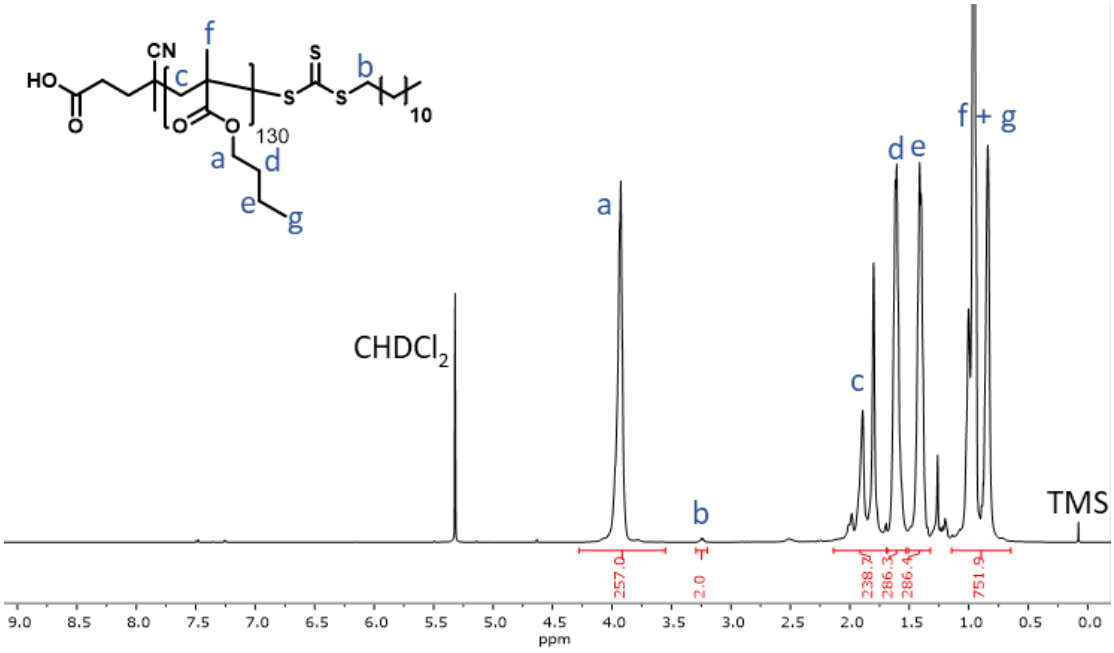

Figure S2. 8. ^{1}H NMR spectra (in CD_2Cl_2) of $PBMA_{130}$.

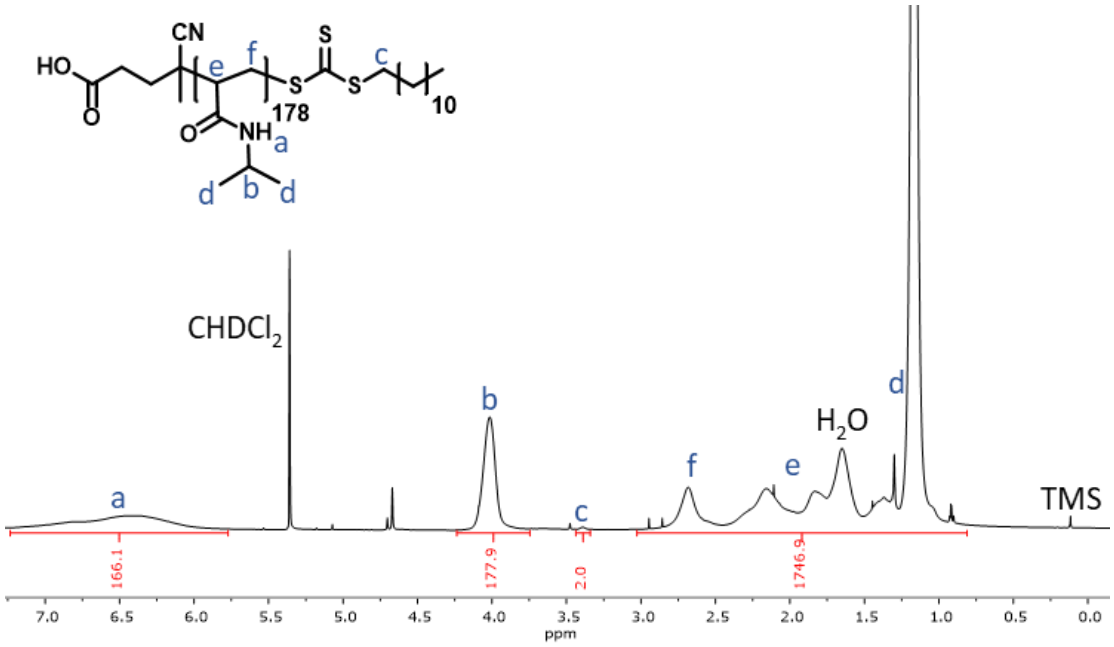

Figure S2. 9. ^{1}H NMR spectra (in CD_2Cl_2) of $PNIPAM_{178}$.

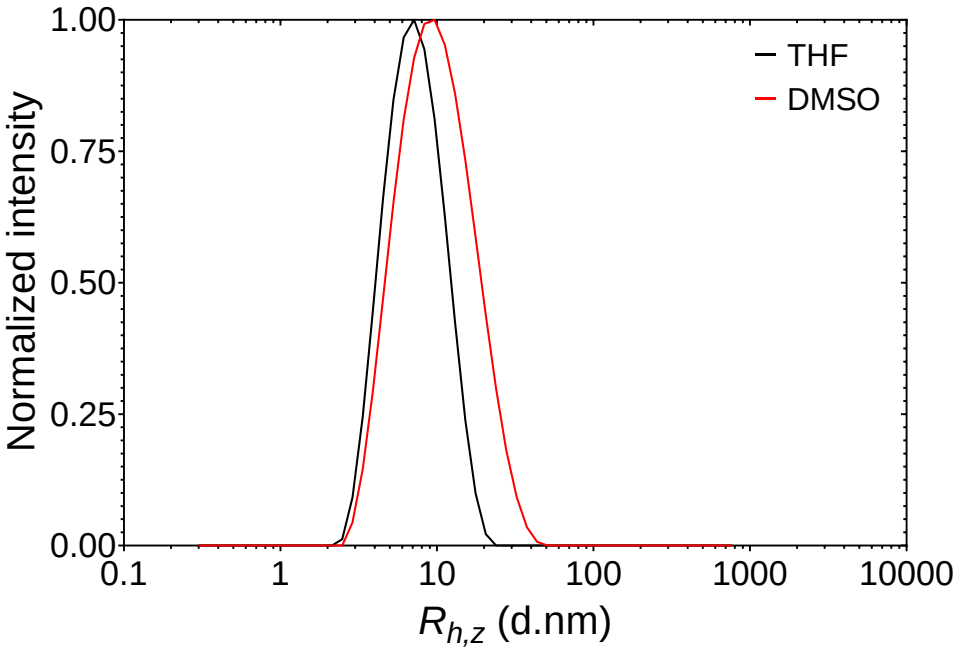

Figure S2. 10. DLS of the PFTMC18-b-PBMA44-b-PNIPAM70 triBCP in tetrahydrofuran (THF, black line, $R_{h,z}$ = 6.96 nm, σ = 1.30 nm), and dimethyl sulfoxide (DMSO, red line, $R_{h,z}$ = 7.04 nm, σ = 1.06 nm).

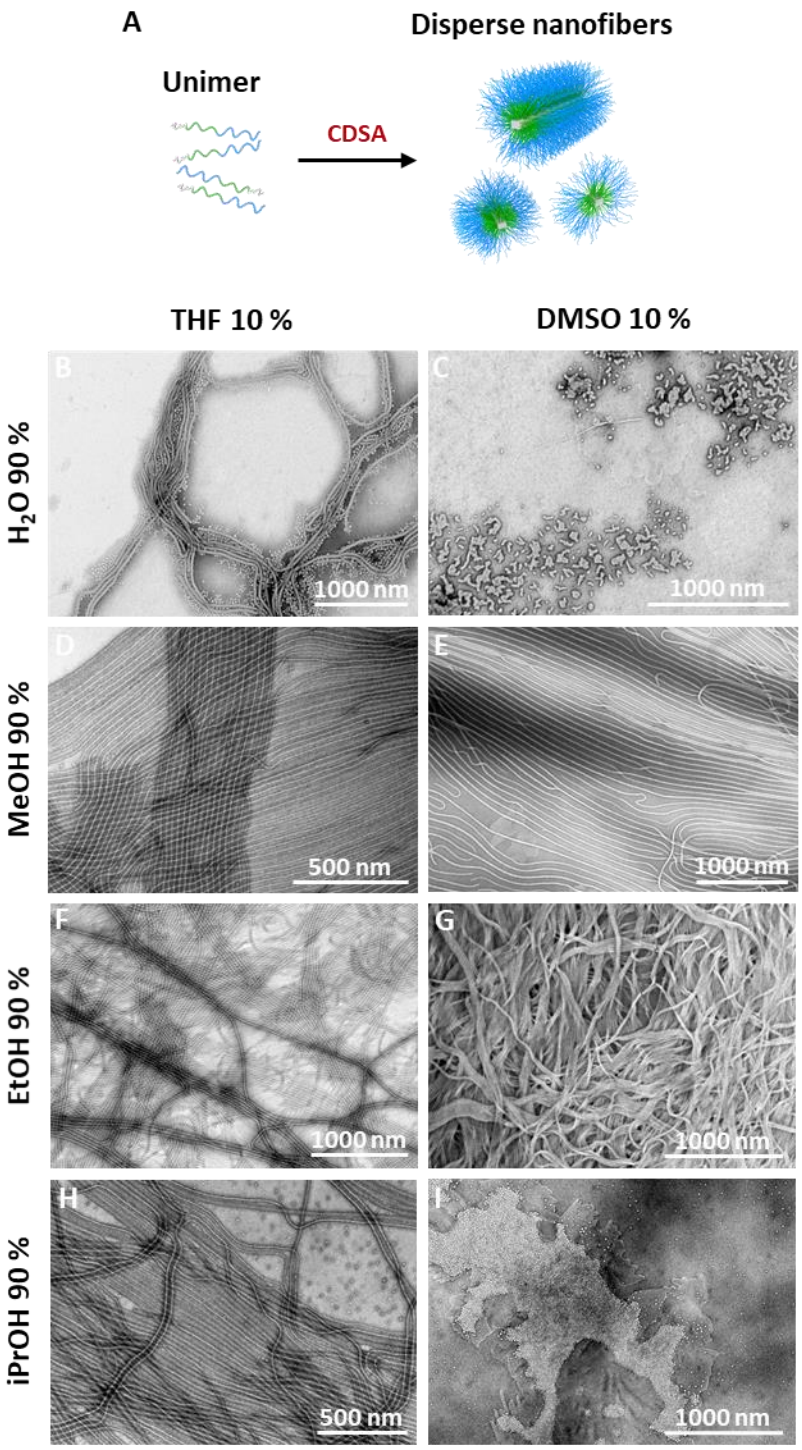

Figure S2. 11. Screening conditions for the spontaneous self-nucleation of $PFTMC_{18}$-*b*-$PBMA_{44}$-*b*-$PNIPAM_{70}$ to yield nanofibers via CDSA A) Schematic representation of spontaneous self-nucleation. B-I) TEM micrographs of the assembly mixtures at different solvent fractions indicated in the figure.

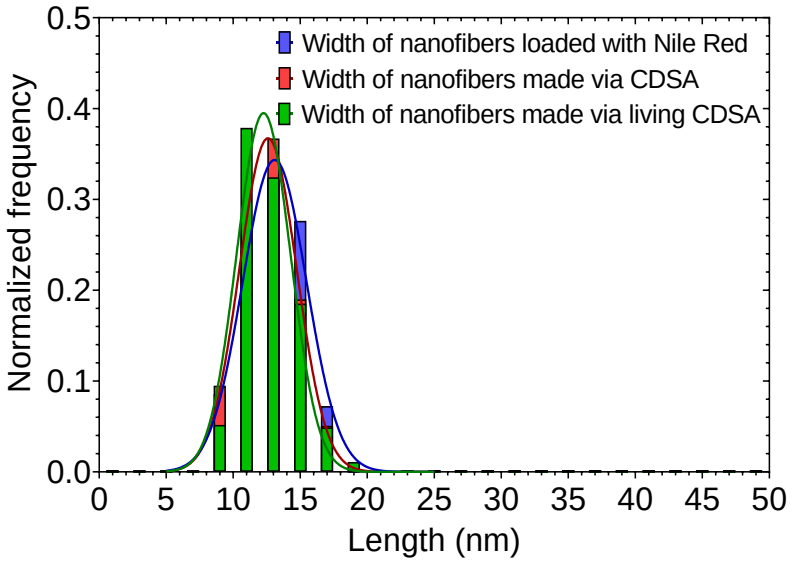

Figure S2. 12. Histogram of the PFTMC$_{18}$-*b*-PBMA$_{44}$-*b*-PNIPAM$_{70}$ nanofiber crystalline core width using measurements from samples at m_{unimer}/m_{seed} of 2.5, 5, 10, 20, 30, and 40 nanofibers made via living CDSA. A minimum of 50 nanofibers were measured per m_{unimer}/m_{seed} added and presented as combined data. n = 368, W_n = 12.3 nm, $Đ$ = 1.03, σ = 2 nm (green). Width of nanofibers made via CDSA n = 158, W_n = 12.6 nm, $Đ$ = 1.03, σ = 2 nm (red). Width of nanofibers made via CDSA loaded with NR n = 152, W_n = 13.1 nm, $Đ$ = 1.02, σ = 2 nm (blue).

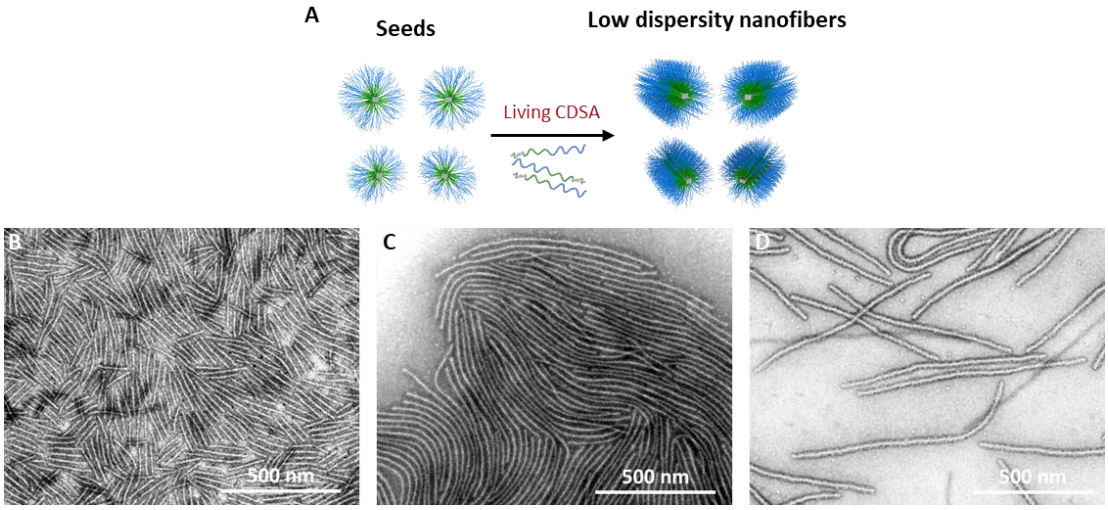

Figure S2. 13. Schematic representation of the generation of low-dispersity nanofibers from PFTMC$_{18}$-*b*-PBMA$_{44}$-*b*-PNIPAM$_{70}$. B-D) TEM images of nanofibers prepared via Living CDSA at various m_{unimer}/m_{seed} ratios added to solutions of seed nanofibers. munimer/mseed = B) 5:1 C) 40:1 D) 50:1.

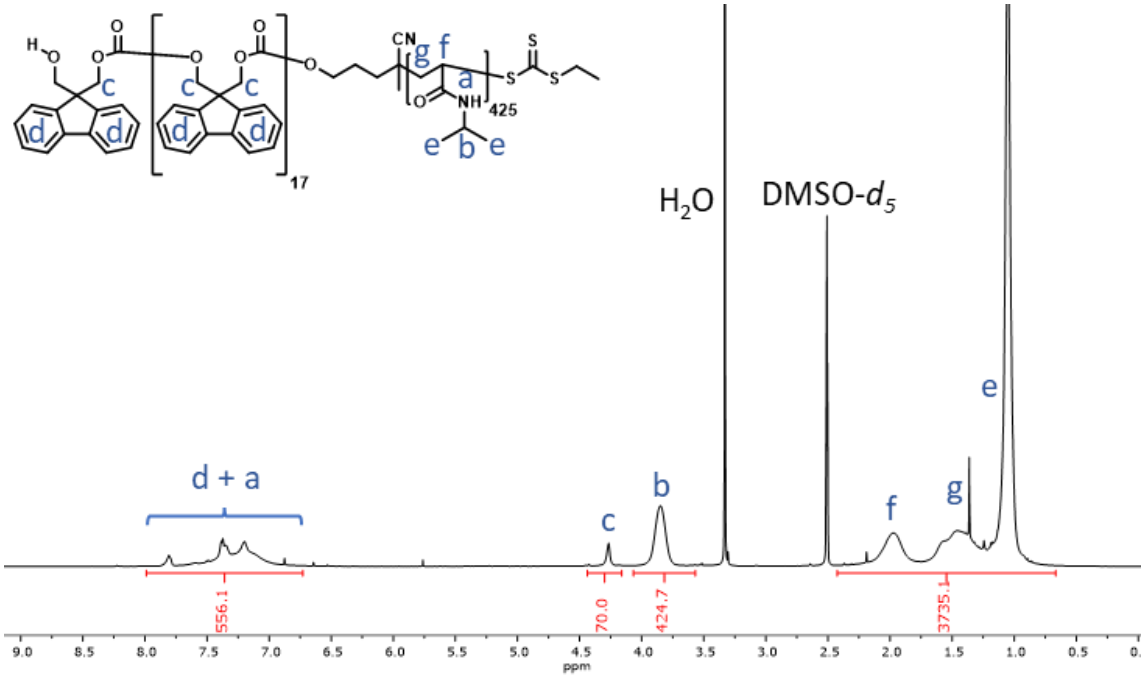

Figure S2. 14. ^{1}H NMR spectra (in DMSO-d_6) of purified PFTMC$_{18}$-*b*-PNIPAM$_{425}$.

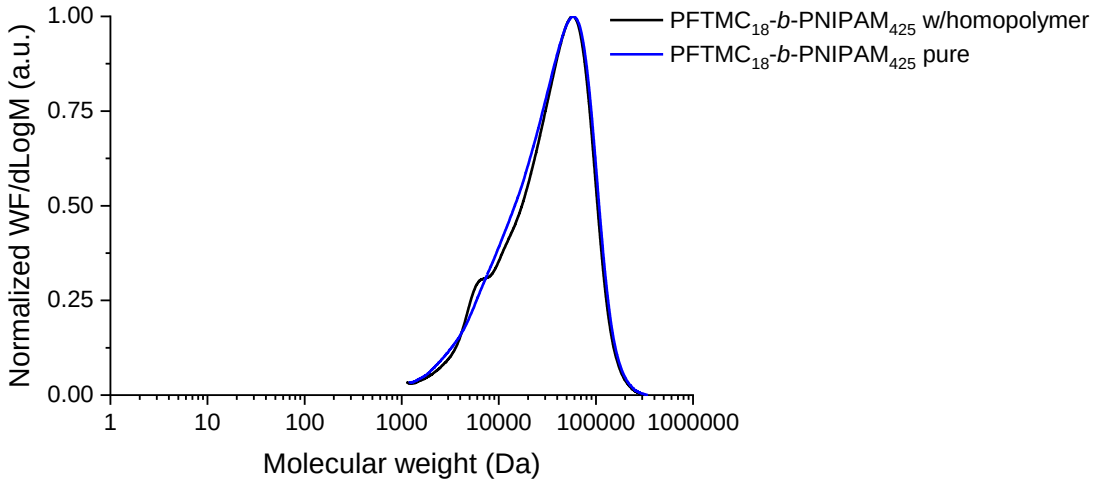

Figure S2. 15. GPC (refractive index) traces of in triethylamine/THF (1% *v/v*) of PFTMC-*b*-PNIPAM before and after flash column chromatography. The y-axis reflects the distribution of weight fractions by molecular weight.

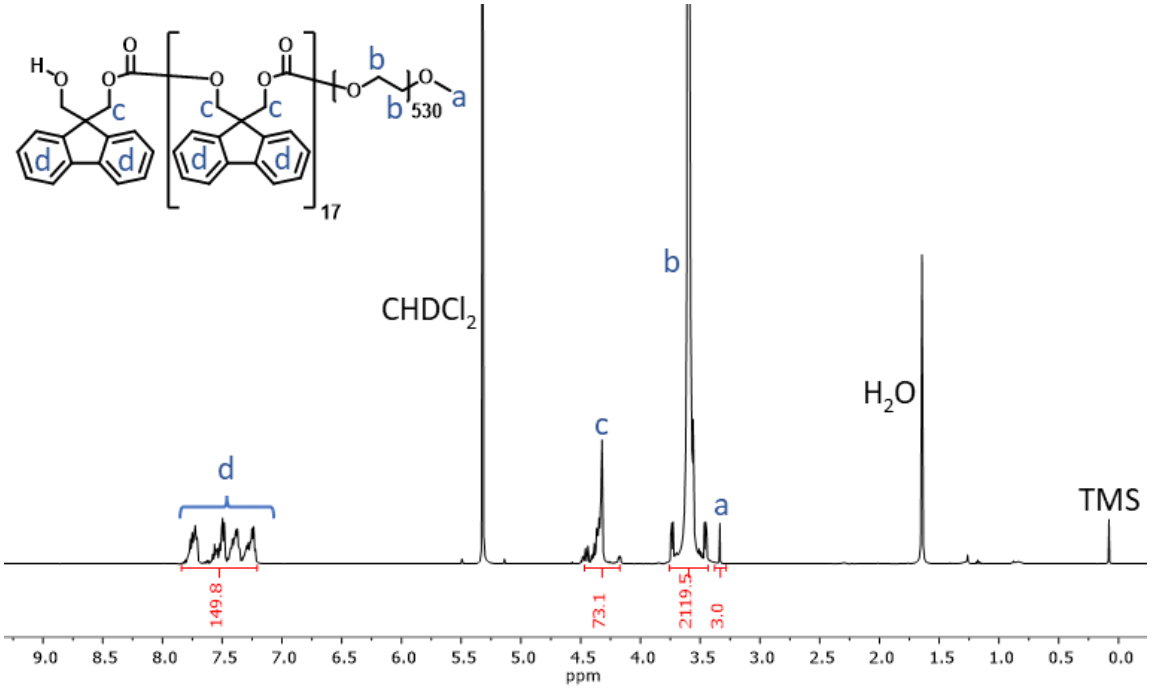

Figure S2. 16. ^{1}H NMR spectra (in CD_2Cl_2) of $PFTMC_{18}$-*b*-PEG_{530}.

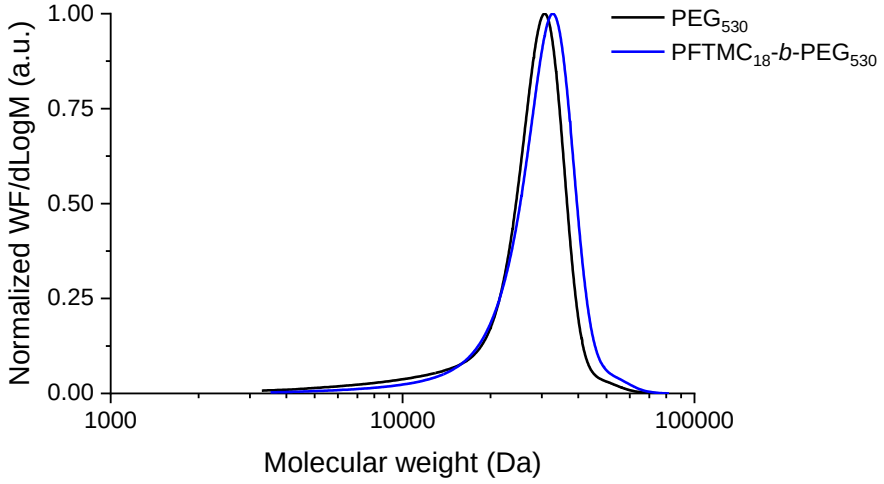

Figure S2. 17. GPC (refractive index) traces eluted in triethylamine/THF (1% *v/v*), 1 mL min^{-1}, 35 °C of PEG_{530} homopolymer (black trace), $PFTMC_{18}$-*b*-PEG_{530} diBCP (blue trace). The y-axis reflects the distribution of weight fractions by molecular weight.

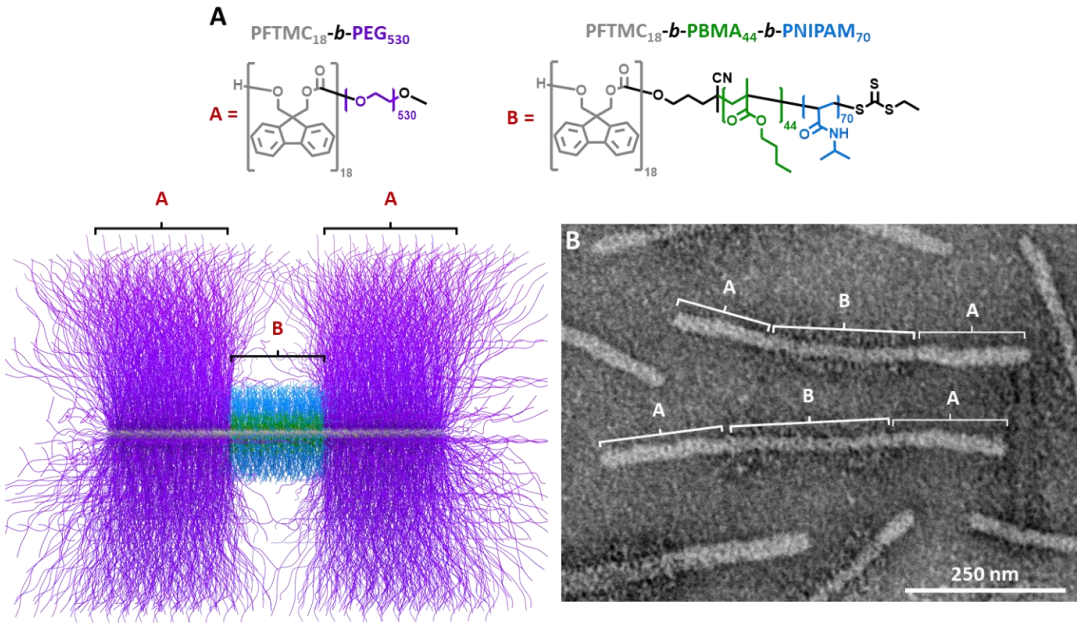

Figure S2. 18. A) Schematic of segmented PFTMC$_{18}$-*b*-PEG$_{530}$-***m***-PFTMC$_{18}$-*b*-PBMA$_{44}$-*b*-PNIPAM$_{70}$-***m***-PFTMC$_{18}$-*b*-PEG$_{530}$ nanofibers, prepared by addition of 1 equivalent of the unimeric PFTMC$_{18}$-*b*-PEG$_{530}$ (in THF) to a solution containing low dispersity 412 nm PFTMC$_{18}$-*b*-PBMA$_{44}$-*b*-PNIPAM$_{70}$ coaxial nanofibers (THF:MeOH, 15:85), after ageing for 48 h. B) TEM of the segmented nanofibers (L_n = 584 nm, $Đ$ = 1.14, σ = 216 nm, n = 101).

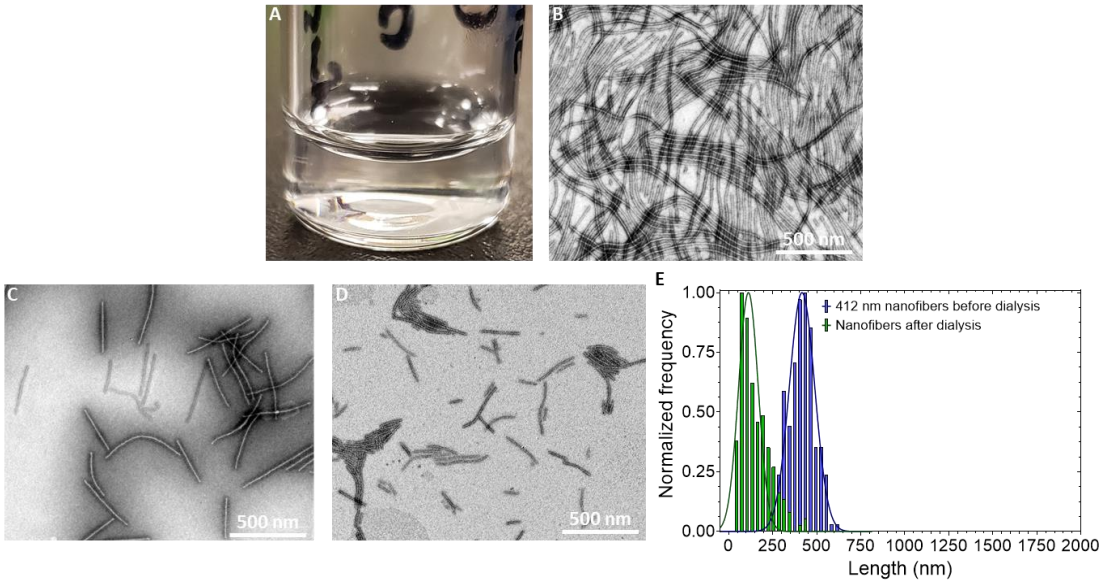

Figure S2. 19. A) Image of the disperse PFTMC$_{18}$-*b*-PBMA$_{44}$-*b*-PNIPAM$_{70}$ nanofiber solution after dialysis against water (0.5 mg/mL) from MeOH:THF (85:15). B) TEM image of the disperse nanofibers in water after dialysis. C-D) 412 nm nanofibers prepared via the seeded growth method by addition of unimer (in THF) to the nanofiber seed solution: C) before dialysis (L_n = 412 nm, $Đ$ = 1.04, σ = 78 nm), and D) after dialysis to water (L_n = 150 nm, $Đ$ = 1.31, σ = 84 nm). E) Histogram of the contour length analysis of the 412 nm nanofibers before and after dialysis to H_2O.

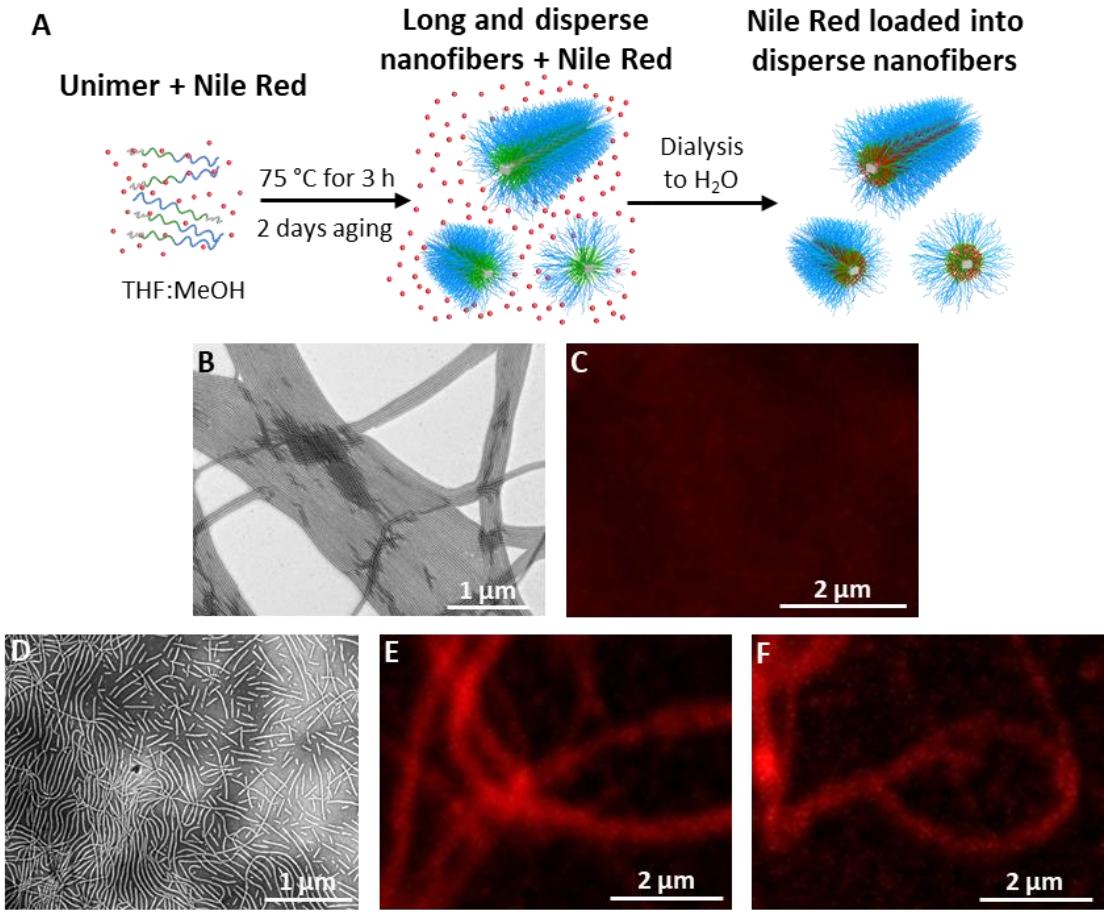

Figure S2. 20. Preparation of NR loaded PFTMC$_{18}$-*b*-PBMA$_{44}$-*b*-PNIPAM$_{70}$ disperse nanofibers. A) Schematic process of NR loading into disperse nanofibers. B) TEM and C) LCSM images of the disperse nanofibers with NR in THF:MeOH (15:85) before dialysis into water, with diffuse NR fluorescence. D) TEM and E-F) LCSM images after dialysis into water revealing encapsulation of NR into the nanofibers.

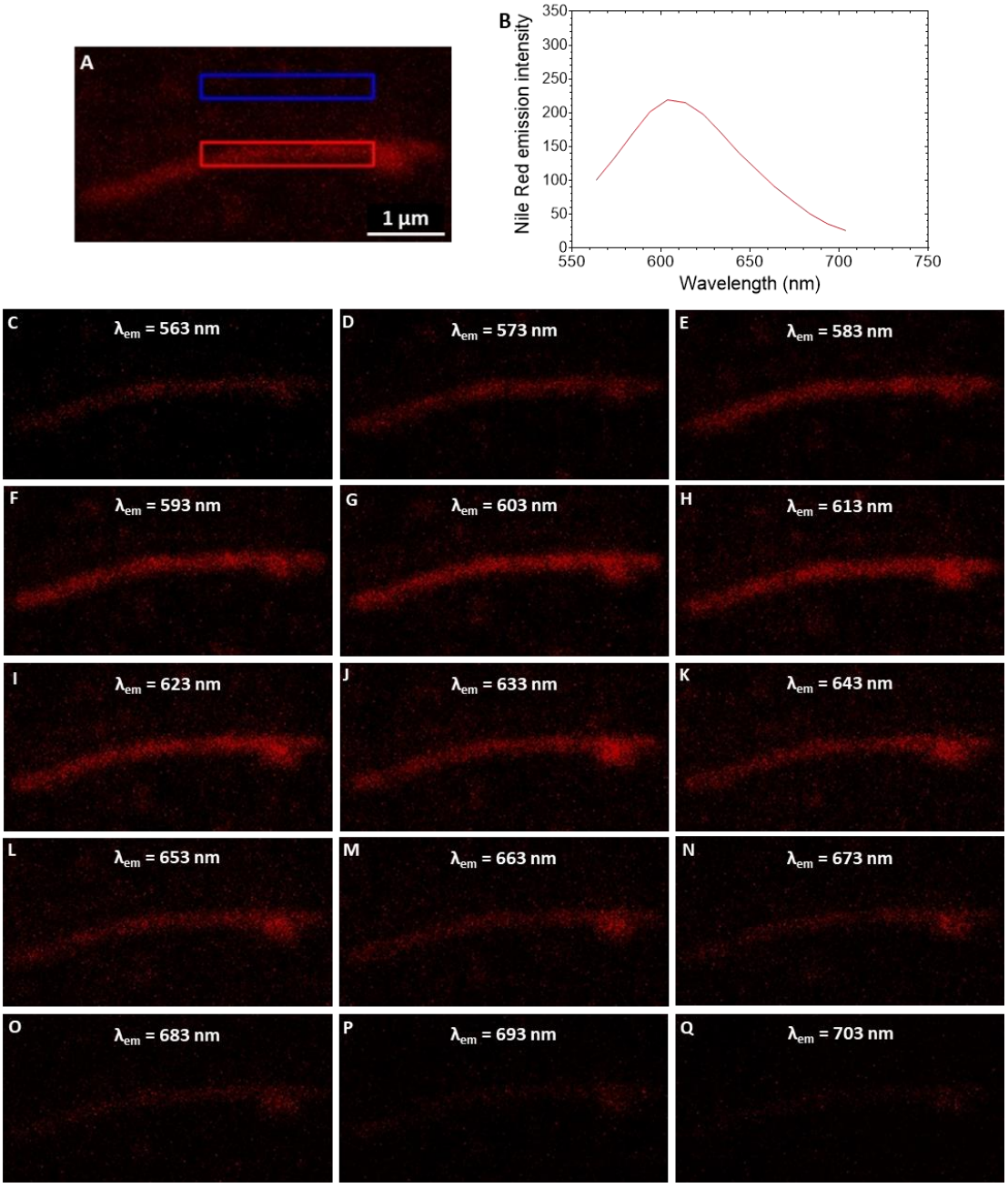

Figure S2. 21. Fluorescence emission spectra of the encapsulated NR in disperse PFTMC$_{18}$-*b*-PBMA$_{44}$-*b*-PNIPAM$_{70}$ nanofibers in water. A) LCSM image of the nanofiber with encapsulated NR merged from observation windows ranging from 563 – 703 nm (10 nm interval, from S12 C-Q). The red rectangle indicates the nanofiber region used for analysis, and the blue rectangle indicates the area used as background emission for data treatment. B) Emission spectra of NR encapsulated in disperse nanofibers imaged via LCSM, with the background emission subtracted. C-Q) Emission windows of encapsulated NR at wavelengths ranging from 563 – 703 nm.

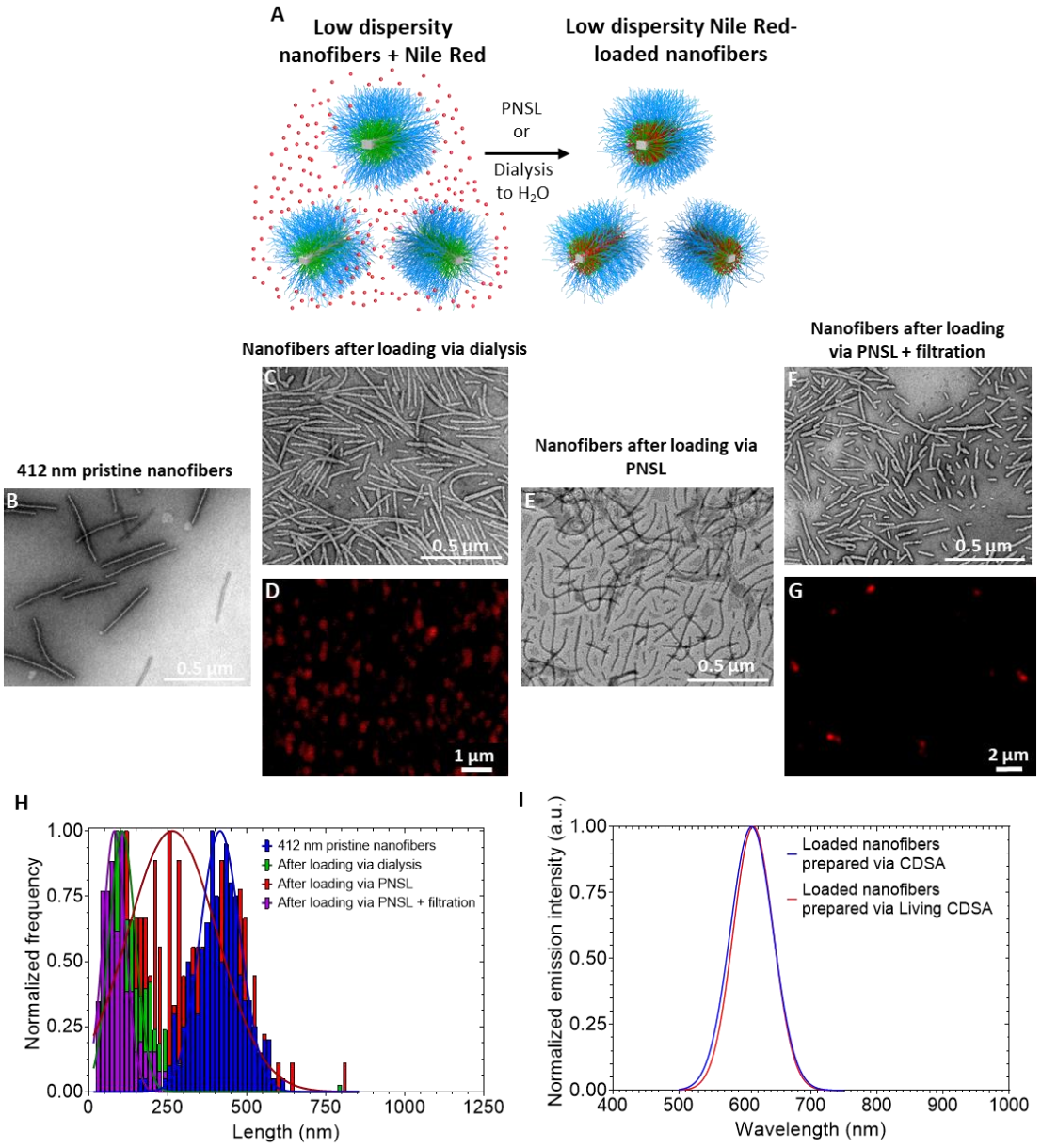

Figure S2. 22. A) Schematic process of loading and encapsulation of NR into low dispersity PFTMC$_{18}$-*b*-PBMA$_{44}$-*b*-PNIPAM$_{70}$ nanofibers via dialysis. B) TEM image of pristine 412 nm nanofibers (L_n = 412 nm, $Đ$ = 1.04, σ = 78 nm). C) TEM (L_n = 159 nm, $Đ$ = 1.41, σ = 101 nm) and D) LCSM Micrographs of 412 nm nanofibers after loading NR via dialysis into H_2O. E) TEM image of the NR loaded (originally pristine) nanofibers after loading via PNSL; L_n = 339 nm, $Đ$ = 1.29, σ = 185 nm F) TEM (L_n = 251 nm, $Đ$ = 1.50, σ = 178 nm) and G) LCSM micrographs of the NR loaded nanofibers after loading via PNSL (from E) and filtration with a nylon-syringe filter of 0.45 µm pore size. The localized fluorescence observed via LCSM provides evidence for the encapsulation of NR into the nanofibers. H) Histogram of the contour length analysis of the pristine 412 nm nanofibers prepared via living CDSA before loading NR and transfer to H_2O (blue), after loading via dialysis (green), after loading via PNSL (red), and after loading via PNSL and filtration (purple). The PNSL process alone reduced the fragmentation of the 412 nm nanofibers by 47% when compared to the dialysis method. H) Fluorescence emission spectra of NR loaded into nanofibers prepared via CDSA and via Living CDSA. The similarity of these spectra indicates that NR is localized in the same environment.

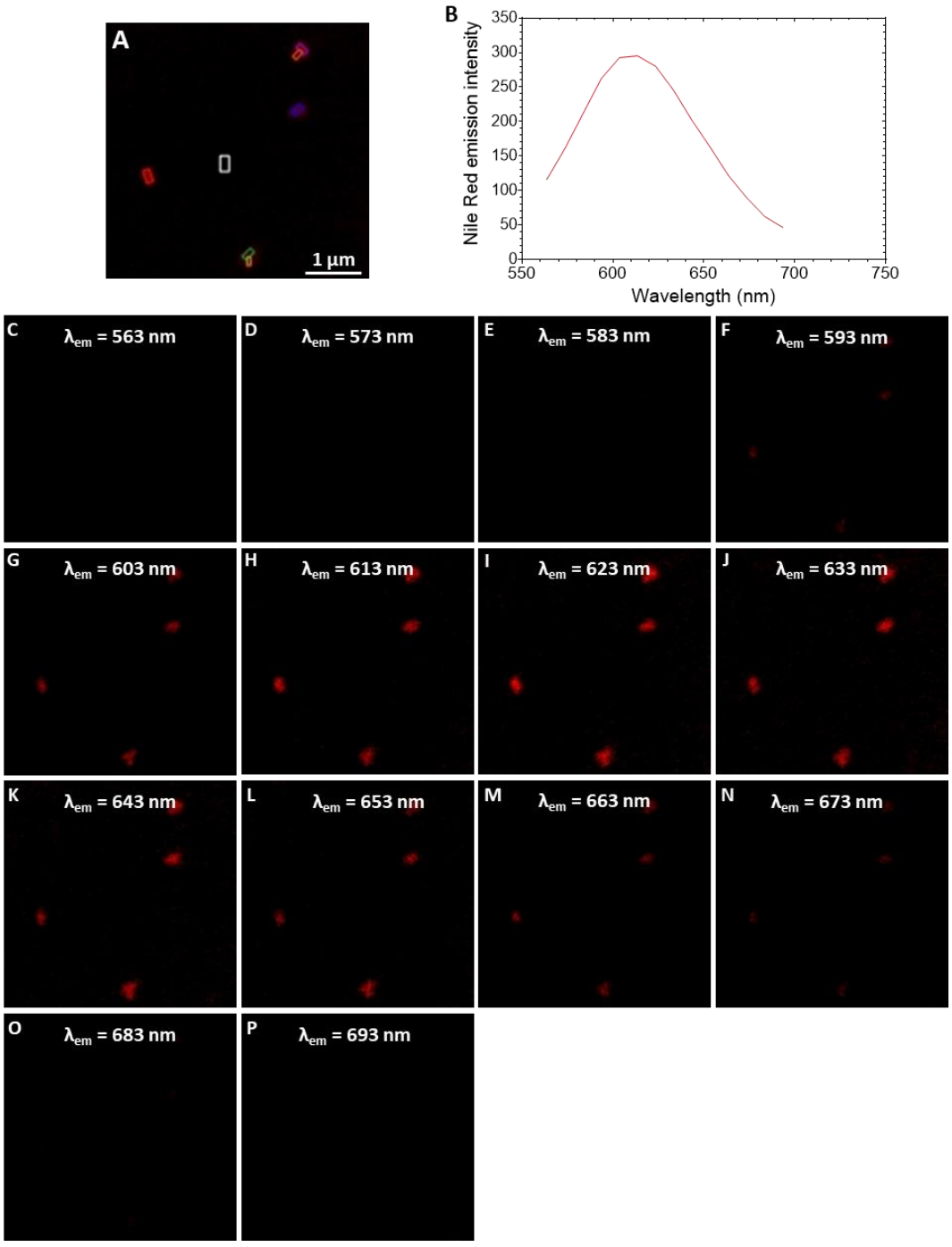

Figure S2. 23. Fluorescence emission spectra of NR encapsulated into preformed PFTMC$_{18}$-*b*-PBMA$_{44}$-*b*-PNIPAM$_{70}$ nanofibers in water. A) LCSM image of preformed nanofibers loaded with NR merged from observation windows ranging from 563 – 693 nm (10 nm interval, from S14C-P). The middle white square indicates the area used as background emission for data treatment. The rest of the squares represent the areas used to assess the emission of the loaded NR in the nanofibers. B) Emission spectra of NR encapsulated in low dispersity nanofibers by LCSM, with the background emission subtracted. C-P) Emission windows of encapsulated NR at wavelengths ranging from 563 – 693 nm.

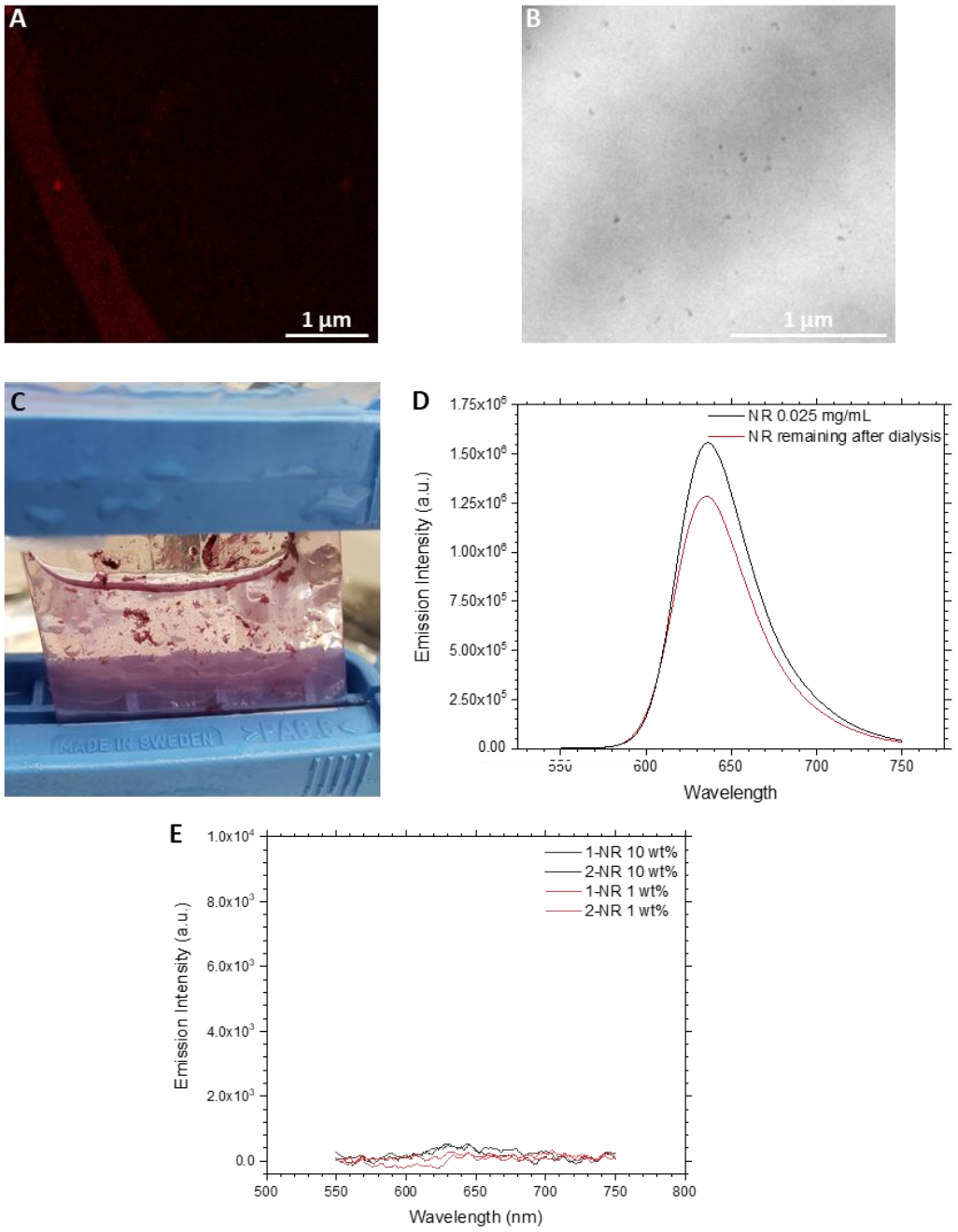

Figure S2. 24. A) LCSM image of NR dialyzed to water from THF:MeOH 15:85 (0.025 mg/mL). No evidence of elongated morphologies are present - the red aggregate-dot and red stripe on the left are regions where an air bubble was present, the dark region is water, and the lack of fluorescence where water is present indicates that the NR fluorescence is quenched in water. B) TEM image of the NR solution dialyzed into water, where dark NR aggregates are observed but no nanoparticles or nanofibers are observed, as expected. C) Precipitate of NR (0.025 mg/mL, 1.5 mL, MeOH) after 10 mins observed during dialysis to H_2O. D) Fluorescence emission spectra of a solution of NR at 0.025 mg/mL in MeOH, and the NR sample dialyzed from MeOH (0.025 mg/mL, 1.5 mL) into water, then lyophilized, and resuspended in MeOH (1.5 mL) for spectroscopic analysis. The presence of a significant emission from NR indicates that dialysis is insufficient for the removal of NR. E) Fluorescence emission spectra of solutions of NR (10 and 1 wt %) transferred to H_2O via PNSL, filtered (0.45 µm, nylon filter), lyophilized and resuspended in MeOH to assess NR removal. λ_{ex} = 540 nm.

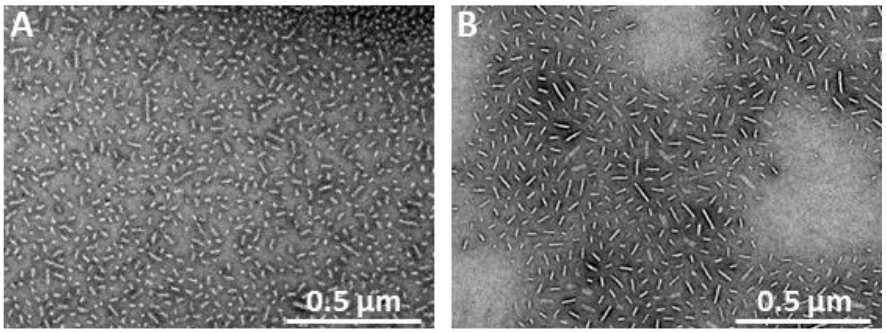

Figure S2. 25. TEM micrographs of PFTMC$_{18}$-*b*-PBMA$_{44}$-*b*-PNIPAM$_{70}$ nanofibers before NR loading and transfer to water via the PNSL method. A) Seeds (L_n = 22 nm, $Đ$ = 1.12, σ = 7.7 nm). B) 84 nm fibers (L_n = 84 nm, $Đ$ = 1.05, σ = 20 nm).

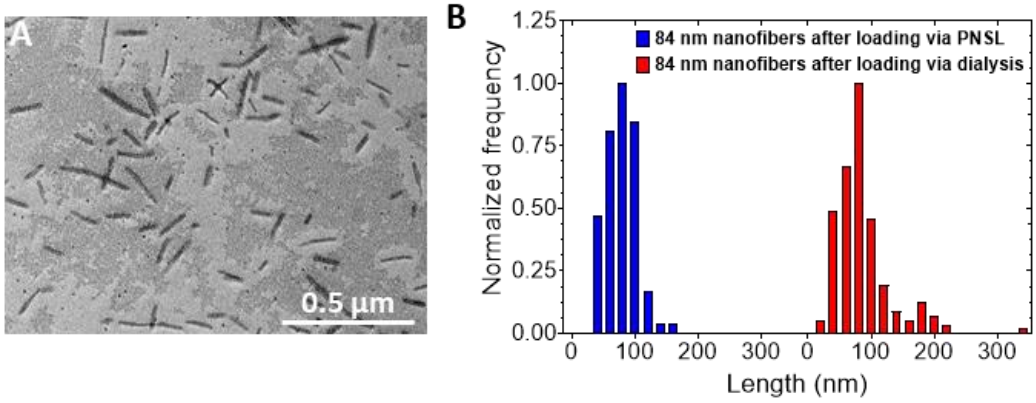

Figure S2. 26. A) TEM micrograph of 84 nm PFTMC$_{18}$-*b*-PBMA$_{44}$-*b*-PNIPAM$_{70}$ nanofibers (L_n = 86 nm, $Đ$ = 1.26, σ = 44 nm) after NR loading and transfer into water via dialysis. B) Countour length histograms of 84 nm nanofibers loaded with NR via PNSL (blue), and via dialysis (red). Our results show that the L_n of both samples is fairly similar, but in the case of the 84 nm nanofibers loaded via dialysis, both fragmentation and an increase in length of the nanofibers is observed. The fragmentation occurs due to the rapid solvent exchange process during dialysis, whereas the increase in length likely arises from hydrophobic and entropically favorable interactions between the PBMA blocks at the end of the nanofibers during the fast solvent exchange, resulting in nanofiber end-fusion and an increase in length.

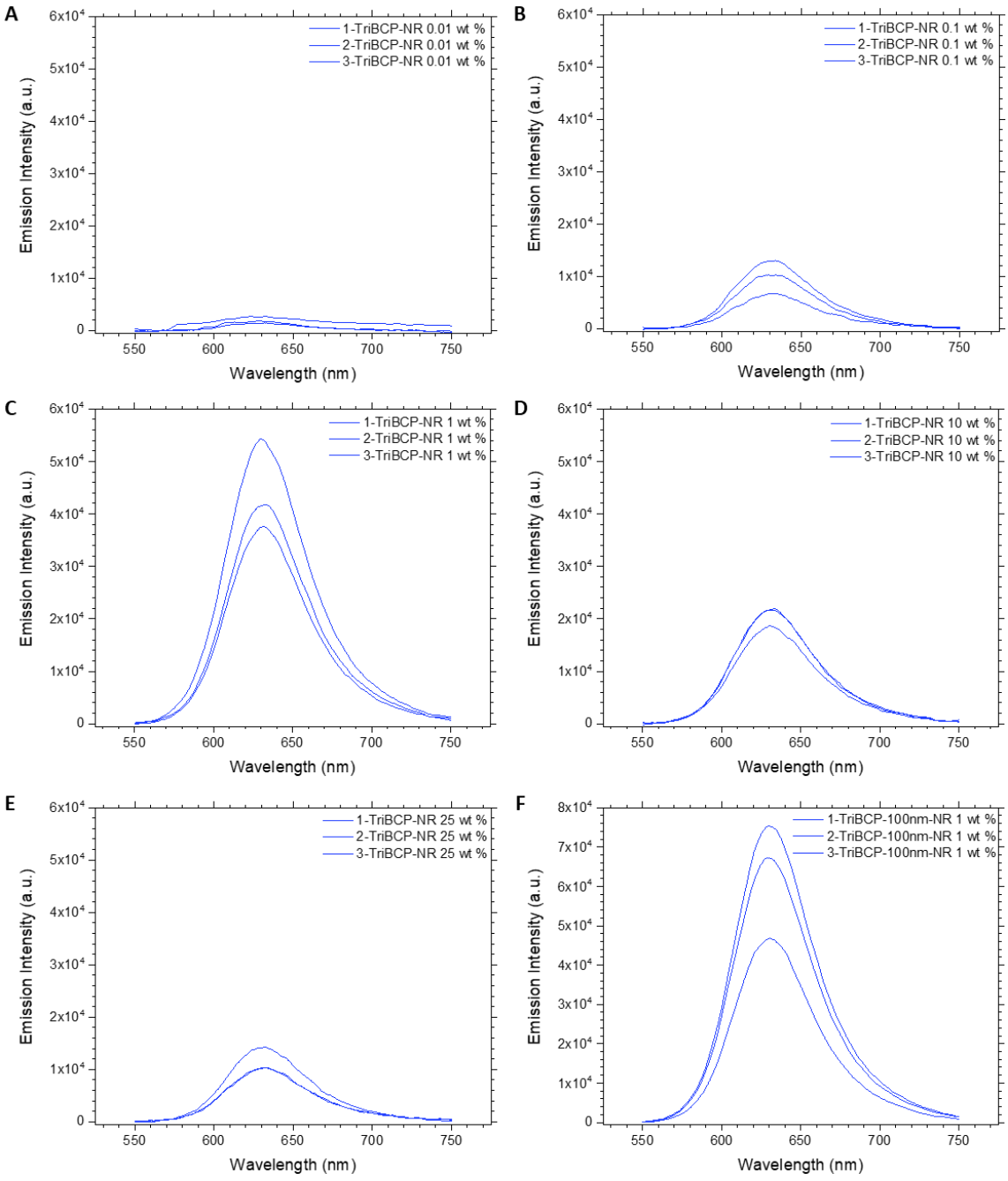

Figure S2. 27. Emission spectra (in MeOH) of the PFTMC$_{18}$-*b*-PBMA$_{44}$-*b*-PNIPAM$_{70}$ (L_n = 25 nm, $Đ$ = 1.08, σ = 7.0 nm) nanofibers loaded with NR via PNSL at different concentrations, followed by filtration: A) 0.01 wt %, B) 0.1 wt %, C) 1 wt %, D) 10 wt %, and E) 25 wt %. F) Emission spectra (in MeOH) of the PFTMC$_{18}$-*b*-PBMA$_{44}$-*b*-PNIPAM$_{70}$ (L_n = 125 nm, $Đ$ = 1.08, σ = 35 nm) nanofibers loaded with NR via PNSL at 1 wt %. λ_{ex} = 540 nm. Each experiment was conducted in triplicate and the spectral traces are labelled accordingly.

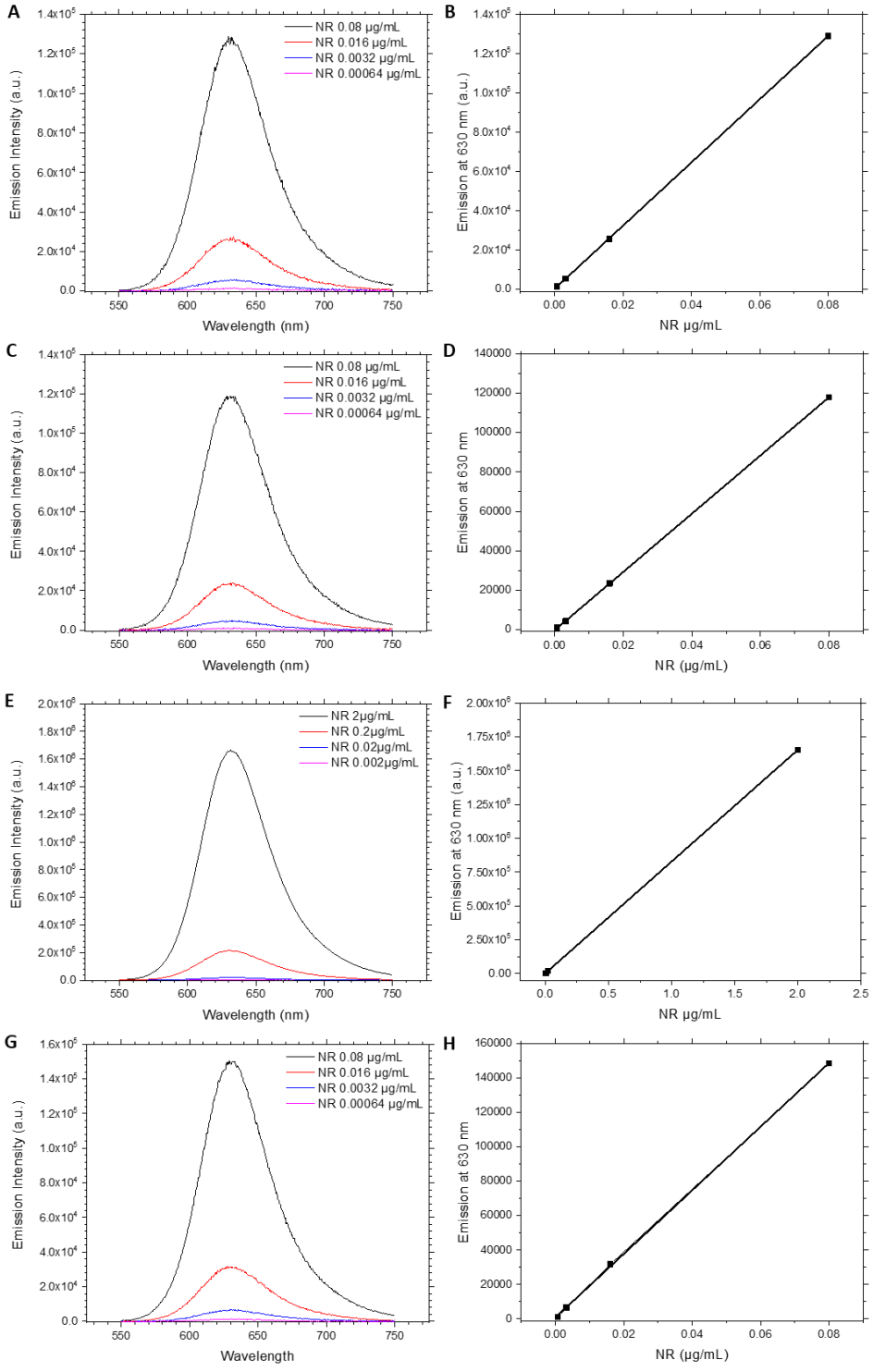

Figure S2. 28. A), C), E) and G) Emission of NR at different concentrations (in MeOH) to construct the calibration curves in B, D, F and H. The emission intensity for the calibration curves was recorded at λ_{ex} = 540 nm. The equation of the line and coefficient of determination for each calibration curve at $\lambda_{ex\text{-}max}$ = 630 nm are as follows: B) $y = 267.2 + 1.61\times10^6 x$; $r^2 = 0.9999$. D) $y = 103.2 + 1.48\times10^6 x$; $r^2 = 0.9999$. F) $y = 2399 + 8.26\times10^6 x$; $r^2 = 0.9999$, and G) $y = 855.1 + 1.85\times10^6 x$; $r^2 = 0.9998$. The equations were used to quantify the loading of NR in the nanofibers from the Figure S2. 27.

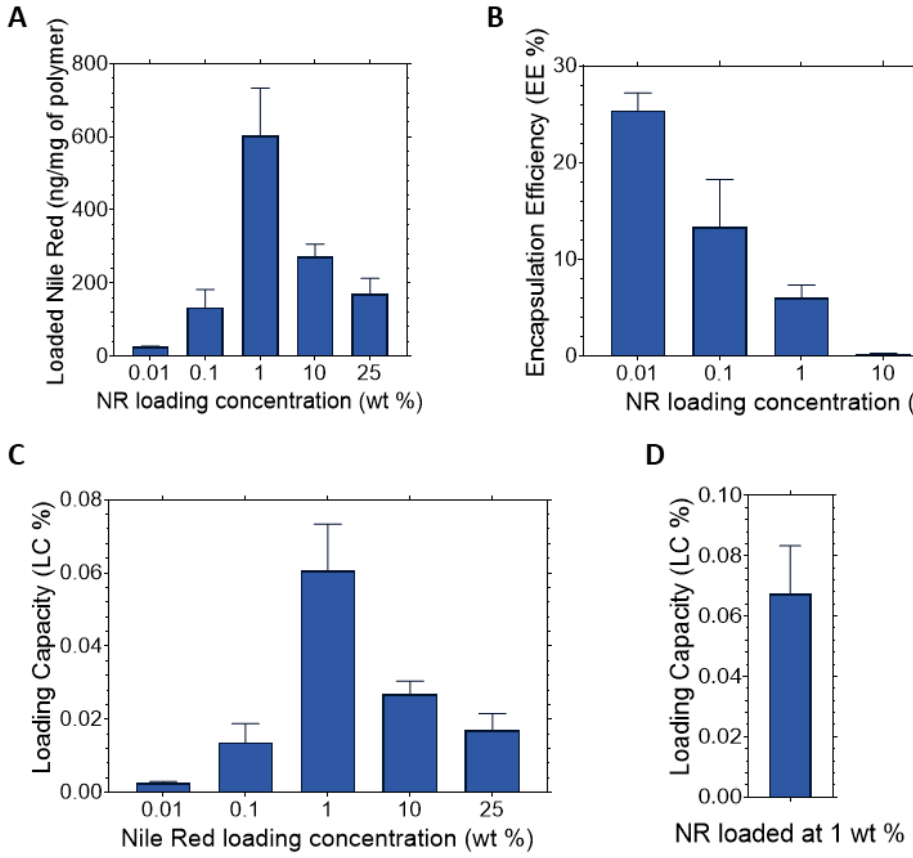

Figure S2. 29. Loading properties of PFTMC$_{18}$-*b*-PBMA$_{44}$-*b*-PNIPAM$_{70}$ L_n = 25 nm ($Đ$ = 1.08, σ = 35 nm) nanofibers with different initial quantities of NR (wt %) used in the loading process; A) Nile Red loaded in ng per mg of triBCP, B) Encapsulation Efficiency (EE %), C) Loading Capacity (LC %). D) LC % of triBCP nanofibers L_n = 125 nm ($Đ$ = 1.08, σ = 35 nm). The EE % and LC % were calculated as follows: EE % = (mass of drug added – mass of non-encapsulated drug)/(mass of drug added)×100, e.g. 25 nm seeds loaded at 1 wt %; EE % = (1000 ng – 940 ng)/(1000 ng)×100=6%, and LC % = (mass of encapsulated drug)/(mass of nanofibers)×100, e.g. 25 nm seeds loaded at 1 wt %; LC % = (60 ng)/(100,000 ng)×100=0.06%.

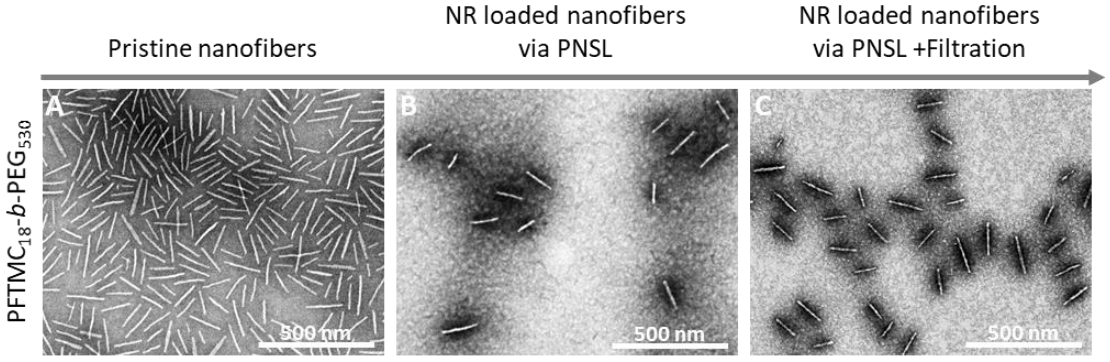

Figure S2. 30. TEM micrographs of the loading process of the PFTMC$_{18}$-*b*-PEG$_{530}$ nanofibers D) before loading (L_n = 108 nm, $Đ$ = 1.08, σ = 30 nm), E) after loading via PNSL (L_n = 114 nm, $Đ$ = 1.06, σ = 28 nm), F) after syringe filtration (L_n = 125 nm, $Đ$ = 1.04, σ = 26 nm).

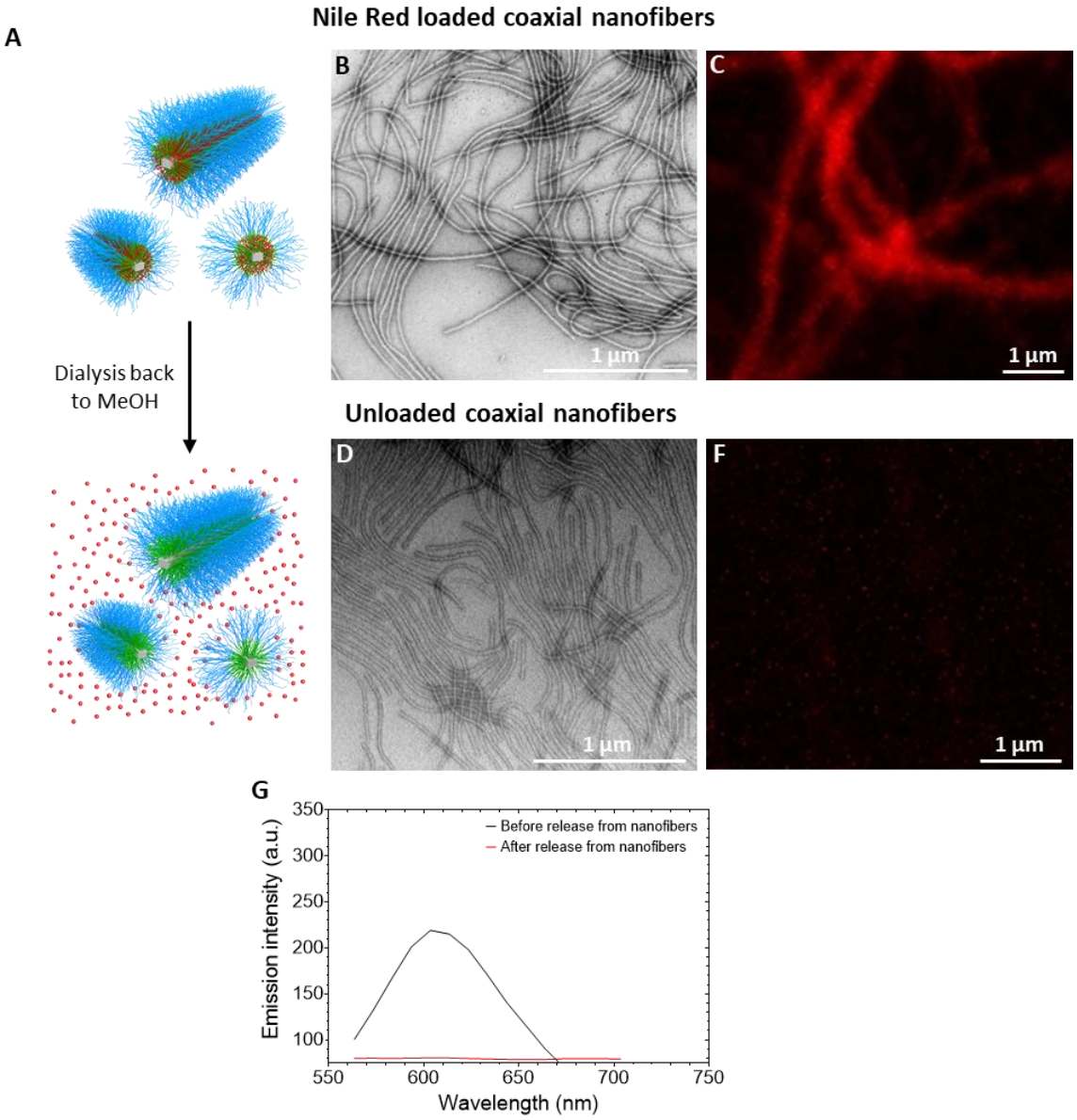

Figure S2. 31. Release of NR from PFTMC$_{18}$-*b*-PBMA$_{44}$-*b*-PNIPAM$_{70}$ nanofibers. A) Schematic of the release process for NR encapsulated in the PBMA block of the nanofibers after dialysis from water back into MeOH. B) TEM image of NR loaded nanofibers in water before dialysis. C) LCSM image of nanofibers in water before dialysis. D-F) TEM and LCSM, respectively, of the nanofibers after dialysis into MeOH showing the nanofibers but no emission from NR. G) LCSM fluorescence emission spectra of the NR loaded nanofibers before (black) and after (red) dialysis into MeOH. The disappearance of the emission from NR is evidence for the release of NR, which is presumably removed via repeated changes of the MeOH dialysate.

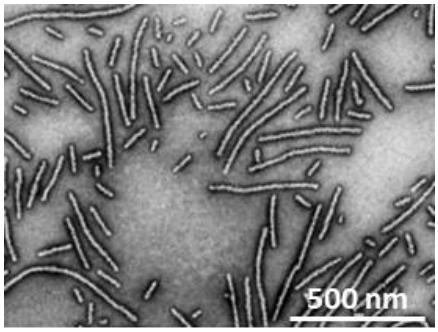

Figure S2. 32. TEM image of the PFTMC$_{18}$-*b*-PBMA$_{44}$-*b*-PNIPAM$_{70}$ nanofibers in S2. 22F after dialysis to MeOH.

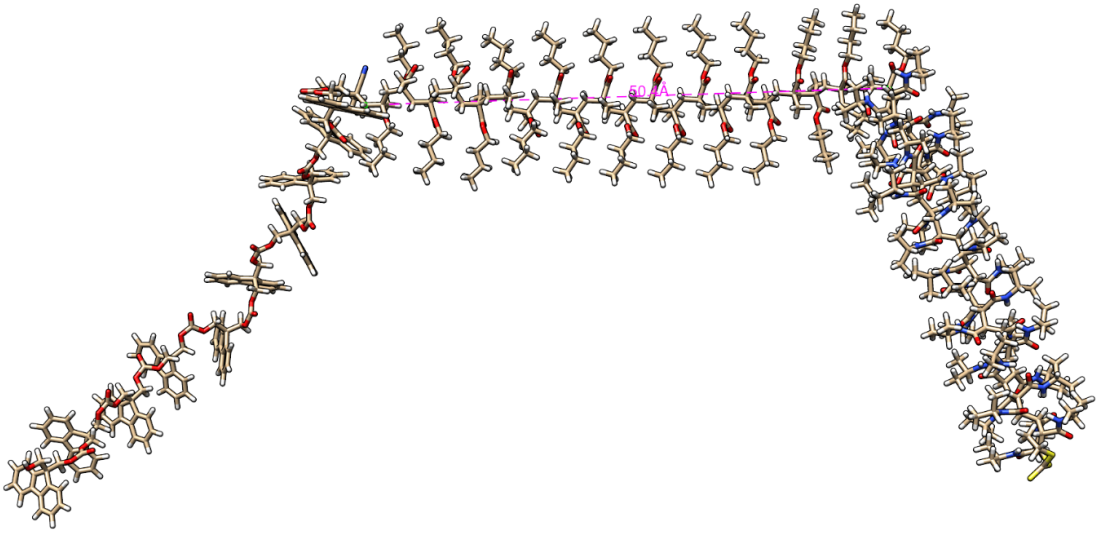

Figure S2. 33. Molecular mechanics simulations of PFTMC$_9$-*b*-PBMA$_{22}$-*b*-PNIPAM$_{35}$. The DP$_n$ of each block was divided in two for computational efficiency (the polymer used in this work was PFTMC$_{18}$-*b*-PBMA$_{44}$-*b*-PNIPAM$_{70}$). The energy minimized structure was computed using the energy minimization function in Chem3D with the MM2 force field, and visualized using UCSF Chimera.[94] The length of the PBMA chains was measured in USCF Chimera, and found to be 5.04 nm for PBMA$_{22}$, and hence 10.1 nm for PBMA$_{44}$.

2.7 References

(1) Petros, R. A.; DeSimone, J. M. Strategies in the Design of Nanoparticles for Therapeutic Applications. *Nat. Rev. Drug Discov.* **2010**, *9* (8), 615–627.

(2) Chariou, P. L.; Ortega-Rivera, O. A.; Steinmetz, N. F. Nanocarriers for the Delivery of Medical, Veterinary, and Agricultural Active Ingredients. *ACS Nano* **2020**, *14* (3), 2678–2701.

(3) Ge, Z.; Liu, S. Functional Block Copolymer Assemblies Responsive to Tumor and Intracellular Microenvironments for Site-Specific Drug Delivery and Enhanced Imaging Performance. *Chem. Soc. Rev.* **2013**, *42* (17), 7289–7325.

(4) Allen, T. M.; Cullis, P. R. Drug Delivery Systems: Entering the Mainstream. *Science* **2004**, *303* (5665), 1818–1822.

(5) Hua, S.; de Matos, M. B. C.; Metselaar, J. M.; Storm, G. Current Trends and Challenges in the Clinical Translation of Nanoparticulate Nanomedicines: Pathways for Translational Development and Commercialization. *Front. Pharmacol.* **2018**, *9* (790), 1–14.

(6) Ekladious, I.; Colson, Y. L.; Grinstaff, M. W. Polymer–Drug Conjugate Therapeutics: Advances, Insights and Prospects. *Nat. Rev. Drug Discov.* **2019**, *18* (4), 273–294.

(7) Naahidi, S.; Jafari, M.; Edalat, F.; Raymond, K.; Khademhosseini, A.; Chen, P. Biocompatibility of Engineered Nanoparticles for Drug Delivery. *J. Control. Release* **2013**, *166* (2), 182–194.

(8) Oltra, N. S.; Nair, P.; Discher, D. E. From Stealthy Polymersomes and Filomicelles to "Self" Peptide-Nanoparticles for Cancer Therapy. *Annu. Rev. Chem. Biomol. Eng.* **2014**, *5* (1), 281–299.

(9) Mansour, H. M.; Sohn, M. J.; Al-Ghananeem, A.; DeLuca, P. P. Materials for Pharmaceutical Dosage Forms: Molecular Pharmaceutics and Controlled Release Drug Delivery Aspects. *Int. J. Mol. Sci.* **2010**, *11* (9), 3298–3322.

(10) Shen, S.; Wu, Y.; Liu, Y.; Wu, D. High Drug-Loading Nanomedicines : Progress , Current Status , and Prospects. *Int. J. Nanomedicine* **2017**, *12*, 4085–4109.

(11) Blanco, E.; Shen, H.; Ferrari, M. Principles of Nanoparticle Design for Overcoming Biological Barriers to Drug Delivery. *Nat. Biotechnol.* **2015**, *33* (9), 941–951.

(12) Zhao, J.; Stenzel, M. H. Entry of Nanoparticles Into Cells: The Importance of Nanoparticle Properties. *Polym. Chem.* **2018**, *9* (3), 259–272.

(13) Webber, M. J.; Langer, R. Drug Delivery by Supramolecular Design. *Chem. Soc. Rev.* **2017**, *46* (21), 6600–6620.

(14) Nasir, I.; Lundqvist, M.; Cabaleiro-Lago, C. Size and Surface Chemistry of Nanoparticles Lead to a Variant Behavior in the Unfolding Dynamics of Human Carbonic Anhydrase. *Nanoscale* **2015**, *7* (41), 17515.

(15) Muhamad, N.; Plengsuriyakarn, T.; Na-Bangchang, K. Application of Active Targeting Nanoparticle Delivery System for Chemotherapeutic Drugs and Traditional/Herbal Medicines in Cancer Therapy: A Systematic Review. *Int. J. Nanomedicine* **2018**, *13*, 3921–3935.

(16) Bazak, R.; Houri, M.; Samar, E. A.; Kamel, S.; Refaat, T. Cancer Active Targeting by Nanoparticles: A Comprehensive Review of Literature. *J Cancer Res Clin Oncol* **2015**, *141* (5), 769–784.

(17) Zhu, X.; Vo, C.; Taylor, M.; Smith, B. R. Non-Spherical Micro- and Nanoparticles in Nanomedicine. *Mater. Horizons* **2019**, *6* (6), 1094–1121.

(18) Truong, N. P.; Whittaker, M. R.; Mak, C. W.; Davis, T. P. The Importance of Nanoparticle Shape in Cancer Drug Delivery. *Expert Opin. Drug Deliv.* **2015**, *12* (1), 129–142.

(19) Banerjee, A.; Qi, J.; Gogoi, R.; Wong, J.; Mitragotri, S. Role of Nanoparticle Size, Shape and Surface Chemistry in Oral Drug Delivery. *J. Control. Release* **2016**, *238* (1), 176–185.

(20) Gaumet, M.; Vargas, A.; Gurny, R.; Delie, F. Nanoparticles for Drug Delivery: The Need for Precision in Reporting Particle Size Parameters. *Eur. J. Pharm. Biopharm.* **2008**, *69* (1), 1–9.

(21) Doncom, K. E. B.; Blackman, L. D.; Wright, D. B.; Gibson Ab, M. I.; O'Reilly, R. K. Dispersity Effects in Polymer Self-Assemblies: A Matter of Hierarchical Control. *Chem. Soc. Rev* **2017**, *46* (14), 4119–4134.

(22) Elsabahy, M.; Wooley, K. L. Design of Polymeric Nanoparticles for Biomedical Delivery Applications. *Chem. Soc. Rev.* **2012**, *41* (7), 2545–2561.

(23) Hinde, E.; Thammasiraphop, K.; Duong, H. T. T.; Yeow, J.; Karagoz, B.; Boyer, C.; Gooding, J. J.; Gaus, K. Pair Correlation Microscopy Reveals the Role of Nanoparticle Shape in Intracellular Transport and Site of Drug Release. *Nat. Nanotechnol.* **2017**, *12* (1), 81–89.

(24) Dasgupta, S.; Auth, T.; Gompper, G. Shape and Orientation Matter for the Cellular Uptake of Nonspherical Particles. *Nano Lett.* **2014**, *14* (2), 687–693.

(25) Zhao, J.; Stenzel, M. H. Entry of Nanoparticles into Cells: The Importance of Nanoparticle Properties. *Polym. Chem.* **2018**, *9* (3), 259–272.

(26) Ngai, J.; Kingston, B. R.; Maiorino, L. The Entry of Nanoparticles into Solid Tumours. *Nat. Mater.* **2020**, *19* (5), 566–575.

(27) Cabral, H.; Miyata, K.; Osada, K.; Kataoka, K. Block Copolymer Micelles in Nanomedicine Applications. *Chem. Rev.* **2018**, *118* (14), 6844–6892.

(28) Kinnear, C.; Moore, T. L.; Rodriguez-Lorenzo, L.; Rothen-Rutishauser, B.; Petri-Fink, A. Form Follows Function: Nanoparticle Shape and Its Implications for Nanomedicine. *Chem. Rev.* **2017**, *117* (17), 11476–11521.

(29) Geng, Y.; Dalhaimer, P.; Cai, S.; Tsai, R.; Tewari, M.; Minko, T.; Discher, D. E. Shape Effects of Filaments versus Spherical Particles in Flow and Drug Delivery. *Nat. Nanotechnol.* **2007**, *2* (4), 249–255.

(30) Zhao, Y.; Wang, Y.; Ran, F.; Cui, Y.; Liu, C.; Zhao, Q.; Gao, Y.; Wang, D.; Wang, S. A Comparison between Sphere and Rod Nanoparticles Regarding Their in Vivo Biological Behavior and Pharmacokinetics. *Sci. Rep.* **2017**, *7* (1), 1–11.

(31) Black, K. C. L.; Wang, Y.; Luehmann, H. P.; Cai, X.; Xing, W.; Pang, B.; Zhao, Y.; Cutler, C. S.; Wang, L. V.; Liu, Y.; Xia, Y. Radioactive 198Au-Doped Nanostructures with Different Shapes for in Vivo Analyses of Their Biodistribution, Tumor Uptake, and Intratumoral Distribution. *ACS Nano* **2014**, *8* (5), 4385–4394.

(32) Yu, Q.; Roberts, M. G.; Houdaihed, L.; Liu, Y.; Ho, K.; Walker, G.; Allen, C.; Reilly, R. M.; Manners, I.; Winnik, M. A. Investigating the Influence of Block Copolymer Micelle Length on Cellular Uptake and Penetration in a Multicellular Tumor Spheroid Model. *Nanoscale* **2021**, *13* (1), 280–291.

(33) Barua, S.; Yoo, J. W.; Kolhar, P.; Wakankar, A.; Gokarn, Y. R.; Mitragotri, S. Particle Shape Enhances Specificity of Antibody-Displaying Nanoparticles. *Proc. Natl. Acad. Sci. U. S. A.* **2013**, *110* (9), 3270–3275.

(34) Champion, J. A.; Mitragotri, S. Shape Induced Inhibition of Phagocytosis of Polymer Particles. *Pharm. Res.* **2009**, *26* (1), 244–249.

(35) Li, Z.; Sun, L.; Zhang, Y.; Dove, A. P.; O'Reilly, R. K.; Chen, G. Shape Effect of Glyco-Nanoparticles on Macrophage Cellular Uptake and Immune Response. *ACS Macro Lett.* **2016**, *5* (9), 1059–1064.

(36) Tritschler, U.; Pearce, S.; Gwyther, J.; Whittell, G. R.; Manners, I. 50th Anniversary Perspective: Functional Nanoparticles from the Solution Self-Assembly of Block Copolymers. *Macromolecules.* **2017**, *50* (9), 3439–3463.

(37) Pearce, A. K.; Wilks, T. R.; Arno, M. C.; O'Reilly, R. K. Synthesis and Applications of Anisotropic Nanoparticles with Precisely Defined Dimensions. *Nat. Rev. Chem.* **2020**, *5* (1), 21–45.

(38) Ridolfo, R.; Arends, J. J.; M van Hest, J. C.; Williams, D. S. Wormlike Nanovector with Enhanced Drug Loading Using Blends of Biodegradable Block Copolymers. *Biomacromolecules* **2020**, *21* (6), 2199–2207.

(39) Wan, X.; Min, Y.; Bludau, H.; Keith, A.; Sheiko, S. S.; Jordan, R.; Wang, A. Z.; Sokolsky-Papkov, M.; Kabanov, A. V. Drug Combination Synergy in Worm-like Polymeric Micelles Improves Treatment Outcome for Small Cell and Non-Small Cell Lung Cancer. *ACS Nano* **2018**, *12* (3), 2426–2439.

(40) Wang, X.; Guerin, G.; Wang, H.; Wang, Y.; Manners, I.; Winnik, M. A. Cylindrical Block Copolymer Micelles and Co-Micelles of Controlled Length and Architecture. *Science* **2007**, *317* (5838), 644–647.

(41) Gilroy, J. B.; Gädt, T.; Whittell, G. R.; Chabanne, L.; Mitchels, J. M.; Richardson, R. M.; Winnik, M. A.; Manners, I. Monodisperse Cylindrical Micelles by Crystallization-Driven Living Self-Assembly. *Nat. Chem.* **2010**, *2* (7), 566–570.

(42) Arno, M. C.; Inam, M.; Coe, Z.; Cambridge, G.; Macdougall, L. J.; Keogh, R.; Dove, A. P.; O'Reilly, R. K. Precision Epitaxy for Aqueous 1D and 2D Poly(ϵ -Caprolactone) Assemblies. *J. Am. Chem. Soc.* **2017**, *139* (46), 16980–16985.

(43) Shin, S.; Menk, F.; Kim, Y.; Lim, J.; Char, K.; Zentel, R.; Choi, T. Living Light-Induced Crystallization-Driven Self-Assembly for Rapid Preparation of Semiconducting Nanofibers. *J. Am. Chem. Soc.* **2018**, *140* (19), 6088–6094.

(44) Schmelz, J.; Schedl, A. E.; Steinlein, C.; Manners, I.; Schmalz, H. Length Control and Block-Type Architectures in Worm-like Micelles with Polyethylene Cores. *J. Am. Chem. Soc.* **2012**, *134* (34), 14217–14225.

(45) Ganda, S.; Stenzel, M. H. Concepts, Fabrication Methods and Applications of Living Crystallization-Driven Self-Assembly of Block Copolymers. *Prog. Polym. Sci.* **2020**, *101* (101195), 1–33.

(46) Nazemi, A.; Boott, C. E.; Lunn, D. J.; Gwyther, J.; Hayward, D. W.; Richardson, R. M.; Winnik, M. A.; Manners, I. Monodisperse Cylindrical Micelles and Block

Comicelles of Controlled Length in Aqueous Media. *J. Am. Chem. Soc.* **2016**, *138* (13), 4484–4493.

(47) Street, S. T. G.; He, Y.; Jin, X.-H.; Hodgson, L.; Verkade, P.; Manners, I. Cellular Uptake and Targeting of Low Dispersity, Dual Emissive, Segmented Block Copolymer Nanofibers. *Chem. Sci.* **2020**, *11* (32), 8394–8408.

(48) Arno, M. C.; Inam, M.; Weems, A. C.; Li, Z.; Binch, A. L. A.; Platt, C. I.; Richardson, S. M.; Hoyland, J. A.; Dove, A. P.; O'Reilly, R. K. Exploiting the Role of Nanoparticle Shape in Enhancing Hydrogel Adhesive and Mechanical Properties. *Nat. Commun.* **2020**, *11* (1), 1–9.

(49) Li, Z.; Zhang, Y.; Wu, L.; Yu, W.; Wilks, T. R.; Dove, A. P.; Ding, H. M.; O'Reilly, R. K.; Chen, G.; Jiang, M. Glyco-Platelets with Controlled Morphologies via Crystallization-Driven Self-Assembly and Their Shape-Dependent Interplay with Macrophages. *ACS Macro Lett.* **2019**, *8* (5), 596–602.

(50) Bains, A.; Cao, Y.; Moffitt, M. G. Multiscale Control of Hierarchical Structure in Crystalline Block Copolymer Nanoparticles Using Microfluidics. *Macromol. Rapid Commun.* **2015**, *36* (22), 2000–2005.

(51) Bains, A.; Wulff, J. E.; Moffitt, M. G. Microfluidic Synthesis of Dye-Loaded Polycaprolactone-Block-Poly(Ethylene Oxide) Nanoparticles: Insights into Flow-Directed Loading and in Vitro Release for Drug Delivery. *J. Colloid Interface Sci.* **2016**, *475* (1), 136–148.

(52) Gou, J.; Feng, S.; Xu, H.; Fang, G.; Chao, Y.; Zhang, Y.; Xu, H.; Tang, X. Decreased Core Crystallinity Facilitated Drug Loading in Polymeric Micelles without Affecting Their Biological Performances. *Biomacromolecules* **2015**, *16* (9), 2920–2929.

(53) He, Y.; Eloi, J. C.; Harniman, R. L.; Richardson, R. M.; Whittell, G. R.; Mathers, R. T.; Dove, A. P.; O'Reilly, R. K.; Manners, I. Uniform Biodegradable Fiber-Like Micelles and Block Comicelles via "Living" Crystallization-Driven Self-Assembly of Poly(l -Lactide) Block Copolymers: The Importance of Reducing Unimer Self-

Nucleation via Hydrogen Bond Disruption. *J. Am. Chem. Soc.* **2019**, *141* (48), 19088–19098.

(54) Finnegan, J.; Pilkington, E.; Alt, K.; Rahim, M. A.; Kent, S. J.; Davis, T. P.; Kempe, K. Stealth Nanorods via the Aqueous Living Crystallisation-Driven Self-Assembly of Poly(2-Oxazoline)S. *Chem. Sci.* **2021**, *12* (21), 7350–7360.

(55) Finnegan, J. R.; He, X.; Street, S. T. G.; Garcia-Hernandez, J. D.; Hayward, D. W.; Harniman, R. L.; Richardson, R. M.; Whittell, G. R.; Manners, I. Extending the Scope of "Living" Crystallization-Driven Self-Assembly: Well-Defined 1D Micelles and Block Comicelles from Crystallizable Polycarbonate Block Copolymers. *J. Am. Chem. Soc.* **2018**, *140* (49), 17127–17140.

(56) Richert, C.; Krupp, F. Encapsulating Organic Crystals (EnOCs). *Synlett* **2017**, *28* (14), 1763–1766.

(57) Mastalerz, M.; Oppel, I. M. Rational Construction of an Extrinsic Porous Molecular Crystal with an Extraordinary High Specific Surface Area. *Angew. Chemie - Int. Ed.* **2012**, *51* (21), 5252–5255.

(58) He, X.; Finnegan, J. R.; Hayward, D. W.; Macfarlane, L. R.; Harniman, R. L.; Manners, I. Living Crystallization-Driven Self-Assembly of Polymeric Amphiphiles: Low-Dispersity Fiber-like Micelles from Crystallizable Phosphonium-Capped Polycarbonate Homopolymers. *Macromolecules* **2020**, *53* (23), 10591–10600.

(59) Chung, J. E.; Yokoyama, M.; Okano, T. Inner Core Segment Design for Drug Delivery Control of Thermo-Responsive Polymeric Micelles. *J. Control. Release* **2000**, *65* (1), 93–103.

(60) Dwyer, A. B.; Chambon, P.; Town, A.; He, T.; Owen, A.; Rannard, S. P. Is Methanol Really a Bad Solvent for Poly(n-Butyl Methacrylate)? Low Dispersity and High Molecular Weight Polymers of n-Butyl Methacrylate Synthesised via ATRP in Anhydrous Methanol. *Polym. Chem.* **2014**, *5* (11), 3608–3616.

(61) Akimoto, J.; Nakayama, M.; Sakai, K.; Okano, T. Temperature-Induced Intracellular Uptake of Thermoresponsive Polymeric Micelles. *Biomacromolecules* **2009**, *10* (6), 1331–1336.

(62) Ke, X.; Ng, V. W. L.; Ono, R. J.; Chan, J. M. W.; Krishnamurthy, S.; Wang, Y.; Hedrick, J. L.; Yang, Y. Y. Role of Non-Covalent and Covalent Interactions in Cargo Loading Capacity and Stability of Polymeric Micelles. *J. Control. Release* **2014**, *193*, 9–26.

(63) Cao, L.; Manners, I.; Winnik, M. A. Influence of the Interplay of Crystallization and Chain Stretching on Micellar Morphologies: Solution Self-Assembly of Coil−Crystalline Poly(Isoprene- Block -Ferrocenylsilane). *Macromolecules* **2002**, *35* (22), 8258–8260.

(64) Hudson, Z. M.; Boott, C. E.; Robinson, M. E.; Rupar, P. A.; Winnik, M. A.; Manners, I. Tailored Hierarchical Micelle Architectures Using Living Crystallization-Driven Self-Assembly in Two Dimensions. *Nat. Chem.* **2014**, *6* (10), 893–898.

(65) Boott, C. E.; Leitao, E. M.; Hayward, D. W.; Laine, R. F.; Mahou, P.; Guerin, G.; Winnik, M. A.; Richardson, R. M.; Kaminski, C. F.; Whittell, G. R.; Manners, I. Probing the Growth Kinetics for the Formation of Uniform 1D Block Copolymer Nanoparticles by Living Crystallization-Driven Self-Assembly. *ACS Nano* **2018**, *12* (9), 8920–8933.

(66) Swift, T.; Hoskins, R.; Telford, R.; Plenderleith, R.; Pownall, D.; Rimmer, S. Analysis Using Size Exclusion Chromatography of Poly(N-Isopropyl Acrylamide) Using Methanol as an Eluent. *J. Chromatogr. A* **2017**, *1508*, 16–23.

(67) Ganachaud, F.; Monteiro, M. J.; Gilbert, R. G.; Dourges, M.-A.; Thang, S. H.; Rizzardo, E. Molecular Weight Characterization of Poly(N-Isopropylacrylamide) Prepared by Living Free-Radical Polymerization. *Macromolecules* **2000**, *33* (18), 6738–6745.

(68) Sander, U.; Wolf, B. A. Solubility of Poly(N-alkylmethacrylate)s in Hydrocarbons and in Alcohols. *Angew. Makromol. Chemie* **1986**, *139* (1), 149–156.

(69) Shen, L.; Wang, H.; Guerin, G.; Wu, C.; Manners, I.; Winnik, M. A. A Micellar Sphere-to-Cylinder Transition of Poly(Ferrocenyldimethylsilane-b-2-Vinylpyridine) in a Selective Solvent Driven by Crystallization. *Macromolecules* **2008**, *41* (12), 4380–4389.

(70) Hsiao, M. S.; Yusoff, S. F. M.; Winnik, M. A.; Manners, I. Crystallization-Driven Self-Assembly of Block Copolymers with a Short Crystallizable Core-Forming Segment: Controlling Micelle Morphology through the Influence of Molar Mass and Solvent Selectivity. *Macromolecules* **2014**, *47* (7), 2361–2372.

(71) Zhou, H.; Lu, Y.; Zhang, M.; Guerin, G.; Manners, I.; Winnik, M. A. PFS-b-PNIPAM: A First Step toward Polymeric Nanofibrillar Hydrogels Based on Uniform Fiber-Like Micelles. *Macromolecules* **2016**, *49* (11), 4265–4276.

(72) Fan, B.; Xue, J. Q.; Guo, X. S.; Cao, X. H.; Wang, R. Y.; Xu, J. T.; Du, B. Y.; Fan, Z. Q. Regulated Fragmentation of Crystalline Micelles of Block Copolymer via Monoamine-Induced Corona Swelling. *Macromolecules* **2018**, *51* (19), 7637–7648.

(73) Yang, J. X.; Fan, B.; Li, J. H.; Xu, J. T.; Du, B. Y.; Fan, Z. Q. Hydrogen-Bonding-Mediated Fragmentation and Reversible Self-Assembly of Crystalline Micelles of Block Copolymer. *Macromolecules* **2016**, *49* (1), 367–372.

(74) Stuart, M. C. A.; Van De Pas, J. C.; Engberts, J. B. F. N. The Use of Nile Red to Monitor the Aggregation Behavior in Ternary Surfactant-Water-Organic Solvent Systems. *J. Phys. Org. Chem.* **2005**, *18* (9), 929–934.

(75) Swain, J.; Mishra, A. K. Nile Red Fluorescence for Quantitative Monitoring of Micropolarity and Microviscosity of Pluronic F127 in Aqueous Media. *Photochem. Photobiol. Sci.* **2016**, *15* (11), 1400–1407.

(76) Drori, R.; Li, C.; Hu, C.; Raiteri, P.; Rohl, A. L.; Ward, M. D.; Kahr, B. A Supramolecular Ice Growth Inhibitor. *J. Am. Chem. Soc.* **2016**, *138* (40), 13396–13401.

(77) Samsonova, L. G.; Selivanov, N. I.; Kopylova, T. N. Spectral Properties of Nile Red in Solutions and Thin Films. *Opt. Spectrosc.* **2014**, *116* (1), 72–76.

(78) Mendenhall, G. D. Luminescence from Nile Red in Poly(n-Butyl Methacrylate). In *Polymer durability : degradation, stabilization, and lifetime prediction*; Clough, R. L., Billingham, N. C., Gillen, K. T., Eds.; American Chemical Society: Washington, DC., 1996; Vol. 249, pp 213–221.

(79) Aspelmeier, T.; Egner, A.; Munk, A. Modern Statistical Challenges in High-Resolution Fluorescence Microscopy. *Annu. Rev. Stat. Its Appl.* **2015**, *2* (1), 163–202.

(80) Chung, J. E.; Yokoyama, M.; Yamato, M.; Aoyagi, T.; Sakurai, Y.; Okano, T. Thermo-Responsive Drug Delivery from Polymeric Micelles Constructed Using Block Copolymers of Poly(N-Isopropylacrylamide) and Poly(Butylmethacrylate). *J. Control. Release* **1999**, *62* (1–2), 115–127.

(81) Robin, M. P.; O'Reilly, R. K. Strategies for Preparing Fluorescently Labelled Polymer Nanoparticles. *Polym. Int.* **2015**, *64* (2), 174–182.

(82) Patra, J. K.; Das, G.; Fraceto, L. F.; Campos, E. V. R.; Rodriguez-Torres, M. D. P.; Acosta-Torres, L. S.; Diaz-Torres, L. A.; Grillo, R.; Swamy, M. K.; Sharma, S.; Habtemariam, S.; Shin, H. S. Nano Based Drug Delivery Systems: Recent Developments and Future Prospects. *J. Nanobiotechnology* **2018**, *16* (71), 1–33.

(83) Li, X.; Jin, B.; Gao, Y.; Hayward, D. W.; Winnik, M. A.; Luo, Y.; Manners, I. Monodisperse Cylindrical Micelles of Controlled Length with a Liquid-Crystalline Perfluorinated Core by 1D "Self-Seeding." *Angew. Chemie - Int. Ed.* **2016**, *55* (38), 11392–11396.

(84) Tao, D.; Wang, Z.; Huang, X.; Tian, M.; Lu, G.; Manners, I.; Winnik, M. A.; Feng, C. Continuous and Segmented Semiconducting Fiber-like Nanostructures with Spatially Selective Functionalization by Living Crystallization-Driven Self-Assembly. *Angew. Chemie - Int. Ed.* **2020**, *59* (21), 2–10.

(85) Schöbel, J.; Karg, M.; Rosenbach, D.; Krauss, G.; Greiner, A.; Schmalz, H. Patchy Wormlike Micelles with Tailored Functionality by Crystallization-Driven Self-Assembly: A Versatile Platform for Mesostructured Hybrid Materials. *Macromolecules* **2016**, *49* (7), 2761–2771.

(86) Pinto Reis, C.; Neufeld, R. J.; Ribeiro, A. J.; Veiga, F. Nanoencapsulation I. Methods for Preparation of Drug-Loaded Polymeric Nanoparticles. *Nanomedicine Nanotechnology, Biol. Med.* **2006**, *2* (1), 8–21.

(87) Pathak, C.; Vaidya, F. U.; Pandey, S. M. Mechanism for Development of Nanobased Drug Delivery System. In *Applications of Targeted Nano Drugs and Delivery Systems: Nanoscience and Nanotechnology in Drug Delivery*; Mohapatra, S. S., Ranjan, S., Dasgupta, N., Kumar Mishra, R., Thomas, S., Eds.; Elsevier: Online, 2019; pp 35–67.

(88) Ridolfo, R.; Ede, B. C.; Diamanti, P.; White, P. B.; Perriman, A. W.; van Hest, J. C. M.; Blair, A.; Williams, D. S. Biodegradable, Drug-Loaded Nanovectors via Direct Hydration as a New Platform for Cancer Therapeutics. *Small* **2018**, *14* (32), 1703774–1703784.

(89) Kumar, R.; Dalvi, S. V.; Siril, P. F. Nanoparticle-Based Drugs and Formulations: Current Status and Emerging Applications. *ACS Appl. Nano Mater.* **2020**, *3* (6), 4944–4961.

(90) Cao, C.; Chen, F.; Garvey, C. J.; Stenzel, M. H. Drug-Directed Morphology Changes in Polymerization-Induced Self-Assembly (PISA) Influence the Biological Behavior of Nanoparticles. *ACS Appl. Mater. Interfaces* **2020**, *12* (27), 30221–30233.

(91) Cao, C.; Zhao, J.; Lu, M.; Garvey, C. J.; Stenzel, M. H. Correlation between Drug Loading Content and Biological Activity: The Complexity Demonstrated in Paclitaxel-Loaded Glycopolymer Micelle System. *Biomacromolecules* **2019**, *20* (4), 1545–1554.

(92) Siddiqui, M.; Rajkumar, S. V. The High Cost of Cancer Drugs and What We Can Do About It. *JMCP* **2012**, *87* (10), 935–943.

(93) Pangborn, A. B.; Giardello, M. A.; Grubbs, R. H.; Rosen, R. K.; Timmers, F. J. Safe and Convenient Procedure for Solvent Purification. *Organometallics* **1996**, *15* (5), 1518–1520.

(94) Dougherty, R. P. Extensions of DAMAS and Benefits and Limitations of Deconvolution in Beamforming. In *Collection of Technical Papers - 11th AIAA/CEAS Aeroacoustics Conference*; 2005.

(95) Pettersen, E. F.; Goddard, T. D.; Huang, C. C.; Couch, G. S.; Greenblatt, D. M.; Meng, E. C.; Ferrin, T. E. UCSF Chimera - A Visualization System for Exploratory Research and Analysis. *J. Comput. Chem.* **2004**, *25* (13), 1605–1612.

(96) Stetsyshyn, Y.; Raczkowska, J.; Lishchynskyi, O.; Awsiuk, K.; Zemla, J.; Dąbczyński, P.; Kostruba, A.; Harhay, K.; Ohar, H.; Orzechowska, B.; Panchenko, Y.; Vankevych, P.; Budkowski, A. Glass Transition in Temperature-Responsive Poly(Butyl Methacrylate) Grafted Polymer Brushes. Impact of Thickness and Temperature on Wetting, Morphology, and Cell Growth. *J. Mater. Chem. B* **2018**, *6* (11), 1621.

(97) Milton Harris, J.; Chess, R. B. Effect of Pegylation on Pharmaceuticals. *Nat. Rev. Drug Discov.* **2003**, *2* (3), 214–221.

Chapter 3

Hydrophobic Cargo Loading at the Core-Corona Interface of Uniform, Length-Tunable Aqueous Diblock Copolymer Nanofibers with a Crystalline Core

This chapter contains unpublished results

Contributions:

Synthesis of polymers, characterization, and self-assembly were conducted by Juan Diego Garcia Hernandez. Loading of nanofibers were conducted in collaboration with Hayley Parkin. Initial scientific design of the experiments was conducted by Juan Diego Garcia Hernandez. Research was conducted at the University of Victoria.

3.1 Abstract

1D core-shell nanoparticles are considered to be among the most promising for biomedical applications such as drug delivery. The versatile living crystallization-driven self-assembly (CDSA) seeded growth method allows access to uniform, length-tunable, and water-dispersible nanofibers from block copolymer (BCP) amphiphiles. A possible hinderance to their use for drug delivery is that encapsulation of cargo within the crystalline core is expected to be difficult. Herein, we demonstrate that non-covalent hydrophobic cargo uptake by diBCP nanofibers with a crystalline poly(fluorenetrimethylenecarbonate) (PFTMC) core and a corona of either poly(*N*-isopropylacrylamide, PNIPAM) or poly(ethylene glycol, PEG) can be achieved at the core-corona interface. The length of the nanofibers was precisely controlled over a wide range of lengths (ca. 50 – 1700 nm, $Đ <$ 1.07), however we focused on low dispersity nanofibers with lengths relevant for drug delivery (100 – 130 nm, $Đ <$ 1.06) for cargo loading experiments. After loading via a solvent switch to water, the nanofibers remained colloidally stable for at least 6 months, and for up to 48 h under enzymatic conditions as observed by the absence of aggregation by TEM and DLS analysis. Our findings indicate that uptake of the hydrophobic fluorescent dye Nile Red (NR), used as a proxy for a therapeutic cargo, is independent of the nature and length of the corona-forming blocks of the nanofibers. Localization of the cargo at the core-corona interface was evidenced by fluorescence spectroscopy.

3.2 Introduction

Advances in the block copolymer (BCP) solution self-assembly field have enabled access to a wide variety of colloidally stable micellar nanostructures with different shapes.[1,2] Such polymer-based nanoparticles have been employed for various applications, with drug-delivery as one of the most promising.[3] Micellar nanoparticles can generally increase the solubility and biodistribution of drug molecules, and decrease non-specific tissue damage, degradation, and side effects.[4,5] The efficacy of a nanoparticle-based therapeutic relies on important characteristics such as their size,[6] shape,[7] and dispersity ($Đ$).[8,9] It is therefore highly desirable to be able to control the morphology and dimensions of micellar nanoparticles that are intended for clinical use and require approval by regulating bodies.[10]

1D core-shell micellar nanoparticles such as nanofibers, cylinders, or worms have often demonstrated significant advantages over conventional spherical nanoparticles for drug delivery,[11] by displaying improved circulation times,[12] tumor penetration,[13,14] and specificity[15] together with lower rates of phagocytosis[16,17] and renal clearance.[18] However, until recently, access to morphologically pure samples of nanofibers that are colloidally stable in aqueous media and possess controlled dimensions and low dispersity was a considerable challenge, and represented a major hurdle for the development of nanofiber-based therapeutics.[1,19,20]

Recently, crystallization-driven self-assembly (CDSA) of amphiphilic BCPs has enabled access to morphologically pure nanofibers with a crystalline core-forming block.[1,21–24] Living CDSA, a seeded growth method, has enabled dimensional control of nanofibers across length scales from ca. 20 nm to > 5 μm, with accompanying low length

dispersities (< 1.1).[1,25–27] Performing the living CDSA in sequence with a range of suitable BCPs, micellar nanoparticles with not only controlled dimensions but also segmented core or corona chemistries have been prepared,[25,26,28–30] yielding nanoparticles with spatially-defined functional groups for targeting,[31] and tracking.[14,31,32] Significantly, several crystallizable BCPs are currently known to undergo living CDSA and are suitable for drug delivery or biomedical applications owing to their biodegradability and limited toxicity.[29,33–37]

Drug-loaded micellar nanoparticles are generally prepared from amorphous BCPs under conditions where cargo encapsulation and nanoparticle formation proceed concurrently. A disadvantage of this method is that the resulting properties of the drug-loaded nanoparticles, such as their size and shape, are directly related to the cargo and the self-assembly process, minimizing the control over the nanoparticle characteristics. In nanoparticles prepared from BCPs with a crystallizable block, the encapsulation of exogenous cargo molecules can decrease the core crystallinity and stability of the resulting nanoparticles.[38–41]

To date, cargo loading of preformed nanofibers with a crystalline core prepared via CDSA or living CDSA can be performed using two main strategies. First, in a method described by Stenzel and coworkers, covalent tethering of drug molecules to the hydrophilic corona-forming block of the nanofibers was acheieved.[32] Second, in an alternative method reported by ourselves,[42] non-covalent encapsulation of cargo was achieved in an outer amorphous core region surrounding an inner crystalline core of triblock copolymer (triBCP) nanofibers with a coaxial-core and a hydrophilic corona prepared via living CDSA.[42] In this case the encapsulation of fluorescent cargo (Nile Red,

NR) was conducted via the preformed-nanoparticle solvent-switch loading (PNSL) method. The PNSL procedure yields loaded nanofibers with lengths relevant for drug delivery (ca. 100 nm) with virtually no fragmentation owing to the controlled solvent-switch transfer to water via a syringe-pump (flow rate = 100 μL/min) and removal of unbound cargo by syringe filtration. The presence of hydrophobic cargo in the outer amorphous poly(butyl methacrylate) (PBMA) core surrounding a crystalline poly(fluorenetrimethylenecarbonate) PFTMC was evidenced using fluorescence spectroscopy and microscopy.[42]

As part of our recent aforementioned study of triBCP nanofibers with a coaxial-core comprising an inner crystalline PFTMC domain, an outer amorphous PBMA region, and a hydrophilic poly(*N*-isopropylacrylamide) (PNIPAM) corona, we performed preliminary comparative studies of hydrophobic cargo uptake by PFTMC-*b*-PEG diBCP nanofibers with only a crystalline PFTMC core. Surprisingly, fluorescence spectroscopy measurements indicated that cargo uptake also occurred in this case and suggested NR localization at the core-corona interface.[42] This indicated a potential third method for cargo uptake by nanofibers with a crystalline core formed by living CDSA. In order to explore this approach in more depth, here we report a detailed study of hydrophobic cargo (NR) uptake at the core-corona interface by a variety of low length dispersity diBCP nanofibers with a crystalline PFTMC core and either PNIPAM or PEG as hydrophilic corona forming-blocks formed via living CDSA.

3.3 Results and Discussion

3.3.1 Design of DiBCP Nanofibers for Uptake of Hydrophobic Cargo

To perform cargo loading via the PNSL method, both the diBCP nanofibers and the hydrophobic cargo need to be soluble in the same organic solvent. Upon transfer to aqueous media the solubility of the hydrophobic cargo will decrease, thereby facilitating its uptake at the core-corona interface of the diBCP nanofibers (Figure 3. 1A). To meet these solubility requirements and to provide colloidal stability in both organic solvent mixtures and aqueous media, the diBCP nanofibers were designed to possess either a PNIPAM or PEG corona-forming block. The PNIPAM and PEG corona-forming blocks were chosen to assess if the nature of the corona block influences the cargo loading process. In addition, the length of the PEG-containing diBCP nanofibers was varied by using different degree of polymerization (DP_n) values (i.e., PEG_{275} and PEG_{530}) to assess the influence on the loading efficiency. The selected DP of each block in the resulting PFTMC-*b*-PNIPAM and PFTMC-*b*-PEG nanofibers were based on previous reports that indicate that core:corona ratios of ca. 1:5 to 1:20 generally favor nanofiber formation by CDSA.[1,43,44] To facilitate comparisons, the DP_n of the PFTMC core-forming block was kept constant at 18 – 19 repeating units. Thus, the three diBCP nanofiber systems used for this work were as follows: $PFTMC_{18}$-*b*-$PNIPAM_{425}$, $PFTMC_{19}$-*b*-PEG_{275}, and $PFTMC_{18}$-*b*-PEG_{530}, (Figure 3. 1B).

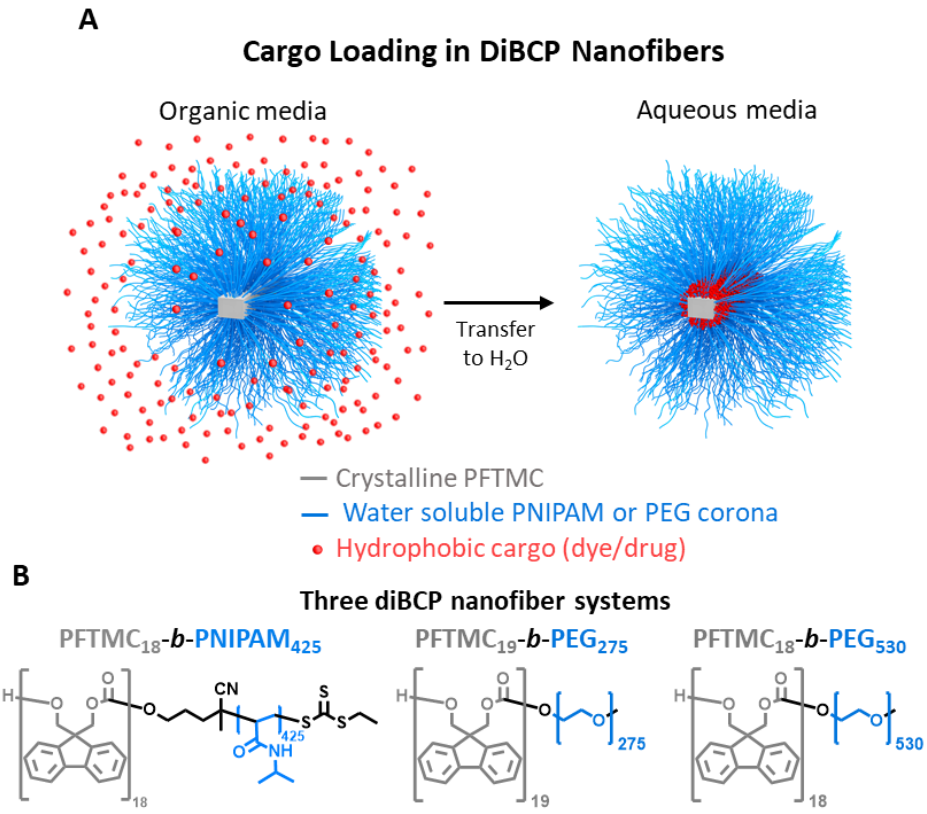

Figure 3. 1. Strategy for the loading of hydrophobic cargo in diBCP nanofibers with a crystalline-PFTMC core at the core-corona interface prepared from PFTMC-*b*-PNIPAM, and PFTMC-*b*-PEG diBCPs. A) Process for the loading of hydrophobic cargo (red dots) at the interface if the crystalline core (gray) with the corona (blue) of the preformed nanofibers upon transfer to H_2O, with the description of each component of the system. B) Structure of color-coded $PFTMC_{18}$-*b*-$PNIPAM_{425}$, $PFTMC_{19}$-*b*-PEG_{275}, and $PFTMC_{18}$-*b*-PEG_{530} diBCPs used in this work.

3.3.2 Synthesis and Characterization of diBCPs: $PFTMC_{18}$-*b*-$PNIPAM_{425}$, $PFTMC_{19}$-*b*-PEG_{275}, and $PFTMC_{18}$-*b*-PEG_{530}

The $PFTMC_{18}$-*b*-$PNIPAM_{425}$ diBCP was prepared using a combination of ring-opening polymerization (ROP) and reversible addition-fragmentation chain-transfer (RAFT) polymerization, following our previously reported procedure.[42] The $PFTMC_{18}$ homopolymer functionalized with the RAFT-CTA was prepared via ROP of the cyclic carbonate spiro[fluorene-9,5′-[1,3]-dioxan]-2′-one (FTMC) monomer using 2-cyano-5-hydroxypentan-2-yl ethyl carbonotrithioate as a small molecule initiator to yield $PFTMC_{18}$-CTA. The $PFTMC_{18}$-CTA homopolymer was characterized using matrix-

assisted laser desorption/ionization-time of flight (MALDI-TOF) mass spectrometry (4,729 m/z, DP_n = 18, Figure S3. 1), ^{1}H NMR spectroscopy (Figure S3. 2), and gel permeation chromatography (GPC, M_n = 4,800, $Đ_M$ = 1.17, polystyrene standards, Figure S3. 3). RAFT polymerization of the PFTMC$_{18}$-CTA with *N*-isopropylacrylamide in dioxane yielded the targeted PFTMC$_{18}$-*b*-PNIPAM$_n$ diBCP. The DP_n value of the PNIPAM block was determined by comparing the relative ^{1}H NMR integration of the PFTMC$_{18}$ block at 4.50 – 4.27 ppm (Figure S3. 2) to the resonance of the PNIPAM block at 4.06 – 3.58 ppm, and corresponded to PFTMC$_{18}$-*b*-PNIPAM$_{425}$ (Figure S3. 4). Tailing towards low molar mass fractions was detected via GPC analysis of the PFTMC$_{18}$-*b*-PNIPAM$_{425}$ diBCP (M_n = 31,800, $Đ_M$ = 1.76, Figure S3. 3). The tailing results from the interaction between the amino-groups present in the PNIPAM block with the GPC column, resulting in an overestimation of the reported dispersity values.[45] Such issues have been observed for the analysis of PNIPAM-containing materials.[46]

The PFTMC-*b*-PEG diBCPs were synthesized via the DBU catalyzed ring-opening polymerization of the FTMC monomer utilizing commercially available PEG methyl ether homopolymers of distinct molecular weights (11 kDa, and 20 kDa) as macroinitiators in dry DCM, following reported procedures.[35,42] The resulting diBCPs were characterized by ^{1}H NMR and GPC, the DP_n values of the diBCPs were obtained via ^{1}H NMR integration of the resonances of the diBCP to the integration of the methyl end-group yielding PFTMC$_{19}$-*b*-PEG$_{275}$ (M_n = 15,200, $Đ_M$ = 1.07 by GPC. Figure S3. 5, 6), and PFTMC$_{18}$-*b*-PEG$_{530}$ (M_n = 26,600, $Đ_M$ = 1.14 by GPC. Figure S3. 7, 8). Polymer characterization data is summarized in Table S3. 1.

3.3.3 Preparation of Low Length Dispersity Nanofibers with Controlled Dimensions

Although the crystallization-driven fiber-growth of PFTMC-*b*-PNIPAM diBCPs was briefly studied in our previous work when it was used for the formation of segmented nanofibers,[42] detailed studies are reported here. In contrast, the living CDSA of PFTMC-*b*-PEG diBCPs has been previously described in depth.[35] Therefore, first, the solution state self-assembly of $PFTMC_{18}$-*b*-$PNIPAM_{425}$ was investigated in detail (Figure 3. 2A). Dynamic light scattering analysis demonstrated that tetrahydrofuran (THF) was a good solvent for both PFTMC and PNIPAM as the diBCP was present in unimeric form in solution (Figure S3. 9). To yield nanofibers of controlled lengths and low dispersities, the formation of length disperse nanofibers via self-nucleation, sonication to yield seeds, and living CDSA (seeded growth) were used in sequence. The self-assembly of $PFTMC_{18}$-*b*-$PNIPAM_{425}$ via spontaneous nucleation to yield nanofibers was attempted in a mixture of THF and methanol (MeOH). MeOH has been used as a selective solvent for PNIPAM and PEG corona-forming blocks of PFTMC-based nanofibers.[35,42] The spontaneous nucleation process involved heating of $PFTMC_{18}$-*b*-$PNIPAM_{425}$ in 15:85 THF:MeOH common:selective solvent ratio (*v/v*) at 70 °C for 3 h, followed by cooling to 20 °C over a period of 2.5 h and ageing for 48 h. Transmission electron microscopy (TEM) analysis revealed a morphologically pure population of long and length-disperse nanofibers (L_n > 2 µm, Figure 3. 2B). Sonication of the solution containing the length disperse nanofibers for 3 h at 0 °C yielded seed nanofibers with an average length L_n = 46 nm ($Đ$ = 1.17, σ = 19 nm) by TEM analysis (Figure 3. 2C).

Nanofibers of controlled length were obtained by adjusting the unimer to seed ratio (m_{unimer}/m_{seed}) of $PFTMC_{18}$-*b*-$PNIPAM_{425}$ unimer (in THF) added to diluted seed nanofiber solutions (THF content: 10 – 20% in MeOH), followed by a 48 h ageing period. By

adjusting the unimer to seed ratio (m_{unimer}/m_{seed}) from 0:1 to 40:1; nanofiber length control was achieved from L_{seed} = 46 nm ($Đ$ = 1.17, σ = 19 nm) to L_n = 1729 nm ($Đ$ = 1.05, σ = 385 nm), as observed via TEM (Figure 3. 2D-G, S3. 10). Low length dispersity PFTMC$_{18}$-*b*-PNIPAM$_{425}$ nanofibers were obtained in each case (Figure 3. 2H, I). Furthermore, a linear trend of the final length of the nanofibers vs m_{unimer}/m_{seed} ratio was obtained. The resulting lengths were consistent with those predicted using the relationship $L_{n(theory)} = (L_{n(seed)} \times {}^{m_{unimer}}/_{m_{seed}}) + L_{n(seed)}$ based on the number of mass equivalents (m_{unimer}/m_{seed}) of unimer added to the seeds ($L_{n(seed)}$ = 46 nm) within experimental error (Figure 3. 2J). The lengths and dispersities of the nanofibers prepared via the seeded growth method remained significatively unchanged after 12 months, when compared to the data collected after 48 h as shown by TEM analysis of the nanofiber samples with 2.5 and 40 equivalents of unimer added. In addition, the values were consistent with complete consumption of added unimer (2.5 eqs, 48 h: L_n = 163 nm, $Đ$ = 1.04, σ = 36 nm, 12 months: L_n = 166 nm, $Đ$ = 1.05, σ = 36 nm, and 40 eqs, 48 h: L_n = 1729 nm $Đ$ = 1.04, σ = 385 nm, 12 months: L_n = 1798 nm $Đ$ = 1.02, σ = 267 nm. Table S3. 2 and Figure S3. 11) . A summary of the contour length analysis of the PFTMC$_{18}$-*b*-PNIPAM$_{425}$ diBCP nanofibers is presented in Table S3. 2. The TEM samples in this work were prepared by casting onto carbon-coated copper grids which were plasma treated to increase the hydrophilicity of the carbon film and negatively stained with a uranyl acetate solution (3 wt % in EtOH). The staining solution interacts favorably with the hydrophilic corona forming-blocks such as PNIPMAM and PEG but not with the hydrophobic PFTMC core block, resulting in a relatively bright nanofiber-core against a dark background when observed via bright field TEM.

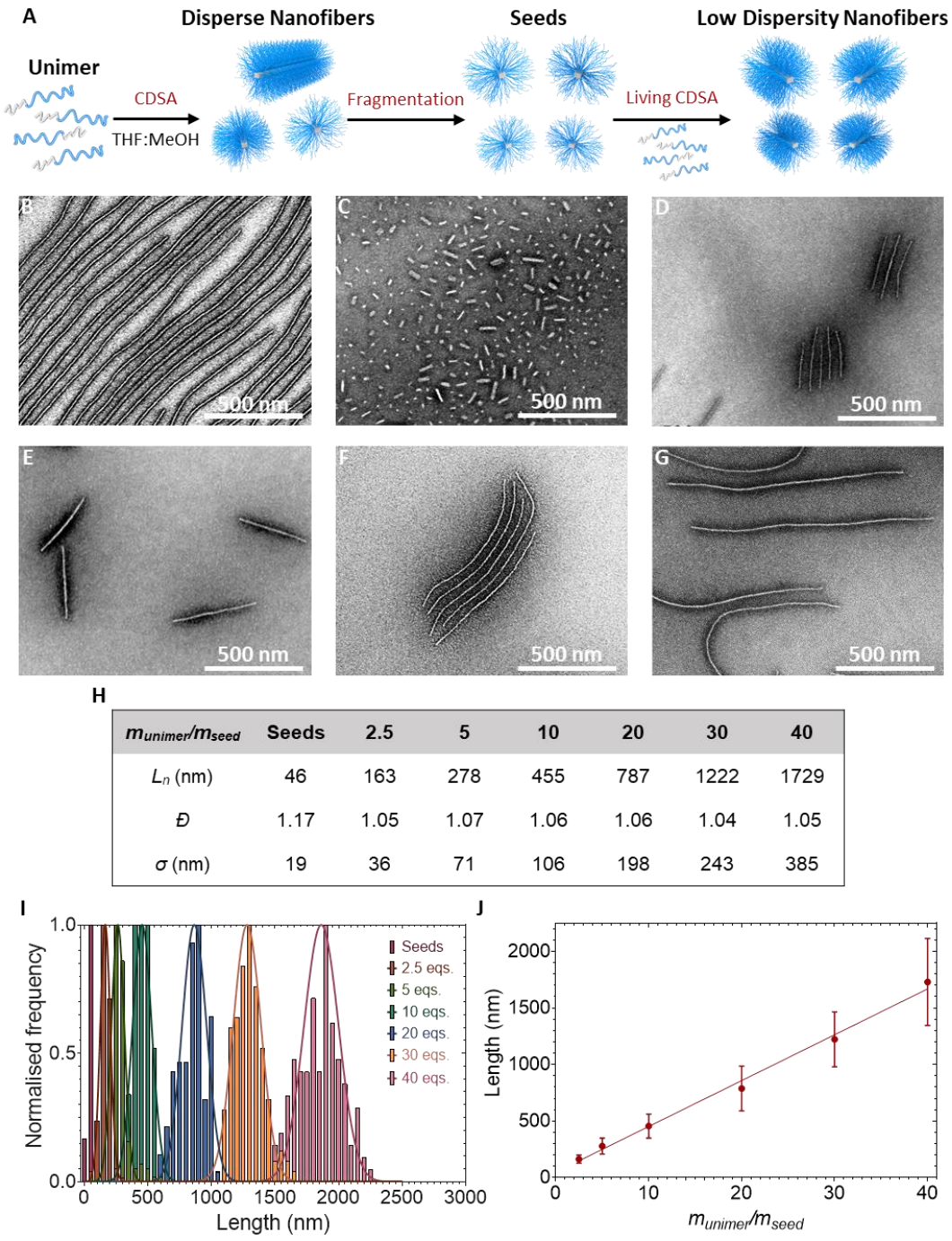

m_{unimer}/m_{seed}	Seeds	2.5	5	10	20	30	40
L_n (nm)	46	163	278	455	787	1222	1729
$Đ$	1.17	1.05	1.07	1.06	1.06	1.04	1.05
σ (nm)	19	36	71	106	198	243	385

Figure 3. 2. Preparation of low dispersity nanofibers of controlled length. A) Schematic representation of the generation of low dispersity $PFTMC_{18}$-*b*-$PNIPAM_{425}$ nanofibers through the living CDSA method. B) TEM micrograph of disperse $PFTMC_{18}$-*b*-$PNIPAM_{425}$ nanofibers (2 mg/mL) prepared in THF:MeOH (15:85 *v/v*), after annealing at 70 °C for 3 h, and ageing for 48 h. C) TEM micrograph of seed nanofibers (46 nm, $Đ$ = 1.17, σ = 19 nm) prepared through sonication of the disperse nanofibers (from B, in THF:MeOH 15:85) for 3h at 0 °C. D-G) TEM images of low dispersity nanofibers prepared through seeded-growth by addition of unimer in THF to nanofiber seed solutions at: D) 5:1 E) 10:1 F) 20:1 and G) 30:1 m_{unimer}/m_{seed} ratios. H) Nanofiber length summary. I) Contour length histograms of seeds and low length dispersity nanofibers of controlled lengths J) Plot of m_{unimer}/m_{seed} against L_n, error bars indicate standard deviation ($n \geq 150$ number of nanofibers). TEM images were stained with uranyl acetate (3 wt % in EtOH).

3.3.4 Cargo Uptake by Low Length Dispersity PFTMC-*b*-PNIPAM, and PFTMC-*b*-PEG DiBCP Nanofibers via the Preformed-Nanoparticle Solvent-Switch Loading (PNSL) Method

We previously found that dialysis was an unsatisfactory method to perform the loading of nanofibers, as this led to inefficient removal of unbound cargo, and a fast rate of solvent exchange (under 10 min) that resulted in nanofiber fragmentation.[42] These issues led to the development of the more efficient PNSL method for cargo encapsulation on coaxial-core triblock copolymer nanofibers.[42] In the current work we used the same PNSL method to achieve cargo uptake of the hydrophobic NR dye as a proxy for a therapeutic cargo by diBCP nanofibers (Figure 3. 3A).

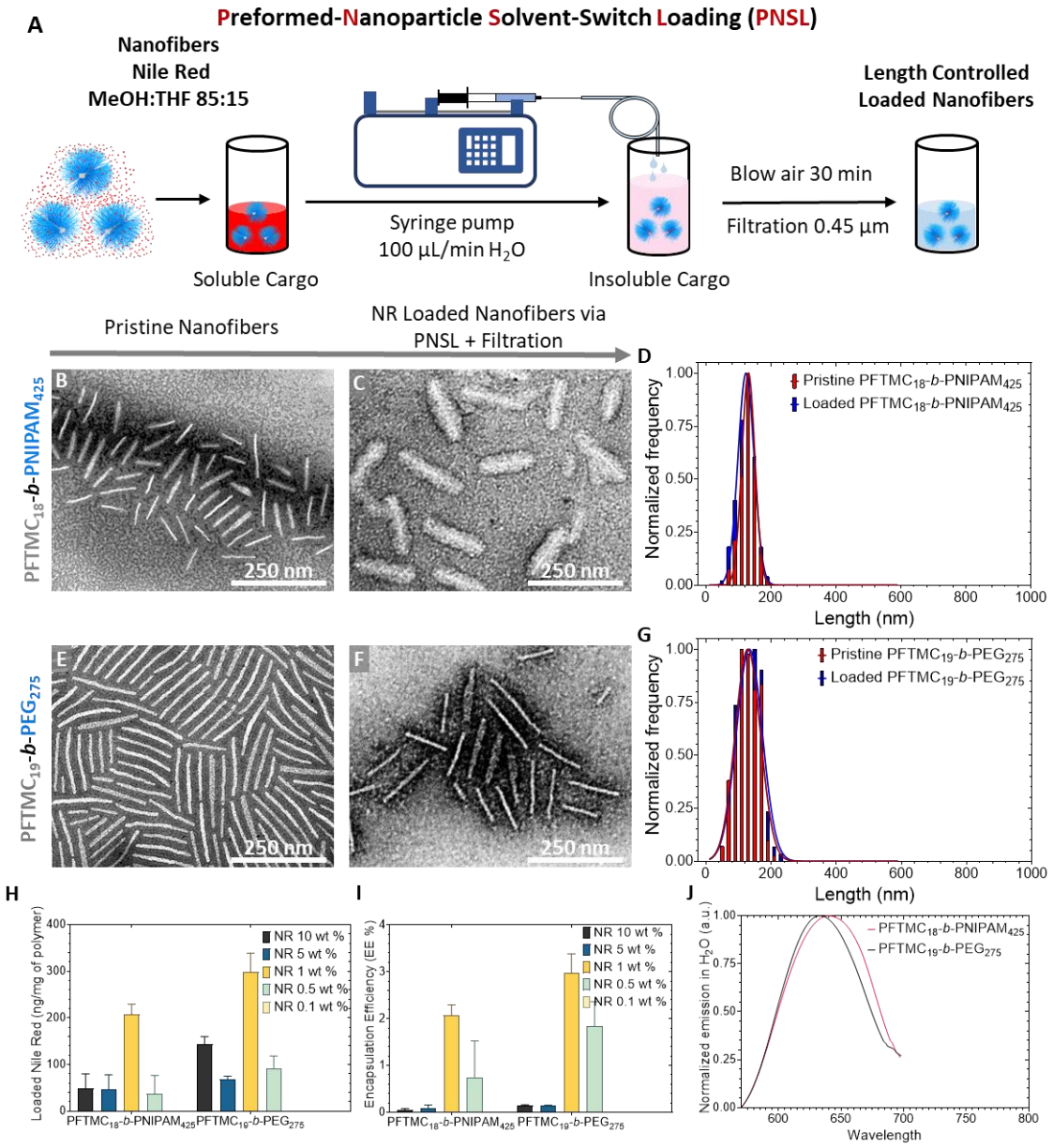

Figure 3. 3. Uptake of model hydrophobic cargo Nile Red (NR) by low dispersity nanofibers of controlled lengths (0.1 mg/mL, 900 µL, in MeOH:THF 85:15) at different NR concentrations (0.1 – 10 wt %, in MeOH). 900 µL of H_2O added at 100 µL/min. A) Schematic process for the uptake of NR onto low dispersity diBCP nanofibers via the PNSL method. TEM micrographs of low dispersity PFTMC$_{18}$-*b*-PNIPAM$_{425}$ diBCP nanofibers; B) before (L_n = 127 nm, $Đ$ = 1.03, σ = 22 nm), and C) after (L_n = 122 nm, $Đ$ = 1.05, σ = 27 nm) NR uptake via the PNSL method and filtration. A possible staining artifact between the PNIPAM-containing nanofibers in water and the uranyl acetate contrast agent may lead to a thicker appearance of the nanofibers in C. D) Contour length histogram of the PFTMC$_{18}$-*b*-PNIPAM$_{425}$ diBCP nanofibers before (B), and after (C) NR uptake and filtration. TEM micrographs of low dispersity PFTMC$_{19}$-*b*-PEG$_{275}$ diBCP nanofibers; E) before (L_n = 127 nm, $Đ$ = 1.06, σ = 32 nm), and F) after (L_n = 133 nm, $Đ$ = 1.06, σ = 32 nm) NR uptake via the PNSL method and filtration. G) Contour length histogram of the PFTMC$_{19}$-*b*-PEG$_{275}$ diBCP nanofibers before (E), and after (F) NR uptake and filtration. H) Quantity of loaded NR (in ng/mg of polymer), and I) Encapsulation Efficiency (EE %) determined by fluorometry of both PFTMC$_{18}$-*b*-PNIPAM$_{425}$, and PFTMC$_{19}$-*b*-PEG$_{275}$ diBCP nanofibers in 'C and F' with respect to the initial NR concentration in solution (wt %). J) Emission spectra of the loaded NR by both PFTMC$_{18}$-*b*-PNIPAM$_{425}$, and PFTMC$_{19}$-*b*-PEG$_{275}$ diBCP nanofibers in water (nanofiber concentration = 0.1 mg/mL).

PFTMC$_{19}$-*b*-PNIPAM$_{425}$ and PFTMC$_{19}$-*b*-PEG$_{275}$ were used to investigate if the chemistry of the corona-forming blocks can influence the cargo uptake process, and PFTMC$_{19}$-*b*-PEG$_{275}$ and PFTMC$_{18}$-*b*-PEG$_{530}$ nanofibers were utilized to assess the effect of the length of the corona (DP_n) in the loading process. Optimization of the loading process was conducted by tuning the concentration of NR in solution (0.1 – 10 wt %) prior to the PNSL process. Nanoparticle sizes ranging from 20 – 200 nm are considered optimal for drug delivery as this size range is below the pore size of commonly targeted tissues related to important pathologies.[3,47] Hence, we prepared nanofibers of length ca. 125 nm via the living CDSA seeded growth method in a mixture of THF:MeOH (15:85) and these were characterized by TEM after 48 h of aging. The length of the resulting PFTMC$_{18}$-*b*-PNIPAM$_{425}$, PFTMC$_{19}$-*b*-PEG$_{275}$, and PFTMC$_{18}$-*b*-PEG$_{530}$ nanofibers after the addition of corresponding unimer to appropriate seed solutions were L_n = 127 nm ($Đ$ = 1.03, σ = 22 nm, Figure 3. 3B), L_n = 127 nm ($Đ$ = 1.06, σ = 32 nm, Figure 3. 3E, S3. 12), and L_n = 114 nm ($Đ$ = 1.06, σ = 28 nm, Figure 3. 4, S3. 13D), respectively. See the supplementary information for experimental details (section 3.5.3).

First, aliquots of a NR solution (1 mg/mL in MeOH) were added to diluted solutions of nanofibers (in MeOH) to obtain a mixture of diBCP nanofibers at 0.1 mg/mL (PFTMC$_{18}$-*b*-PNIPAM$_{425}$, PFTMC$_{19}$-*b*-PEG$_{275}$), whilst the NR concentration was varied from 0.1 – 10 wt % (each experiment conducted in triplicate, n = 3). In the case of PFTMC$_{18}$-*b*-PEG$_{530}$ nanofibers the same procedure as above was conducted but the NR concentration was kept at 1 wt %. The resulting nanofiber with NR solutions were continuously homogenized via an orbital shaker. While being homogenized, H_2O was added to the vials containing the nanofibers and NR at a rate of 100 µL/min via a syringe

pump. To remove the organic solvents and drive cargo uptake, the organic solvents were left to evaporate for 12 h in the dark at room temperature, followed by the introduction of a gentle flow of air into the vials (for 30 min). The colloidal solutions of the resulting loaded nanofibers in H_2O were subsequently filtered through 0.45 µm Nylon syringe filters to remove residual unloaded NR and were then diluted to the original volume of the samples through the gravimetric addition of water. TEM and contour length analysis of the nanofibers after loading and filtration revealed no significant change of both nanofiber length and dispersity, indicating that no fragmentation occurred; PFTMC$_{18}$-*b*-PNIPAM$_{425}$ L_n = 122 nm ($Đ$ = 1.05, σ = 27 nm, Figure 3. 3C-D), PFTMC$_{19}$-*b*-PEG$_{275}$ L_n = 133 nm ($Đ$ = 1.06, σ = 32 nm, Figure 3. 3F-G), and PFTMC$_{18}$-*b*-PEG$_{530}$ L_n = 125 nm ($Đ$ = 1.06, σ = 32 nm, Figure 3. 4B-C). The nanofibers showed good solubility in water for at least 6 months after the loading and filtration, as indicated by the absence of precipitates in the vials containing the loaded nanofibers (Figure S3. 14A). Consistent with these observations, DLS analysis of the loaded nanofibers revealed no large-sized aggregates present in aqueous solution after 6 months (Figure S3. 14B). Together, the absence of precipitates, the TEM, and DLS data indicate that the nanofibers remain colloidally stable in solution and unchanged in dimensions for at least 6 months (Figure S3. 14A-B). Nanoparticles utilized for drug delivery need to bypass a range of biological barriers prior to successful payload delivery, such as enzymatic degradation.[3] Liver microsomes are subcellular fractions of hepatocytes that contain cytochrome P450 enzymes that are involved in metabolism.[48] Hence, to assess their stability to enzymatic degradation, a sample of PFTMC$_{18}$-*b*-PEG$_{275}$ nanofibers (L_n = 127 nm by TEM) was transferred to PBS medium via the PNSL method, incubated at 37 °C with liver microsomes, and

Coenzyme II-reduced tetrasodium salt (NADPH, 1 mM). DLS and TEM revealed that the nanofibers remain stable for at least 48 h under the given enzymatic conditions (Figure S3. 14C-D), which provides an excellent timeframe for the nanofibers to deliver cargo before losing colloidal stability arising from degradation.[47]

3.3.5 Quantification of NR Uptake by Low Dispersity PFTMC-*b*-PNIPAM, and PFTMC-*b*-PEG DiBCP Nanofibers: Assessment of the Influence of the Composition and Length of the Corona-Block

The uptake of NR by the nanofibers was evaluated via fluorometric assays of freeze-dried samples resuspended in MeOH (Figure S3. 15, 16, 17). The results are expressed in ng of NR per mg of diBCP (ng/mg of polymer), Encapsulation Efficiency (EE %), and Loading Capacity (LC %). Our findings indicate that the maximum uptake of NR, fluorescence emission, EE %, and LC % by $PFTMC_{18}$-*b*-$PNIPAM_{425}$ and $PFTMC_{19}$-*b*-PEG_{275} nanofiber systems was achieved using a concentration of 1 wt % of NR (Figure 3. 3H-I, S3. 18). At higher NR concentrations it appears that the loading is decreased due to rapid self-aggregation of the dye. The $PFTMC_{18}$-*b*-$PNIPAM_{425}$ nanofibers absorbed an average maximum of 207 ng of NR/mg of polymer (2.1 EE %, 0.02 LC %, 2.0 mol %, Figure 3. 3H-I, S3. 18), whereas for the $PFTMC_{19}$-*b*-PEG_{275} nanofibers the value was 298 ng of NR/mg of polymer (3.0 EE %, 0.03 LC %, 1.4 mol %, Figure 3. 3H-I, S3. 18). Within experimental error, the loading efficiency of both sets of nanofibers appears to be similar. To corroborate that syringe-filtration was an efficient method to remove unbound NR, control experiments where NR (1µg/mL) was transferred to water via the PNSL method with and without filtration were conducted (Figure S3. 19). No significant emission from the filtered NR solution was detected, whereas the emission of the nonfiltered NR solution closely matched the emission of the calibration curve at 1 µg/mL of NR (in Figure S3.

17B). Therefore, syringe-filtration was determined to be an efficient method to purify unbound NR from diBCP nanofibers (Figure S3. 19). Together, the PNSL and filtration circumvent nanofiber fragmentation and also the formation of hydrophobic drug aggregates which cannot be removed by dialysis against water and may otherwise exaggerate the encapsulation efficiency of nanoparticles.

Next, assessment of the NR loading on PFTMC$_{18}$-*b*-PEG$_{530}$ diBCPs nanofibers was conducted (Figure 3. 4). The nanofibers were loaded via the PNSL method at the optimal loading concentration found in the previous section (1 wt % of NR, Figure 3. 3H-I). As mentioned before, the length and dispersity of the loaded PFTMC$_{18}$-*b*-PEG$_{530}$ diBCP nanofibers presented no significant change (L_n = 125 nm, $Đ$ = 1.06, σ = 32 nm, Figure 3. 4A-C) and good colloidal stability for up to six months in aqueous solutions (Figure S3. 14A-B). It was found that 233 ng of NR per mg of diBCP were loaded on average as analyzed by fluorescence spectroscopy (2.2 EE %, 0.02 LC %, 2.1 mol %, Figure 3. 4D, S3. 20). To compare the amount of NR loaded to diBCP nanofibers with long and short PEG-coronas, the amount of NR (ng/mg of polymer) and the EE % of PFTMC$_{18}$-*b*-PEG$_{530}$ and PFTMC$_{19}$-*b*-PEG$_{275}$ (from Figure 3. 3H-I, loaded at NR 1 wt %) were plotted together. The quantity of loaded NR and the EE % were found similar at the same NR loading concentration (1 wt %) for both PFTMC-*b*-PEG nanofiber systems within experimental error (Figure 3. 4D).

The amount of NR loaded on nanofibers with a PNIPAM$_{425}$ corona and with both short (PEG$_{275}$) and long (PEG$_{530}$) PEG-coronas were compared via a Welch's analysis of variance (ANOVA) test ($P < 0.05$, Figure S3. 21). The outcome of this analysis revealed that there was no statistically significant difference among the means of the three diBCP

systems loaded with NR at 1 wt % ($PFTMC_{18}$-*b*-$PNIPAM_{425}$: 207 ± 22 ng/mg of polymer, $PFTMC_{19}$-*b*-PEG_{275}: 298 ± 40 ng/mg of polymer, and $PFTMC_{18}$-*b*-PEG_{530} nanofibers: 233 ± 75 ng/mg of polymer). Hence, the cargo uptake performance does not appear to be significantly influenced by either the composition or length of the corona of diBCP nanofibers with a crystalline PFTMC core. Since the PFTMC DP_n was kept constant (DP_n = 18 – 19) and the core radii appears similar by TEM (ca. 4.5 nm. Figure S3. 22), the crystalline-core surface area available for NR loading remained unchanged on the three diBCP nanofiber systems studied. The similar quantities of NR loaded by the three diBCP nanofiber systems are in good agreement with a loading mechanism where cargo accumulates at the core-corona interface where a dependency on the PFTMC core surface area available for loading would be expected.

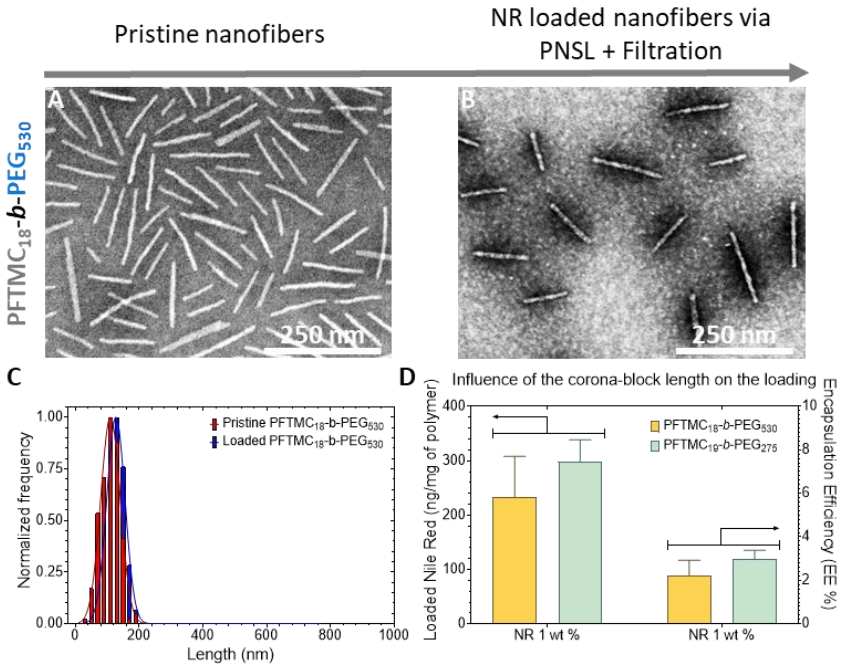

Figure 3. 4. TEM micrographs of low dispersity $PFTMC_{18}$-*b*-PEG_{530} diBCP nanofibers; A) before (L_n = 114 nm, $Đ$ = 1.06, σ = 28 nm), and B) after (L_n = 125 nm, $Đ$ = 1.06, σ = 32 nm) NR uptake via the PNSL method and filtration. C) Contour length histogram of the $PFTMC_{19}$-*b*-PEG_{530} diBCP nanofibers before (A), and after (B) NR cargo uptake and filtration. D) Amount of loaded NR (in ng/mg of polymer), and Encapsulation Efficiency (EE %) determined by fluorometry of $PFTMC_{18}$-*b*-PEG_{530}, at initial 1 wt % of NR. For comparison, data of the NR loaded at 1 wt % of NR by $PFTMC_{19}$-*b*-PEG_{275} diBCP nanofibers is presented in D, from Figure 3. 3G.

3.3.6 Evidence for the Uptake of Nile Red at the Core-Corona Interface of the Nanofibers

Fluorescence measurements of the nanofibers in H_2O revealed that the NR was indeed associated with the nanofibers in the three diBCP systems, but in slightly different polar environments (Figure 3. 3J, S3. 23). The NR emission from NR-loaded PFTMC$_{19}$-*b*-PNIPAM$_{425}$ nanofibers in water was found at λ_{max} = 639 nm whereas that for the PFTMC$_{18}$-*b*-PEG$_{275}$ analogues was marginally blue-shifted, with a λ_{max} = 632 nm (Figure 3. 3J), which indicates that the local environment is less polar. The NR emission from PFTMC$_{18}$-*b*-PEG$_{530}$ loaded diBCP nanofibers in H_2O where the PEG block is even longer was slightly further blue-shifted by 5 nm (λ_{max} = 627 nm, Figure S3. 23) . This may result from the shielding effect that a larger DP_n of PEG$_{530}$ corona provides to the NR from water molecules.

The NR emission from the three diBCP nanofiber systems (λ_{max} = 627 – 639 nm) is significantly red-shifted from that reported for NR encapsulated on triBCP nanofibers where the NR is located in the hydrophobic environment of the poly(butyl methacrylate) outer core (λ_{max} = 610 nm).[42] The PFTMC core of the diBCP nanofibers is highly crystalline[35] and insoluble in the solvent medium used for NR loading and is therefore highly unlikely to permit cargo encapsulation. Moreover, if core uptake was possible the fluorescence signature would be characteristic of NR localized within a hydrophobic environment (i.e. substantially blue-shifted by a further 20 nm). The NR fluorescence emission from the diBCP nanofiber systems (λ_{max} = 627 – 639 nm) therefore most likely arises from localization at the core-corona interface where the key interactions are with the exposed surface of the crystalline PFTMC core, other NR molecules, the corona chains, and the water molecules that swell the corona. The similar quantities of NR loaded by the diBCP nanofibers, the relatively small range of NR emission (λ_{max} = 632 – 639 nm), and

their consistent colloidal stability are in agreement with the described cargo loading mechanism involving adsorption at the core-corona interface.

3.4 Summary and Conclusions

We report studies of the cargo loading of diBCP nanofibers with controlled lengths and low length dispersities. The lengths selected (ca. 100 – 130 nm) were within the range (50 – 200 nm) that are most promising for drug delivery applications.[3,47] Three diBCP nanofiber systems were studied; $PFTMC_{18}$-*b*-$PNIPAM_{425}$, $PFTMC_{19}$-*b*-PEG_{275}, and $PFTMC_{18}$-*b*-PEG_{530}. The nanofibers were preformed via the living CDSA seeded growth method and subsequently loaded with NR via the PNSL method and purified by filtration. The resulting solution of loaded nanofibers remained colloidally stable for up to 6 months, and for at least 48 h under metabolic enzymatic conditions.

Fluorescence spectroscopy analysis revealed that both the composition and the length of the corona-forming blocks of $PFTMC_{18\text{-}19}$-based diBCP nanofibers ($PNIPAM_{425}$, PEG_{275}, PEG_{530}) do not significantly influence the quantity of NR loaded. On average the preformed diBCP nanofibers can load ca. 250 ng of NR per mg of polymer. The NR fluorescent emission (λ_{max} = 627 – 639 nm) on the three loaded diBCP nanofiber systems indicates that the NR localizes at the core-corona interface, where unfavorable interactions between the hydrophobic NR and water molecules are minimized. Furthermore, the fluorescent emission of NR in diBCP nanofibers (λ_{max} = 627 – 639 nm) is significantly red-shifted compared to that encapsulated in the outer amorphous core of triBCP nanofibers (λ_{max} = 610 nm) owing to the more polar environment in the former case.[42] In line with the above, the surface area available for cargo loading was essentially identical for the three diBCP nanofiber systems, as the PFTMC DP_n was kept constant (DP_n = 18-19) and the

core radii were similar. This highlighted the good agreement between the quantity of cargo loaded by the three nanofiber systems used in this work and the proposed loading mechanism onto preformed nanofibers, where cargo is believed to accumulate at the core-corona interface and seems directly related to the surface area of the crystalline-core of diBCP nanofibers.

Prior to this work, the only example of length-controlled, non-covalently loaded polymeric nanofibers was achieved via a triBCP coaxial-core nanofiber approach reported by our group.[42] The amount of cargo loaded by the diBCP nanofibers studied in the present work is ca. two to three times smaller than the quantity reported for coaxial-core nanofibers. However, diBCP nanofibers are simpler to prepare. Furthermore, optimization of hydrophobic cargo uptake by diBCP nanofibers should be achievable by increasing the DP_n of the core-forming block which should increase the radius and therefore the surface area of the hydrophobic nanofiber core. Relevant studies are the subject of current work in our group. In the future, we envisage that either a diBCP or a triBCP coaxial-core nanofiber system could be selected based on the loading requirements related to the potency of a drug or the solubility requirements of a nanofiber-based therapeutic. We are also exploring the development of nanofibers for therapeutic applications with spatially-defined functionality for tracking and targeting purposes.[31]

3.5 Supporting Information

3.5.1 General Considerations and Instrumentation

Methoxy PEGs were purchased from Polymer Source. FTMC was synthesized according to the procedure reported by Finnegan et al.[35] Synthesis of 2-cyano-5-hydroxypentan-2-yl ethyl carbonotrithioate was prepared according to the procedure reported by Arno et al.[29] The PEGs and RAFT-CTAs were dried via vacuum desiccation over phosphorus pentoxide prior to use. All other reagents and solvents were purchased from Sigma-Aldrich (Canada), Combi-Blocks (USA), VWR (Canada), or Fisher Scientific (Canada) and used as received unless otherwise noted. Solvents for self-assembly were of HPLC grade and were filtered through PTFE, nylon, or cellulose membranes with a pore size of 200 nm before use. All reactions were carried out in an MBraun 200B glove box under a nitrogen atmosphere or using standard Schlenk line techniques. RAFT polymerizations were performed in custom-made schlenk-vials to fit dry heating blocks. 1,8-Diazabicyclo[5.4.0]undec-7-ene (DBU) was dried over CaH_2, and purified by distillation under reduced pressure. Anhydrous solvents were dried and purified using an MBraun Grubbs/Dow solvent purification system.[49]

Ultrasonication

Micelle sonication was carried out using a Fisherbrand 112xx series advanced ultrasonic cleaner (FB-11203). The instrument was operated in sweep mode at 80% power and 37 MHz at 10 °C.

NMR Spectroscopy

^{1}H NMR spectra were obtained using a Bruker 500 MHz spectrometer with CD_2Cl_2 (^{1}H NMR: δ = 5.32 ppm), or DMSO-d_6 (^{1}H NMR: δ = 2.50 ppm) as the solvents. Chemical shifts are quoted in parts per million, with spectra referenced to the residual solvent peak. Multiplicities are abbreviated as brs (broad singlet), s (singlet), d (doublet), t (triplet), q (quartet), p (pentet), m (multiplet) and *app.* (apparent) or combinations thereof.

Gel permeation chromatography (GPC)

GPC was conducted on a Malvern OMNISEC chromatograph equipped with a refractive index (RI), UV/Vis photodiode detector array, light scattering detector and viscometer. Triethylamine/THF (1% *v/v*) was used as the eluent, with the flow rate set at 1 mL/min. The columns used were grade T3000, followed by T5000 (Viscotek) at a constant temperature of 35 °C. The calibration (universal) of the RI detector was carried out using polystyrene standards (Viscotek). Samples were prepared at 1 mg/mL in eluent and filtered through a polytetrafluorethylene membrane filter, pore size = 0.2 μm.

Matrix-assisted laser desorption/ionization-time of flight mass spectrometry (MALDI-TOF MS)

MALDI-TOF MS measurements performed using a Bruker Ultraflextreme running in linear mode. Samples were prepared using a *trans*-2-[3-(4-*tert*-butylphenyl)-2-methyl-2-propenylidene]malononitrile matrix (20 mg/mL in THF) and the polymer sample (2 mg/mL in THF), mixed in a 10:1 (*v*/*v*) ratio. Approximately 3 μL of the mixed solution was deposited onto a stainless-steel sample plate and allowed to air dry.

Transmission electron microscopy (TEM)

TEM images were obtained on a JEOL 1011 microscope with an 11 Megapixel CCD camera, operated at 80 kV. Samples were prepared by drop-casting 7.5 μL of the micelle solution onto a carbon-coated copper grid, followed by drop-casting 10 μL of uranyl acetate in EtOH (3 wt %). Sample concentrations for TEM analysis were either 0.5 or 0.1 mg/mL based on nanofiber concentration. Copper grids (400 mesh) were purchased from Ted Pella, and carbon films (ca. 6 nm) were prepared on mica sheets by carbon sputtering with a Leica ACE 600 carbon coater. The carbon films were deposited onto the copper grids by floatation on water and the carbon-coated grids were allowed to dry in air.

For micelle contour length analysis, a minimum of 150 nanofibers in several images were traced manually using the ImageJ software package developed at the US National Institute of Health. The number average micelle length (L_n) or width (W_n) and weight average micelle length (L_w) were calculated using eq. S1-2 from measurements of the contour lengths (L_i) of individual micelles, where N_i is the number of micelles of length L_i, and n is the number of micelles examined in each sample. The distribution of micelle lengths is characterized by $Đ = L_w/L_n$.

$$L_n = \frac{\sum_{i=1}^{n} N_i L_i}{\sum_{i=1}^{n} Ni} \qquad L_w = \frac{\sum_{i=1}^{n} N_i L_i^2}{\sum_{i=1}^{n} NiLi} \quad \text{(Eq. S2. 1-2)}$$

Spectroscopic Experiments

UV-Vis spectra were recorded at 25°C by using a Biotek Cytation 5 multimode plate reader or a PTI QM40 fluorometer.

Biotek Cytation 5 multimode plate reader. Fluorescence measurements (0.1 mL of sample) were obtained with the Biotek Cytation 5 multimode plate reader and were conducted at 25°C in a Costar 96-well plate (clear bottom, black sides, and with the lid).

The samples were excited at 540 nm and the emission was recorded from 570 – 700 nm. The bottom optics was used with a gain of 100 (a.u.). To determine the excitation wavelength to use, excitation scans were recorded with the emission detected at 665 nm, with excitation wavelengths scanned from 400 - 650 nm. The emission of NR from the loaded nanofibers was studied in H_2O and in MeOH. Analysis of the NR content in the nanofibers was determined by measuring the fluorescence of NR in MeOH or H_2O after the PNSL process, and compared against a calibration curve (Figure S3. 17A-B). The loaded nanofibers or non-encapsulated NR in water, were freeze dried and resuspended in MeOH (0.9 mL) for spectroscopic analysis (Figure S3. 15, 16, 19).

PTI QM40 fluorometer. Fluorescence measurements (1 mL of sample) were obtained by using a PTI QM40 fluorometer at 25°C in a quartz glass cuvette (PCS8501 type, 10.0 mm light path). The slits were set to 2 nm bandpass. All measurements were corrected for the fluctuations of the lamp intensity and transmission of the optics. The samples were excited at 540 nm and the emission was recorded from 570 - 700 nm To determine the excitation wavelength to use, excitation scans were recorded with the emission detected at 665 nm, with excitation wavelengths scanned from 400 - 650 nm. The emission of NR from the loaded nanofibers was studied in H_2O and in MeOH. Analysis of the NR content in the nanofibers was determined by measuring the fluorescence of NR in MeOH or H_2O after the PNSL process, and analyzed against a calibration curve (Figure S3. 19B-C). The loaded nanofibers in water, were freeze dried and resuspended in MeOH (1.5 mL) for spectroscopic analysis (Figure S3. 19A).

Dynamic Light Scattering (DLS)

Dynamic light scattering (DLS) experiments were carried out using a Zetasizer Pro. Samples of different polymer concentrations were prepared in filtered solvents by passing through a 0.45 μm membrane filter into an optical quartz glass cuvette (PCS8501 type, 10.0 mm light path). The correlation function was acquired in real time and analyzed with a function capable of modelling multiple exponentials (Cumulant analysis). This process enabled the diffusion coefficients for the component particles to be extracted, and these were subsequently expressed as the intensity weighted mean hydrodynamic size ($R_{h,z}$) by using the Stokes-Einstein relationship for coated spheres in THF (Refractive Index = 1.41, Dispersant Viscosity = 0.455, Dispersant Dielectric Constant = 7.5), or H_2O (Refractive Index = 1.33, Dispersant Viscosity = 0.887, Dispersant Dielectric Constant = 78.5 with core properties of polystyrene latex (Refractive Index = 1.590, Absorption = 0.010).

3.5.2 Synthetic Procedures

3.5.2.1 Synthesis of PFTMC$_{18}$-CTA

Scheme S3. 1. Synthesis of PFTMC$_{18}$-CTA by ring-opening polymerization of FTMC.

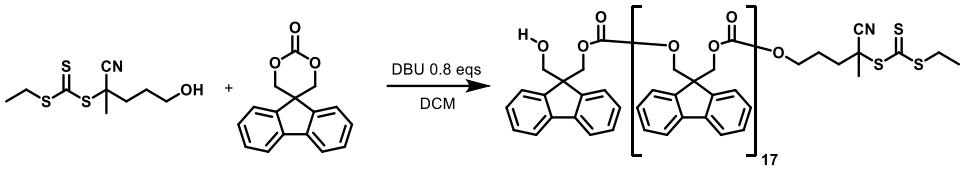

To a solution of 2-cyano-5-hydroxypentan-2-yl ethyl carbonotrithioate[29] in anhydrous CH_2Cl_2 (500 µL, 100 mg/mL, 0.2 mmol, 1.0 eq), DBU (24 µL, 24.4 mg, 0.16 mmol, 0.8 eq) was added in an oven-dried round bottom flask equipped with a magnetic stirring bar. To the stirring solution, FTMC (1.01 g, 4.0 mmol, 20 eq) in anhydrous CH_2Cl_2 (6 mL) was added, and the reaction mixture was stirred at room temperature for 1 h, before the reaction mixture was quenched by the addition of benzoic acid (100 mg). The crude product was purified by precipitation into ice-cold diethyl ether three times, followed by precipitation into ice-cold MeOH three times, and drying *in vacuo* to yield PFTMC$_{18}$-CTA as a yellow solid (1.0 g, 95%).

MALDI-TOF MS $[M]^+$ found: 4729.3, DP_n: 18.

GPC: M_n = 4,800, $Đ_M$ = 1.17.

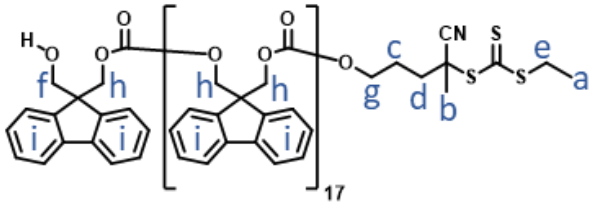

^{1}H NMR (500 MHz, CD_2Cl_2) δ 7.78 – 7.69 (36H, m, Hi), 7.61 – 7.47 (36H, m, Hi), 7.44 – 7.34 (36H, m, Hi), 7.32 – 7.19 (36H, m, Hi), 4.50 – 4.27 (70H, m, Hh), 4.07 (2H, t, *J* = 5.2 Hz, Hg), 3.70 (2H, d, *J* = 6.4 Hz, Hf), 3.31 (2H, dd, *J* = 7.4 Hz, He), 2.22 – 2.13 (1H, m, Hd), 2.06 – 1.98 (1H, m, Hd), 1.87 (2H, h, Hc), 1.80 (3H, s, Hb), 1.31 (3H, t, *J* =

7.4 Hz, Ha). The ^{1}H ratio of g/f indicates the CTA capping efficiency. ^{1}H integration is based on 'f' (HOCH_2).

3.5.2.2 Synthesis of PFTMC$_{18}$-*b*-PNIPAM$_{425}$

Scheme S3. 2. Synthesis of PFTMC$_{18}$-*b*-PNIPAM$_{425}$ by RAFT polymerization.

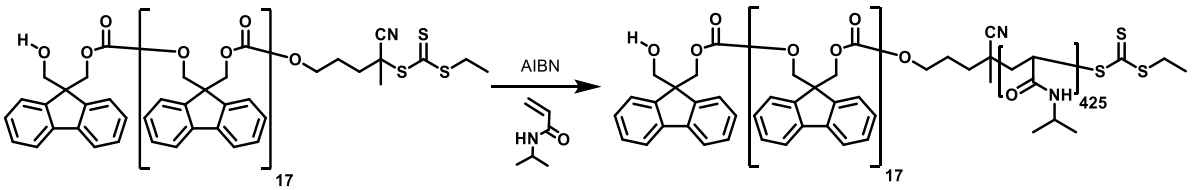

PFTMC$_{18}$-CTA (50 mg, 0.004 mmol, 1 eq), *N*-isopropylacrylamide (192 mg, 1.7 mmol, 400 eq), and AIBN (0.2 mg, 0.001 mmol, 0.3 eq) were dissolved in dioxane (4 mL) in a custom-made schlenk-vial followed by four freeze-pump-thaw cycles. The vial with the reaction mixture was placed in a preheated dry heating block and heated to 70 °C for 18 h. The reaction was quenched by submersion in liquid nitrogen. The product was precipitated three times in ice-cold diethyl ether. The product was dried *in vacuo* to yield PFTMC-*b*-PNIPAM as a white-yellow solid. GPC analysis indicated the presence of PFTMC homopolymer (as evidenced by a lower M_w shoulder with increased absorbance at 268 nm via UV/Vis). The PFTMC homopolymer was removed via flash chromatography (hexane/ethyl acetate, 40:60 to ethyl acetate, then CH_2Cl_2:MeOH:H_2O, 65:35:2 to elute the diblock copolymer). The residual silica-gel was removed via dissolution in THF (50 mL), followed by centrifugation (4500 rpm, 10 mins) and decantation five times. The resulting polymer was dried and precipitated in ice-cold diethyl ether to yield PFTMC$_{18}$-*b*-PNIPAM$_{425}$ as a white-yellow solid (175 mg, 91%).

GPC: M_n = 31,800, $Đ_M$ = 1.76. This value is likely overestimated due to GPC column absorption effects (see main text).

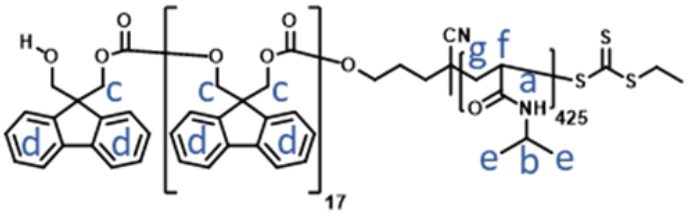

^{1}H NMR (500 MHz, DMSO-d_6) δ 7.99 – 6.72 (556H, m, Ha + Hd), 4.44 – 4.17 (70H, m, Hc), 4.06 – 3.58 (425H, m, Hb), 2.43 – 0.67 (m, 3735H, He + Hf + Hg). ^{1}H integration is based on 'c' (OCH_2C) from the PFTMC, matching the value on the homopolymer.

3.5.2.3 Synthesis of PFTMC$_{19}$-*b*-PEG$_{275}$

Scheme S3. 3. Synthesis of PFTMC$_{19}$-*b*-PEG$_{275}$ by organocatalytic ring-opening polymerization.

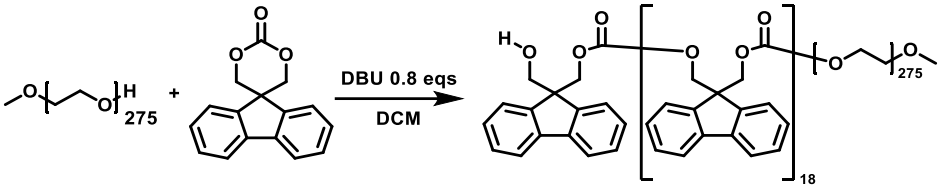

PEG$_{275}$ (500 mg, 0.04 mmol, 1 eq) and DBU (5.2 µL, 5.3 mg, 0.03 mmol, 0.8 eq) were dissolved in the minimum volume of anhydrous CH_2Cl_2 in a round bottom flask equipped with a magnetic stirring bar. To the stirring solution, FTMC (219 mg, 0.87 mmol, 20 eq) in anhydrous CH_2Cl_2 (1.5 mL) was added, and the reaction mixture was stirred at room temperature for 3 h, before the reaction mixture was quenched by the addition of benzoic acid (20 mg). The crude product was purified by precipitation into ice-cold diethyl ether three times. The resulting solid was dried *in vacuo* to yield PFTMC$_{19}$-PEG$_{275}$ as a white solid (689 mg, 96%).

GPC: M_n = 15,200, $Đ_M$ = 1.07.

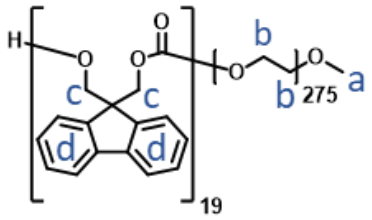

^{1}H NMR (500 MHz, CD_2Cl_2) δ 7.84 – 7.68 (38H, m, Hd), 7.63 – 7.47 (38H, m, Hd), 7.46 – 7.32 (38H, m, Hd), 7.32 – 7.20 (38H, m, Hd), 4.47 – 4.17 (76H, m, Hc), 3.77 – 3.42 (1102H, m, Hb), 3.34 (3H, s, Ha). ^{1}H integration is based on 'a' ($CH_2OC\mathit{H}_3$) from the terminal methyl group of the PEG.

3.5.2.4 Synthesis of PFTMC$_{18}$-*b*-PEG$_{530}$

Scheme S3. 4. Synthesis of PFTMC18-b-PEG530 by organocatalytic ring-opening polymerization.

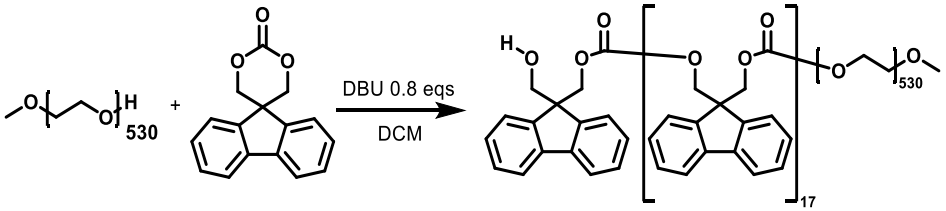

PEG$_{530}$ (500 mg, 0.02 mmol, 1 eq) and DBU (2.9 µL, 2.9 mg, 0.02 mmol, 0.8 eq) were dissolved in the minimum volume of anhydrous CH_2Cl_2 in a round bottom flask equipped with a magnetic stirring bar. To the stirring solution, FTMC (122 mg, 0.49 mmol, 20 eq) in anhydrous CH_2Cl_2 (1 mL) was added, and the reaction mixture was stirred at room temperature for 3 h, before the reaction mixture was quenched by the addition of benzoic acid (10 mg). The crude product was purified by precipitation into ice-cold diethyl ether three times and dried *in vacuo* (515 mg, 83%). 300 mg of the collected white solid was then dissolved in 20 mL of THF in a 50 mL centrifuge with a stir bar. 10 mL of hexane was added to the stirring solution and centrifuged. To the supernatant an extra 6 mL of hexanes was added, stirred, and centrifuged. The resulting solid was dried *in vacuo* to yield PFTMC$_{18}$-PEG$_{530}$ as a white solid (210 mg, 70%).

GPC: M_n = 26,600, $Đ_M$ = 1.14.

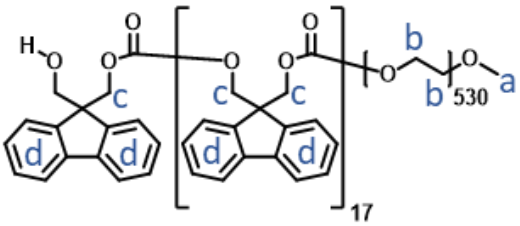

^{1}H NMR (500 MHz, CD_2Cl_2) δ 7.84 – 7.68 (37H, m, Hd), 7.63 – 7.47 (37H, m, Hd), 7.46 – 7.32 (38H, m, Hd), 7.32 – 7.20 (37H, m, Hd), 4.47 – 4.17 (73H, m, Hc), 3.77 – 3.42 (2120H, m, Hb), 3.34 (3H, s, Ha). ^{1}H integration is based on 'a' ($CH_2OC\mathit{H}_3$) from the terminal methyl group of the PEG.

3.5.3 Self-Assembly Procedures

Composition of all solvents given in *v:v*

Self-nucleation of PFTMC$_{18}$-*b*-PNIPAM$_{425}$. PFTMC$_{18}$-*b*-PNIPAM$_{425}$ (8 mg) were placed in a vial, followed by addition of a mixture of 15:85 THF:MeOH (4 mL). The resulting solution (2 mg/mL in 15:85 THF:MeOH) was manually shaken for ~15 s and annealed for 3 h at 75 °C. The solution was cooled to 20 °C over 3 h, and aged for 48 h. The resulting solution contained morphologically pure nanofibers with disperse lengths, as analyzed via TEM.

Preparation of PFTMC$_{18}$-*b*-PNIPAM$_{425}$ seed nanofibers. PFTMC$_{18}$-*b*-PNIPAM$_{425}$ disperse nanofibers (4 mL, 2 mg/mL, in 15:85 THF:MeOH) were fragmented by ultrasonication for 3 h at 0 °C. The resulting seed nanofibers were analyzed by TEM (L_n = 46 nm, $Đ$ = 1.17, σ = 19 nm).

Preparation PFTMC$_{18}$-*b*-PNIPAM$_{425}$ nanofibers of controlled length and low dispersity by seeded growth (living CDSA). For seeded growth assemblies with $m_{unimer}/m_{seed} \leq 10$: aliquots of PFTMC$_{18}$-*b*-PNIPAM$_{425}$ unimer (10 mg/mL in THF), equivalent to corresponding m_{unimer}/m_{seed}, were added to diluted seed nanofiber solutions in MeOH (200 µL). The self-assembly solutions in MeOH (0.1 mg/mL, THF content: 10 – 20% in MeOH) were manually shaken for ~15 s and aged for 48 h at 20 ºC.

For seeded growth assemblies with m_{unimer}/m_{seed} 20, 30, and 40: aliquots of PFTMC$_{18}$-*b*-PNIPAM$_{425}$ unimer (10 mg/mL in THF), equivalent to corresponding m_{unimer}/m_{seed}, were added to diluted seed nanofiber solution in MeOH (100 µL). The unimer was added in intervals of 10 m_{unimer}/m_{seed} every 24 h. The self-assembly solutions (0.1 mg/mL, THF/MeOH 10:90) were manually shaken for ~15 s and aged 48 h at 20 ºC.

Preparation of 125 nm PFTMC$_{18}$-*b*-PNIPAM$_{425}$ nanofibers of controlled length and low dispersity by seeded growth (living CDSA). To a diluted seed solution (L_n = 46 nm, $Đ$ = 1.17, σ = 19 nm, 2 mL, 0.615 mg/mL, in MeOH), PFTMC$_{18}$-*b*-PNIPAM$_{425}$ unimer (10 mg/mL in THF, m_{unimer}/m_{seed} equivalent to 1.7) was added in two portions (2 × 104.5 µL), 24 h apart. The self-assembly solution (~2.2 mL, 1.5 mg/mL, THF:MeOH 12:88) was manually shaken for ~15 s after each addition, and then aged for 48 h at 20 ºC. The resulting nanofibers were analyzed by TEM (L_n = 127 nm, $Đ$ = 1.03, σ = 22 nm).

Preparation of 125 nm PFTMC$_{19}$-*b*-PEG$_{275}$ nanofibers of controlled length and low dispersity by seeded growth (living CDSA). To a diluted seed solution (L_n = 30 nm, $Đ$ = 1.22, σ = 14 nm, 2.7 mL, 0.414 mg/mL, in MeOH), PFTMC$_{19}$-*b*-PEG$_{275}$ unimer (10 mg/mL in THF, m_{unimer}/m_{seed} equivalent to 3.1) was added in two portions (2 × 173.3 µL), 24 h apart. The self-assembly solution (~3.05 mL, 1.5 mg/mL, THF:MeOH 15:85) was manually shaken for ~15 s after each addition, and then aged for 48 h at 20 ºC. The resulting nanofibers were analyzed by TEM (L_n = 127 nm, $Đ$ = 1.06, σ = 32 nm).

Preparation of 125 nm PFTMC$_{18}$-*b*-PEG$_{530}$ nanofibers of controlled length and low dispersity by seeded growth (living CDSA). To a diluted seed solution (L_n = 32 nm, $Đ$ = 1.25, σ = 16 nm, 2.7 mL, 0.435 mg/mL, in MeOH), PFTMC$_{18}$-*b*-PEG$_{530}$ unimer (10 mg/mL in THF, m_{unimer}/m_{seed} equivalent to 2.9) was added in two portions (2 × 189 µL), 24 h apart. The self-assembly solution (~3.05 mL, 1.5 mg/mL, THF:MeOH 15:85) was manually shaken for ~15 s after each addition, and then aged for 48 h at 20 ºC. The resulting nanofibers were analyzed by TEM (L_n = 114 nm, $Đ$ = 1.06, σ = 28 nm).

3.5.4 Nile Red (NR) Loading Procedures

Preparation of low dispersity nanofibers loaded with NR. Vials containing either of the three diBCP nanofiber solutions of a given length (i.e. 125 or 114 nm nanofibers) were prepared by adding THF, MeOH and NR to obtain final solutions containing nanofibers (0.1 mg/mL) and NR (10, 1, 0.1, or 0.01 *w*/*w*) in MeOH:THF (15:85, 0.9 – 2 mL). The resulting solutions were placed in an orbital shaker (300 rpm), and H_2O (same volume as prepared nanofiber solution e.g. 0.9 mL) was infused into the vials via syringe pump at a rate of 100 µL/min. The vials were left uncapped but protected from light in the orbital shaker for 12 h, before residual organic solvent was evaporated by gently blowing air for 30 min. Finally, the solutions were passed through a Nylon syringe-filter (0.45 µm pore size) and made up to a final volume in H_2O equal to the originally prepared nanofiber solution (e.g. 0.9 mL, as measured by weight, using the density of water). For quantification of the loaded NR, analysis of aliquots of the loaded nanofibers in H_2O (0.2 or 1 mL) were freeze dried and resuspended in MeOH to an equal volume of the aliquot taken in MeOH (e.g. 0.45 or 1 mL).

Control experiments with NR. Control experiments to investigate NR removal via filtration were carried out with by transferring the NR (equivalent to 1 wt %) to H_2O via the PNSL method, followed by a gentle flow of air (30 min). Samples with and without filtration through a Nylon syringe-filter (0.45 µm pore size) were made up to a final volume in H_2O equal to the originally prepared solution (as measured by weight, using the density of water). For spectroscopic analysis, 1 mL of the resulting solutions were freeze-dried and resuspended in MeOH (1 mL).

3.5.5 Supplementary Tables

Table S3. 1. Summary of molecular weight data for $PFTMC_{18}$-CTA, $PFTMC_{18}$-*b*-$PNIPAM_{425}$, $PFTMC_{19}$-*b*-PEG_{275} and $PFTMC_{18}$-*b*-PEG_{530} polymers.

Polymer	M_n (g/mol) GPC	M_w (g/mol) GPC	$Đ_M$ GPC	DP_n NMR	DP_n MALDI-TOF
$PFTMC_m$	4,800	5,600	1.17	m =18	18
$PFTMC_{18}$-*b*-$PNIPAM_n$	31,800	55,900	1.76	n = 425	-
$PFTMC_o$-*b*-PEG_p	15,200	16,200	1.07	o = 19 p = 275	-
$PFTMC_q$-*b*-PEG_r	26,600	30,300	1.14	q = 18 r = 530	-

Table S3. 2. Statistical analysis of contour length measurements for $PFTMC_{18}$-*b*-$PNIPAM_{425}$ diBCP nanofibers prepared via seeded growth at 20 °C, in DMSO:MeOH solvent mixtures (DMSO = 10 – 20%), measured via TEM. The number of nanofibers measured is represented by n, and σ represents the standard deviation of the measured length, and L_n/eq corresponds to the L_n of the nanofibers per mass equivalent of triBCP in the sample.

Length	m_{unimer}/m_{seed}								
	Seeds	2.5	2.5[a]	5	10	20	30	40	40[a]
n	172	156	153	158	193	150	151	150	155
L_n (nm)	46	163	165	278	455	787	1222	1729	1798
L_w (nm)	54	171	174	296	482	837	1270	1814	1837
Đ	1.17	1.04	1.05	1.06	1.06	1.06	1.04	1.04	1.02
L_n/eq (nm)	46	47	47	46	42	38	40	42	44
σ (nm)	19	36	36	71	106	198	243	385	267
σ / L_n	0.41	0.22	0.22	0.26	0.23	0.25	0.20	0.22	0.16

[a] Measured 12 months after the sample was originally prepared.

3.5.6 Supplementary Figures

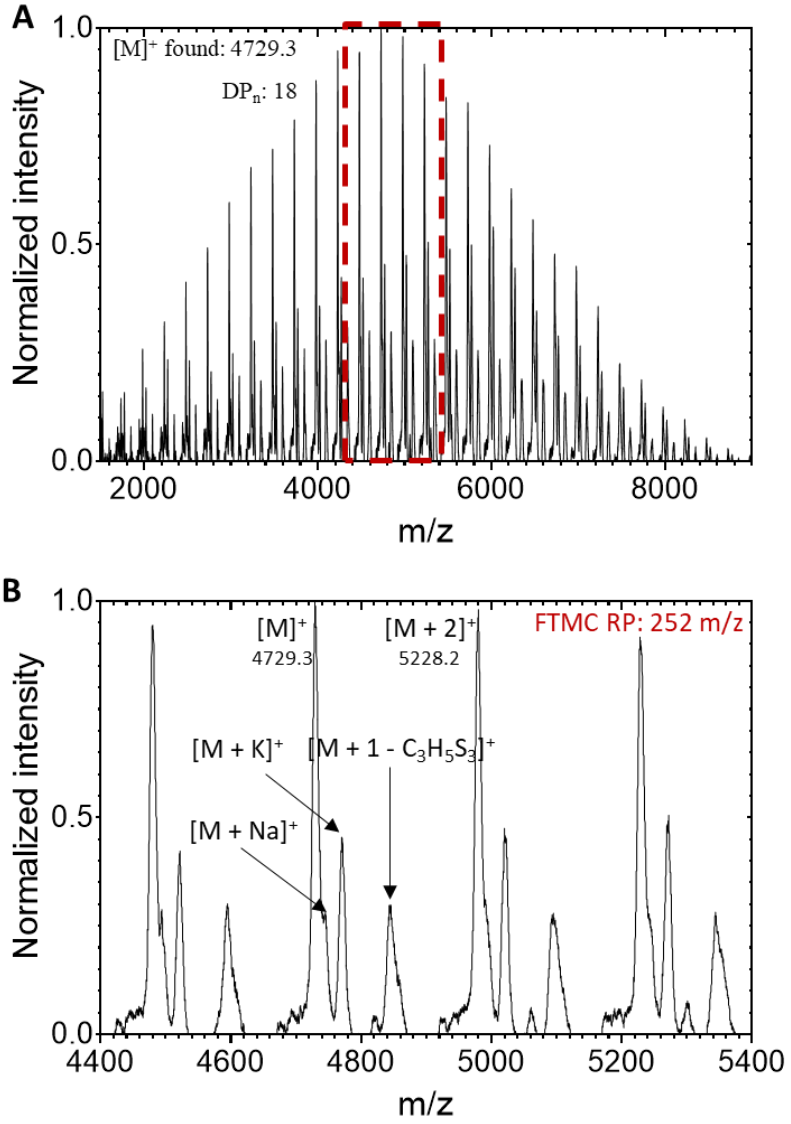

Figure S3. 1. MALDI-TOF MS spectra of $PFTMC_{18}$. The red square represents the area expanded in B.. RP: repeating unit. Reproduced from ref [42]

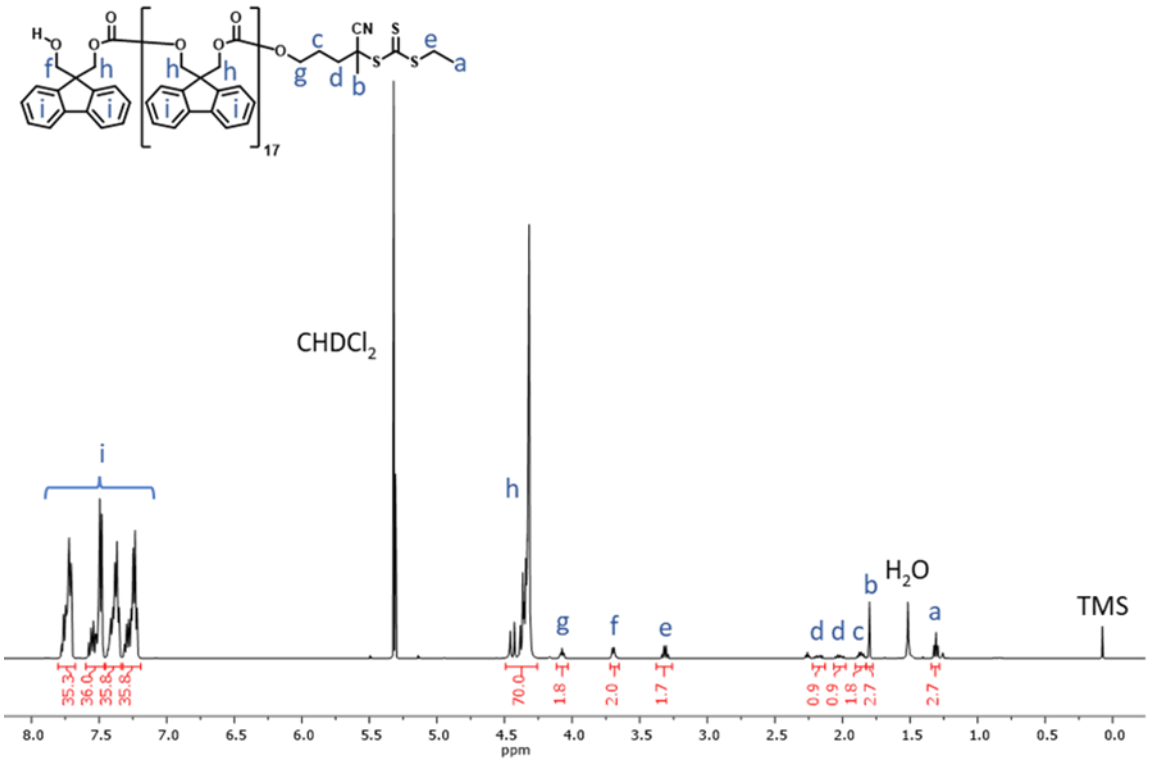

Figure S3. 2. ^{1}H NMR spectra (in CD_2Cl_2) of $PFTMC_{18}$-CTA. Reproduced from ref [42].

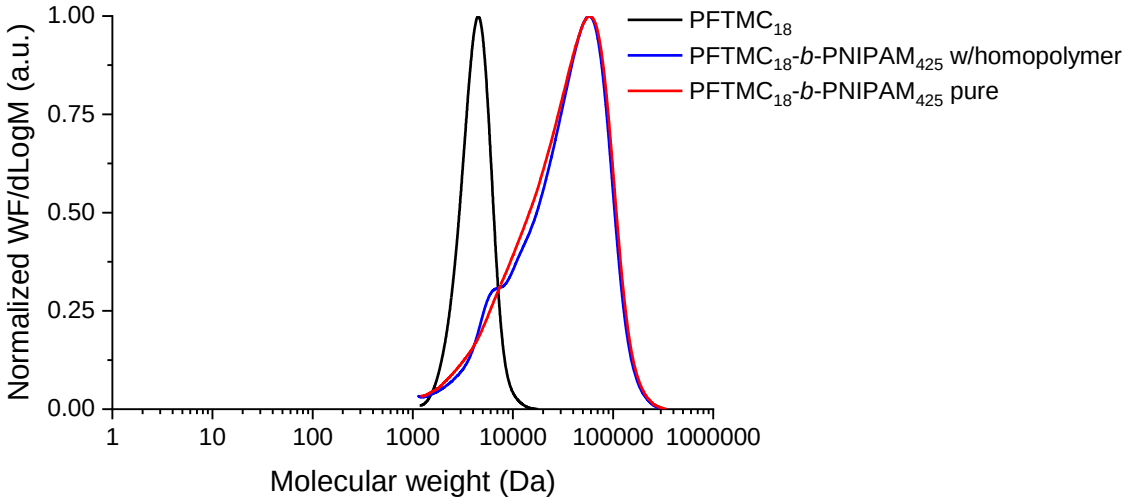

Figure S3. 3. GPC (refractive index) traces of in triethylamine/THF (1% *v/v*) 1 mL min^{-1}, at 35 °C of $PFTMC_{18}$ homopolymer capped with the CTA (black trace, 1 mg/mL), $PFTMC_{18}$-*b*-$PNIPAM_{425}$ diBCP before (blue trace, 1 mg/mL), and after flash column chromatography (red trace, 1 mg/mL). The y-axis reflects the distribution of weight fractions by molecular weight. The GPC trace of the diBCP was unchanged when a lower concentration was used (0.25 mg/mL).

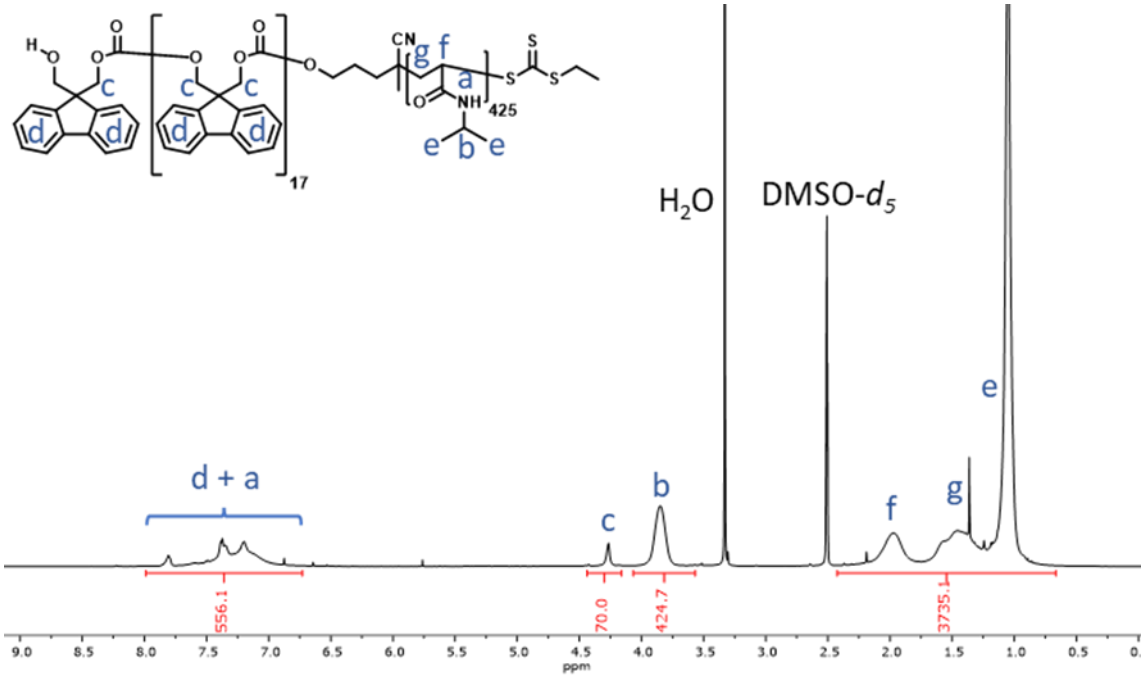

Figure S3. 4. ^{1}H NMR spectra (in DMSO-d_6) of purified PFTMC$_{18}$-*b*-PNIPAM$_{425}$. Reproduced from ref [42].

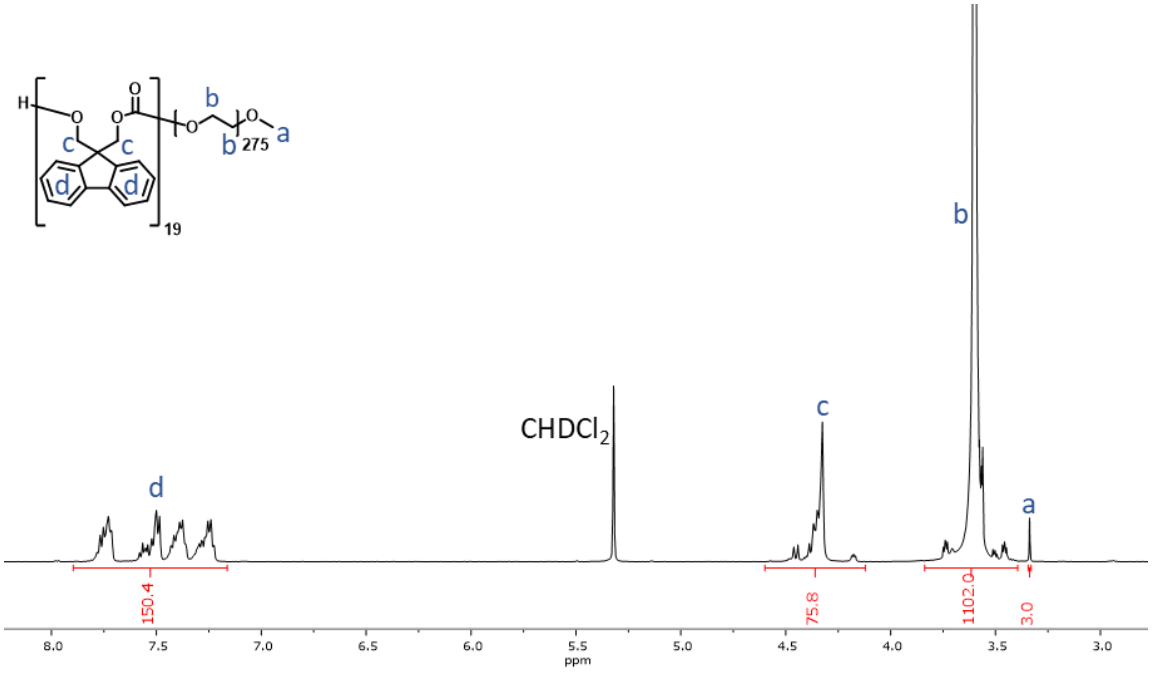

Figure S3. 5. ^{1}H NMR spectra (in CD_2Cl_2) of PFTMC$_{19}$-*b*-PEG$_{275}$.

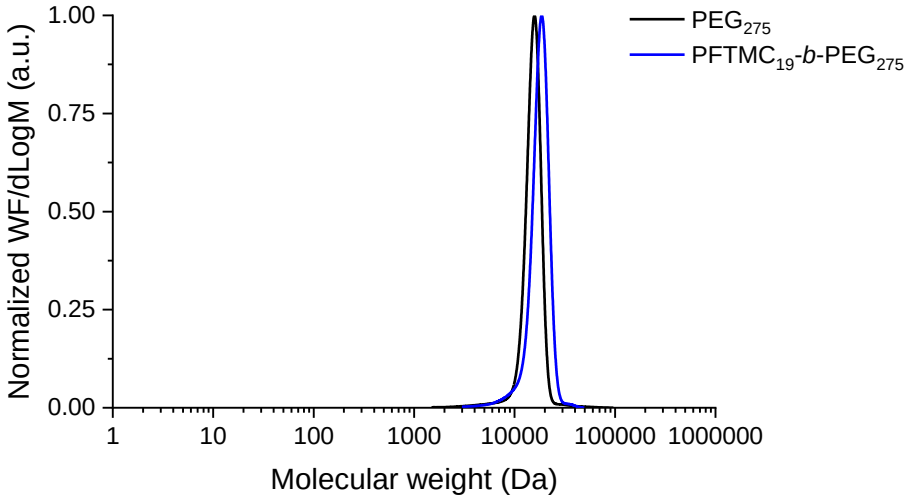

Figure S3. 6. GPC (refractive index) traces eluted in triethylamine/THF (1% *v/v*), 1 mL/min, at 35 °C of PEG_{275} homopolymer (black trace, 1 mg/mL), $PFTMC_{19}$-*b*-PEG_{275} diBCP (blue trace, 1 mg/mL). The y-axis reflects the distribution of weight fractions by molecular weight.

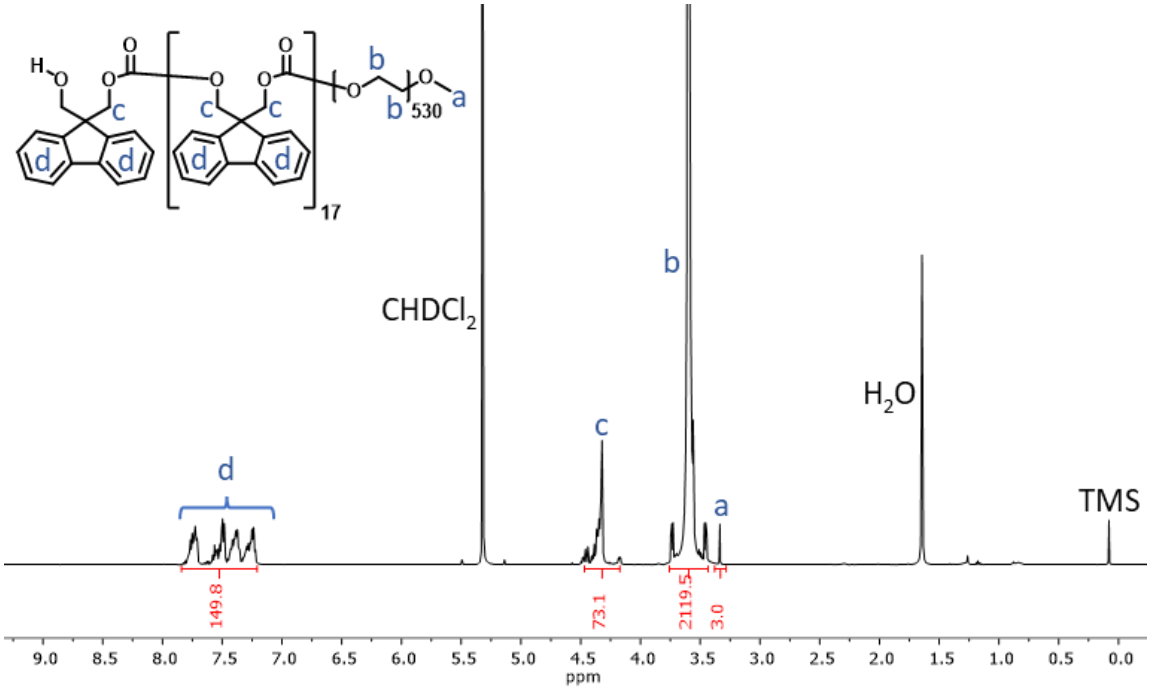

Figure S3. 7. ^{1}H NMR spectra (in CD_2Cl_2) of $PFTMC_{18}$-*b*-PEG_{530}. Reproduced from ref [42].

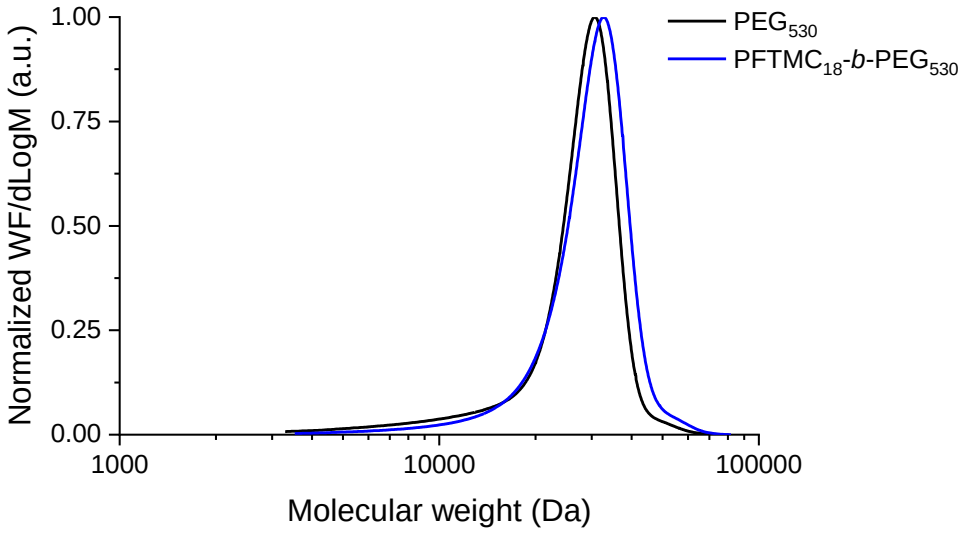

Figure S3. 8. GPC (refractive index) traces eluted in triethylamine/THF (1% *v/v*), 1 mL/min, at 35 °C of PEG_{530} homopolymer (black trace, 1 mg/mL), $PFTMC_{18}$-*b*-PEG_{530} diBCP (blue trace, 1 mg/ mL). The y-axis reflects the distribution of weight fractions by molecular weight.

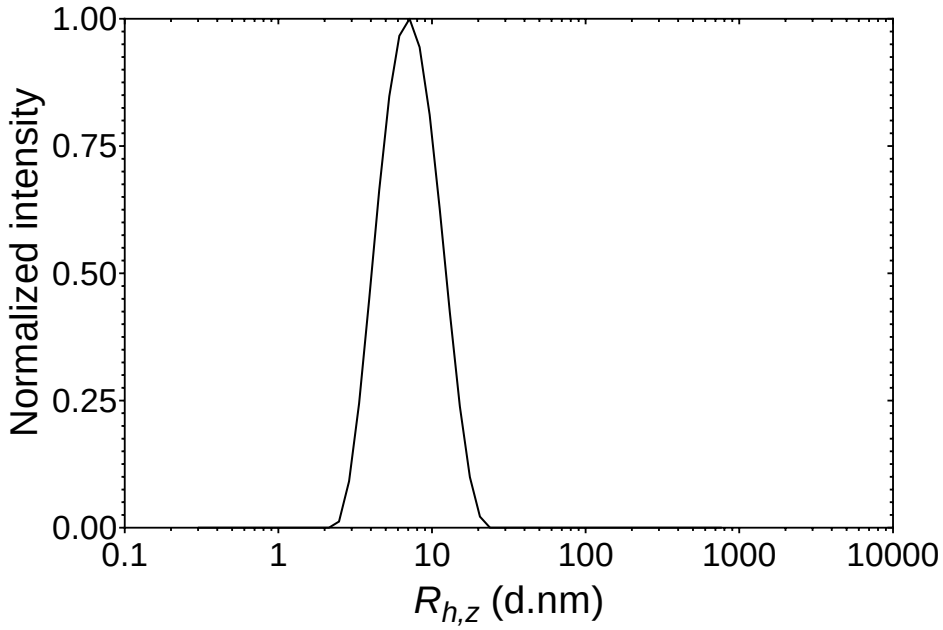

Figure S3. 9. DLS of the $PFTMC_{18}$-*b*-$PNIPAM_{425}$ diBCP in tetrahydrofuran (THF); $R_{h,z}$ = 9.3 nm, σ = 2.22 nm.

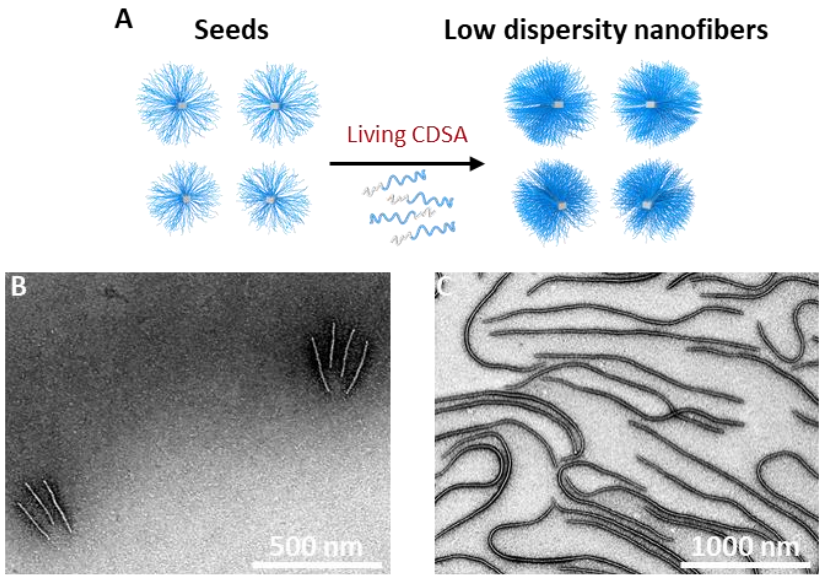

Figure S3. 10. A) Schematic representation of the generation of low-dispersity nanofibers made from PFTMC$_{18}$-*b*-PNIPAM$_{425}$. B-C) TEM micrographs of nanofibers prepared via Living CDSA at various m_{unimer}/m_{seed} ratios added to solutions of seed nanofibers. m_{unimer}/m_{seed} = B) 2.5:1 C) 40:1.

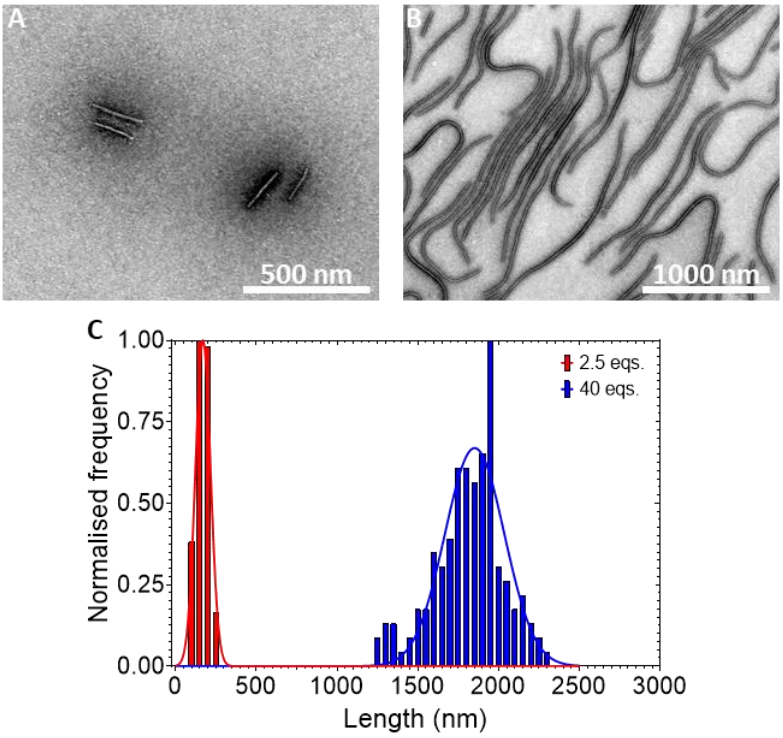

Figure S3. 11. TEM micrographs of nanofibers prepared through seeded-growth after 12 months of the addition of unimer in THF to nanofiber seed solutions (L_n = 46 nm, $Đ$ = 1.17, σ = 19 nm, in THF:MeOH 15:85 *v/v*) at: A) 2.5:1 m_{unimer}/m_{seed} ratio (L_n = 167 nm, $Đ$ = 1.05, σ = 37 nm), and B) 40:1 m_{unimer}/m_{seed} ratio (L_n = 1798 nm $Đ$ = 1.02, σ = 267 nm). C) Contour length histograms of the nanofibers in A (red) and B (blue).

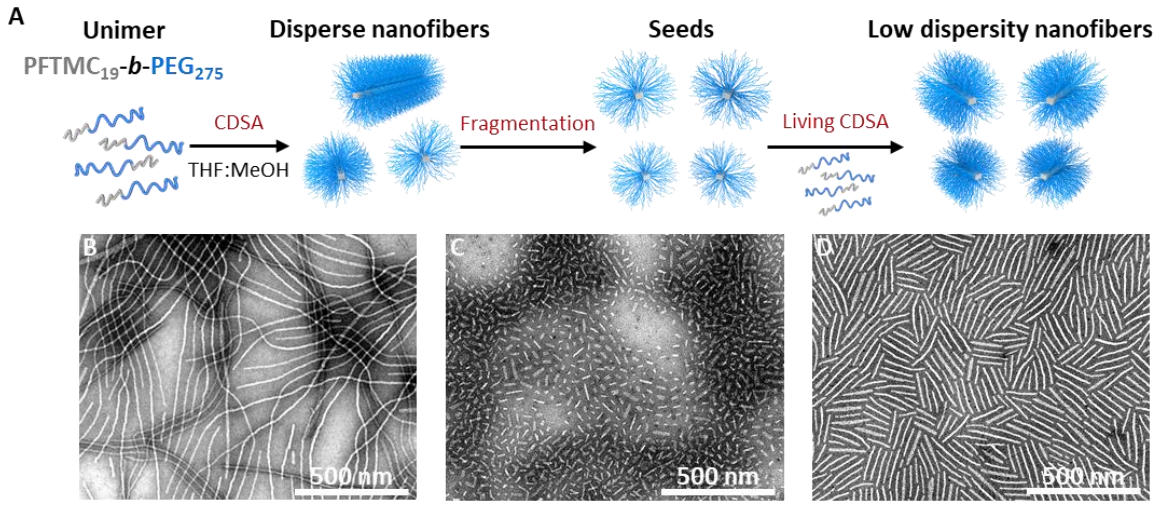

Figure S3. 12. A) Schematic representation of the generation of low dispersity PFTMC$_{19}$-*b*-PEG$_{275}$ nanofibers through the living CDSA method. B) TEM of disperse PFTMC$_{19}$-*b*-PEG$_{275}$ nanofibers (1.5 mg/mL) prepared in THF:MeOH (15:85 *v/v*), after annealing at 70 °C for 3 h, and aged for 48 h. C) TEM of seed nanofibers (L_n = 30 nm, $Đ$ = 1.22, σ = 14 nm) prepared through sonication of the disperse nanofibers (from B, in THF:MeOH) for 3h at 0 °C. D) TEM micrograph of low dispersity nanofibers (L_n = 127 nm, $Đ$ = 1.06, σ = 32 nm) prepared through seeded-growth by addition of unimer in THF to the nanofiber seed solution at: 3.1:1 m_{unimer}/m_{seed} ratio.

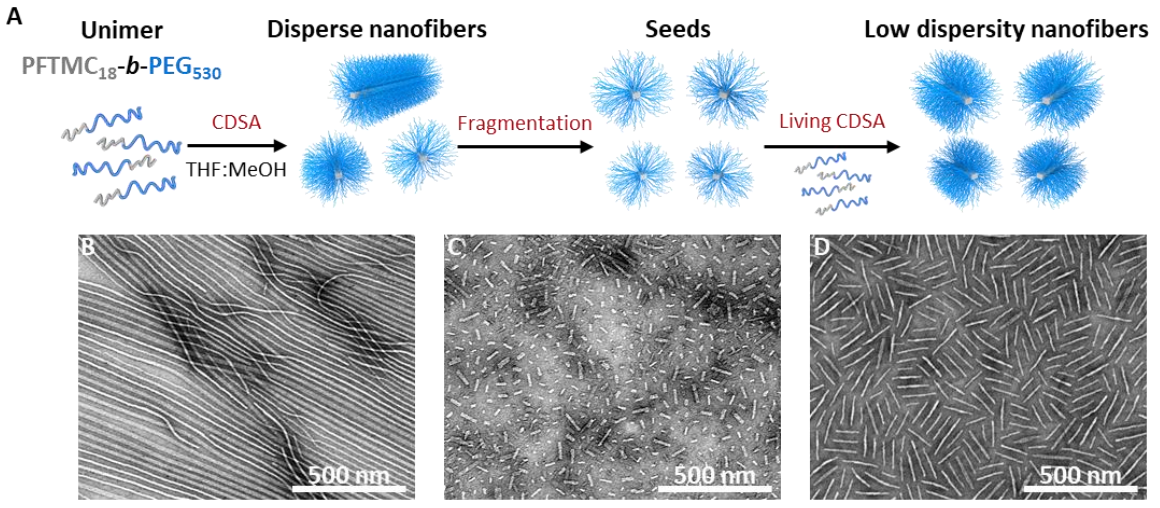

Figure S3. 13. A) Schematic representation of the generation of low dispersity PFTMC$_{18}$-*b*-PEG$_{530}$ nanofibers through the living CDSA method. B) TEM of disperse PFTMC$_{18}$-*b*-PEG$_{530}$ nanofibers (1.5 mg/mL) prepared in THF:MeOH (15:85 *v/v*), after annealing at 70 °C for 3 h, and aged for 48 h. C) TEM of seed nanofibers (L_n = 32 nm, $Đ$ = 1.25, σ = 16 nm) prepared through sonication of the disperse nanofibers (from B, in THF:MeOH) for 3h at 0 °C. D) TEM micrograph of low dispersity nanofibers (L_n = 114 nm, $Đ$ = 1.06, σ = 28 nm) prepared through seeded-growth by addition of unimer in THF to the nanofiber seed solution at: 3.1:1 m_{unimer}/m_{seed} ratio.

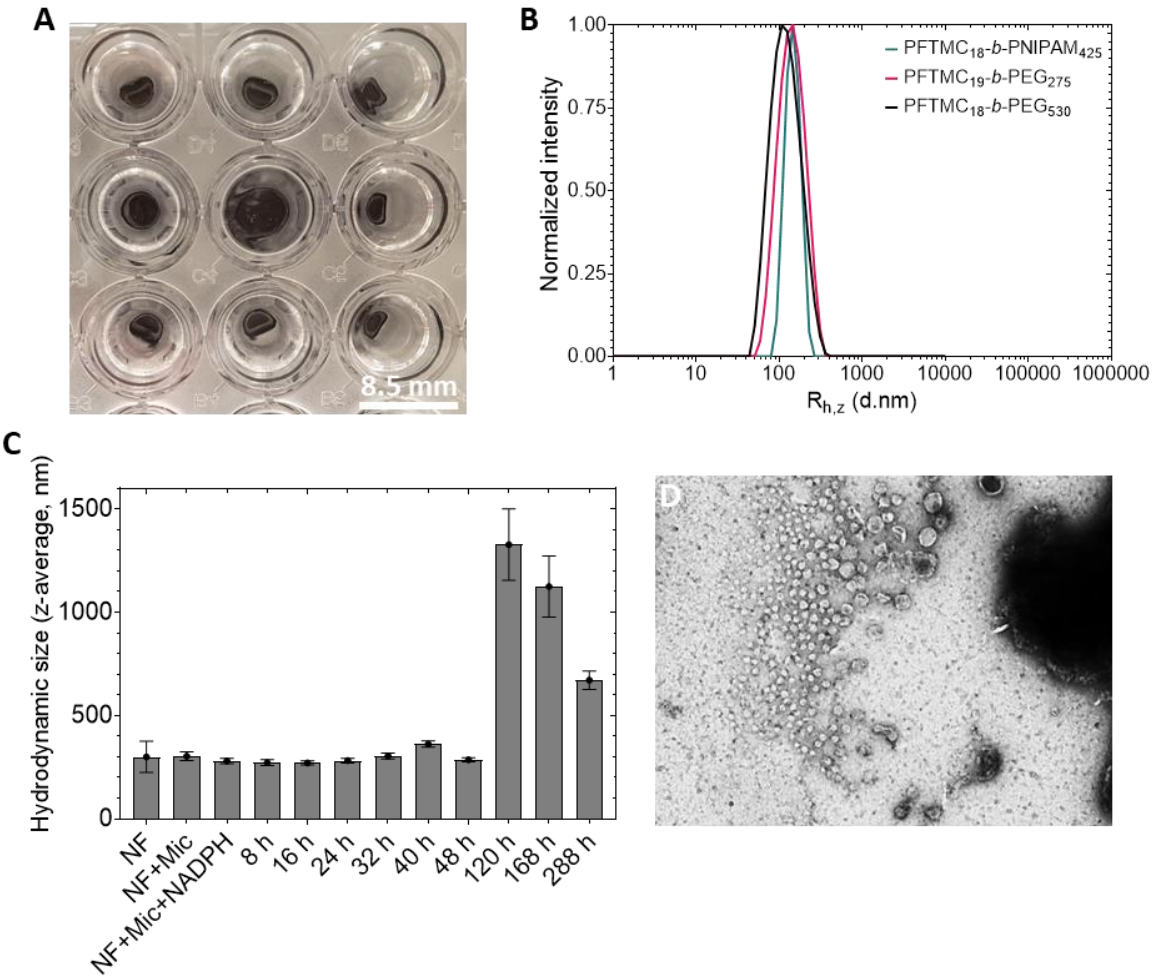

Figure S3. 14. A) Digital images of the vials containing loaded (via PNSL, NR 1 wt %) and filtered nanofibers in water after 6 months. The image shows clear aqueous solutions with no signs of precipitation by the nanofibers at the bottom of the vials, the dark objects in each vial result from the lids at the top of the vials. The vials were placed in a well-plate and the images were recorded from the bottom; $PFTMC_{18}$-*b*-$PNIPAM_{425}$ (1st column), $PFTMC_{19}$-*b*-PEG_{275} (2nd column), and $PFTMC_{18}$-*b*-PEG_{530} (3rd column). B) DLS analysis after 6 months of the nanofibers loaded at 1 wt % of NR in H_2O; $PFTMC_{18}$-*b*-$PNIPAM_{425}$ ($R_{h,z}$ = 127 nm, $Đ$ = 1.19, green trace. $L_{n(\text{loaded})}$ = 116 nm by TEM), $PFTMC_{19}$-*b*-PEG_{275} ($R_{h,z}$ = 136 nm, $Đ$ = 1.21, pink trace. $L_{n(\text{loaded})}$ = 133 nm by TEM), and $PFTMC_{18}$-*b*-PEG_{530} ($R_{h,z}$ = 108 nm, $Đ$ = 1.29, dark trace. $L_{n(\text{loaded})}$ = 125 nm by TEM). C) Time-dependant microsome degradation assay of $PFTMC_{19}$-*b*-PEG_{275} nanofibers (1µM, L_n = 127 nm by TEM Figure 3. 3E) measured by DLS at 37 °C in phosphate buffer (1 mL) supplemented with microsomes (from liver, pooled, rat (Sprague-Dawley), 0.5 mg/mL) and Coenzyme II reduced tetrasodium salt (NADPH, 1 mM). The $PFTMC_{19}$-*b*-PEG_{275} nanofibers remained stable for up to 48 h. The hydrodynamic radius of the nanofibers was ca. two times larger in PBS ($R_{h,z}$ = 250 nm) than in H_2O ($R_{h,z}$ = 136 nm, Figure S3. 14B), this may arise from a difference in the ionic strength of the medium or the viscosity of the media.[50] The distinct $R_{h,z}$ value of microsomes was removed from the chart. NF: $PFTMC_{19}$-*b*-PEG_{275} nanofibers; Mic: microsomes; NADPH: Coenzyme II reduced tetrasodium salt. D) TEM micrograph of the solution containing the nanofibers under enzymatic conditions after 120 h (5 days). The sphere-like aggregates may correspond to PFTMC fractions that will likely aggregate in aqueous media. The dark ill-defined aggregates interact well with the staining solution (in EtOH) suggesting the presence of PEG homopolymer or PEG-microsome aggregates.

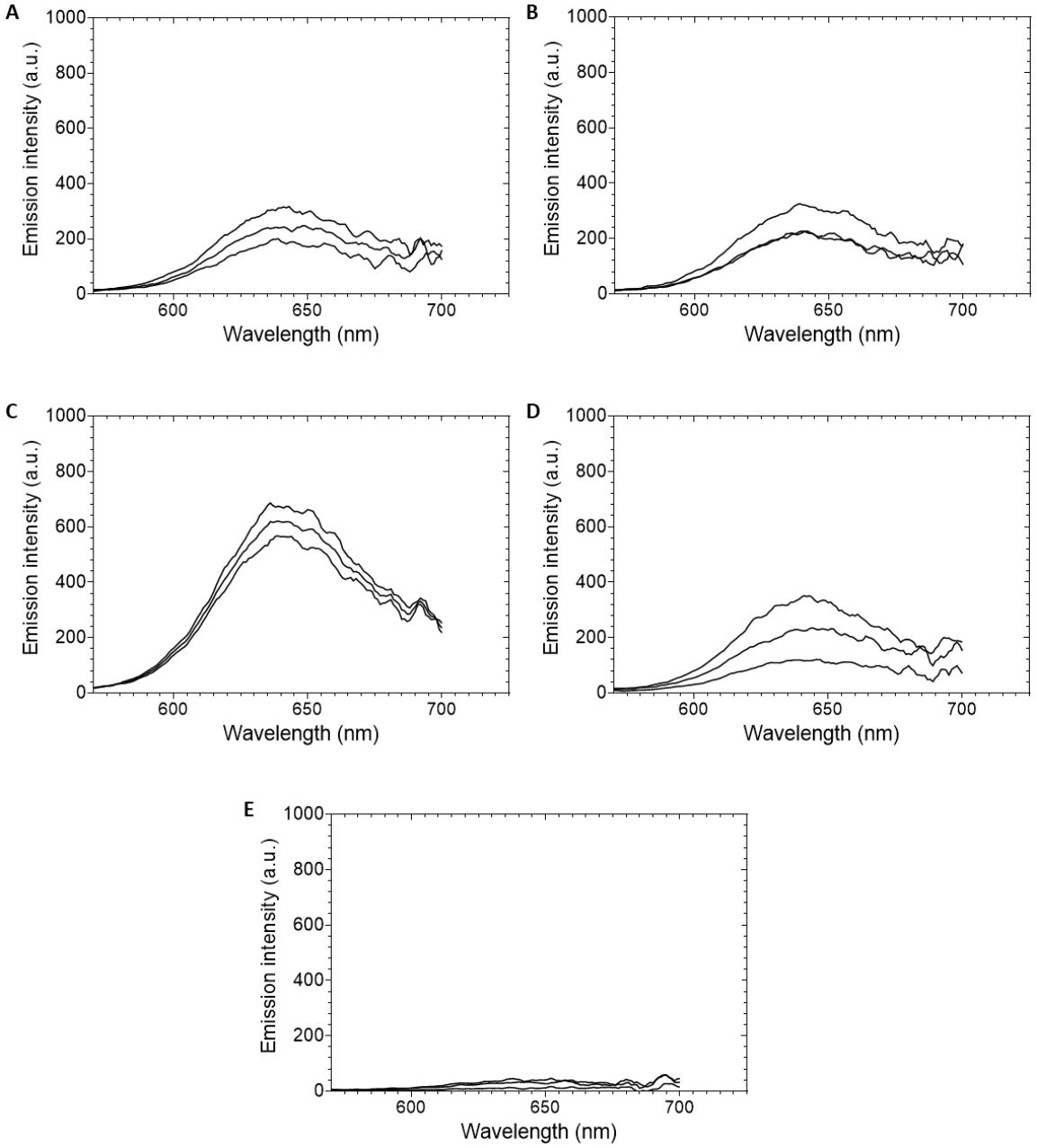

Figure S3. 15. Emission spectra (in MeOH) of the $PFTMC_{18}$-*b*-$PNIPAM_{425}$ (L_n = 127 nm, $Đ$ = 1.03, σ = 22 nm) preformed nanofibers loaded with NR via PNSL at different concentrations, followed by filtration: A) 10 wt %, B) 5 wt %, C) 1 wt %, D) 0.5 wt %, and E) 0.1 wt %. Each experiment was conducted in triplicate. λ_{ex} = 540 nm.

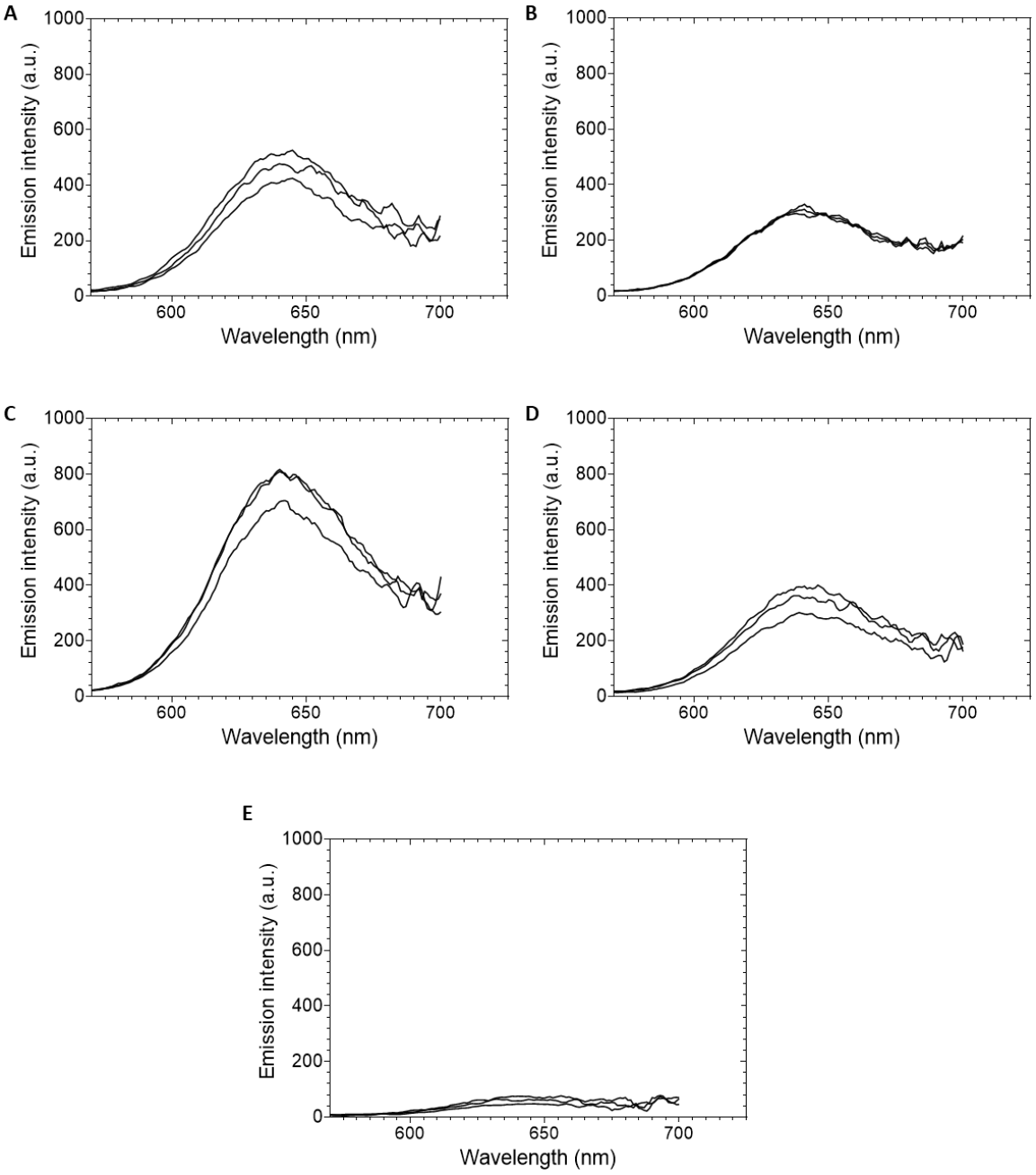

Figure S3. 16. Emission spectra (in MeOH) of the PFTMC$_{19}$-*b*- PEG$_{275}$ (L_n = 127 nm, $Đ$ = 1.06, σ = 32 nm) preformed nanofibers loaded with NR via PNSL at different concentrations, followed by filtration: A) 10 wt %, B) 5 wt %, C) 1 wt %, D) 0.5 wt %, and E) 0.1 wt %. Each experiment was conducted in triplicate. λ_{ex} = 540 nm.

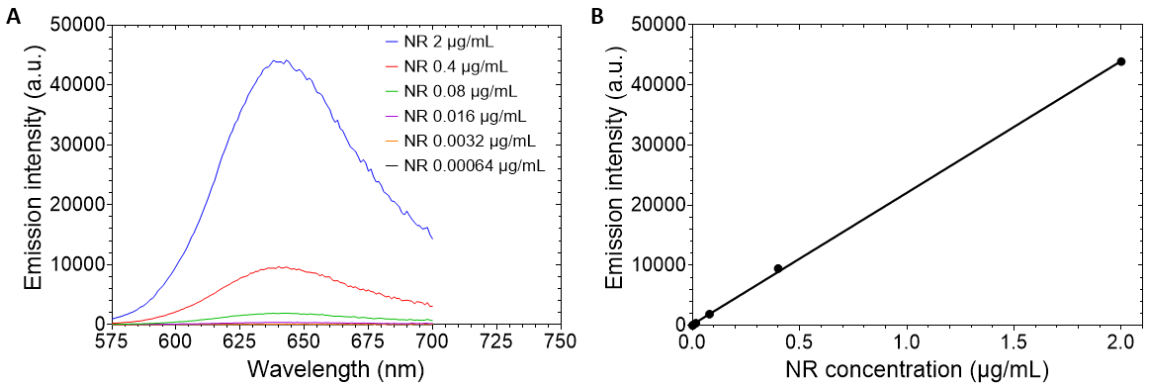

Figure S3. 17. A) Emission data for NR at different concentrations (in MeOH). This was used to prepare the calibration curve in B. The emission intensity for the calibration curves was recorded with λ_{ex} = 540 nm. B) Calibration curve of A. The equation of the line and the coefficient of determination for the calibration curve at $\lambda_{ex\text{-}max}$ = 640 nm is as follows: $y = 146.1 + 2.19\times10^4 x$; $r^2 = 0.9997$. The equation was used to quantify the loading of NR in the nanofibers from the Figure S3. 15, 16.

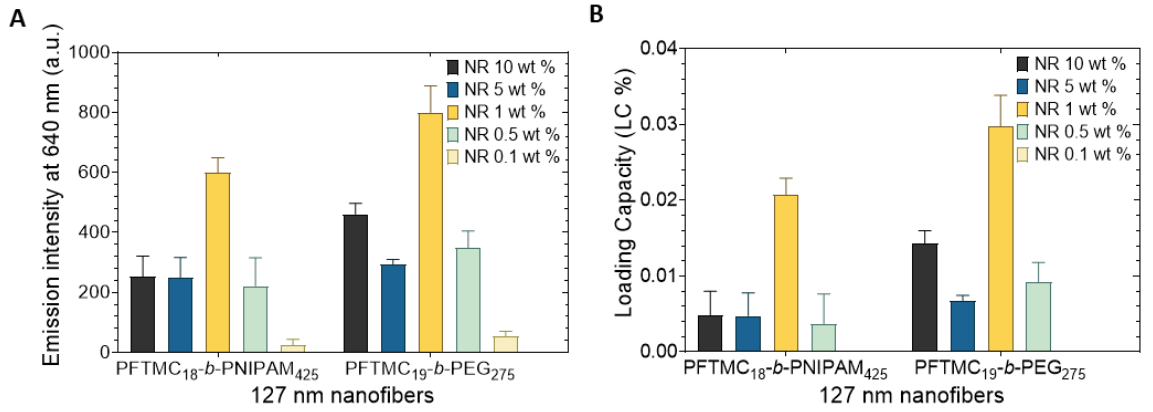

Figure S3. 18. Loading properties of L_n = 127 nm nanofibers made from PFTMC$_{18}$-*b*-PNIPAM$_{425}$ ($Đ$ = 1.03, σ = 22 nm, Figure 3. 3B), and PFTMC$_{19}$-*b*-PEG$_{275}$ ($Đ$ = 1.06, σ = 32 nm, Figure 3. 3E) with different initial quantities of NR (1 – 10 wt %) used in the loading process; A) Nile Red loaded in ng per mg of diBCP. A) Emission intensity, and B) Loading Capacity (LC %) of diBCP nanofibers. The EE % (in Figure 3. 3I, 4D) and LC % were calculated as follows: EE % = (mass of drug added – mass of non-encapsulated drug)/(mass of drug added) ×100, e.g. 127 nm PFTMC$_{19}$-*b*-PEG$_{275}$ nanofibers loaded at 1 wt %; EE % = (900 ng – 873 ng)/(900 ng)×100=3.0%, and LC % = (mass of encapsulated drug)/(mass of nanofibers)×100, e.g. 127 nm PFTMC$_{19}$-*b*-PEG$_{275}$ nanofibers loaded at 1 wt %; LC % = (27 ng)/(90,000 ng)×100 = 0.03%.

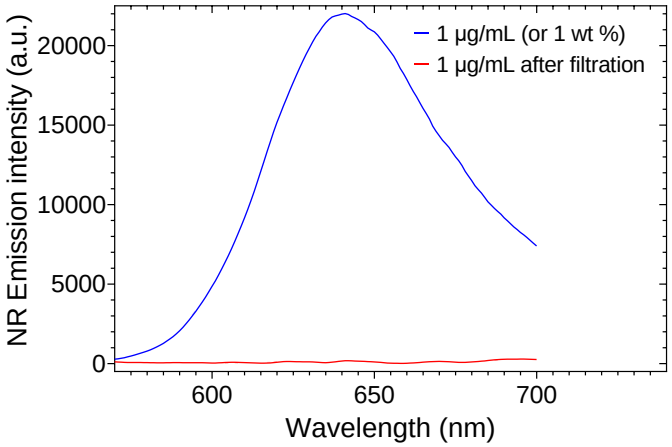

Figure S3. 19. Validating syringe-filtration as a purification process to remove nonbounded NR. Emission of NR at 1 µg/mL after transfer to via the PNSL method, freeze-drying, and resuspension in MeOH for spectroscopic analysis (blue line), and emission of NR at 1 µg/mL after transfer to water via the PNSL method *with filtration*, freeze-drying, and resuspension in MeOH for spectroscopic analysis (red line).

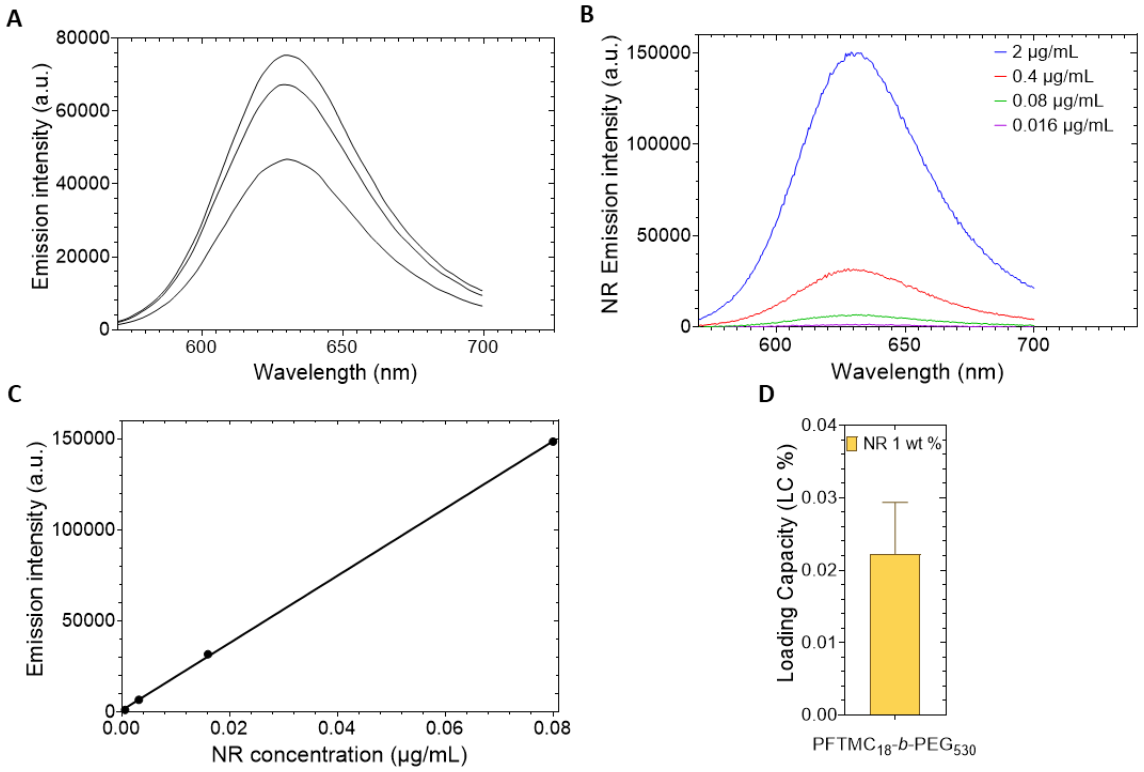

Figure S3. 20. A) Emission spectra (in MeOH) of the PFTMC$_{18}$-*b*-PEG$_{530}$ (L_n = 114 nm, $Đ$ = 1.06, σ = 28 nm) preformed nanofibers loaded with NR via PNSL at 1 wt % NR, followed by filtration. B) Emission of NR at different concentrations (in MeOH) to prepare the calibration curve in C. The emission intensity for the calibration curves was recorded at λ_{ex} = 540 nm. C) Calibration curve of B. The equation of the line and the coefficient of determination for the calibration curve at $\lambda_{ex\text{-}max}$ = 640 The equation of the line and the coefficient of determination for the calibration curve at $\lambda_{ex\text{-}max}$ = 640 nm is as follows: B) $y = 146.1 + 2.19\times10^4$ x; r^2 = 0.9997. The equation was used to quantify the loading of NR in the nanofibers from A. D) Loading capacity of PFTMC$_{18}$-*b*-PEG$_{530}$ nanofibers loaded at 1 wt % of NR.

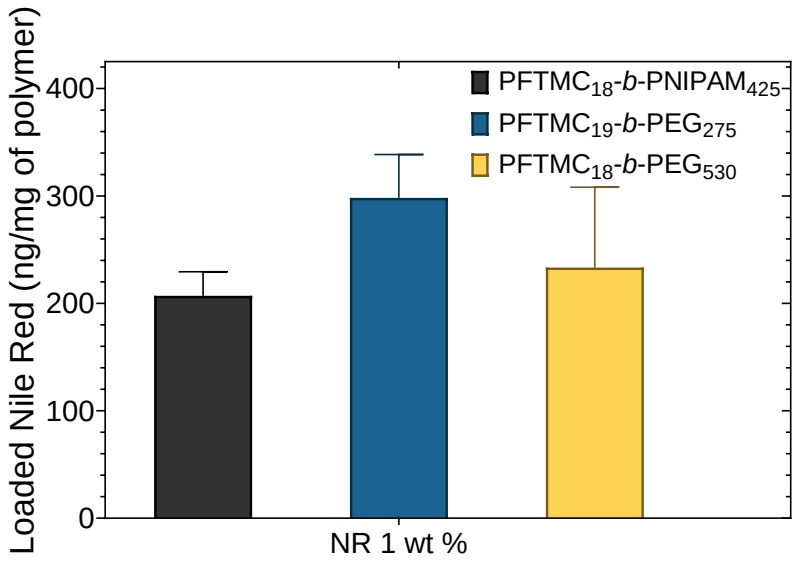

Figure S3. 21. Loaded NR (in ng/mg of polymer) determined by fluorometry of the three diBCP nanofiber systems utilized in this work (Figure 3. 3H-I, 4D); $PFTMC_{18}$-*b*-$PNIPAM_{425}$, $PFTMC_{19}$-*b*-PEG_{275}, and $PFTMC_{18}$-*b*-PEG_{530} diBCP. A Welch's analysis of variance (ANOVA, GraphPad Prism 9, V 9.2.0) test of the data of this figure indicates that there are no significant differences among the means ($p < 0.05$).

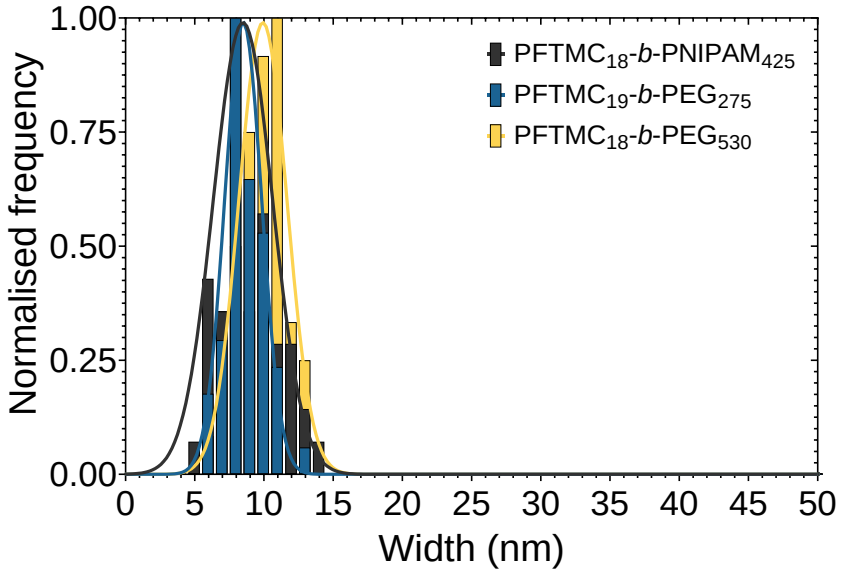

Figure S3. 22. Contour width histograms of nanofibers from TEM micrographs of $PFTMC_{18}$-*b*-$PNIPAM_{425}$ W_n = 8.9 nm ($Đ$ = 1.06, σ = 2.1 nm, dark, from Figure 3. 3B), $PFTMC_{19}$-*b*-PEG_{275} W_n = 8.6 nm ($Đ$ = 1.03, σ = 1.5 nm, blue, from Figure 3. 3E), and $PFTMC_{19}$-*b*-PEG_{530} W_n = 9.8 nm ($Đ$ = 1.03, σ = 1.6 nm, yellow, from Figure 3. 4A). The nanofibers used for width measurements were cast from 15:85 THF:MeOH. $n \geq 50$ number of counted nanofibers.

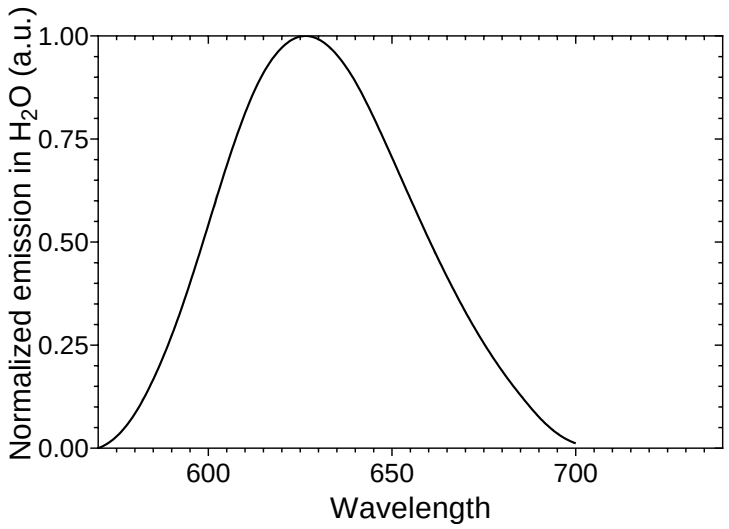

Figure S3. 23. Emission spectra of NR loaded (at initial 1 wt %) by PFTMC$_{18}$-*b*-PEG$_{530}$ diBCP nanofibers (0.1 mg/mL) in water.

3.6 References

(1) Tritschler, U.; Pearce, S.; Gwyther, J.; Whittell, G. R.; Manners, I. 50th Anniversary Perspective: Functional Nanoparticles from the Solution Self-Assembly of Block Copolymers. *Macromolecules.* **2017**, *50* (9), 3439–3463.

(2) Mai, Y.; Eisenberg, A. Self-Assembly of Block Copolymers. *Chem. Soc. Rev.* **2012**, *41* (18), 5969–5985.

(3) Elsabahy, M.; Wooley, K. L. Design of Polymeric Nanoparticles for Biomedical Delivery Applications. *Chem. Soc. Rev.* **2012**, *41* (7), 2545–2561.

(4) Allen, T. M.; Cullis, P. R. Drug Delivery Systems: Entering the Mainstream. *Science* **2004**, *303* (5665), 1818–1822.

(5) Hua, S.; de Matos, M. B. C.; Metselaar, J. M.; Storm, G. Current Trends and Challenges in the Clinical Translation of Nanoparticulate Nanomedicines: Pathways for Translational Development and Commercialization. *Front. Pharmacol.* **2018**, *9* (790), 1–14.

(6) Banerjee, A.; Qi, J.; Gogoi, R.; Wong, J.; Mitragotri, S. Role of Nanoparticle Size, Shape and Surface Chemistry in Oral Drug Delivery. *J. Control. Release* **2016**, *238* (1), 176–185.

(7) Zhao, J.; Stenzel, M. H. Entry of Nanoparticles into Cells: The Importance of Nanoparticle Properties. *Polym. Chem.* **2018**, *9* (3), 259–272.

(8) Gaumet, M.; Vargas, A.; Gurny, R.; Delie, F. Nanoparticles for Drug Delivery: The Need for Precision in Reporting Particle Size Parameters. *Eur. J. Pharm. Biopharm.* **2008**, *69* (1), 1–9.

(9) Doncom, K. E. B.; Blackman, L. D.; Wright, D. B.; Gibson Ab, M. I.; O'Reilly, R. K. Dispersity Effects in Polymer Self-Assemblies: A Matter of Hierarchical Control. *Chem. Soc. Rev* **2017**, *46* (14), 4119–4134.

(10) Cabral, H.; Miyata, K.; Osada, K.; Kataoka, K. Block Copolymer Micelles in Nanomedicine Applications. *Chem. Rev.* **2018**, *118* (14), 6844–6892.

(11) Kinnear, C.; Moore, T. L.; Rodriguez-Lorenzo, L.; Rothen-Rutishauser, B.; Petri-Fink, A. Form Follows Function: Nanoparticle Shape and Its Implications for Nanomedicine. *Chem. Rev.* **2017**, *117* (17), 11476–11521.

(12) Geng, Y.; Dalhaimer, P.; Cai, S.; Tsai, R.; Tewari, M.; Minko, T.; Discher, D. E. Shape Effects of Filaments versus Spherical Particles in Flow and Drug Delivery. *Nat. Nanotechnol.* **2007**, *2* (4), 249–255.

(13) Black, K. C. L.; Wang, Y.; Luehmann, H. P.; Cai, X.; Xing, W.; Pang, B.; Zhao, Y.; Cutler, C. S.; Wang, L. V.; Liu, Y.; Xia, Y. Radioactive 198Au-Doped Nanostructures with Different Shapes for in Vivo Analyses of Their Biodistribution, Tumor Uptake, and Intratumoral Distribution. *ACS Nano* **2014**, *8* (5), 4385–4394.

(14) Yu, Q.; Roberts, M. G.; Houdaihed, L.; Liu, Y.; Ho, K.; Walker, G.; Allen, C.; Reilly, R. M.; Manners, I.; Winnik, M. A. Investigating the Influence of Block Copolymer Micelle Length on Cellular Uptake and Penetration in a Multicellular Tumor Spheroid Model. *Nanoscale* **2021**, *13* (1), 280–291.

(15) Barua, S.; Yoo, J. W.; Kolhar, P.; Wakankar, A.; Gokarn, Y. R.; Mitragotri, S. Particle Shape Enhances Specificity of Antibody-Displaying Nanoparticles. *Proc. Natl. Acad. Sci. U. S. A.* **2013**, *110* (9), 3270–3275.

(16) Champion, J. A.; Mitragotri, S. Shape Induced Inhibition of Phagocytosis of Polymer Particles. *Pharm. Res.* **2009**, *26* (1), 244–249.

(17) Li, Z.; Sun, L.; Zhang, Y.; Dove, A. P.; O'Reilly, R. K.; Chen, G. Shape Effect of Glyco-Nanoparticles on Macrophage Cellular Uptake and Immune Response. *ACS Macro Lett.* **2016**, *5* (9), 1059–1064.

(18) Zhao, Y.; Wang, Y.; Ran, F.; Cui, Y.; Liu, C.; Zhao, Q.; Gao, Y.; Wang, D.; Wang, S. A Comparison between Sphere and Rod Nanoparticles Regarding Their in Vivo Biological Behavior and Pharmacokinetics. *Sci. Rep.* **2017**, *7* (1), 1–11.

(19) Pearce, A. K.; Wilks, T. R.; Arno, M. C.; O'Reilly, R. K. Synthesis and Applications of Anisotropic Nanoparticles with Precisely Defined Dimensions. *Nat. Rev. Chem.* **2020**, *5* (1), 21–45.

(20) Truong, N. P.; Quinn, J. F.; Whittaker, M. R.; Davis, T. P.; And, F. Polymeric Filomicelles and Nanoworms: Two Decades of Synthesis and Application. *Polym. Chem* **2016**, *7* (26), 4295–4312.

(21) Massey, J. A.; Temple, K.; Cao, L.; Rharbi, Y.; Raez, J.; Winnik, M. A.; Manners, I. Self-Assembly of Organometallic Block Copolymers: The Role of Crystallinity of the Core-Forming Polyferrocene Block in the Micellar Morphologies Formed by Poly(Ferrocenylsilane-b-Dimethylsiloxane) in n-Alkane Solvents. *J. Am. Chem. Soc.* **2000**, *122* (47), 11577–11584.

(22) Jiang, N.; Yu, T.; Darvish, O. A.; Qian, S.; Mkam Tsengam, I. K.; John, V.; Zhang, D. Crystallization-Driven Self-Assembly of Coil-Comb-Shaped Polypeptoid Block Copolymers: Solution Morphology and Self-Assembly Pathways. *Macromolecules* **2019**, *52* (22), 8867–8877.

(23) Yin, R.; Sahoo, D.; Xu, F.; Huang, W.; Zhou, Y. Scalable Preparation of Crystalline Nanorods through Sequential Polymerization-Induced and Crystallization-Driven Self-Assembly of Alternating Copolymers. *Polym. Chem.* **2020**, *11* (13), 2312–2317.

(24) Nabiyan, A.; Biehl, P.; Schacher, F. H. Crystallization vs Metal Chelation: Solution Self-Assembly of Dual Responsive Block Copolymers. *Macromolecules* **2020**, *53* (13), 5056–5067.

(25) Gilroy, J. B.; Gädt, T.; Whittell, G. R.; Chabanne, L.; Mitchels, J. M.; Richardson, R. M.; Winnik, M. A.; Manners, I. Monodisperse Cylindrical Micelles by Crystallization-Driven Living Self-Assembly. *Nat. Chem.* **2010**, *2* (7), 566–570.

(26) Macfarlane, L.; Zhao, C.; Cai, J.; Qiu, H.; Manners, I. Emerging Applications for Living Crystallization-Driven Self-Assembly. *Chem. Sci.* **2021**, *12* (13), 4661–4682.

(27) Ganda, S.; Stenzel, M. H. Concepts, Fabrication Methods and Applications of Living Crystallization-Driven Self-Assembly of Block Copolymers. *Prog. Polym. Sci.* **2020**, *101* (101195), 1–33.

(28) Wang, X.; Guerin, G.; Wang, H.; Wang, Y.; Manners, I.; Winnik, M. A. Cylindrical Block Copolymer Micelles and Co-Micelles of Controlled Length and Architecture. *Science* **2007**, *317* (5838), 644–647.

(29) Arno, M. C.; Inam, M.; Coe, Z.; Cambridge, G.; Macdougall, L. J.; Keogh, R.; Dove, A. P.; O'Reilly, R. K. Precision Epitaxy for Aqueous 1D and 2D Poly(ϵ -Caprolactone) Assemblies. *J. Am. Chem. Soc.* **2017**, *139* (46), 16980–16985.

(30) Schmelz, J.; Schedl, A. E.; Steinlein, C.; Manners, I.; Schmalz, H. Length Control and Block-Type Architectures in Worm-like Micelles with Polyethylene Cores. *J. Am. Chem. Soc.* **2012**, *134* (34), 14217–14225.

(31) Street, S. T. G.; He, Y.; Jin, X.-H.; Hodgson, L.; Verkade, P.; Manners, I. Cellular Uptake and Targeting of Low Dispersity, Dual Emissive, Segmented Block Copolymer Nanofibers. *Chem. Sci.* **2020**, *11* (32), 8394–8408.

(32) Ganda, S.; Wong, C. K.; Stenzel, M. H. Corona-Loading Strategies for Crystalline Particles Made by Living Crystallization-Driven Self-Assembly. *Macromolecules* **2021**, *54* (14), 6662–6669.

(33) He, Y.; Eloi, J. C.; Harniman, R. L.; Richardson, R. M.; Whittell, G. R.; Mathers, R. T.; Dove, A. P.; O'Reilly, R. K.; Manners, I. Uniform Biodegradable Fiber-Like Micelles and Block Comicelles via "Living" Crystallization-Driven Self-Assembly of Poly(l -Lactide) Block Copolymers: The Importance of Reducing Unimer Self-Nucleation via Hydrogen Bond Disruption. *J. Am. Chem. Soc.* **2019**, *141* (48), 19088–19098.

(34) Finnegan, J.; Pilkington, E.; Alt, K.; Rahim, M. A.; Kent, S. J.; Davis, T. P.; Kempe, K. Stealth Nanorods via the Aqueous Living Crystallisation-Driven Self-Assembly of Poly(2-Oxazoline)S. *Chem. Sci.* **2021**, *12* (21), 7350–7360.

(35) Finnegan, J. R.; He, X.; Street, S. T. G.; Garcia-Hernandez, J. D.; Hayward, D. W.; Harniman, R. L.; Richardson, R. M.; Whittell, G. R.; Manners, I. Extending the Scope of "Living" Crystallization-Driven Self-Assembly: Well-Defined 1D Micelles and Block Comicelles from Crystallizable Polycarbonate Block Copolymers. *J. Am. Chem. Soc.* **2018**, *140* (49), 17127–17140.

(36) Merg, A. D.; Van Genderen, E.; Bazrafshan, A.; Su, H.; Zuo, X.; Touponse, G.; Blum, T. B.; Salaita, K.; Abrahams, J. P.; Conticello, V. P. Seeded Heteroepitaxial Growth of Crystallizable Collagen Triple Helices: Engineering Multifunctional Two-Dimensional Core-Shell Nanostructures. *J. Am. Chem. Soc.* **2019**, *141* (51), 20107–20117.

(37) Bousmail, D.; Chidchob, P.; Sleiman, H. F. Cyanine-Mediated DNA Nanofiber Growth with Controlled Dimensionality. *J. Am. Chem. Soc.* **2018**, *140* (30), 9518–9530.

(38) Bains, A.; Cao, Y.; Moffitt, M. G. Multiscale Control of Hierarchical Structure in Crystalline Block Copolymer Nanoparticles Using Microfluidics. *Macromol. Rapid Commun.* **2015**, *36* (22), 2000–2005.

(39) Bains, A.; Wulff, J. E.; Moffitt, M. G. Microfluidic Synthesis of Dye-Loaded Polycaprolactone-Block-Poly(Ethylene Oxide) Nanoparticles: Insights into Flow-Directed Loading and in Vitro Release for Drug Delivery. *J. Colloid Interface Sci.* **2016**, *475* (1), 136–148.

(40) Gou, J.; Feng, S.; Xu, H.; Fang, G.; Chao, Y.; Zhang, Y.; Xu, H.; Tang, X. Decreased Core Crystallinity Facilitated Drug Loading in Polymeric Micelles without Affecting Their Biological Performances. *Biomacromolecules* **2015**, *16* (9), 2920–2929.

(41) Zhuo, X.; Lei, T.; Miao, L.; Chu, W.; Li, X.; Luo, L.; Gou, J.; Zhang, Y.; Yin, T.; He, H.; Tang, X. Disulfiram-Loaded Mixed Nanoparticles with High Drug-Loading and Plasma Stability by Reducing the Core Crystallinity for Intravenous Delivery. *J. Colloid Interface Sci.* **2018**, *529* (1), 34–43.

(42) Garcia-Hernandez, J. D.; Street, S. T. G.; Kang, Y.; Zhang, Y.; Manners, I. Cargo Encapsulation in Uniform, Length-Tunable Aqueous Nanofibers with a Coaxial Crystalline and Amorphous Core. *Macromolecules* **2021**, *54* (12), 5784–5796.

(43) Cao, L.; Manners, I.; Winnik, M. A. Influence of the Interplay of Crystallization and Chain Stretching on Micellar Morphologies: Solution Self-Assembly of Coil−Crystalline Poly(Isoprene- Block -Ferrocenylsilane). *Macromolecules* **2002**, *35* (22), 8258–8260.

(44) Hudson, Z. M.; Boott, C. E.; Robinson, M. E.; Rupar, P. A.; Winnik, M. A.; Manners, I. Tailored Hierarchical Micelle Architectures Using Living Crystallization-Driven Self-Assembly in Two Dimensions. *Nat. Chem.* **2014**, *6* (10), 893–898.

(45) Ganachaud, F.; Monteiro, M. J.; Gilbert, R. G.; Dourges, M.-A.; Thang, S. H.; Rizzardo, E. Molecular Weight Characterization of Poly(N-Isopropylacrylamide) Prepared by Living Free-Radical Polymerization. *Macromolecules* **2000**, *33* (18), 6738–6745.

(46) Swift, T.; Hoskins, R.; Telford, R.; Plenderleith, R.; Pownall, D.; Rimmer, S. Analysis Using Size Exclusion Chromatography of Poly(N-Isopropyl Acrylamide) Using Methanol as an Eluent. *J. Chromatogr. A* **2017**, *1508*, 16–23.

(47) Blanco, E.; Shen, H.; Ferrari, M. Principles of Nanoparticle Design for Overcoming Biological Barriers to Drug Delivery. *Nat. Biotechnol.* **2015**, *33* (9), 941–951.

(48) Caldwell, G. W.; Yan, Z. Cytochrome P450-Mediated Metabolic Stability Assay in Liver Microsomes. In *Cytochrome P450: In Vitro Methods and Protocols*; Caldwell, G. W., Yan, Z., Eds.; Humana Press: New York, 2021; pp 229–242.

(49) Pangborn, A. B.; Giardello, M. A.; Grubbs, R. H.; Rosen, R. K.; Timmers, F. J. Safe and Convenient Procedure for Solvent Purification. *Organometallics* **1996**, *15* (5), 1518–1520.

(50) Malvern Panalytical. *Dynamic Light Scattering : An Introduction in 30 Minutes*; Worcestershire, 2010.

Chapter 4

Fiber-Like Micelle Networks from the Solution Self-Assembly of B-A-B Triblock Copolymers with Crystallizable Terminal Polycarbonate Segments

This chapter contains unpublished results

Contributions:

Synthesis of polymers, and characterization were conducted by Juan Diego Garcia Hernandez. Self-assembly experiments were conducted in collaboration with Dr. Yuetong Kang and Dr. Tomoya Fukui. AFM was conducted by Dr. Yuetong Kang. Initial scientific design of the project conducted by Juan Diego Garcia Hernandez with input from Dr. John Finnegan. Research was conducted at the University of Victoria.

4.1 Abstract

Although the formation of spherical micelle networks from the solution self-assembly of B-A-B triblock copolymers (triBCPs) with solvophobic terminal ‘B’ blocks has been widely studied, the introduction of intermicellar linkages between fiber-like micelles are virtually unexplored. Herein, a B-A-B triBCP was used to achieve nanofiber aggregation via the crystallization of the solvophobic terminal blocks in the cores of distinct nanofibers that are subsequently linked together via the solvophilic coronal ‘A’ block. The triBCP used in this work, $PFTMC_{14}$-*b*-PEG_{900}-*b*-$PFTMC_{14}$, contains two crystallizable terminal poly(fluorenetrimethylenecarbonate) (PFTMC) ‘B’ blocks linked together via a poly(ethylene glycol) (PEG) ‘A’ block. Performing the seeded growth / living crystallization-driven self-assembly (CDSA, at 20 °C) with the triBCP at low concentration (2 mg/mL) and with a low fraction of common solvent (10%), led to the formation of low dispersity flower-like nanofibers with crystalline PFTMC cores and looped coronal chains of controlled lengths. In contrast, when self-assembly of the triBCP was conducted at high concentration (> 5 mg/mL) with high common solvent fraction (20%) at ≥ 70 °C with subsequent cooling to 20 °C, networks of nanofibers were obtained. Networks were also accessible from preformed nanofibers of controlled length prepared from $PFTMC_{15}$-*b*-PEG_{265} diBCP via the addition of the triBCP under similar conditions. Bundling and entanglement of the nanofibers were observed by TEM and AFM. Macroscopic gels were formed when self-assembly was performed at very high concentrations (e.g. 20 mg/mL) and common solvent fractions (20%). Upon future extension to aqueous systems, the nanofiber network formation process would provide a

route to hierarchical assemblies that are of potential interest as gel-like scaffolds for tissue engineering as well as other applications.

4.2 Introduction

The fabrication of high precision functional materials with hierarchical order remains a fundamental challenge for nanoscience.[1,2] Hierarchical assemblies generally possess distinct characteristic properties compared with their constituent molecular or nanoparticle building blocks,[3] enabling their use in a diverse range of applications. For example, as artificial muscles[4] and hydrogels,[5] in nanomedicine,[6,7] optoelectronics,[8,9] and for the sequestration of aromatic species.[10] The vast majority of self-assembled building blocks utilize interactions such as charge-transfer,[11] solvophobic,[12] ion-binding,[4,13] crystallization,[14] π–π stacking,[8,15] and covalent bonding.[16] The use of a combination of these interactions to prepare hierarchical assemblies has been the subject of many investigations.[17–20]

Triblock copolymers (triBCPs) with solvophobic terminal segments have been extensively used for the non-covalent association of spherical micelles.[21–23] At low concentrations, but above the critical micelle concentration, the solvophobic terminal blocks aggregate to form the micelle core of spherical flower-like micelles with a looped corona, also known as spherical rosettes.[21] At higher concentrations, the solvophobic terminal segments can bridge the spherical flower-like micelles into extended nanoparticle networks.[21] Although polymers have been extensively studied to introduce interparticle crosslinks between spherical micelles,[23–32] analogous formation of networks from 1D cylindrical micelles is virtually unexplored. An early example from Lee and coworkers describes the formation of supramolecular nanocylinders from a coil-rod-coil low

molecular weight amphiphile which transition to a nematic gel of reversibly bridged nanocyclinders on addition of a rod-coil-rod analogue.[22] More recently, coordination-driven hierarchical assembly of 1D micelles has been reported where nanocylinders are linked via Pd complexation.[33] In this paper we describe the formation of networks of nanofibers driven by the crystallization of the core-forming solvophobic terminal blocks of a B-A-B triBCP.

A key reason that networks formed from cylindrical micelles remain unexplored arises from the challenge of preparing morphologically pure fiber-like micelles from the self-assembly of BCPs with an amorphous core-forming block.[34] Recently, BCPs with crystallizable core-forming block have been shown to provide a general route to 1D fiber-like micelles via an approach termed crystallization-driven self-assembly (CDSA). This method has allowed access to nanofibers with a wide variety of different crystalline core compositions.[34–40] This approach involves the use of amphiphilic block copolymers with a crystallizable core-forming block which directs the self-assembly into morphologies with low curvature of the core-corona interface and a solvophilic corona-forming block that provides colloidal solubility.[34,37] Moreover, the development of an ambient temperature seeded-growth method termed living CDSA has enabled length control and the formation of fiber-like micelle samples with low length dispersity.[36,38,41–44] The living CDSA method has allowed access to a myriad of morphologies in addition to nanofibers, including 2D platelets as well as segmented and hierarchical assemblies.[17,18,52,53,44–51]

Previously, we reported the formation of flower-like nanofibers made from B-A-B triBCPs via CDSA methods (Figure 4. 1A).[54] The triBCP consisted of two crystallizable poly(ferrocenyldimethylsilane) (PFS) core-forming ‘B’ terminal blocks together with a

poly(dimethylsiloxane) (PDMS) corona-forming ‘A’ central segment. The seeded-growth process, living CDSA, yielded uniform flower-like cylindrical micelles of controlled length. The PDMS corona was found to exclusively exist in a looped conformation, and the two PFS segments of each copolymer chain participated in the formation of the crystalline core-forming block of flower-like cylindrical micelles. No evidence of interfiber bridging by the triBCPs to yield network-like structures was detected in this earlier work (Figure 4. 1A).[54]

In this study we have targeted the development of a nanofiber linking strategy which involves the CDSA of a B-A-B triBCP where the terminal solvophobic and crystallizable B blocks participate in the formation of the crystalline cores of different nanofibers. The triBCP selected contains crystallizable poly(fluorenetrimethylenecarbonate) (PFTMC) terminal blocks. PFTMC BCPs have previously been shown the form morphologically pure nanofiber assemblies via CDSA which possess significant potential for biomedical applications.[55,56] Poly(ethylene glycol) (PEG) was used as a biocompatible solvophilic central ‘A’ block which was targeted for the formation of the nanofiber linkages (Figure 4. 1B, ii). We anticipated that the PFTMC-*b*-PEG-*b*-PFTMC triBCP would also self-assemble into flower-like nanofibers with a crystalline PFTMC core and a looped PEG corona under certain experimental conditions (e.g., involving reduced triBCP concentration. Figure 4. 1B, i), as observed in our previous report for related materials.[54] This study opens the door to the formation of hierarchical assemblies of linked nanofibers that may ultimately find applications in the biomedical field for drug delivery and tissue engineering where noncytotoxic linkers are required.[57]

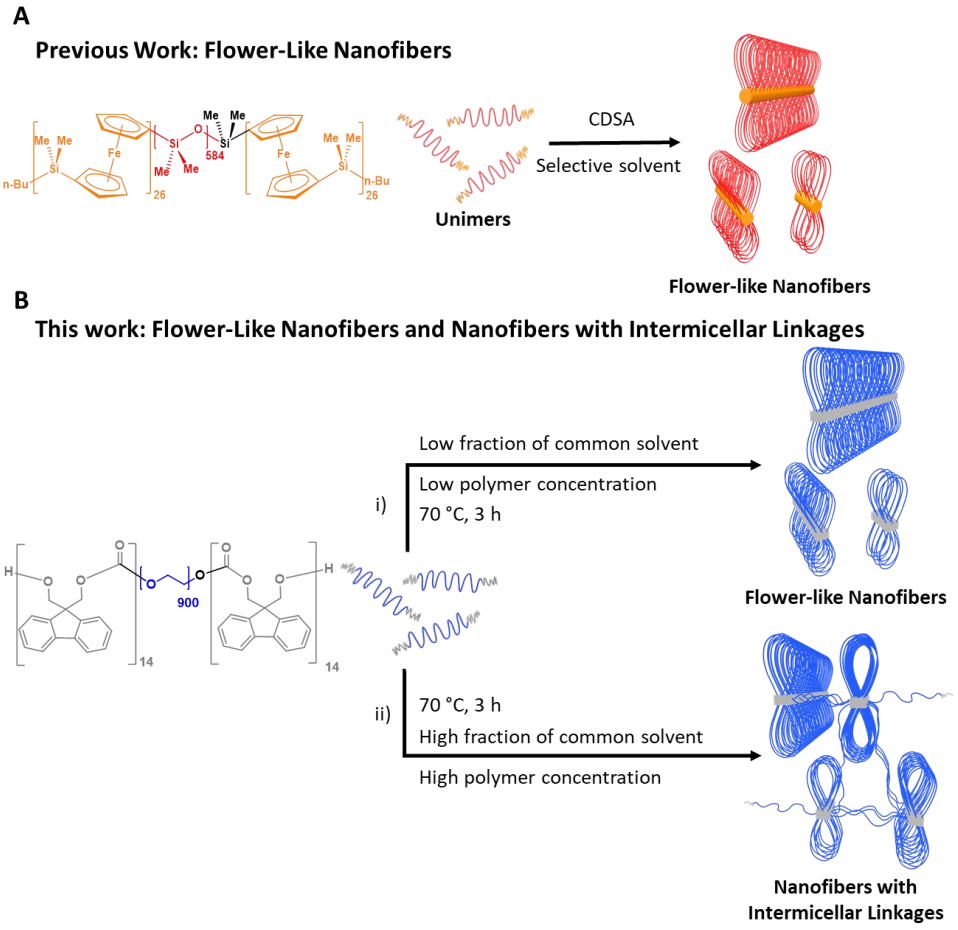

Figure 4. 1. Conceptual design of the intermicellar linking of nanofibers via crystallization of B-A-B triBCP. A) Previous work on the preparation of flower-like nanofibers with PFS-*b*-PDMS-*b*-PFS triBCP.[54] B) Scheme of the $PFTMC_{14}$-*b*-PEG_{900}-*b*-$PFTMC_{14}$ triBCP structure, and the self-assembly conditions explored to i) yield flower-like nanofibers or ii) nanofibers with intermicellar linkages driven by crystallization of the triBCP. Section A has been adapted from reference [54].

4.3 Results and Discussion

4.3.1 Synthesis and Characterization of the $PFTMC_{14}$-*b*-PEG_{900}-*b*-$PFTMC_{14}$ triBCP

The B-A-B PFTMC-*b*-PEG-*b*-PFTMC triBCP was synthesized via the diazabicyclo[5.4.0]undec-7-ene (DBU) catalyzed ring-opening polymerization of the FTMC monomer utilizing diol-PEG as a macroinitiator in dry DCM (Scheme S1). The diol-PEG was characterized using matrix-assisted laser desorption/ionization-time of flight (MALDI-TOF) mass spectrometry (M_n = 35,000 g/mol, Figure S4. 1), and gel permeation chromatography (GPC, $Đ_M$ = 1.17, polystyrene standards, Figure S4. 2). After the

polymerization, the triBCP was purified and isolated as a white solid (in a yield of 70%). The triBCP was characterized via GPC (M_n = 32,300, $Đ_M$ = 1.19, Figure S4. 2), and the degree of polymerization (DP_n) of each block was determined by ^{1}H NMR integration using end-group analysis. This data indicated that the structure of the triBCP was $PFTMC_{14}$-*b*-PEG_{900}-*b*-$PFTMC_{14}$ (Figure S4. 3). A $PFTMC_{15}$-*b*-PEG_{265} diBCP was also used to prepare nanofibers during our studies and this material was synthesized by following an analogous, previously reported procedure[55] (DP_n calculated by ^{1}H NMR via end-group analysis. M_n = 13,200, $Đ_M$ = 1.16 by GPC, Table S4. 1, Figure S4. 4-5). A summary of the characterization of the polymers used in this work is presented in Table S4. 1.

4.3.2 Self-Assembly of $PFTMC_{14}$-*b*-PEG_{900}-*b*-$PFTMC_{14}$ TriBCP into Flower-Like Nanofibers

The solution state self-assembly of the $PFTMC_{14}$-*b*-PEG_{900}-*b*-$PFTMC_{14}$ was initially investigated at conditions under which no linkages between micelles were expected to occur. These involved a low triBCP concentration and low fraction of common solvent (10% DMSO in MeOH as selective solvent). Previous work has established that intermicellar linking is disfavored by decreasing the triBCP polymer concentration,[21] and also that the rate of CDSA is more rapid in poorer solvents for the crystallizable core-forming block, which suggests that low fractions of common solvent should favor the formation of discrete rather than linked nanofibers.[58] When a solution of the $PFTMC_{14}$-*b*-PEG_{900}-*b*-$PFTMC_{14}$ triBCP (2 mg/mL) in 10:90 DMSO:MeOH *v/v* was heated to 70 °C for 3 h, then cooled to 20 °C and aged for 48 h, discrete, long, length-disperse nanofibers (lengths >3 μm, Figure 4. 2A-B) were detected via transmission electron microscopy (TEM) analysis. The nanofibers presumably possess a looped corona as the absence of

nanofiber linkages and aggregates by TEM indicated that both terminal PFTMC chains in each triBCP participate in core formation in the same nanofiber.

Seed nanofibers were prepared by sonication of the long and length-disperse $PFTMC_{14}$-*b*-PEG_{900}-*b*-$PFTMC_{14}$ nanofibers for 3 h, at 15 – 20 °C, in 10:90 DMSO:MeOH. TEM analysis revealed short seed nanofibers of $L_{n(seed)}$ = 25 nm in length ($Đ$ = 1.12, σ = 9 nm, Figure 4. 2C). Two different orientations of the seed nanofibers were observed by TEM, consistent to a rectangular cross-section, the seeds can lay on their largest face or on their edge[55] (Figure 4. 2C). The living CDSA method was then used to prepare nanofibers of controlled dimensions and low length-dispersities. For this, unimeric $PFTMC_{14}$-*b*-PEG_{900}-*b*-$PFTMC_{14}$ in DMSO (10 mg/mL) was added to diluted nanofiber seed solutions ($L_{n(seed)}$ = 25 nm, 0.1 mg/mL, in 10:90 DMSO:MeOH mixtures), followed by a 48 h aging period. By tuning the unimer-to-seed ratio (m_{unimer}/m_{seed}) from 0:1 to 40:1, length control of the nanofibers was achieved from $L_{n(seed)}$ = 25 nm ($Đ$ = 1.12, σ = 9 nm) to L_n = 806 nm ($Đ$ = 1.06, σ = 192 nm), as evidenced by TEM (Figure 4. 2D-I, S6). Within error, the experimental length of the resulting nanofibers is consistent with the predicted length, $L_{n(theory)}$, given by $L_{n(theory)} = (L_{n(seed)} \times ({}^{m_{unimer}}/_{m_{seed}}) + L_{n(seed)}).,(eq.1)$ of unimer added to 25 nm (σ = 9 nm) seed solutions and the anticipated linear relationship between the final length and m_{unimer}/m_{seed} ratio was observed (Figure 4. 2I-J). The formation of discrete low-length dispersity nanofibers with controlled dimensions that matched the predicted nanofiber lengths according to *eq. 1* indicated that no significant intermicellar linking of nanofibers occurs using CDSA at low polymer concentration (2 mg/mL) and low common solvent fraction (~10% DMSO. Figure 4. 2H, J). A summary of the statistical

analysis of the contour length measurements of $PFTMC_{14}$-*b*-PEG_{900}-*b*-$PFTMC_{14}$ nanofibers prepared via the seeded growth method is presented in Table S4. 2.

To further characterize the discrete nanofibers atomic force microscopy (AFM) measurements were performed on a low-length dispersity sample prepared via the living CDSA method (in MeOH, m_{unimer}/m_{seed} = 30. L_n = 670 nm, $Đ$ = 1.05, σ = 155 nm, by TEM). By AFM, the core height and width dimensions of the discrete nanofibers were 7.5 nm (σ = 0.5 nm) and 25 nm (σ = 1.2 nm), respectively (Figure S4. 7). These dimensions are in close agreement with the reported sizes of the $PFTMC_{18}$-core of discrete diBCP nanofibers.[55] Furthermore, the PFTMC chains are oriented perpendicular to the substrate with the height value of 7.5 nm corresponding to one-chain fold of $PFTMC_n$ (DP_n = 18), in agreement with a previous report.[55] Significantly, the width and height data is consistent with the formation of discrete nanofibers without intermicellar linking which would lead to substantially larger values (see section 4.3.3). In combination with the aforementioned TEM data, this AFM evidence indicates that the terminal PFTMC segments in each triBCP participate in the core formation of the nanofibers with a looped PEG corona yielding flower-like nanofibers.

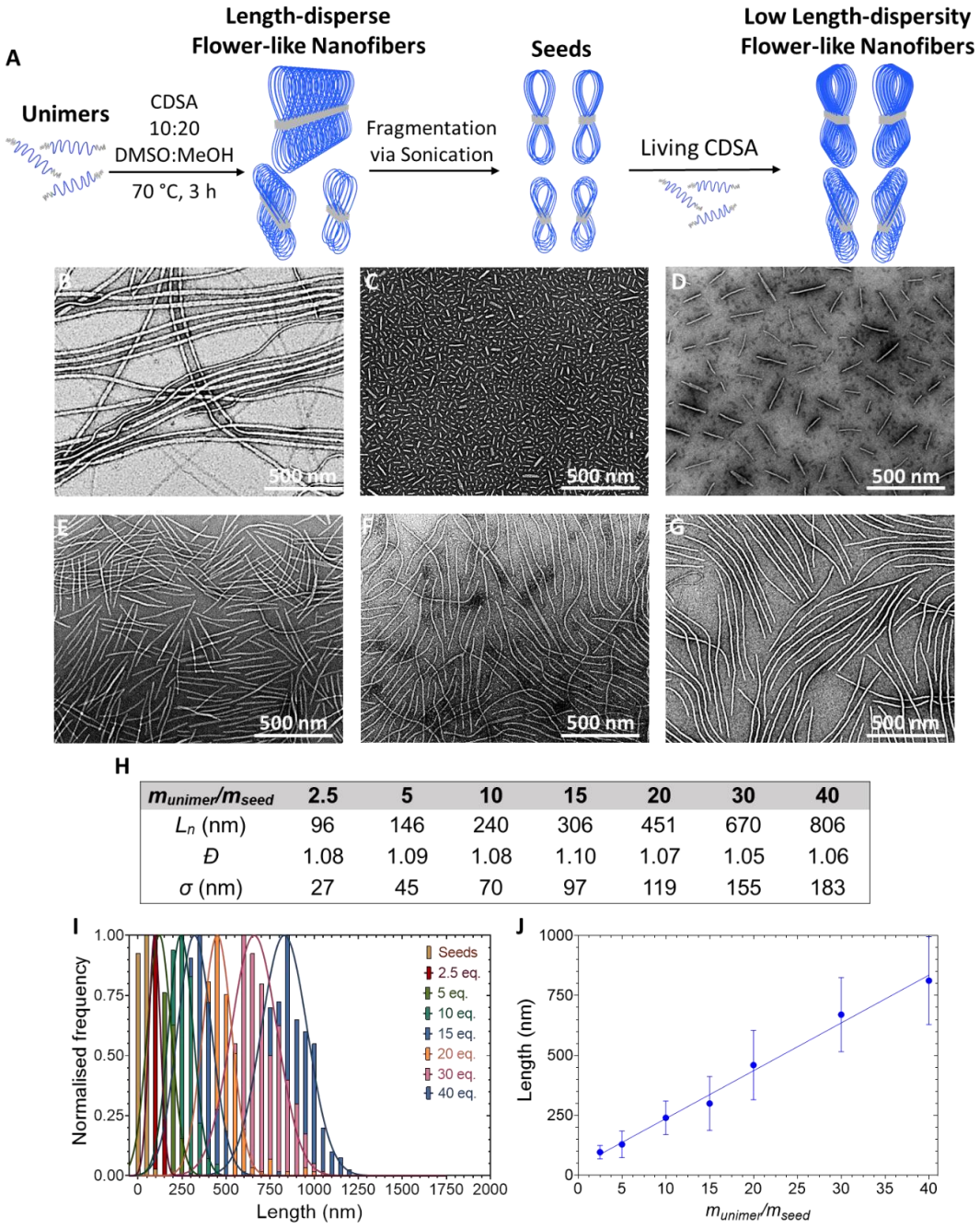

m_{unimer}/m_{seed}	2.5	5	10	15	20	30	40
L_n (nm)	96	146	240	306	451	670	806
$Đ$	1.08	1.09	1.08	1.10	1.07	1.05	1.06
σ (nm)	27	45	70	97	119	155	183

Figure 4. 2. Preparation of low dispersity flower-like nanofibers of controlled lengths via the Living CDSA method. A) Schematic representation of the preparation process of low dispersity flower-like nanofibers prepared from $PFTMC_{14}$-*b*-PEG_{900}-*b*-$PFTMC_{14}$. B) Disperse nanofibers prepared in DMSO:MeOH (10:90) via CDSA. C) TEM image of seed nanofibers (25 nm, $Đ$ = 1.12, σ = 9 nm) prepared via the sonication of the disperse nanofibers in A. D-G) TEM images of the resulting low dispersity flower-like nanofibers prepared through the seeded-growth method via the addition of $PFTMC_{14}$-*b*-PEG_{900}-*b*-$PFTMC_{14}$ unimer in DMSO to nanofiber seed solutions at $m_{unimver}/m_{seed}$ ratio of D) 5:1 E) 15:1 F) 30:1 and G) 40:1, respectively. H) nanofiber length analysis summary. I) Contour length histograms of the seeds and low-dispersity flower-like nanofibers. J) Plot of nanofiber average length (L_n) versus m_{unimer}/m_{seed} ratio. TEM images were stained with uranyl acetate (3 wt% in EtOH).

4.3.3 Effect of the B-A-B TriBCP Concentration and the Fraction of Common Solvent on Fiber-like Micelle Network Formation

Following the preparation of $PFTMC_{14}$-*b*-PEG_{900}-*b*-$PFTMC_{14}$ flower-like nanofibers we attempted to access samples with intermicellar linkages between particles. For comparison, a sample was prepared via CDSA at identical solvent and experimental conditions as in Figure 4. 2B, but at a higher triBCP concentration (5 mg/mL). Therefore, the sample was prepared using a 10:90 DMSO:MeOH *v/v* solvent mixture, heated to 70 °C for 3 h, subsequently cooled to 20 °C, and aged for 48 h. Long length-disperse nanofibers (>3 μm) were observed via TEM analysis (Figure 4. 3B). The blue arrows in Figure 4. 3D, indicate overlapping nanofibers and nanofibers whose ends are in close proximity but not linked. The red arrow points towards an area where it seems that two nanofibers could be linked, in contrast to Figure 4. 2B where no similar nanofiber arrangements were found. Inspection of the vial containing the sample revealed a few macroscopic gel-like aggregates highlighted in red circles (Figure S4. 8A). Together, the TEM data and the formation of small gel-like aggregates suggested that a small degree of nanofiber network-formation at 5 mg/mL (10:90 DMSO:MeOH) may be occurring, but further investigations were needed. These results prompted us to find optimal conditions to achieve nanofiber linking via an increase of the common solvent fraction.

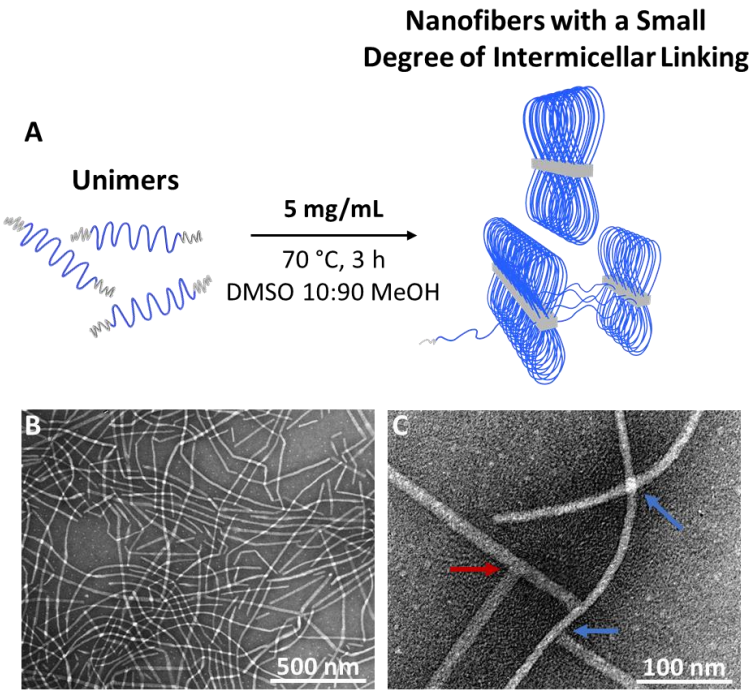

Figure 4. 3. $PFTMC_{14}$-*b*-PEG_{900}-*b*-$PFTMC_{14}$ triBCP concentration dependence on the intermicellar nanofiber formation process of the flower-like nanofibers. A) Schematic illustration of flower-like nanofibers with a small degree of intermicellar linking prepared via CDSA). B-C) TEM images of flower-like nanofibers with a small degree of intermicellar linking 5 mg/mL in DMSO:MeOH 10:90 (*v/v*).

The small degree of intermicellar linking of the flower-like nanofibers observed at 5 mg/mL with 10% DMSO (Figure 4. 3, S8A) encouraged us to find conditions to achieve a higher degree of micellar network formation via an increase of the fraction of common solvent. This would be expected to slow nanofiber formation due to greater unimer solubility,[58] which would be expected to favor the incorporation of the two terminal core-forming PFTMC blocks in different nanofibers. Therefore, CDSA was performed at the same 'high' triBCP concentration (5 mg/mL, as in Figure 4. 3), but the fraction of common solvent was increased from 10% to 20% DMSO (80% MeOH, Figure 4. 4). The sample was prepared by heating to 70 °C for 3 h, subsequently cooled to 20 °C, and aged for 48 h. TEM analysis of the sample prepared with 20% DMSO revealed the formation of straight fiber-like aggregates of few μm long (Figure 4. 4B-E, S9), with some aggregates displaying a corkscrew twist. The morphological conformation of the fiber-like aggregates prepared

at 5 mg/mL and 20% DMSO (Figure 4. 4B-E) contrasts significatively with the appearance of the discrete flower-like nanofibers and of nanofibers with a small degree of intermicellar linking observed by TEM (Figure 4. 2B, 3). Contour width analyses (Figure 4. 4F) were conducted on $PFTMC_{14}$-*b*-PEG_{900}-*b*-$PFTMC_{14}$ intermicellar linked nanofibers (Figure 4. 4B-E, S9) and discrete triBCP flower-like nanofibers (Figure 4. 2B), from TEM micrographs. The number-average width (W_n) of the former fiber-like aggregates was W_n = 50 nm ($Đ$ = 1.18, σ = 22 nm), whereas the number-average width of the discrete flower-like nanofibers was considerably smaller i.e., W_n = 11 nm ($Đ$ = 1.04, σ = 2 nm, Figure 4. 4F). Hence by TEM, the width of the fiber-like aggregates prepared with 20% DMSO content corresponds to ~five-times the width of discrete triBCP nanofibers implying that the former can be regarded as nanofiber bundles.

Tapping mode AFM analysis of the triBCP fiber-like aggregates (5 mg/mL, 20:80 DMSO:MeOH) revealed the presence of large linear assemblies (AFM samples diluted to 0.05 mg/mL in MeOH and casted on a silicon wafer. Figure 4. 4G). The AFM profile of the nanofiber aggregates revealed structures with heights ranging from 40 – 100 nm and widths larger than 100 nm (Figure 4. 4H). In contrast, the dimensions of discrete flower-like triBCP nanofibers (2 mg/mL, 10:90 DMSO:MeOH. Figure 4. 2B) were considerably smaller with heights and widths of 7.5 nm and 25 nm, respectively, via AFM analysis (Figure S4. 7), consistent with the dimensions of the crystalline $PFTMC_{18}$ block in diBCP nanofibers (height = 8.5, and width = 25 nm).[55,56] Furthermore, the formation of macroscopic gel particles accompanied by a noticeable increase in the viscosity and light scattering was observed for a sample of the fiber-like aggregates (5 mg/mL, 20% DMSO.

Figure S4. 8B) when compared to an analogous sample containing only 10% of DMSO (Figure S4. 8A).

To provide further evidence for the intermicellar linking of nanofibers, dynamic light scattering (DLS) measurements were conducted on three different length-disperse nanofiber samples; intermicellar linked PFTMC$_{14}$-*b*-PEG$_{900}$-*b*-PFTMC$_{14}$ triBCP nanofibers (5 mg/mL, 20:80 DMSO:MeOH. Figure 4. 4B-E, S9), discrete flower-like triBCP nanofibers (2 mg/mL, 10:90 DMSO:MeOH. Figure 4. 2B), and PFTMC$_{15}$-*b*-PEG$_{265}$ diBCP (5 mg/mL, 20:80 DMSO:MeOH. Figure S4. 10). The nanofiber solutions were prepared similarly via CDSA by heating to 70 °C for 3 h, then cooled to 20 °C and aged for 48 h. Analysis of the three samples of length-disperse nanofibers was conducted with nanofiber solutions diluted in MeOH (0.015 mg/mL, Figure 4. 4I). By DLS, the mean hydrodynamic size ($R_{h,z}$) of the intermicellar linked triBCP nanofibers was ca. three-times larger ($R_{h,z}$ = 706 nm, $Đ$ = 1.35, green trace) than the hydrodynamic size of both discrete flower-like nanofibers ($R_{h,z}$ = 225 nm, $Đ$ = 1.19, pink trace), and diBCP nanofibers ($R_{h,z}$ = 193 nm, $Đ$ = 1.22, black trace). The DLS trace of the intermicellar linked triBCP nanofibers (green trace) shows a shoulder towards the lower hydrodynamic size region that may arise from a small population of nanofibers that do not participate on the linked network (Figure 4. 4I). Taken together, the evidence collected via TEM (including contour width analysis), AFM, the increase in light scattering and viscosity, the formation of macroscopic gel particles, and DLS corroborate the formation of intermicellar networks via the linking of nanofibers formed at high polymer concentration and high common solvent (Figure 4. 4A-I, S8-9).

To explore if a higher degree of nanofiber network formation can be achieved, the concentration of the triBCP was increased from 5 to 20 mg/mL (in 20:80 DMSO:MeOH). The sample was prepared by heating to 70 °C for 3 h, subsequently cooled to 20 °C, and aged for 48 h. Large macroscopic gel particles of size 2 – 4 mm were observed on the walls of sample vials (Figure 4. 4J, S11A), indicating a higher degree of intermicellar linkages being formed (compared to Figure 4. 4B-E, G). AFM and TEM analysis revealed the formation of intermicellar linked nanofiber networks of several μm long with heights (by AFM) and widths ranging from ca. 40 – 100 nm (Figure S4. 11B-C). For comparison, a 20 mg/mL sample at high common solvent fraction (20:80 DMSO:MeOH) containing discrete nanofibers from the analogous diBCP $PFTMC_{15}$-*b*-PEG_{265} was prepared by an identical experimental procedure. Visual inspection of the diBCP nanofiber solution revealed it to be clear with no evidence of macroscopic aggregates (Figure S4. 12A). Discrete length-disperse diBCP nanofibers with a length of ca. 2 – 3 μm were observed by TEM and no evidence for micelle linking was detected (Figure S4. 12B). These results highlight the ability of the triBCP to yield intermicellar networks of nanofibers at high polymer concentration, and high common solvent content using a thermal CDSA procedure.

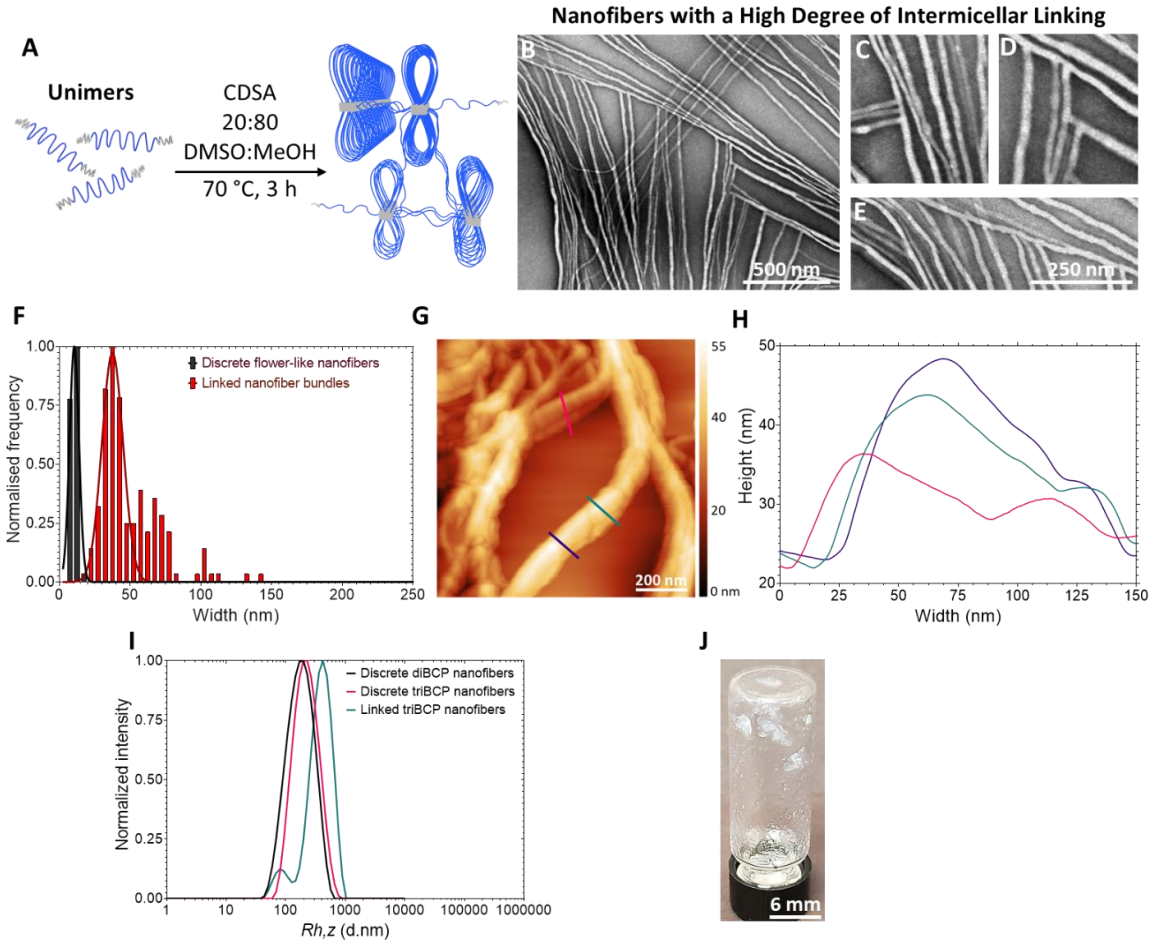

Figure 4. 4. Effect of the fraction of common solvent on fiber-like micelle network formation of PFTMC$_{14}$-*b*-PEG$_{900}$-*b*-PFTMC$_{14}$ nanofibers. A) Schematic representation of the preparation of nanofibers with a high degree of intermicellar linking driven by the crystallization of the PFTMC segments on distinct nanofibers at 5 mg/mL, 20:80 DMSO:MeOH *v/v*, heating to 70 °C for 3 h, and aging for 48 h; B-E) TEM micrographs of nanofibers with a high degree of intermicellar linking where straight nanofiber bundles and T-junctions are observed. F) Contour width histograms of intermicellar linked triBCP nanofibers (W_n = 50 nm, $Đ$ = 1.18, σ = 22 nm, on Figure 4. 4B-E, and S9), and discrete flower-like triBCP nanofibers (W_n = 11 nm, $Đ$ = 1.04, σ = 2 nm, Figure 4. 3B). G-H) Tapping mode AFM micrograph and heigh profile of PFTMC$_{14}$-*b*-PEG$_{900}$-*b*-PFTMC$_{14}$ intermicellar linked nanofiber networks (5 mg/mL, 20:80 DMSO:MeOH) diluted to 0.05 mg/mL in MeOH (cast on a silicon wafer). I) DLS analysis of PFTMC$_{14}$-*b*-PEG$_{900}$-*b*-PFTMC$_{14}$ intermicellar linked nanofiber networks (5 mg/mL, 20:80 DMSO:MeOH, green trace), discrete PFTMC$_{14}$-*b*-PEG$_{900}$-*b*-PFTMC$_{14}$ flower-like nanofibers (2 mg/mL, 10:90 DMSO:MeOH, pink trace), and PFTMC$_{15}$-*b*-PEG$_{265}$ diBCP nanofibers (5 mg/mL 20:80 DMSO:MeOH, black trace). DLS samples diluted to 0.015 mg/mL in MeOH for analysis. J) Digital image of the vial containing triBCP nanofibers with a high degree of intermicellar linking (20 mg/mL 20:80 DMSO:MeOH).

4.3.4 Formation of Diblock Copolymer Nanofiber Networks via TriBCP linking

We attempted to introduce intermicellar linking to discrete PFTMC-*b*-PEG diBCP nanofibers via the addition of the triBCP linker using the living CDSA procedure. To facilitate the epitaxial growth of triBCP at the termini of diBCP nanofibers the DP_n of the PFTMC block of the latter was designed to closely match that of the PFTMC blocks of the triBCP ($PFTMC_{14}$-*b*-PEG_{900}-*b*-$PFTMC_{14}$). Furthermore, the DP_n of the PEG block of the diBCP was 265, around three-times shorter than the PEG_{900} segment of the triBCP. This was expected to ensure that the corona of the diBCP nanofibers does not pose a significant steric barrier for the linking process. Low dispersity $PFTMC_{15}$-*b*-PEG_{265} diBCP nanofibers were prepared via living CDSA (L_n = 359 nm, $Đ$ = 1.06, σ = 89 nm, in 10:90 DMSO:MeOH. Figure 4. 5A, S14D, see supplementary discussion of the self-assembly procedure and Figure S4. 13-14).

Two separate solutions of these diBCP nanofibers with different concentrations 0.5 or 5mg/mL (in 10:90 DMSO:MeOH) were prepared and the temperature of the self-assembly solution was kept at 50 °C for 15 min prior to the addition of the triBCP. To these solutions, 1 equivalent of triBCP unimer was added in one portion (5 µL in DMSO, 5 or 50 mg/mL, respectively). The solutions were kept at 50 °C for 2 h, subsequently cooled to 20 °C and aged for 48 h. The polymer concentration after the addition of unimer to the two samples were 0.91 to 9.1 mg/mL, respectively (18:82 DMSO:MeOH *v/v*). TEM examination of the nanofibers formed in the experiment conducted at 0.91 mg/mL revealed that elongation had taken place to give a length increase (L_n = 691 nm, $Đ$ = 1.03, σ = 112 nm, Figure 4. 5B-D, S15A) with discernible newly grown segments, compared to the length of the initial diBCP nanofibers (L_n = 359, $Đ$ = 1.06, Figure 4. 5A). The resulting length of the nanofibers is in agreement (L_n = 691 nm, $Đ$ = 1.03) with that expected for the addition

of 1 equivalent of triBCP unimer to diBCP nanofibers with L_n = 359 nm (σ = 89 nm, Figure 4. 5A) with experimental error. In addition, only a small number of linked nanofibers was observed by TEM (Figure 4. 5E) and no macroscopic gel particles were observed via visual inspection of the vial containing the sample (Figure S4. 15B). From these results it can be inferred that no significant internanofiber linking of diBCP nanofibers occurs for the 0.91 mg/mL sample. Instead, the triBCP unimer appears to give discrete segmented B-***m***-A-***m***-B nanofibers with flower-like nanofiber terminal segments derived from the triBCP and a central segment derived from the diBCP (Figure 4. 5B-E, S15A-B. **'*m*'** used to distinguish between different fiber-like micelle segments). In contrast, TEM analysis of the sample at 9.1 mg/mL revealed a large number of nanofiber bundles (Figure 4. 5F-J, S15C), reminiscent to the nanofiber micelle networks formed when the triBCP alone undergoes CDSA at high concentration and with a large fraction of common solvent (Figure 4. 4, S9, S11). Visual inspection of the sample revealed a cloudy solution and the formation of macroscopic gel particles (Figure S4. 15D). This suggests that the triBCP can effectively link $PFTMC_{15}$-*b*-PEG_{265} diBCP nanofibers under conditions of high concentration (9.1 mg/mL), high common solvent content (DMSO, 18%), and high temperature (50 °C), Figure 4. 5, S15. For a summary of these and supplementary experiments see Table S4. 3, the Supplementary Discussion on intermicellar linking studies with $PFTMC_{15}$-*b*-PEG_{265} diBCP nanofibers conducted at 20 °C via the addition of the triBCP (Figure S4. 16), and thermally-induced unimer dissociation analysis of $PFTMC_{15}$-*b*-PEG_{265} diBCP nanofibers (Figure S4. 17).

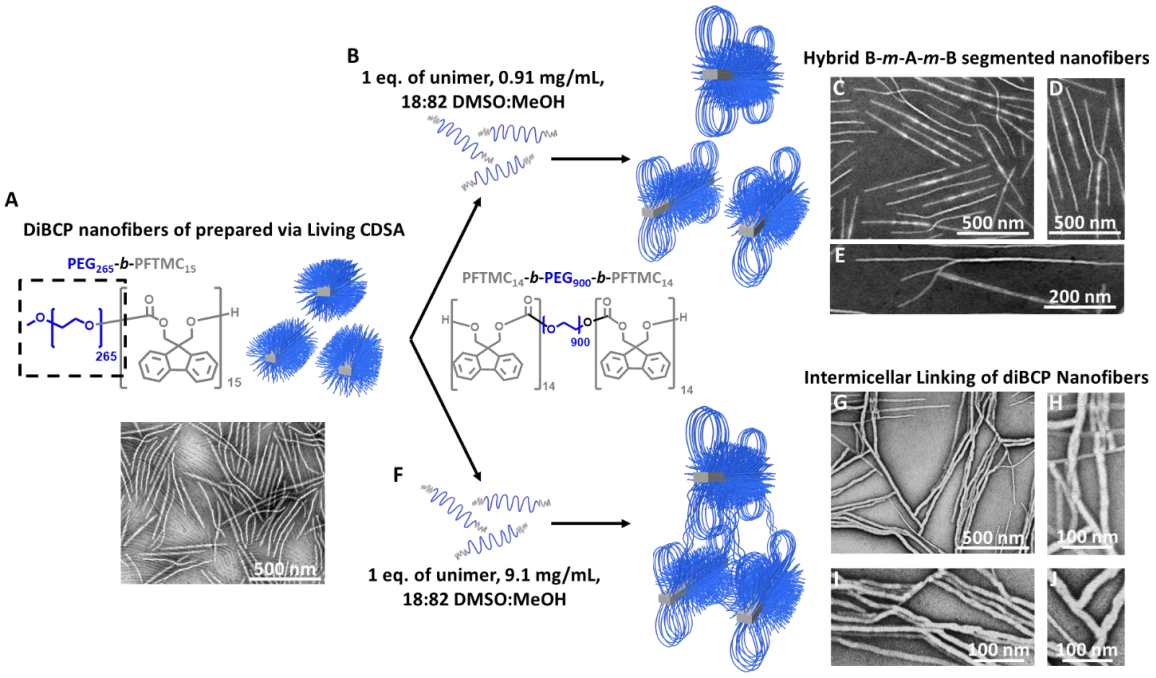

Figure 4. 5. Preparation of discrete hybrid B-*m*-A-*m*-B segmented nanofibers ($PFTMC_{14}$-*b*-PEG_{900}-*b*-$PFTMC_{14}$-*m*-$PFTMC_{15}$-*b*-PEG_{265}-*m*-$PFTMC_{14}$-*b*-PEG_{900}-*b*-$PFTMC_{14}$) and intermicellar linked nanofibers prepared from $PFTMC_{14}$-*b*-PEG_{265} seed nanofibers (L_n = 359 nm, $Đ$ = 1.06, σ = 89 nm) by the addition of the B-A-B triBCP. '*m*' used to distinguish between different fiber-like micelle segments. A) Schematic representation and TEM micrograph of $PFTMC_{14}$-*b*-PEG_{265} seed nanofibers. B) Preparation of discrete hybrid B-A-B segmented nanofibers by adding 1 equivalent of triBCP unimer to 0.5 mg/mL diBCP nanofiber solution. C-E) TEM micrographs of discrete hybrid B-A-B segmented nanofibers (L_n = 691 nm, $Đ$ = 1.03, σ = 112 nm). F) Preparation of intermicellar diBCP nanofiber networks by adding 1 equivalent of triBCP unimer to a 5 mg/mL diBCP nanofiber solution. G-J) TEM micrographs of interlinked nanofibers.

4.4 Summary and Conclusions

In summary, the self-assembly of a B-A-B $PFTMC_{14}$-*b*-PEG_{900}-*b*-$PFTMC_{14}$ triBCP with two crystalline terminal PFTMC 'B' blocks was studied. At low polymer concentrations (< 5 mg/mL), and low fraction of common solvent (~10% DMSO) the triBCP yielded length-disperse flower-like nanofibers via the CDSA method (after heating and cooling). The living CDSA process enabled access to discrete low dispersity flower-like nanofibers of tunable lengths from L_n = 25 – 806 nm ($Đ \leq 1.10$). At these conditions, the PEG_{900} block of the triBCP assumed a looped conformation allowing the two $PFTMC_{14}$-block ends to crystallize in the nanofiber core, yielding flower-like nanofibers as evidenced by TEM and AFM analysis.

Nanofiber linked networks were obtained via the CDSA of the triBCP at high polymer concentrations (> 5 mg/mL), high common solvent for the triBCP (> 18% DMSO), and a heating and cooling cycle. These three parameters were found critical to achieve nanofiber network formation via the novel internanofiber linking method, as shown by TEM, AFM, and DLS analysis. The intermicellar nanofiber networks arranged in linear nanofiber bundles and yielded macroscopic gel-like aggregates. The intermicellar linking was only accomplish when the triBCP was used as opposed to when a diBCP was used. In addition, low dispersity PFTMC$_{15}$-*b*-PEG$_{265}$ diBCP nanofibers (L_n = 358, $Đ$ = 1.06) were noncovalently linked by addition of the triBCP yielding internanofiber networks and macroscopic gel-like aggregates. To our knowledge, this is the first report of the intermicellar linking of crystalline core diBCP and triBCP nanofibers via the addition of an A-B-A triBCP linker.

The evidence collected indicates a competitive mechanism between the crystallization-driven nanofiber growth (CDSA and living CDSA) and the internanofiber linking process. This work has potential applications in the fields of tissue engineering and materials reinforcement. It also allows access to new hierarchical conformations of nanomaterials able to form intermicellar networks via a triBCP linker. This methodology may be extended to other BCP systems known to undergo CDSA.

4.5 Supporting Information

4.5.1 General Considerations and Instrumentation

1,8-diazabicyclo[5.4.0]undec-7-ene (DBU) was purchased from Aldrich, dried over CaH_2, and purified by distillation under reduced pressure. Fluorene for the synthesis of the spiro[fluorene-9,5′-[1,3]-dioxan]-2′-one (FTMC) monomer was purchased from Combi Blocks (United States). FTMC monomer was synthesized according to the procedure reported by Finnegan et al.[55] The methoxy and diol PEGs used were purchased from Polymer Source and dried via vacuum desiccation over phosphorus pentoxide prior to use. Anhydrous solvents were dried and purified using an MBraun Grubbs/Dow solvent purification system.[59] All other reagents and solvents were purchased from Sigma-Aldrich (Canada), VWR (Canada), Fisher Scientific (Canada) and used as received unless otherwise noted. Solvents for self-assembly were HPLC grade and were filtered through PTFE or nylon membranes with a pore size of 0.2 μm before use. All reactions were carried out in an MBraun 200B glove box under a nitrogen atmosphere or using standard Schlenk line techniques.

Ultrasonication

Sonication of micelles was carried out in a Fisherbrand 112xx series advanced ultrasonic cleaner (FB-11203). The instrument was operated in sweep mode at 80% power and 37 MHz at for 3 h at 15 – 20 °C.

NMR Spectroscopy

^{1}H NMR spectra were obtained from a Bruker 500 MHz spectrometer with CD_2Cl_2 (^{1}H NMR: δ = 5.32 ppm;) as the solvent. Chemical shifts are quoted in parts per million (ppm), with spectra referenced to the residual solvent peak. Multiplicities are abbreviated as brs (broad singlet), s (singlet), d (doublet), t (triplet), q (quartet), p (pentet), m (multiplet) and *app.* (apparent) or combinations thereof.

Gel permeation chromatography (GPC)

GPC was conducted on a Malvern OMNISEC chromatograph equipped with a refractive index (RI), UV/Vis photodiode detector array, light scattering detector and viscometer. Triethylamine/THF (1% *v/v*) was used as the eluent, with the flow rate set at 1 mL/min. The columns used were grade T3000, followed by T5000 (Viscotek) at a constant temperature of 35 °C. The calibration (universal) of the RI detector was carried out using polystyrene standards (Viscotek). Samples were prepared at 1 mg/mL in eluent and filtered through a polytetrafluoroethylene membrane filter, pore size = 0.2 µm.

Matrix-assisted laser desorption/ionization-time of flight mass spectrometry (MALDI-TOF MS)

MALDI-TOF MS measurements performed using a Bruker Ultraflextreme running in linear mode. Samples prepared using a trans-2-[3-(4-tert-butylphenyl)-2-methyl-2-propenylidene]malononitrile matrix (20 mg/mL in THF) and the polymer sample (2 mg/mL in THF), mixed in a 10:1 (v/v) ratio. Approximately 3 µL of the mixed solution was deposited onto a stainless-steel sample plate and allowed to dry in air.

Transmission electron microscopy (TEM)

TEM images were obtained on a JEOL 1011 microscope with an 11 Megapixel CCD camera, at the electron acceleration voltage of 80 kV. Samples were prepared by drop-casting 8 µL of the micelle solution onto a carbon-coated copper grid, followed by drop-casting 8 µL of uranyl acetate in EtOH (3 wt %). Sample concentration for TEM analysis was either 0.5 or 0.1 mg/mL based on nanofiber concentration. Copper grids (400 mesh) were purchased from Ted Pella, and carbon films (ca. 6 nm) were prepared on mica sheets by carbon sputtering with a Leica ACE 600 carbon coater. The carbon films were deposited onto the copper grids by floatation on water and the carbon-coated grids allowed to dry in air. All samples examined via TEM were cast onto a plasma treated carbon-coated

copper grids and negatively stained with a 3 wt% uranyl acetate solution (in ethanol). The staining solution interacted well with the PEG corona-block but not with the PFTMC crystalline-core, resulting in the observation of a bright nanofiber-core against a dark background.[55]

For micelle contour lengths and widths analysis, a minimum of 150 nanofibers in several images were traced manually using the ImageJ software package developed at the US National Institute of Health. The number average micelle length (L_n) or width (W_n) and weight average micelle length (L_w) were calculated using eq. S1-2 from measurements of the contour lengths (L_i) of individual micelles, where N_i is the number of micelles of length L_i, and n is the number of micelles examined in each sample. The distribution of micelle lengths is characterized by $Đ = L_w/L_n$.

$$L_n = \frac{\sum_{i=1}^{n} N_i L_i}{\sum_{i=1}^{n} Ni} \qquad L_w = \frac{\sum_{i=1}^{n} N_i L_i^2}{\sum_{i=1}^{n} NiLi} \quad \text{(eq. S1-2)}$$

Atomic Force Microscopy

AFM analysis was obtained using a 5500 Atomic Force Microscope (Agilent Technologies). The images were recorded in the AC mode with a scanning speed of 1.0 μm/s in an area of 4.0 μm^2 at 1024 × 1024 resolution. The tips employed (Tap150Al-G, Budget Sensors) consisted of a conical silicon tip with aluminum reflective coating and a resonance frequency and force constant of 150 kHz and 5N/m, respectively. The samples for AFM were prepared on a silicon wafer by casting the nanofiber solution (in ~ 100% MeOH, 20 μL, 0.05 mg/mL) onto the clean silicon wafer. The silicon wafer was gently dried from the sides with a filter paper and dried via vacuum desiccation.

Dynamic light scattering

Dynamic light scattering (DLS) experiments were carried out using a Zetasizer Pro. The nanofiber samples were prepared in filtered MeOH through a 0.45 μm membrane filter into an optical quartz glass cuvette (PCS8501 type, 10.0 mm light path). The correlation function was acquired in real time and analysed with a function capable of modelling multiple exponentials (Cumulant analysis). This process enabled the diffusion coefficients for the component particles to be extracted, and these were subsequently expressed as the intensity weighted mean hydrodynamic size ($R_{h,z}$) Stokes-Einstein relationship for coated spheres, with core properties of polystyrene latex (RI = 1.590, Absorption = 0.010, dispersant RI = 1.33, dispersant viscosity = 0.548, dispersant dielectric constant 33).

UV-Vis absorbance

UV-Vis absorbance spectra was recorded on a Varian Cary 100 Bio spectrophotometer at different temperatures (25 – 90 °C). Figure S4. 17, was constructed with the absorbance measured at 301 nm. The diBCP nanofiber samples (1 mL, 0.5 mg/mL) were prepared in filtered 20:80 DMSO:MeOH solvent through a 0.45 μm membrane filter into an optical quartz glass cuvette (PCS8501 type, 10.0 mm light path).

4.5.2 Synthetic procedures

4.5.2.1 Synthesis of PFTMC$_{14}$-*b*-PEG$_{900}$-*b*- PFTMC$_{14}$

Scheme S4. 1. Synthesis of PFTMC$_{14}$-*b*-PEG$_{900}$-*b*-PFTMC$_{14}$ by organocatalytic ring-opening polymerization.

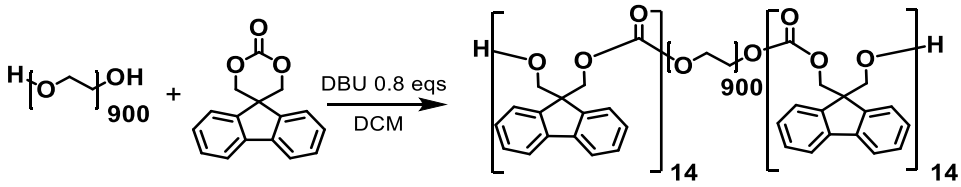

To a solution of diol-PEG$_{900}$ in the minimum amount of anhydrous CH_2Cl_2 (100 mg, 0.003 mmol, 1.0 eq), DBU (0.3 µL, 0.3 mg, 0.002 mmol, 0.8 eq) was added in an oven-dried round bottom flask equipped with a magnetic stirring bar. To the stirring solution, FTMC (25.3 mg, 0.1 mmol, 40 eq) in anhydrous CH_2Cl_2 (0.5 mL) was added, and the reaction mixture was stirred at room temperature for 5 h, before the reaction mixture was quenched by the addition of benzoic acid (20 mg). The crude product was purified by precipitation into ice-cold diethyl ether three times, followed by drying *in vacuo*. The PFTMC$_{14}$-*b*-PEG$_{900}$-*b*-PFTMC$_{14}$ was obtained as a white sticky solid solid (88 mg, 70%). Monomer conversion 70%

GPC: M_n = 32,300, $Đ_M$ = 1.19.

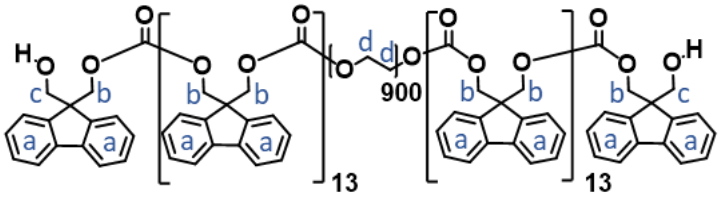

^{1}H NMR (500 MHz, CD_2Cl_2) δ 7.84 – 7.66 (56H, m, Ha), 7.53 (56H, m, Ha), 7.47 – 7.34 (56H, m, Ha), 7.34 – 7.20 (56H, m, Ha), 4.50 – 4.29 (110H, m, Hb), 4.19 – 4.16 (4H m, Hc), 3.60 (3600H, m, Hd). ^{1}H integration is based on 'c' (OHC*H*$_2$C) from the flanking FTMCs at the termini of the triBCP.

4.5.2.2 Synthesis of PFTMC$_{15}$-*b*-PEG$_{265}$

Scheme S4. 2. Synthesis of PFTMC$_{15}$-*b*-PEG$_{265}$ by organocatalytic ring-opening polymerization.

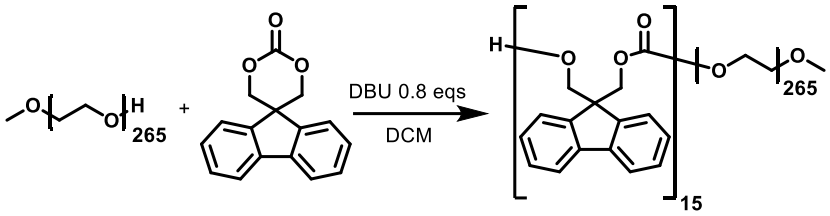

PEG$_{265}$ (500 mg, 0.02 mmol, 1 eq) and DBU (2.9 µL, 2.9 mg, 0.02 mmol, 0.8 eq) were dissolved in the minimum volume of anhydrous CH_2Cl_2 in a round bottom flask equipped with a magnetic stirring bar. To the stirring solution, FTMC (122 mg, 0.49 mmol, 20 eq) in anhydrous CH_2Cl_2 (1 mL) was added, and the reaction mixture was stirred at room temperature for 3 h, before the reaction mixture was quenched by the addition of benzoic acid (10 mg). The crude product was purified by precipitation into ice-cold diethyl ether three times. 300 mg of the collected white solid was then dissolved in 20 mL of THF in a 50 mL centrifuge with a stir bar. 10 mL of hexane was added to the stirring solution and centrifuged, to the supernatant an extra 6 mL of hexanes were added, stirred and centrifuged. The resulting solid was dried *in vacuo* to yield PFTMC$_{15}$-PEG$_{265}$ as a white solid (210 mg, 70%). Monomer conversion 75%

GPC: M_n = 13,200, $Đ_M$ = 1.16.

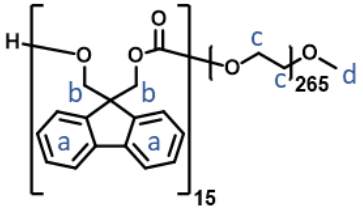

^{1}H NMR (500 MHz, CD_2Cl_2) δ 7.88 – 7.68 (30H, m, Ha), 7.67 – 7.50 (31H, m, Ha), 7.50 – 7.37 (31H, m, Ha), 7.37 – 7.24 (31H, m, Ha), 4.54 – 4.20 (62H, m, Hb), 3.80 – 3.48 (1060H, m, Hc), 3.38 (3H, s, Hd). ^{1}H integration is based on 'd' (CH_2OCH_3) from the terminal methyl group of the PEG.

4.5.3 Self-assembly procedures

Composition of all solvents given in *v:v*

Self-nucleation of PFTMC$_{14}$-*b*-PEG$_{900}$-*b*-PFTMC$_{14}$.

2 mg/mL PFTMC$_{14}$-*b*-PEG$_{900}$-*b*-PFTMC$_{14}$ 10:90 DMSO:MeOH self-assembly solution. 6 mg of PFTMC$_{14}$-*b*-PEG$_{900}$-*b*-PFTMC$_{14}$ (300 µL, 20 mg/mL unimer solution in DMSO) was added to MeOH (2.7 mL) in a vial. The resulting solution (1 mg/mL in 10:90 DMSO:MeOH) was manually shaken for ~ 15 s and annealed for 3 h at 70 °C. The solution was cooled to 20 °C over 3 h, and aged for 48 h. The resulting solution contained morphologically pure flower-like nanofibers with disperse lengths as analysed by TEM.

5 mg/mL PFTMC$_{14}$-*b*-PEG$_{900}$-*b*-PFTMC$_{14}$ 10:90 DMSO:MeOH self-assembly solution. 2 mg of polymer were placed in a vial and 400 µL (10:90 DMSO:MeOH) of solvent mixture were added. The resulting solution (5 mg/mL in in 10:90 DMSO:MeOH) was manually shaken for ~ 15 s and annealed for 3 h at 70 °C. The solution was cooled to 20 °C over 3 h, and aged for 48 h. The resulting solution contained morphologically pure flower-like nanofibers with disperse lengths as analysed by TEM, minimal degree of corona-linking was observed.

5 mg/mL PFTMC$_{14}$-*b*-PEG$_{900}$-*b*-PFTMC$_{14}$ 20:80 DMSO:MeOH self-assembly solution. 2 mg of polymer were placed in a vial and 400 µL (20:80 DMSO:MeOH) of solvent mixture were added. The resulting solution (5 mg/mL in in 20:80 DMSO:MeOH) was manually shaken for ~ 15 s and annealed for 3 h at 70 °C. The solution was cooled to 20 °C over 3 h, and aged for 48 h. The resulting solution contained morphologically pure nanofibers with disperse lengths as analysed by TEM, a high degree of corona-linking was observed.

20 mg/mL PFTMC$_{14}$-*b*-PEG$_{900}$-*b*-PFTMC$_{14}$ 20:90 DMSO:MeOH self-assembly solution. 4 mg of polymer were placed in a vial and 200 µL (20:90 DMSO:MeOH) of solvent mixture were added. The resulting solution (20 mg/mL in 20:90 DMSO:MeOH) was manually shaken for ~ 15 s and annealed for 3 h at 70 °C. The solution was cooled to 20 °C over 3 h, and aged for 48 h. The resulting solution contained morphologically pure nanofibers with disperse lengths as analysed by TEM, a high degree of corona-linking was observed.

Preparation of PFTMC$_{14}$-*b*-PEG$_{900}$-*b*-PFTMC$_{14}$ flower-like nanofibers of controlled lengths

Preparation of PFTMC$_{14}$-*b*-PEG$_{900}$-*b*-PFTMC$_{14}$ flower-like seed nanofibers. The disperse PFTMC$_{14}$-*b*-PEG$_{900}$-*b*-PFTMC$_{14}$ flower-like nanofibers (2 mL, diluted to 1 mg/mL with MeOH) were fragmented by ultrasonication for 3 h at 15 – 20 °C. The resulting nanofibers were analysed by TEM (L_n = 25 nm, $Đ$ = 1.12, σ = 9 nm).

Preparation PFTMC$_{14}$-*b*-PEG$_{900}$-*b*-PFTMC$_{14}$ flower-like nanofibers of controlled length and low dispersity via seeded growth (living CDSA). For the seeded growth experiments with $m_{unimer}/m_{seed} \leq 10$: aliquots of PFTMC$_{14}$-*b*-PEG$_{900}$-*b*-PFTMC$_{14}$ unimer (10 mg/mL in DMSO), equivalent to corresponding m_{unimer}/m_{seed}, were added to diluted seed nanofiber solutions in MeOH (500 µL). The resulting self-assembly solutions (~15% DMSO) were manually shaken for ~ 15 s and aged for 48 h at 20 ºC.

For seeded growth assemblies with m_{unimer}/m_{seed} 15, 20, 30, and 40: aliquots of PFTMC$_{14}$-*b*-PEG$_{900}$-*b*-PFTMC$_{14}$ unimer (10 mg/mL in DMSO), equivalent to corresponding m_{unimer}/m_{seed}, were added to diluted seed nanofiber solution in MeOH (300

μL). The unimer was added in intervals of 10 m_{unimer}/m_{seed} every 24 h. The self-assembly solutions (~15% DMSO) were manually shaken for ~ 15 s and aged at 20 ºC.

Self-nucleation of PFTMC$_{15}$-*b*-PEG$_{265}$.

5 mg/mL PFTMC$_{15}$-*b*-PEG$_{265}$ 15:85 DMSO:MeOH self-assembly solution. 5 mg of PFTMC$_{15}$-*b*-PEG$_{265}$ were placed in a vial and 1 mL (15:85 DMSO:MeOH) of solvent mixture were added. The resulting solution (5 mg/mL in 15:85 DMSO:MeOH) was manually shaken for ~ 15 s and annealed for 3 h at 70 °C. The solution was cooled to 20 °C over 3 h, and aged for 48 h. The resulting solution contained morphologically pure flower-like nanofibers with disperse lengths as analysed by TEM.

5 mg/mL PFTMC$_{15}$-*b*-PEG265 20:80 DMSO:MeOH self-assembly solution. 2 mg of polymer were placed in a vial and 400 μL (20:80 DMSO:MeOH) of solvent mixture were added. The resulting solution (5 mg/mL in in 20:80 DMSO:MeOH) was manually shaken for ~ 15 s and annealed for 3 h at 70 °C. The solution was cooled to 20 °C over 3 h, and aged for 48 h. The resulting solution contained morphologically pure nanofibers with disperse lengths as analysed by TEM, a high degree of corona-linking was observed.

20 mg/mL PFTMC$_{15}$-*b*-PEG$_{265}$ 20:80 DMSO:MeOH self-assembly solution. 20 mg of PFTMC$_{15}$-*b*-PEG$_{265}$ were placed in a vial and 500 μL (20:80 DMSO:MeOH) of solvent mixture were added. The resulting solution (20 mg/mL in 20:80 DMSO:MeOH) was manually shaken for ~ 15 s and annealed for 3 h at 70 °C. The solution was cooled to 20 °C over 3 h, and aged for 48 h. The resulting solution contained morphologically pure flower-like nanofibers with disperse lengths as analysed by TEM.

Preparation of PFTMC$_{15}$-*b*-PEG$_{265}$ diBCP seed nanofibers. The disperse PFTMC$_{15}$-*b*-PEG$_{265}$ diBCP nanofibers (1 mL, 5 mg/mL) were fragmented by ultrasonication for 3 h at 15 – 20 °C. The resulting nanofibers were analysed by TEM (L_n = 50 nm, $Đ$ = 1.13, σ = 18 nm).

Preparation of PFTMC$_{15}$-*b*-PEG$_{265}$ diBCP nanofibers of controlled length and low dispersity via seeded growth (living CDSA). For the seeded growth experiments with $m_{unimer}/m_{seed} \leq 10$: aliquots of PFTMC$_{14}$-*b*-PEG$_{265}$ unimer (10 mg/mL in DMSO), equivalent to corresponding m_{unimer}/m_{seed}, were added to diluted seed nanofiber solutions in MeOH (200 µL). The resulting self-assembly solutions (~15% DMSO) were manually shaken for ~ 15 s and aged for 48 h at 20 ºC.

For seeded growth assemblies with m_{unimer}/m_{seed} 20, and 30: aliquots of PFTMC$_{15}$-*b*-PEG$_{265}$ unimer (10 mg/mL in DMSO), equivalent to corresponding m_{unimer}/m_{seed}, were added to diluted seed nanofiber solution in MeOH (200 µL). The unimer was added in intervals of 10 m_{unimer}/m_{seed} every 24 h. The self-assembly solutions (~15% DMSO) were manually shaken for ~ 15 s and aged at 20 ºC.

Preparation of 359 nm PFTMC$_{18}$-*b*-PEG$_{265}$ nanofibers with controlled length and low dispersity by seeded growth (living CDSA). To a diluted seed solution PFTMC$_{18}$-*b*-PEG$_{265}$ (50 nm, 0.5 mL, 0.782 mg/mL, in MeOH), PFTMC$_{18}$-*b*-PEG$_{265}$ unimer (50 mg/mL in DMSO, m_{unimer}/m_{seed} equivalent to 6) was added in two portions (2 × 23.5 µL), 24 h apart. The self-assembly solution (5 mg/mL, 10:90 DMSO:MeOH) was manually shaken for ~ 15 s and aged for 48 h at 20 ºC. TEM. The resulting solution contained morphologically pure diBCP nanofibers with low length-dipersity nanofibers as analysed by TEM (L_n = 359 nm, $Đ$ = 1.06, σ = 89 nm).

Preparation B-*m*-A-*m*-B segmented nanofibers, and corona-linking experiments via the addition of triBCP unimer to diBCP nanofiber solutions. A block = PFTMC$_{18}$-*b*-PEG$_{265}$, B block = PFTMC$_{14}$-*b*-PEG$_{900}$-*b*-PFTMC$_{14}$.

50 µL of either 0.5 mg/mL (diluted in 10:90 DMSO:MeOH) or 5 mg/mL the diBCP (359 nm, PFTMC$_{18}$-*b*-PEG$_{265}$) nanofiber solutions were placed in vials. A set of samples were kept at 20 ºC and another set was heated to 50 °C for 15 min. Then, 1 m_{unimer}/m_{seed} equivalents of triBCP unimer (5 µL, 5 mg/mL or 50 mg/mL in DMSO) were added to the vials containing the diBCP nanofibers as shown in Table S4. 3. The resulting solutions were manually shaken for ~ 15 s and kept at their respective temperature for 2 h before cooling down to 20 ºC, if applicable, and aged for 48 h at 20 ºC.

4.5.4 Supplementary Discussion

Solution State Self-Assembly of PFTMC$_{15}$-*b*-PEG$_{265}$ diBCP

The solution state self-assembly of PFTMC$_{15}$-*b*-PEG$_{265}$ was investigated via CDSA using a spontaneous nucleation protocol (5 mg/mL, DMSO:MeOH 15:85, Figure S4. 13), followed by sonication and seeded growth (Figure S4. 14), as analyzed by TEM. Via the seeded growth method, PFTMC$_{15}$-*b*-PEG$_{265}$ nanofibers of tuned lengths (195 to 1235 nm) and low length-dispersities ($Đ$ < 1.06) were obtained by adding modulated quantities of PFTMC$_{15}$-*b*-PEG$_{265}$ unimer (in DMSO, m_{unimer}/m_{seed} = 2.5 – 30) to seed solutions, as examined by TEM (Figure S4. 14C-I). The experimental lengths of the resulting diBCP nanofibers were consistent with the experimental error associated with the addition of unimer to a seed solution of 50 nm (σ = 18 nm). The seeded growth experiments of PFTMC$_{15}$-*b*-PEG$_{265}$ diBCP nanofibers revealed a linear dependency of the final length vs m_{unimer}/m_{seed} ratio, characteristic of the seeded growth process (Figure S4. 14J). A summary of the PFTMC$_{15}$-*b*-PEG$_{265}$ diBCP nanofibers contour length statistical analysis is presented in Table S4. 4.

Studies at 20 °C of the Intermicellar Linking of PFTMC$_{15}$-*b*-PEG$_{265}$ diBCP Nanofibers via the Addition of the Telechelic triBCP

Two solutions containing PFTMC$_{15}$-*b*-PEG$_{265}$ diBCP nanofibers (L_n = 359 nm, $Đ$ = 1.06, σ = 89nm, 0.5 mg/mL, DMSO:MeOH 10:90. Figure 4. 5A, S14D) were kept at 20 °C, and 1 equivalent of triBCP unimer (5 µL in DMSO, 5 mg/mL or 50 mg/mL) was added in one portion to each sample (Figure S4. 16). The resulting concentration of polymer in each experiment corresponded to 0.91 mg/mL (Figure S4. 16A-B) and 9.1 mg/mL (Figure S4. 16C-D), both samples were aged for 48 h prior to analysis (18:82 DMSO:MeOH). For the sample cointaining 0.91 mg/mL of polymer, discrete nanofibers of controlled

dimensions that match the predicted length of a seeded growth process were observed by TEM (L_n = 822 nm, $Đ$ = 1.03, σ = 133 nm. Figure S4. 16A). The length of the resulting nanofibers is in good agreement with the experimental error associated with the addition of 1 equivalent of unimer to diBCP nanofibers of L_n = 359 nm (σ = 89 nm). The well-behaved increase of the length, the newly grown segments, and the absence of intermicellar linked networks confirmed the formation of segmented 'hybrid' flower-like(triBCP)-***m***-nanofiber(diBCP)-***m***-flower-like(triBCP) nanofibers by TEM (PFTMC$_{14}$-*b*-PEG$_{900}$-*b*-PFTMC$_{14}$-***m***-PFTMC$_{15}$-*b*-PEG$_{265}$-***m***-PFTMC$_{14}$-*b*-PEG$_{900}$-*b*-PFTMC$_{14}$, Figure S4. 16A). Visual inspection of the vial containing the 0.91 mg/mL sample revealed a clear non-viscous solution with no evidence of macroscopic aggregates (Figure S4. 16B). The sample prepared containing 9.1 mg/mL of polymer, contained both discrete hybrid nanofibers and intermicellar linked nanofibers, via TEM analysis (Figure S4. 16C). A cloudy solution arising from the scatered light of partially linked nanofibers was observed via visual inspection of the sample (Figure S4. 16D).

Thermally-induced unimer dissociation from diBCP nanofibers PFTMC$_{15}$-*b*-PEG$_{265}$

To corroborate that no diBCP nanofiber dissociation and self-seeding[60] occurred upon heating the diBCP nanofiber solutions at 50 °C (L_n = 359 nm, 0.5 mg/mL, in 20:80 DMSO:MeOH), variable-temperature UV-Vis absorbance measurements (250 – 600 nm) were conducted from 25 – 90 °C with 5 °C intervals. The absorbance corresponding to the fluorene moiety of the PFTMC-block was analysed at 301 nm (Figure S4. 17). The sharp change in slope at 70 °C indicates that at this temperature and above the diBCP nanofibers undergo thermally-induced unimer dissociation. The observed increase in absorbance

results from a higher availability of PFTMC moieties (unimer) in solution that are able to interact with the instrument beam (Figure S4. 17). Since no significat unimer-dissociation occurs at 50 °C no self-seeding can take place. Hence, the nanofiber length increase from preformed diBCP nanofibers (L_n = 359 nm) at 0.91 mg/mL (at either 50 or 20 ° C, 18:82 DMSO:MeOH) results exclusively from the crystallization-driven fiber growth (living CDSA) of the 1 equivalent of triBCP added to the diBCP nanofiber solution (Figure S4. 15A, S16A).

4.5.5 Supplementary Tables

Table S4. 1. Summary of molar mass data for PEG homopolymers and PFTMC-containing block copolymers.

Polymer	M_n (g/mol) GPC	M_w (g/mol) GPC	$Đ_M$ GPC	DP_n NMR
PEG_m	24,500	28,900	1.17	m =900[a]
PEG_n	10,600	11,200	1.06	n = 265[a]
$PFTMC_l$-*b*-PEG_{900}-*b*-$PFTMC_l$	32,300	38,400	1.19	l = 14
$PFTMC_n$-*b*-PEG_{265}	13,300	15,300	1.15	n = 15

[a]PEG DP_n obtained by ^{1}H NMR end-group analysis of the block copolymers.

Table S4. 2. Statistical analysis of contour length measurements for $PFTMC_{14}$-*b*-PEG_{900}-*b*-$PFTMC_{14}$ flower-like nanofibers prepared via seeded growth at 20 °C, in DMSO:MeOH solvent mixtures (DMSO = 10 – 20 %), measured via TEM. The number of nanofibers measured is represented by n, and σ represents the standard deviation of the measured length, and L_n/eq corresponds to the L_n of the nanofibers per mass equivalent of triBCP in the sample.

Length	m_{unimer}/m_{seed}							
	Seeds	2.5	5	10	15	20	30	40
n	346	276	316	302	250	252	249	259
L_n (nm)	25	96	146	240	306	451	670	806
L_w (nm)	29	104	159	260	337	483	706	854
Đ	1.12	1.08	1.09	1.08	1.10	1.07	1.05	1.06
L_n/eq (nm)	25	28	24	22	19	21	22	20
σ (nm)	9	27	45	70	97	119	155	183
σ / L_n	0.35	0.29	0.31	0.29	0.31	0.26	0.23	0.23

Table S4. 3. Summary of the corona-linking experiment conditions via the addition of the $PFTMC_{14}$-*b*-PEG_{900}-*b*-$PFTMC_{14}$ triBCP to the $PFTMC_{15}$-*b*-PEG_{265} diBCP nanofiber solutions of Ln = 359 nm ($Đ$ = 1.06, σ = 89).

Sample No.	Temp.	Vol. Seed (µL)	Seed conc. (mg/mL)	M_{unimer}/M_{seed}	Unimer (µL)	Conc. (mg/mL)	% DMSO
1	50 °C	50	0.5	1.0	5*	0.91	18%
2	50 °C	50	5.0	1.0	5°	9.1	18%
3	20 °C	50	0.5	1.0	5*	0.91	18%
4	20 °C	50	5.0	1.0	5°	9.1	18%

*Unimer concentration = 5 mg/mL. °Unimer concentration = 50 mg/mL.

Table S4. 4. Statistical analysis of contour length measurements for $PFTMC_{15}$-*b*-PEG_{265} diBCP nanofibers prepared via seeded growth at 20 °C, in DMSO:MeOH solvent mixtures (DMSO = 10 – 20%), measured via TEM. The number of nanofibers measured is represented by n, and σ represents the standard deviation of the measured length, and L_n/eq corresponds to the L_n of the nanofibers per mass equivalent of triBCP in the sample.

Length	m_{unimer}/m_{seed}					
	Seeds	2.5	5	10	20	30
n	153	154	157	159	165	155
L_n (nm)	50	195	359	633	1012	1235
L_w (nm)	57	201	380	652	1041	1287
Đ	1.13	1.03	1.06	1.03	1.02	1.04
L_n/eq (nm)	50	55	59	57	48	40
σ (nm)	18	34	89	112	173	256
σ / L_n	0.36	0.17	0.25	0.18	0.17	0.21

4.5.6 Supplementary Figures

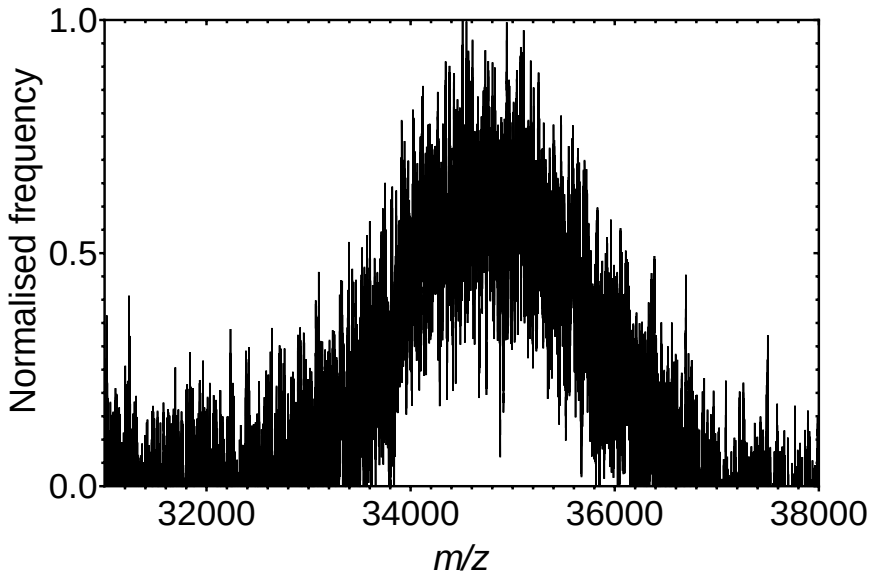

Figure S4. 1. MALDI-TOF MS spectra of the diol-PEG_{900} used as macroinitiator for the synthesis of the $PFTMC_{14}$-*b*-PEG_{900}-*b*-$PFTMC_{14}$ triBCP.

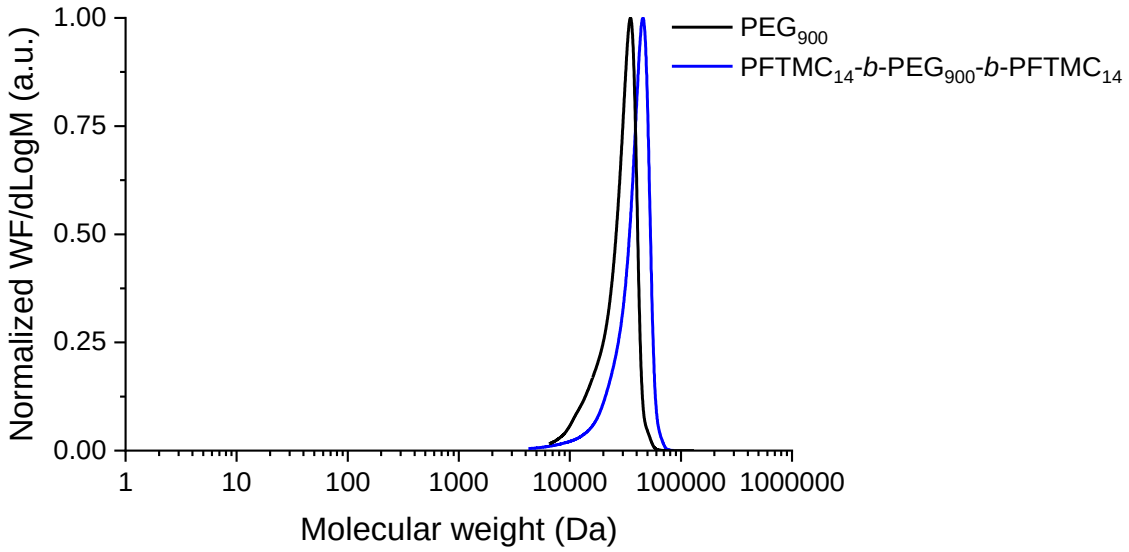

Figure S4. 2. GPC (refractive index) traces eluted in triethylamine/THF (1% *v/v*), 1 mL min^{-1}, 35 °C of PEG_{900} homopolymer (black trace), and $PFTMC_{14}$-*b*-PEG_{900}-$PFTMC_{14}$ triBCP (blue trace). The y-axis reflects the distribution of weight fractions by molecular weight.

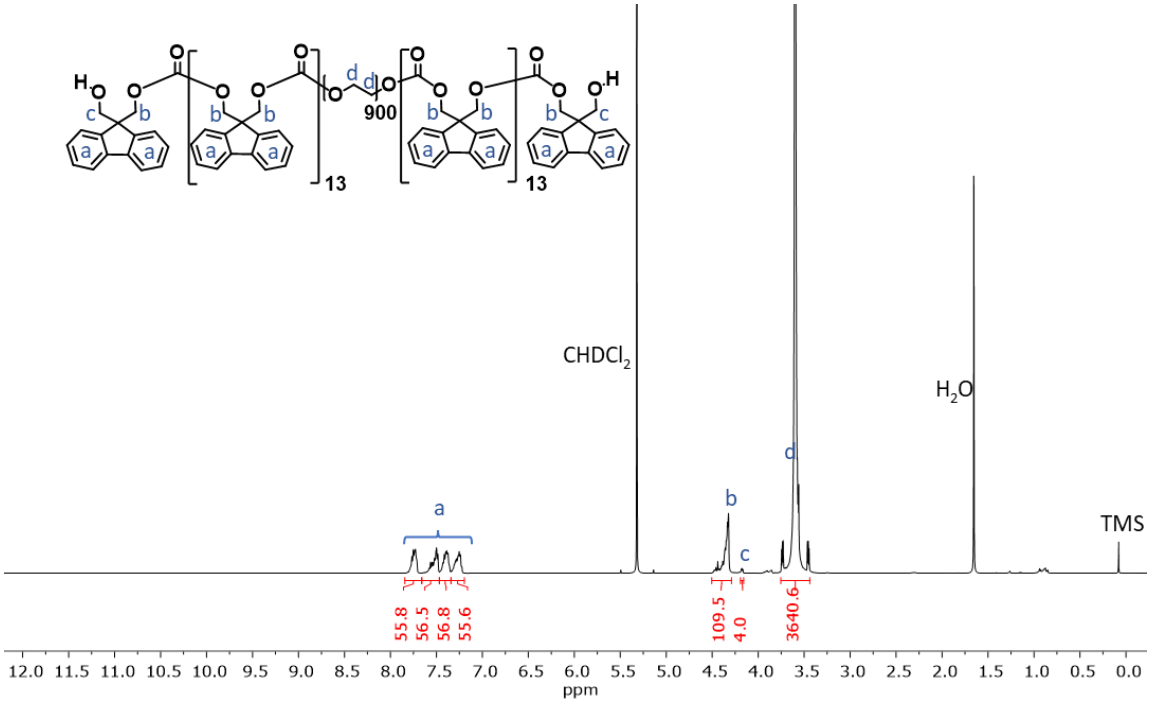

Figure S4. 3. ^{1}H NMR spectra (in CD_2Cl_2) of $PFTMC_{14}$-*b*-PEG_{900}-$PFTMC_{14}$.

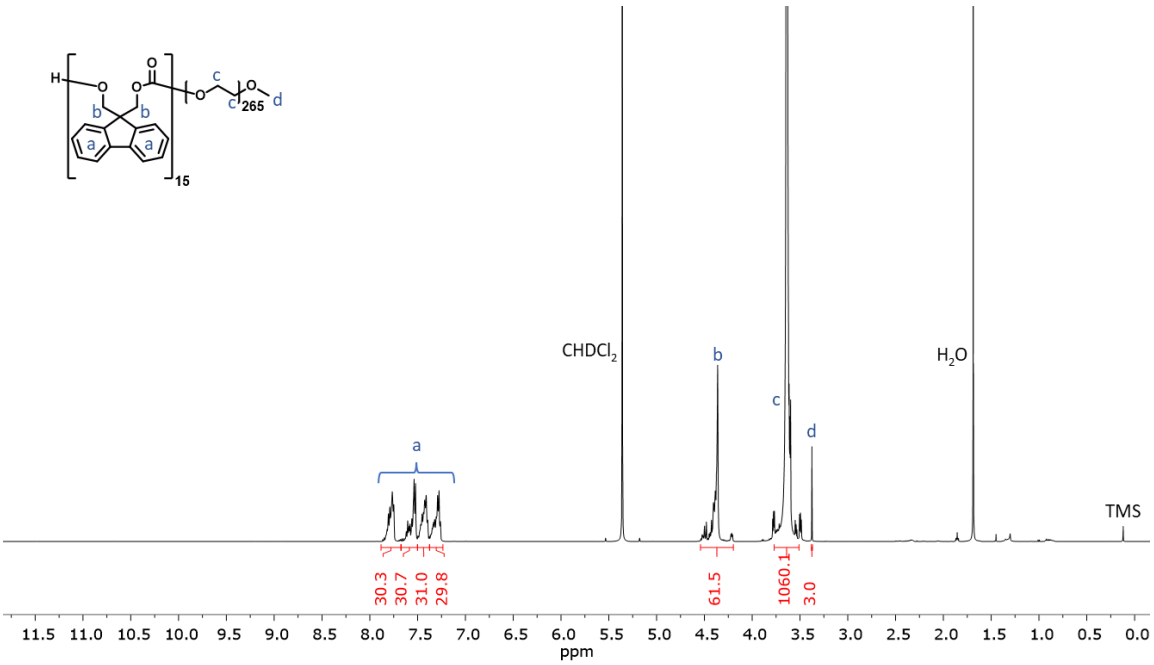

Figure S4. 4. ^{1}H NMR spectra (in CD_2Cl_2) of $PFTMC_{15}$-*b*-PEG_{265}.

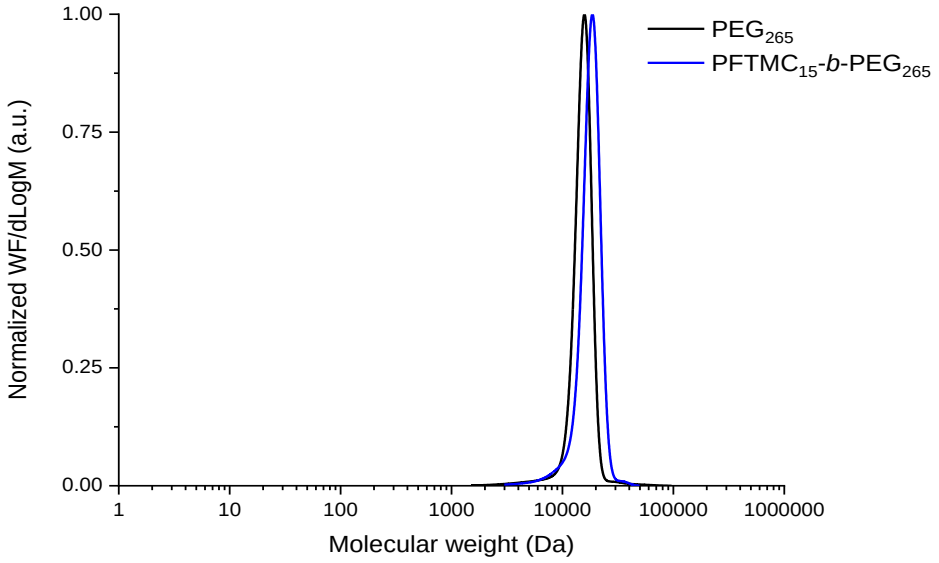

Figure S4. 5. GPC (refractive index) traces eluted in triethylamine/THF (1% *v/v*), 1 mL min^{-1}, 35 °C of PEG_{265} homopolymer (black trace), and $PFTMC_{15}$-*b*-PEG_{265} diBCP (blue trace). The y-axis reflects the distribution of weight fractions by molecular weight.

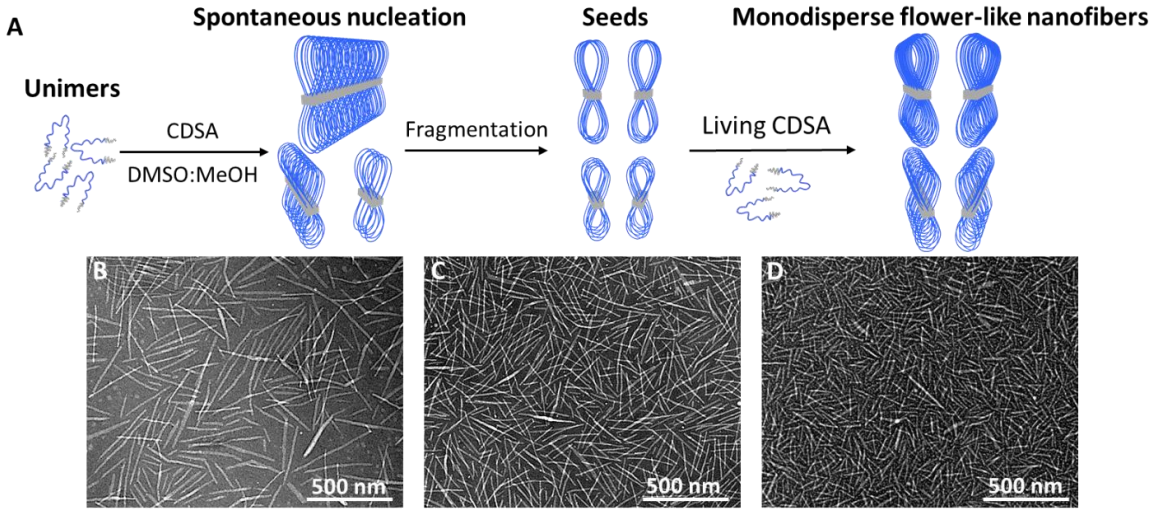

Figure S4. 6. Preparation of low dispersity nanofibers of controlled lengths via living CDSA method. A) Schematic representation of the preparation process of low dispersity nanofibers prepared from PFTMC$_{14}$-*b*-PEG$_{900}$-*b*-PFTMC$_{14}$. B-D) TEM images of the resulting low dispersity flower-like nanofibers prepared through the seeded-growth method via ther addition of PFTMC$_{14}$-*b*-PEG$_{900}$-*b*-PFTMC$_{14}$ unimer in DMSO to nanofiber seed solutions at $m_{unimver}/m_{seed}$ ratios of B) 2.5:1 C) 10:1, and D) 20:1, respectively.

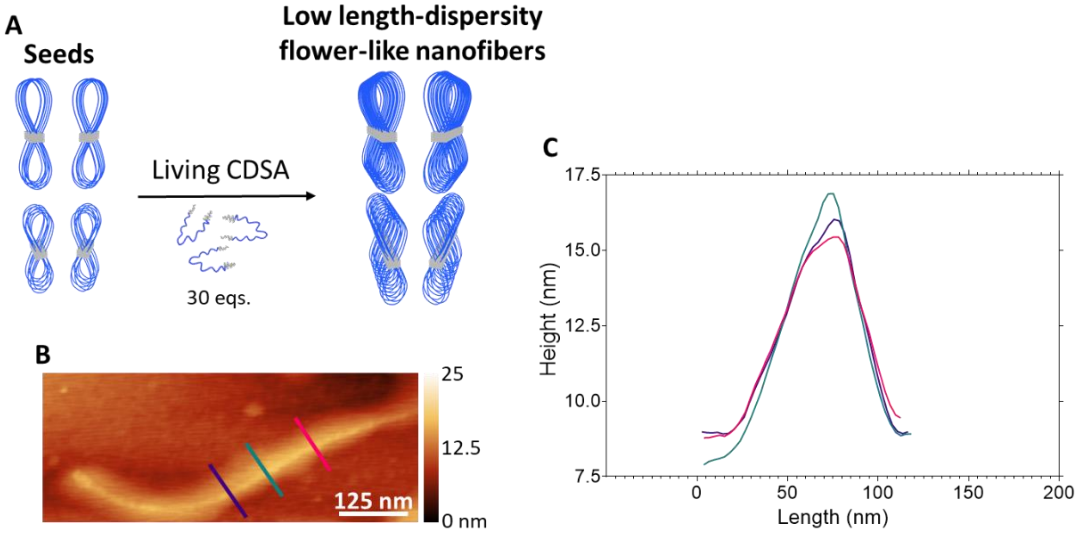

Figure S4. 7. A) Schematic representation of the preparation of low dispersity flower-like nanofibers prepared from PFTMC$_{14}$-*b*-PEG$_{900}$-*b*-PFTMC$_{14}$ via the living CDSA method. B) Tapping mode AFM micrograph on a silicon wafer of low dispersity flower-like nanofibers prepared by adding PFTMC$_{14}$-*b*-PEG$_{900}$-*b*-PFTMC$_{14}$ unimer in DMSO to a solution of nanofiber seeds in ~10:90 DMSO:MeOH (L_n = 670 nm, $Đ$ = 1.05, σ = 155 nm, by TEM). C) Color-coded Height profile of the the low length-dispersity flower-like nanofiber in B.

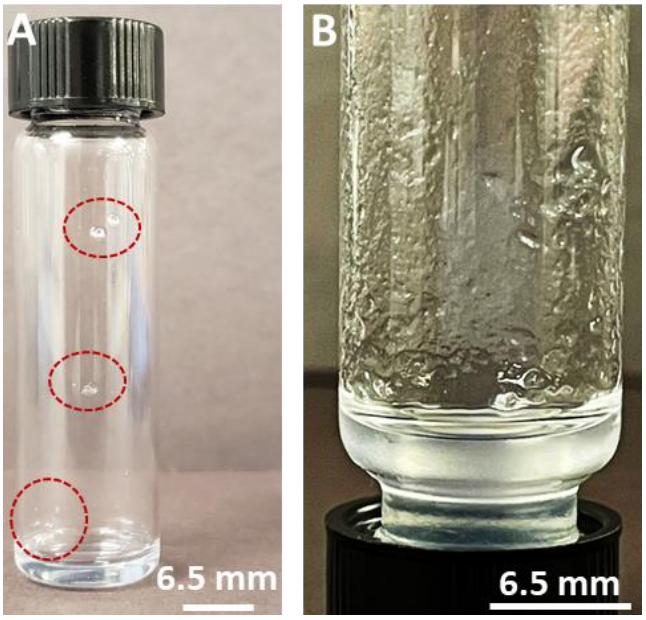

Figure S4. 8. Digital images of the vials containing $PFTMC_{14}$-*b*-PEG_{900}-*b*-$PFTMC_{14}$ triBCP nanofiber networks (2 mg, 400 µL, 5 mg/mL) at different extents by modifying the fraction of common solvent: A) 10:90 DMSO:MeOH *v/v*. B) 20:80 DMSO:MeOH *v/v*. The digital images were recorded after the samples were heated to 70 °C for 3 h, cooled to 20 °C and aged for 48 h.

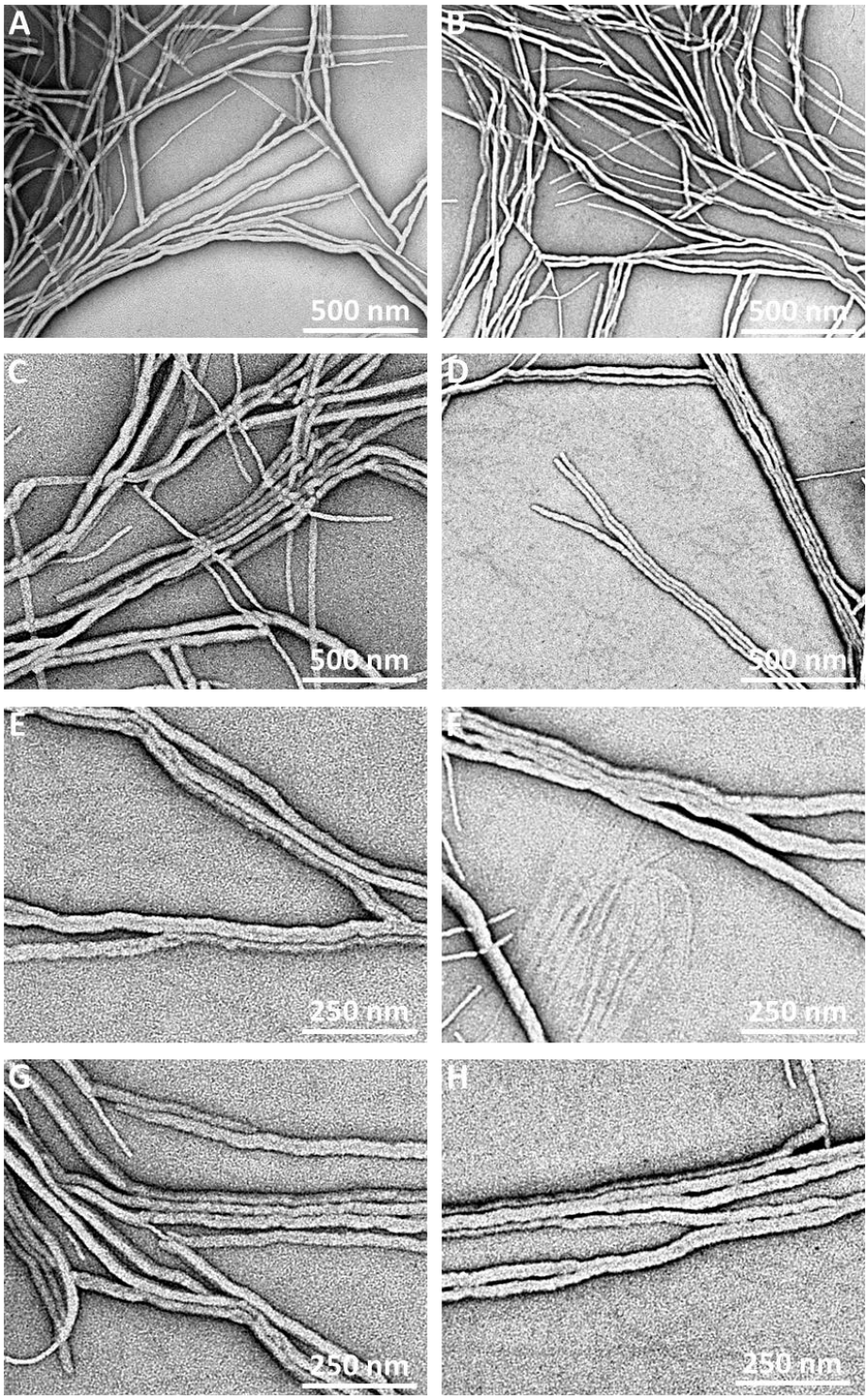

Figure S4. 9. A-H) TEM micrographs of $PFTMC_{14}$-*b*-PEG_{900}-*b*-$PFTMC_{14}$ nanofiber networks prepared CDSA by heating to 70 °C for 3 h, subsequently cooled to 20 °C, and aged for 48 h (2 mg, 400 µL, 5 mg/mL, 20:80 DMSO:MeOH). The samples were casted into plasma-treated carbon-coated copper grids.

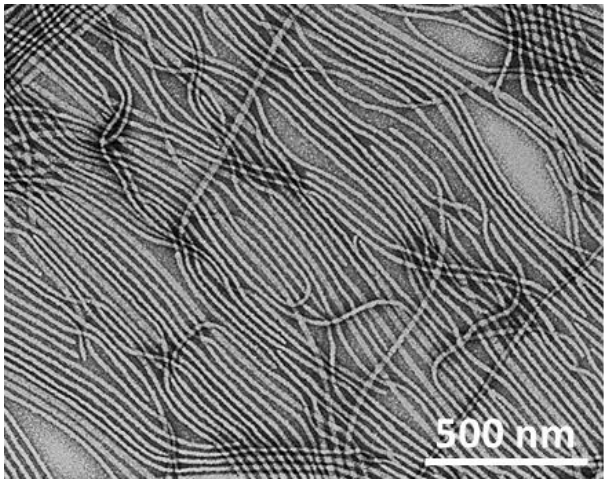

Figure S4. 10. TEM micrograph of PFTMC$_{15}$-*b*-PEG$_{265}$ disperse nanofibers (400 µL, 5 mg/mL) prepared in 20:80 DMSO:MeOH via CDSA by heating to 70 °C for 2 h, and subsequently cooled to 20 °C and aged for 48 h.

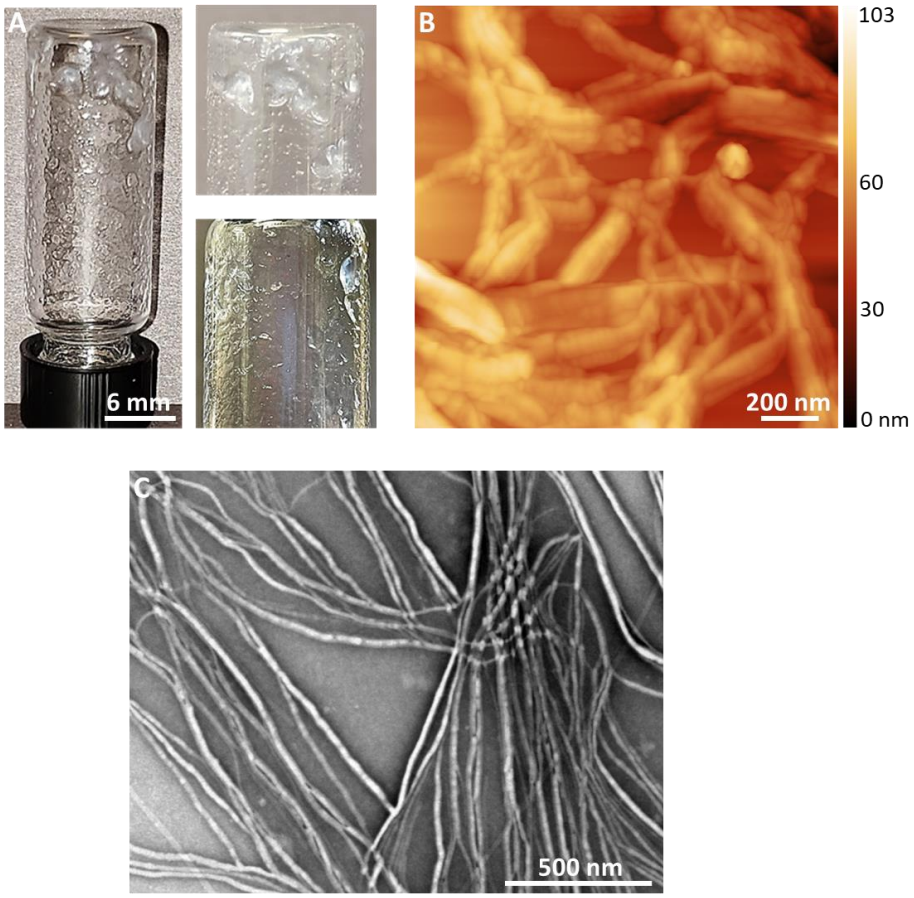

Figure S4. 11. A) Digital image of the vial containing PFTMC$_{14}$-*b*-PEG$_{900}$-*b*-PFTMC$_{14}$ triBCP nanofiber networks (20 mg/mL, 500 µL, 20:80 DMSO:MeOH) prepared via CDSA by heating to 70 °C for 2 h, and subsequently cooled to 20 °C and aged for 48 h. B) Tapping mode AFM micrograph on a silicon wafer of triBCP nanofiber networks in A. C) TEM micrograph of the triBCP nanofiber networks in A.

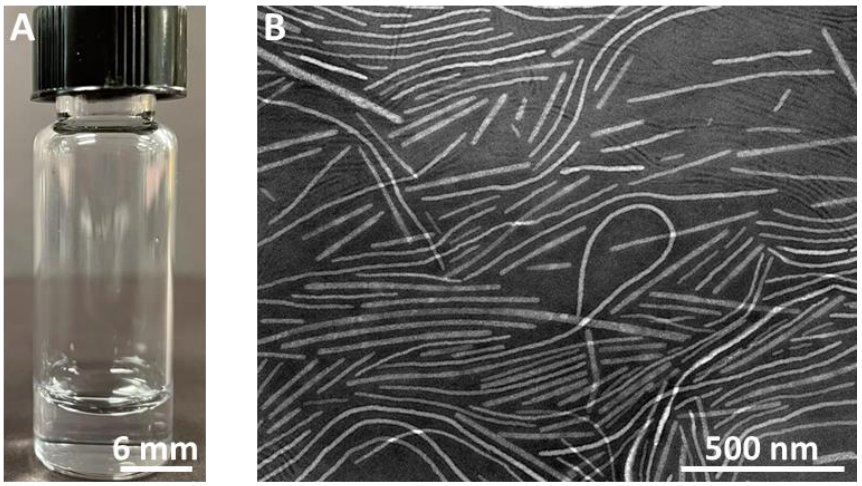

Figure S4. 12. A) Digital image of the vial containing discrete PFTMC$_{15}$-*b*-PEG$_{265}$ diBCP nanofibers (20 mg/mL, 500 µL, 20:80 DMSO:MeOH) prepared via CDSA by heating to 70 °C for 2 h, and subsequently cooled to 20 °C and aged for 48 h. B) TEM micrograph of the diBCP mnanofibers in A.

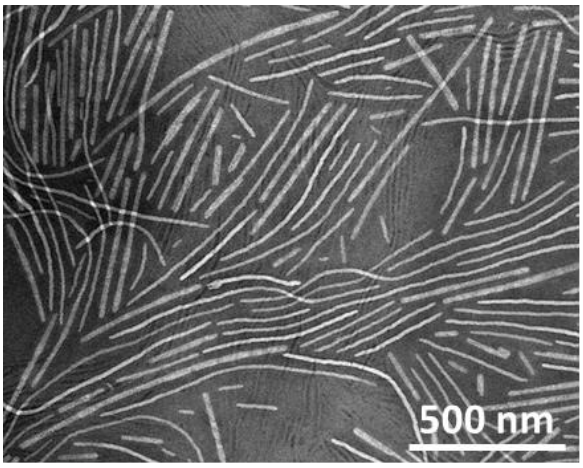

Figure S4. 13. TEM micrograph of PFTMC$_{15}$-*b*-PEG$_{265}$ disperse nanofibers (1 mL, 5 mg/mL) prepared in DMSO:MeOH (15:85) via CDSA. The sample was heated to 70 °C for 3 h, subsequently cooled to 20 °C and aged for 48 h.

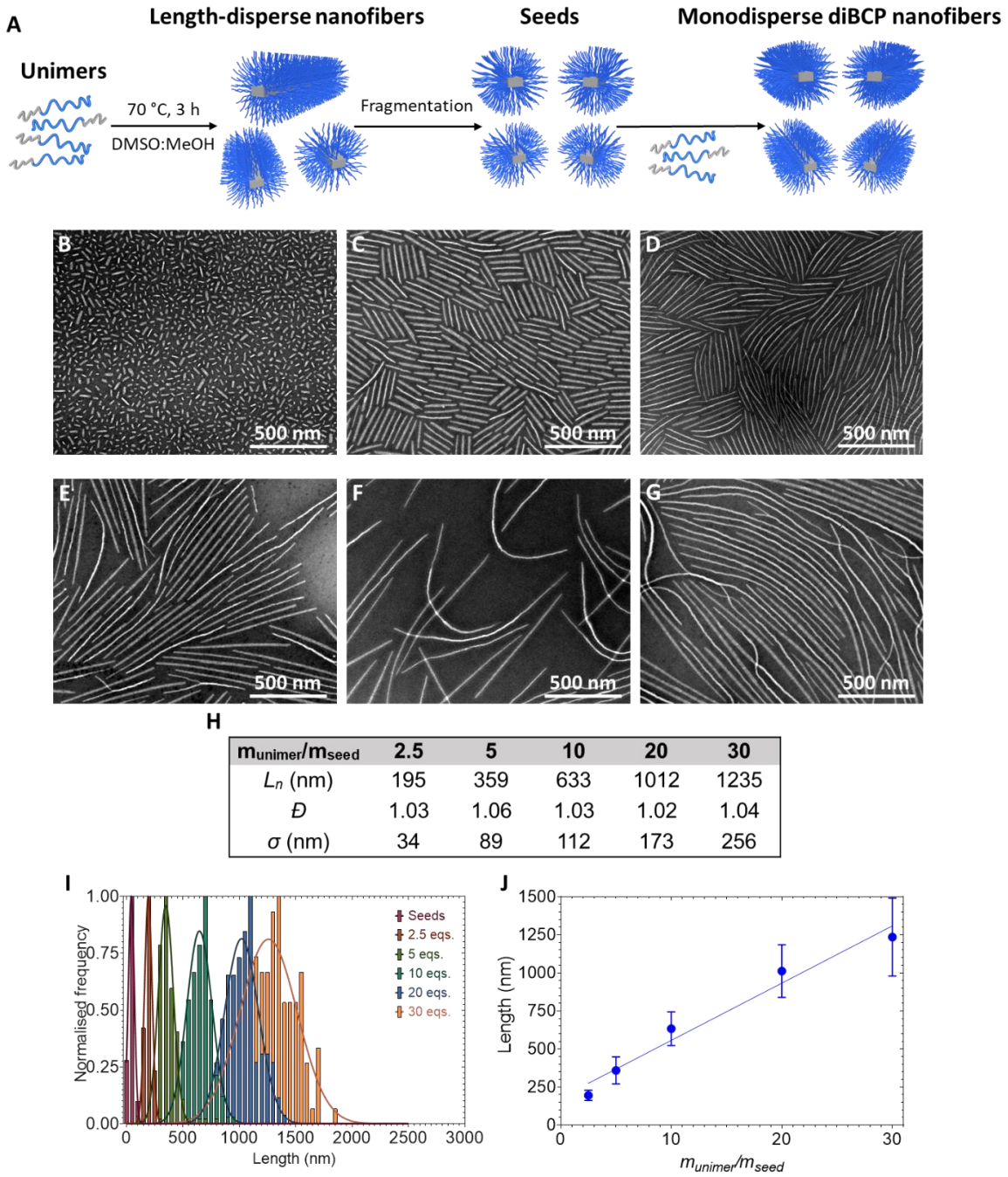

m_{unimer}/m_{seed}	2.5	5	10	20	30
L_n (nm)	195	359	633	1012	1235
$Đ$	1.03	1.06	1.03	1.02	1.04
σ (nm)	34	89	112	173	256

Figure S4. 14. Preparation of low dispersity diBCP nanofibers of controlled lengths via the Living CDSA method. A) Schematic representation of the preparation process of low dispersity flower-like nanofibers prepared from $PFTMC_{15}$-*b*-PEG_{265}. B) TEM image of seed nanofibers (50 nm, $Đ$ = 1.13, σ = 18 nm) prepared via the sonication of the disperse nanofibers in DMSO:MeOH (15:85). D-G) TEM images of the resulting low dispersity flower-like nanofibers prepared through the seeded-growth method via the addition of $PFTMC_{15}$-*b*-PEG_{265} unimer in DMSO to nanofiber seed solutions at $m_{unimver}/m_{seed}$ ratio of C) 2.5:1, D) 5:1, E) 10:1, F) 20:1, and G) 30:1, respectively. H) nanofiber length analysis summary. I) Contour length histograms of the seeds and low-dispersity flower-like nanofibers. J) Plot of nanofiber length (L_n) versus m_{unimer}/m_{seed} ratio. TEM images were stained with uranyl acetate (3 wt % in EtOH).

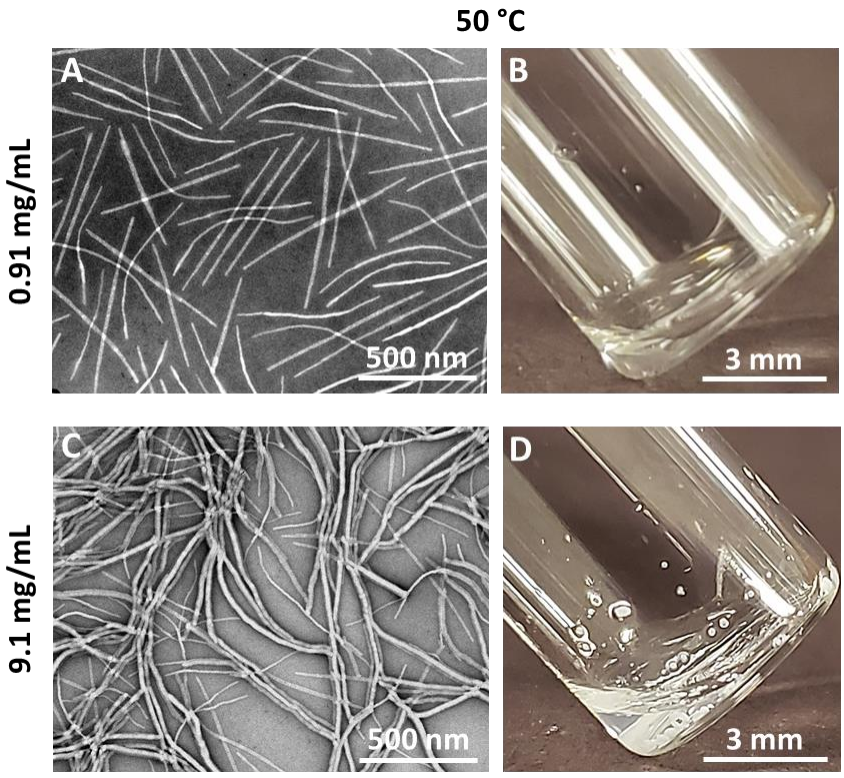

Figure S4. 15. Linking experiments conducted at 50 °C (18:82 DMSO:MeOH). A) TEM micrograph of hybrid B-A-B (PFTMC$_{14}$-*b*-PEG$_{900}$-*b*-PFTMC$_{14}$-*m*-PFTMC$_{15}$-*b*-PEG$_{265}$-*m*-PFTMC$_{14}$-*b*-PEG$_{900}$-*b*-PFTMC$_{14}$) segmented nanofibers after the addition of 1 m_{unimer}/m_{seed} equivalents of PFTMC$_{14}$-*b*-PEG$_{900}$-*b*-PFTMC$_{14}$ triBCP unimer (5 µL, 5 mg/mL) to PFTMC$_{15}$-*b*-PEG$_{265}$ diBCP nanofibers (359 nm, $Đ$ = 1.06, σ = 89 nm, 50 µL, 0.5 mg/mL, at 50 °C). The concentration of polymer in the resulting solution was 0.91 mg/mL. B) Digital image of the vial containing the hybrid nanofibers in A. C) TEM micrograph of hybrid B-*m*-A-m-B nanofibers and partially linked nanofibers after the addition of 1 m_{unimer}/m_{seed} equivalents of PFTMC$_{14}$-*b*-PEG$_{900}$-*b*-PFTMC$_{14}$ triBCP unimer (5 µL, 50 mg/mL) to PFTMC$_{15}$-*b*-PEG$_{265}$ diBCP nanofibers (359 nm, $Đ$ = 1.06, σ = 89 nm, 50 µL, 5.0 mg/mL, at 50 °C). The concentration of polymer in the resulting solution was 9.1 mg/mL. D) Digital image of the vial containing the hybrid nanofibers and partially linked nanofibers in C.

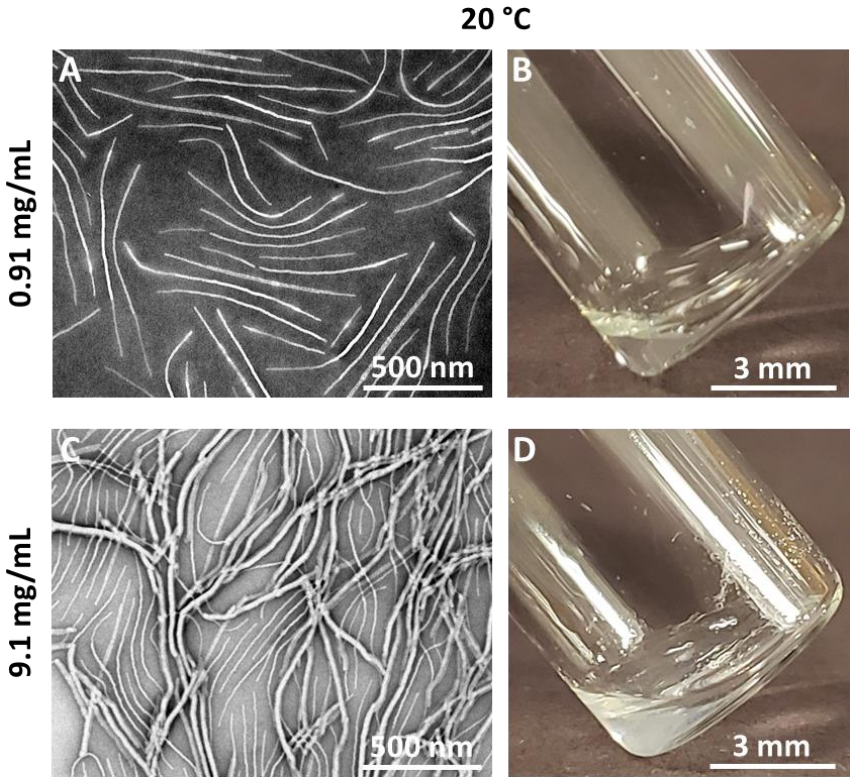

Figure S4. 16. Linking experiments conducted at 20 °C (18:82 DMSO:MeOH). A) TEM micrograph of hybrid B-A-B ($PFTMC_{14}$-*b*-PEG_{900}-*b*-$PFTMC_{14}$-*m*-$PFTMC_{15}$-*b*-PEG_{265}-*m*-$PFTMC_{14}$-*b*-PEG_{900}-*b*-$PFTMC_{14}$) segmented nanofibers after the addition of 1 m_{unimer}/m_{seed} equivalents of $PFTMC_{14}$-*b*-PEG_{900}-*b*-$PFTMC_{14}$ triBCP unimer (5 µL, 5 mg/mL) to $PFTMC_{15}$-*b*-PEG_{265} diBCP nanofibers (359 nm, $Đ$ = 1.06, σ = 89 nm, 50 µL, 0.5 mg/mL, at 20 °C). The concentration of polymer in the resulting solution was 0.91 mg/mL. B) Digital image of the vial containing the hybrid nanofibers in A. C) TEM micrograph of hybrid B-A-B nanofibers and partially linked nanofibers after the addition of 1 m_{unimer}/m_{seed} equivalents of $PFTMC_{14}$-*b*-PEG_{900}-*b*-$PFTMC_{14}$ triBCP unimer (5 µL, 50 mg/mL) to $PFTMC_{15}$-*b*-PEG_{265} diBCP nanofibers (359 nm, $Đ$ = 1.06, σ = 89 nm, 50 µL, 5.0 mg/mL, at 20 °C). The concentration of polymer in the resulting solution was 9.1 mg/mL. D) Digital image of the vial containing the hybrid nanofibers and partially linked nanofibers in C.

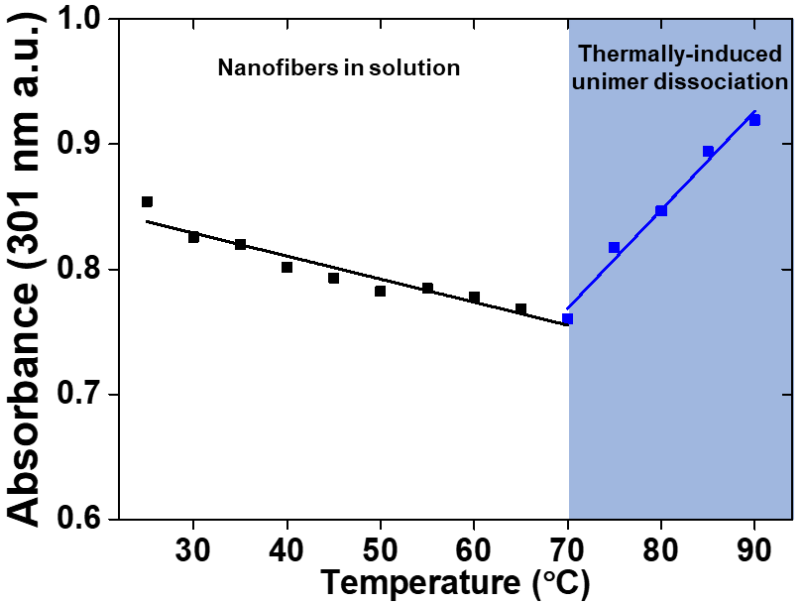

Figure S4. 17. Ultraviolet absorbance measurements conducted at 301 nm of $PFTMC_{15}$-*b*-PEG_{265} nanofibers diluted in MeOH (L_n = 359 nm, $Đ$ = 1.06, σ = 89 nm, 0.5 mg/mL) to determine the thermal annealing temperature. The change in slope (blue region) indicate thermally-induced unimer dissociation resulting in a higher absorbance from individual PFTMC moieties released to the solution. The nanofiber solution heated was heated from 25 – 90 °C in 5 °C intervals and the absorbance was recorded at each temperature interval.

4.6 References

(1) Li, Z.; Cai, B.; Yang, W.; Chen, C.-L. Hierarchical Nanomaterials Assembled from Peptoids and Other Sequence-Defined Synthetic Polymers. *Chem. Rev.* **2021**, *121* (22), 14031–14087.

(2) Lu, Y.; Lin, J.; Wang, L.; Zhang, L.; Cai, C. Self-Assembly of Copolymer Micelles: Higher-Level Assembly for Constructing Hierarchical Structure. *Chem. Rev.* **2020**, *120* (9), 4111–4140.

(3) Jangizehi, A.; Ahmadi, M.; Seiffert, S. Emergence, Evidence, and Effect of Junction Clustering in Supramolecular Polymer Materials. *Mater. Adv.* **2021**, *2* (5), 1425–1453.

(4) King-Chi Leung, F.; van den Enk, T.; Kajitani, T.; Chen, J.; A Stuart, M. C.; Kuipers, J.; Fukushima, T.; Feringa, B. L. Supramolecular Packing and Macroscopic Alignment Controls Actuation Speed in Macroscopic Strings of Molecular Motor Amphiphiles. *J. Am. Chem. Soc* **2018**, *140* (50), 17724–17733.

(5) Cook, M. T.; Haddow, P.; Kirton, S. B.; McAuley, W. J. Polymers Exhibiting Lower Critical Solution Temperatures as a Route to Thermoreversible Gelators for Healthcare. *Adv. Funct. Mater.* **2021**, *31* (8), 1–25.

(6) Sun, Y.; Gao, F.; Yao, Y.; Jin, H.; Li, X.; Lin, S. Light-Induced Reversible Hierarchical Self-Assembly of Amphiphilic Diblock Copolymers into Microscopic Vesicles with Tunable Optical and Nanocarrier Properties. *ACS Macro Lett.* **2021**, *10* (5), 525–530.

(7) Liu, M.; Khan, A. R.; Ji, J.; Lin, G.; Zhao, X.; Zhai, G. Crosslinked Self-Assembled Nanoparticles for Chemo-Sonodynamic Combination Therapy Favoring Antitumor, Antimetastasis Management and Immune Responses. *J. Control. Release* **2018**, *290* (1), 150–164.

(8) Peng, R.; Pang, B.; Hu, D.; Chen, M.; Zhang, G.; Wang, X.; Lu, H.; Cho, K.; Qiu, L. An ABA Triblock Copolymer Strategy for Intrinsically Stretchable Semiconductors. *J. Mater. Chem. C* **2015**, *3* (15), 3606.

(9) Chen, H.; Zhang, W.; Ren, S.; Zhao, X.; Jiao, Y.; Wang, Y.; Stoddart, J. F.; Guo, X. Temperature-Triggered Supramolecular Assembly of Organic Semiconductors. *Adv. Mater.* **2021**, *Early Access*.

(10) Liu, S.; Chen, D.; Zheng, J.; Zeng, L.; Jiang, J.; Jiang, R.; Zhu, F.; Shen, Y.; Wu, D.; Ouyang, G. The Sensitive and Selective Adsorption of Aromatic Compounds with Highly Crosslinked Polymer Nanoparticles. *Nanoscale* **2015**, *7* (40), 16943–16951.

(11) Li, Y.; Liu, T.; Liu, H.; Tian, M.-Z.; Li, Y. Self-Assembly of Intramolecular Charge-Transfer Compounds into Functional Molecular Systems. *Acc. Chem. Res.* **2014**, *47* (4), 1186–1198.

(12) Fussell, S. L.; Bayliss, K.; Coops, C.; Matthews, L.; Li, W.; Briscoe, W. H.; Faers, M. A.; Royall, C. P.; Van Duijneveldt, J. S. Reversible Temperature-Controlled Gelation in Mixtures of PNIPAM Microgels and Non-Ionic Polymer Surfactant. *Soft Matter* **2019**, *15* (42), 8578–8588.

(13) Zhang, M.; Fives, C.; Waldron, K. C.; Zhu, X. X. Self-Assembly of a Bile Acid Dimer in Aqueous Solutions: From Nanofibers to Nematic Hydrogels. *Langmuir* **2017**, *33* (4), 1084–1089.

(14) Wang, X.; Guerin, G.; Wang, H.; Wang, Y.; Manners, I.; Winnik, M. A. Cylindrical Block Copolymer Micelles and Co-Micelles of Controlled Length and Architecture. *Science* **2007**, *317* (5838), 644–647.

(15) Fukui, T.; Garcia-Hernandez, J. D.; MacFarlane, L. R.; Lei, S.; Whittell, G. R.; Manners, I. Seeded Self-Assembly of Charge-Terminated Poly(3-Hexylthiophene) Amphiphiles Based on the Energy Landscape. *J. Am. Chem. Soc.* **2020**, *142* (35), 15038–15048.

(16) Schröder, H. V.; Zhang, Y.; Link, A. J. Dynamic Covalent Self-Assembly of Mechanically Interlocked Molecules Solely Made from Peptides. *Nat. Chem.* **2021**, *13* (9), 850–857.

(17) Qiu, H.; Hudson, Z. M.; Winnik, M. A.; Manners, I. Multidimensional Hierarchical Self-Assembly of Amphiphilic Cylindrical Block Comicelles. *Science* **2015**, *347* (6228), 1329–1332.

(18) Dou, H.; Li, M.; Qiao, Y.; Harniman, R.; Li, X.; Boott, C. E.; Mann, S.; Manners, I. Higher-Order Assembly of Crystalline Cylindrical Micelles into Membrane-Extendable Colloidosomes. *Nat. Commun.* **2017**, *8*, 1–8.

(19) Hu, W.; Wang, Z.; Xiao, Y.; Zhang, S.; Wang, J. Advances in Crosslinking Strategies of Biomedical Hydrogels. *Biomater. Sci.* **2019**, *7* (3), 843–855.

(20) Gobbo, P.; Patil, A. J.; Li, M.; Harniman, R.; Briscoe, W. H.; Mann, S. Programmed Assembly of Synthetic Protocells into Thermoresponsive Prototissues. *Nat. Mater.* **2018**, *17* (12), 1145–1153.

(21) Winnik, M. A.; Yekta, A. Associative Polymers in Aqueous Solution. *Curr. Opin. Colloid Interface Sci.* **1997**, *2* (4), 424–436.

(22) Ryu, J.-H.; Lee, M. Transformation of Isotropic Fluid to Nematic Gel Triggered by Dynamic Bridging of Supramolecular Nanocylinders. *J. Am. Chem. Soc.* **2005**, *127* (41), 14170–14171.

(23) Kim, H.-J.; Kim, T.; Lee, M. Responsive Nanostructures from Aqueous Assembly of Rigid-Flexible Block Molecules. *Acc. Chem. Res.* **2011**, *44* (1), 72–82.

(24) Tsitsilianis, C.; Serras, G.; Ko, C.-H.; Jung, F.; Papadakis, C. M.; Rikkou-Kalourkoti, M.; Patrickios, C. S.; Schweins, R.; Chassenieux, C. Thermoresponsive Hydrogels Based on Telechelic Polyelectrolytes: From Dynamic to "Frozen" Networks. *Macromolecules* **2018**, *51* (6), 2169–2179.

(25) Jin, J.; Wu, D.; Sun, P.; Liu, L.; Zhao, H. Amphiphilic Triblock Copolymer Bioconjugates with Biotin Groups at the Junction Points: Synthesis, Self-Assembly, and Bioactivity. *Macromolecules* **2011**, *44* (7), 2016–2024.

(26) Nielsen, J. E.; Zhu, K.; Sande, S. A.; Kováčik, L.; Cmarko, D.; Knudsen, K. D.; Nyström, B. Structural and Rheological Properties of Temperature-Responsive

Amphiphilic Triblock Copolymers in Aqueous Media. *J. Phys. Chem. B* **2017**, *121* (18), 4885–4899.

(27) Zinn, T.; Willner, L.; Lund, R. Telechelic Polymer Hydrogels: Relation between the Microscopic Dynamics and Macroscopic Viscoelastic Response. *ACS Macro Lett.* **2016**, *5* (12), 1353–1356.

(28) Resendes, R.; Massey, J. A.; Temple, K.; Cao, L.; Power-Billard, K. N.; Winnik, M. A.; Manners, I. Supramolecular Organometallic Polymer Chemistry: Multiple Morphologies and Superstructures from the Solution Self-Assembly of Polyferrocene-Block-Polysiloxane-Block-Polyferrocene Triblock Copolymers. *Chem. Eur. J.* **2001**, *7* (11), 2414–2424.

(29) Graaf, A. J. de; Boere, K. W. M.; Kemmink, J.; Fokkink, R. G.; Nostrum, C. F. van; Rijkers, D. T. S.; Gucht, J. van der; Wienk, H.; Baldus, M.; Mastrobattista, E.; Vermonden, T.; Hennink, W. E. Looped Structure of Flowerlike Micelles Revealed by ^{1}H NMR Relaxometry and Light Scattering. *Langmuir* **2011**, *27* (16), 9843–9848.

(30) Najafi, M.; Kordalivand, N.; Moradi, M.-A.; Dikkenberg, J. van den; Fokkink, R.; Friedrich, H.; Sommerdijk, N. A. J. M.; Hembury, M.; Vermonden, T. Native Chemical Ligation for Cross-Linking of Flower-Like Micelles. *Biomacromolecules* **2018**, *19* (9), 3766–3775.

(31) Lee, E. S.; Oh, K. T.; Kim, D.; Youn, Y. S.; Bae, Y. H. Tumor pH-Responsive Flower-like Micelles of Poly(l-Lactic Acid)-b-Poly(Ethylene Glycol)-b-Poly(l-Histidine). *J. Control. Release* **2007**, *123* (1), 19–26.

(32) Liu, B.; Chen, H.; Li, X.; Zhao, C.; Liu, Y.; Zhu, L.; Deng, H.; Li, J.; Li, G.; Guo, F.; Zhu, X. pH-Responsive Flower-Like Micelles Constructed via Oxime Linkage for Anticancer Drug Delivery. *RSC Adv.* **2014**, *4* (90), 48943–48951.

(33) Lunn, D. J.; Gould, O. E. C.; Whittell, G. R.; Armstrong, D. P.; Mineart, K. P.; Winnik, M. A.; Spontak, R. J.; Pringle, P. G.; Manners, I. Microfibres and

Macroscopic Films from the Coordination-Driven Hierarchical Self-Assembly of Cylindrical Micelles. *Nat. Commun.* **2016**, *7* (12371), 1–10.

(34) Tritschler, U.; Pearce, S.; Gwyther, J.; Whittell, G. R.; Manners, I. 50th Anniversary Perspective: Functional Nanoparticles from the Solution Self-Assembly of Block Copolymers. *Macromolecules.* **2017**, *50* (9), 3439–3463.

(35) Massey, J. A.; Temple, K.; Cao, L.; Rharbi, Y.; Raez, J.; Winnik, M. A.; Manners, I. Self-Assembly of Organometallic Block Copolymers: The Role of Crystallinity of the Core-Forming Polyferrocene Block in the Micellar Morphologies Formed by Poly(Ferrocenylsilane-b-Dimethylsiloxane) in n-Alkane Solvents. *J. Am. Chem. Soc.* **2000**, *122* (47), 11577–11584.

(36) Macfarlane, L.; Zhao, C.; Cai, J.; Qiu, H.; Manners, I. Emerging Applications for Living Crystallization-Driven Self-Assembly. *Chem. Sci.* **2021**, *12* (13), 4661–4682.

(37) Ganda, S.; Stenzel, M. H. Concepts, Fabrication Methods and Applications of Living Crystallization-Driven Self-Assembly of Block Copolymers. *Prog. Polym. Sci.* **2020**, *101* (101195), 1–33.

(38) Foster, J. C.; Varlas, S.; Couturaud, B.; Coe, Z.; O'Reilly, R. K. Getting into Shape: Reflections on a New Generation of Cylindrical Nanostructures' Self-Assembly Using Polymer Building Blocks. *J. Am. Chem. Soc.* **2019**, *141* (7), 2742–2753.

(39) Nishimura, T.; Sumi, N.; Mukai, S.; Sasaki, Y.; Akiyoshi, K. Supramacromolecular Injectable Hydrogels by Crystallization-Driven Self-Assembly of Carbohydrate-Conjugated Poly(2-Isopropyloxazoline)s for Biomedical Applications. *J. Mater. Chem. B* **2019**, *7* (41), 6362–6369.

(40) Truong, N. P.; Quinn, J. F.; Whittaker, M. R.; Davis, T. P.; And, F. Polymeric Filomicelles and Nanoworms: Two Decades of Synthesis and Application. *Polym. Chem* **2016**, *7* (26), 4295–4312.

(41) Gilroy, J. B.; Gädt, T.; Whittell, G. R.; Chabanne, L.; Mitchels, J. M.; Richardson, R. M.; Winnik, M. A.; Manners, I. Monodisperse Cylindrical Micelles by Crystallization-Driven Living Self-Assembly. *Nat. Chem.* **2010**, *2* (7), 566–570.

(42) Shin, S.; Menk, F.; Kim, Y.; Lim, J.; Char, K.; Zentel, R.; Choi, T. Living Light-Induced Crystallization-Driven Self-Assembly for Rapid Preparation of Semiconducting Nanofibers. *J. Am. Chem. Soc.* **2018**, *140* (19), 6088–6094.

(43) Nie, J.; Wang, Z.; Huang, X.; Lu, G.; Feng, C. Uniform Continuous and Segmented Nanofibers Containing a π-Conjugated Oligo(p-Phenylene Ethynylene) Core via "Living" Crystallization-Driven Self-Assembly: Importance of Oligo(p-Phenylene Ethynylene) Chain Length. *Macromolecules* **2020**, *53* (15), 6299–6313.

(44) Schmelz, J.; Schedl, A. E.; Steinlein, C.; Manners, I.; Schmalz, H. Length Control and Block-Type Architectures in Worm-like Micelles with Polyethylene Cores. *J. Am. Chem. Soc.* **2012**, *134* (34), 14217–14225.

(45) Nazemi, A.; Boott, C. E.; Lunn, D. J.; Gwyther, J.; Hayward, D. W.; Richardson, R. M.; Winnik, M. A.; Manners, I. Monodisperse Cylindrical Micelles and Block Comicelles of Controlled Length in Aqueous Media. *J. Am. Chem. Soc.* **2016**, *138* (13), 4484–4493.

(46) Qian, J.; Li, X.; Lunn, D. J.; Gwyther, J.; Hudson, Z. M.; Kynaston, E.; Rupar, P. A.; Winnik, M. A.; Manners, I. Uniform, High Aspect Ratio Fiber-like Micelles and Block Co-Micelles with a Crystalline π-Conjugated Polythiophene Core by Self-Seeding. *J. Am. Chem. Soc.* **2014**, *136* (11), 4121–4124.

(47) Finnegan, J. R.; Lunn, D. J.; Gould, O. E. C.; Hudson, Z. M.; Whittell, G. R.; Winnik, M. A.; Manners, I. Gradient Crystallization-Driven Self-Assembly: Cylindrical Micelles with "Patchy" Segmented Coronas via the Coassembly of Linear and Brush Block Copolymers. *J. Am. Chem. Soc.* **2014**, *136* (39), 13835–13844.

(48) Ganda, S.; Wong, C. K.; Stenzel, M. H. Corona-Loading Strategies for Crystalline Particles Made by Living Crystallization-Driven Self-Assembly. *Macromolecules* **2021**, *54* (14), 6662–6669.

(49) Pearce, S.; He, X.; Hsiao, M.-S.; Harniman, R. L.; MacFarlane, L. R.; Manners, I. Uniform, High-Aspect-Ratio, and Patchy 2D Platelets by Living Crystallization-Driven Self-Assembly of Crystallizable Poly(Ferrocenyldimethylsilane)-Based Homopolymers with Hydrophilic Charged Termini. *Macromolecules* **2019**, *52* (16), 6068–6079.

(50) Li, X.; Gao, Y.; Boott, C. E.; Hayward, D. W.; Harniman, R.; Whittell, G. R.; Richardson, R. M.; Winnik, M. A.; Manners, I. "Cross" Supermicelles via the Hierarchical Assembly of Amphiphilic Cylindrical Triblock Comicelles. *J. Am. Chem. Soc* **2016**, *138*.

(51) Hudson, Z. M.; Boott, C. E.; Robinson, M. E.; Rupar, P. A.; Winnik, M. A.; Manners, I. Tailored Hierarchical Micelle Architectures Using Living Crystallization-Driven Self-Assembly in Two Dimensions. *Nat. Chem.* **2014**, *6* (10), 893–898.

(52) Zhang, Y.; Shaikh, H.; Sneyd, A. J.; Tian, J.; Xiao, J.; Blackburn, A.; Rao, A.; Friend, R. H.; Manners, I. Efficient Energy Funneling in Spatially Tailored Segmented Conjugated Block Copolymer Nanofiber-Quantum Dot or Rod Conjugates. *J. Am. Chem. Soc.* **2021**, *143* (18), 7032–7041.

(53) Zhang, Y.; Pearce, S.; Eloi, J.-C.; Harniman, R. L.; Tian, J.; Cordoba, C.; Kang, Y.; Fukui, T.; Qiu, H.; Blackburn, A.; Richardson, R. M.; Manners, I. Dendritic Micelles with Controlled Branching and Sensor Applications. *Cite This J. Am. Chem. Soc* **2021**, *143* (15), 5805–5814.

(54) Zhang, Q.; He, Y.; Oliver, A. M.; Pearce, S.; Harniman, R. L.; Whittell, G. R.; Liu, Y.; Du, S.; Leng, J.; Manners, I. Low Length Dispersity Fiber-like Micelles from an A–B–A Triblock Copolymer with Terminal Crystallizable Poly(Ferrocenyldimethylsilane) Segments via Living Crystallization-Driven Self-Assembly. *Polym. Chem.* **2019**, *10* (29), 3973–3982.

(55) Finnegan, J. R.; He, X.; Street, S. T. G.; Garcia-Hernandez, J. D.; Hayward, D. W.; Harniman, R. L.; Richardson, R. M.; Whittell, G. R.; Manners, I. Extending the Scope of "Living" Crystallization-Driven Self-Assembly: Well-Defined 1D Micelles and Block Comicelles from Crystallizable Polycarbonate Block Copolymers. *J. Am. Chem. Soc.* **2018**, *140* (49), 17127–17140.

(56) Garcia-Hernandez, J. D.; Street, S. T. G.; Kang, Y.; Zhang, Y.; Manners, I. Cargo Encapsulation in Uniform, Length-Tunable Aqueous Nanofibers with a Coaxial Crystalline and Amorphous Core. *Macromolecules* **2021**, *54* (12), 5784–5796.

(57) Caliari, S. R.; Burdick, J. A. A Practical Guide to Hydrogels for Cell Culture. *Nat. Methods* **2016**, *13* (5), 405–414.

(58) Boott, C. E.; Leitao, E. M.; Hayward, D. W.; Laine, R. F.; Mahou, P.; Guerin, G.; Winnik, M. A.; Richardson, R. M.; Kaminski, C. F.; Whittell, G. R.; Manners, I. Probing the Growth Kinetics for the Formation of Uniform 1D Block Copolymer Nanoparticles by Living Crystallization-Driven Self-Assembly. *ACS Nano* **2018**, *12* (9), 8920–8933.

(59) Pangborn, A. B.; Giardello, M. A.; Grubbs, R. H.; Rosen, R. K.; Timmers, F. J. Safe and Convenient Procedure for Solvent Purification. *Organometallics* **1996**, *15* (5), 1518–1520.

(60) Xu, J.; Zhou, H.; Yu, Q.; Guerin, G.; Manners, I.; Winnik, M. A. Synergistic Self-Seeding in One-Dimension: A Route to Patchy and Block Comicelles with Uniform and Controllable Length. *Chem. Sci.* **2019**, *10* (8), 2280–2284.

Chapter 5

Length-Tunable Water-Soluble Block Copolymer Nanofibers and Segmented Nanofibers with a Crystalline Core and a Polyfructose Corona for Cancer Targeting and Drug-Loading

This chapter contains unpublished results

Contributions:

This research was conducted by Juan Diego Garcia Hernandez. Helpful discussions were provided by Dr. Chuanqi Zhao. Research was conducted at the University of Victoria.

5.1 Abstract

Passive targeting can be achieved by tuning the dimensions of a nanoparticle vector. Nanofibers have been highlighted as promising drug-delivery vehicles owing to morphological advantages such as long circulation times and specificity. Herein, both passive and active targeting are incorporated in one polymeric nanofiber system. The nanofibers were prepared from amphiphilic diblock copolymers (diBCP), PFTMC-*b*-PFr, with poly(fluorenetrimethylenecarbonate) (PFMTC) and polyfructose (PFr). PFTMC is a hydrophobic, biodegradable, and crystallizable polymer that has been used as the core-forming block. PFr is a nontoxic and water-soluble polymer used as corona-forming block with the ability to target the GLUT5 receptor which is overexpressed in triple negative breast cancer (TNBC) tissue. The ability to control the length of the nanofibers using the living crystallization-driven self-assembly (CDSA) method in the presence of a PFr corona-forming block offered the potential of both passive and active targeting. The length of the PFTMC-*b*-PFr nanofibers was controlled from ca. 50 – 1200 nm. PFTMC-*b*-PFr nanofibers (L_n = 395 nm) were transferred to water and were found stable for at least 2 weeks, with no significant change on the length and length-dispersity observed. In addition, triblock and pentablock nanofibers were prepared via sequential living CDSA with different spatially-defined segments designed to provide distinct functions. Finally, preliminary experiments involving a study of the uptake of curcumin, a well-known hydrophobic drug, were performed. This proof-of-concept work may facilitate the future development of size-tunable polyfructose containing nanofiber therapeutics.

5.2 Introduction

Nanoparticle-based therapeutics have been at the forefront for the treatment of cancer[1,2] and the severe acute respiratory syndrome coronavirus 2 (SARS-CoV-2) caused by the COVID-19 virus.[3] Polymeric nanoparticles represent promising drug-delivery vehicle alternatives to traditional free-drug therapies. The properties of the nanovectors such as size, shape, and surface chemistry influence its overall performance.[4,5] Nanofibers possess morphological advantages that involve high circulation times,[6] tumor penetration,[7,8] and low renal[9] and phagocytosis[10,11] clearance, when compared to spherical counterparts. However, morphologically pure polymeric nanofibers are usually challenging to prepare via amorphous core-forming block copolymer (BCP) self-assembly, as control of the different factors that influence micelle morphology is difficult,[12] and spherical micelles and vesicles dominate the phase diagram.[13] To overcome this issue, crystallization-driven self-assembly (CDSA) of amphiphilic BCPs has attracted much attention as a mean to access to morphologically pure BCP nanofiber micelles with a crystalline core-forming block and a solvophilic corona-forming block.[14–18] Moreover, the addition of unimeric BCP to small nanofiber seeds (prepared via sonication) has allowed control of nanofiber length from ca. 20 nm to few μm, with length dispersities $Đ < 1.1$ via a method termed living CDSA.[19,20] Sequential living CDSA with different BCPs has also allowed the preparation of nanofibers with segmented corona chemistries for a range of applications.[8,21–23]

In general, nanoparticle drug vectors can associate with therapeutic molecules that are otherwise insoluble and, therefore, require a delivery vehicle.[24] The binding between a drug and the nanoparticle increases the circulation time of the pharmaceutical molecule by

providing a protective 'barrier' that can help to lower unwanted early interactions and side effects.[25] Typically, the release of a drug from a nanoparticle vector at specific tissues or sections of the body would increase the therapeutic efficiency while reducing systemic toxicity.[26] Two main targeting strategies have been developed to increase the efficiency of nanoparticle-based therapeutics towards specific tissues: passive and active targeting.[27] Passive targeting relies on distribution profiles and circulation times of nanovectors which are directly linked to the physical properties of the nanoparticles such as size,[28] shape,[29] and dispersity (*Đ*).[5,30,31] Active targeting involves the functionalization of nanoparticles with moieties or functional groups such as folic acid or antibodies, among others, to interact with specific cell populations.[32–35] Despite the vast progress in the field of nanoparticle-based therapeutics the design, synthesis, and successful delivery of cargo remains a major challenge as there is no universal strategy suited for every situation.[34,36]

Triple-negative breast cancer (TNBC) accounts for 10 – 15% of diagnosed breast cancers and is considered an aggressive cancer with poor prognosis.[37] Treatment of TNBC is challenging owing to the absence of estrogen and progesterone receptors with no overexpression of the human epithermal growth factor receptor 2, which makes targeting of TNBC an onerous task.[38] Breast cancer cells transport fructose and overexpress the fructose transporter GLUT5; remarkably, GLUT5 is not overexpressed in healthy breast tissue.[39] Fructose and polyfructose (PFr) can be found in nature,[40,41] are part of the human diet,[42,43] and are approved by the food and drug administration (FDA).[44] Therefore, fructose and PFr are suitable targeting candidates for TNBC. Nanoparticles with a PFr corona-forming block have demonstrated in vitro targeting abilities towards TNBC tissue.[45] Furthermore, BCP spheres,[45–48] platelets,[22,49] and rod-like micelles[50,51] with PFr corona-

forming blocks have been reported. Similarly, BCP spheres, platelets, and nanofibers with glucose- and mannose-containing coronas have also been synthesized.[11,52,53] To our knowledge, control over the length of BCP nanofibers with PFr coronas with low length-dispersities ($Đ$ < 1.1) and potential ability to target TNBC[45,51] have not been reported.

In this work, we sought to develop diBCP nanofibers that simultaneously possess both passive and active targeting for TNBC tissue. Passive targeting can be attained by both the nanoparticle morphology (i.e. fiber-like), and by tuning the length of the nanofibers.[5] To achieve active targeting, PFr was selected as a corona-forming block to target the GLUT5 receptor. Poly(fluorenetrimethylenecarbonate) (PFTMC) was selected as the core-forming block as it has been used to prepare nanofibers of controlled dimensions via living CDSA and is noncytotoxic.[54] Hence, the synthesis and self-assembly of PFTMC-*b*-PFr diBCPs was investigated. Triblock and pentablock segmented nanofibers were targeted via sequential living CDSA to prepare nanofibers with functional segments. The role of each nanofiber segment may contribute to overcome the different biological barriers encountered in the human body to effectively increase the efficiency of the drug delivery process.[1,21,36] Curcumin is a natural therapeutic agent extracted from *Curcuma longa* that has been used as antioxidant, antimicrobial, anti-inflammatory, antiviral, anticancer, and recently for treatment of SARS-CoV-2 caused by the COVID-19 virus.[55-57] Hydrogen bonding between fructose and curcumin has been used to prepare well-defined capsules via self-assembly.[58] Based on these precedents, curcumin uptake by PFTMC-*b*-PFr nanofibers was briefly investigated.

5.3 Results and Discussion

5.3.1 Synthesis and Characterization of PFTMC$_{18}$-*b*-PFr$_{92}$ DiBCP

The core-to-corona ratio of the diBCP was based on previous reports that indicate that ratios between 1:5 to 1:20 generally yield nanofiber micelles.[15,59,60] To meet with such requirement a 1:5 ratio was targeted (e.g. PFTMC$_{18}$-*b*-PFr$_{92}$). The PFTMC$_{18}$-*b*-PFr$_{92}$ diBCP (Figure 5. 1) was prepared using a combination of ring-opening polymerization (ROP) and reversible addition-fragmentation chain-transfer (RAFT) polymerization, following a reported procedure.[61] The monomers spiro[fluorene-9,5′-[1,3]-dioxan]-2′-one (FTMC), and the 1-*O*-acryloyl-2,3:4,5-di-*O*-isopropylidene-*β*-D-fructopyranose (fructose monomer) were prepared according to procedures reported by Finnegan et al,[54] and Lu et al,[47] respectively. ROP of the FTMC monomer using 2-cyano-5-hydroxypentan-2-yl ethyl carbonotrithioate as both small molecule initiator and chain transfer agent (CTA) yielded PFTMC$_{18}$-CTA. The PFTMC$_{18}$-CTA homopolymer was characterized using matrix-assisted laser desorption/ionization-time of flight (MALDI-TOF) mass spectrometry (4,729 m/z, DP_n = 18, Figure S5. 1),[61] ^{1}H NMR spectroscopy (Figure S5. 2),[61] and gel permeation chromatography (GPC, M_n = 4,800, $Đ_M$ = 1.17, polystyrene standards, Figure S5. 3).[61] RAFT polymerization of the PFTMC$_{18}$-CTA with the fructose monomer in dimethylacetamide yielded the targeted PFTMC$_{18}$-*b*-PPFr$_n$ diBCP (protected polyfructose) (PPFr). The DP_n value of the PPFr block was determined by comparing the relative ^{1}H NMR integration of the PFTMC$_{18}$ block at 7.87 – 7.25 ppm to the resonance of the PPFr block at 4.80 – 3.58 ppm, and 1.66 – 1.21 and corresponded to PFTMC$_{18}$-*b*-PPFr$_{92}$. (Figure S5. 4). Compared to the trace of the PFTMC$_{18}$ homopolymer, GPC analysis of the PFTMC$_{18}$-*b*-PPFr$_{92}$ diBCP indicated an increase of molecular weight (M_n = 15,600, $Đ_M$ =

1.26, Figure S5. 3). Removal of the isopropylidene protecting groups from the $PPFr_{92}$ block was conducted in trifluoroacetic acid:H_2O (TFA:H_2O) according to a modified procedure reported by Ganda and coworkers.[22] The DP_n value of the PFr block was determined by comparing the relative integration of the resonances in the ^1H NMR spectrum of the $PFTMC_{18}$ block at 7.95 – 7.06 (144H, Ha, OC*H*$_2$C) to the resonance of the deprotected PFr block at 4.51 – 3.36 ppm, and 2.05 – 1.21 and corresponded to $PFTMC_{18}$-*b*-PFr_{92} (Figure 5. 1, S5). The good agreement by ^1H NMR analysis between the DP_n of the $PFTMC_{18}$ block and the DP_n of the protected $PPFr_{92}$ and the deprotected PFr_{92} blocks underscored the successful conversion of $PPFr_{92}$ to PFr_{92} and the good stability of the $PFTMC_{18}$-*b*-PFr_{92} diBCP to the reaction conditions (Figure S5. 2, 4-5). Polymer characterization data is summarized in Table S5. 1.

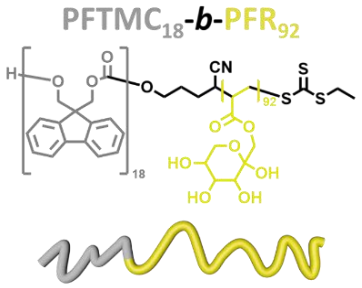

Figure 5. 1. Color coded structure of the $PFTMC_{18}$-*b*-PFr_{92} diBCP used in this work.

5.3.2 Preparation of Low Length-Dispersity Nanofibers with Controlled Dimensions

Next, the solution state self-assembly of $PFTMC_{18}$-*b*-PFr_{92} was investigated in detail (Figure 5. 2). Dynamic light scattering (DLS) analysis revealed that dimethylformamide (DMF) was a good solvent for both PFTMC and PFr as the diBCP was present in unimeric form when solubilized in DMF with a mean hydrodynamic size of $R_{h,z}$ = 9.8 nm (σ = 3.3 nm. Figure S5. 6). The self-assembly of $PFTMC_{18}$-*b*-PFr_{92} via CDSA involving spontaneous (homogeneous) nucleation to yield nanofibers was attempted in a

mixture of DMF and MeOH. MeOH had been used successfully for the preparation of PFTMC-based nanofibers,[54,61] hence, it was used as a selective solvent for the hydrophilic PFr corona-forming block and as a poor solvent for the hydrophobic PFTMC core-forming block. Spontaneous nucleation of $PFTMC_{18}$-*b*-PFr_{92} was conducted by heating the diBCP to 75 °C for 3 h in DMF:MeOH (common:selective solvent ratio, *v/v*), followed by cooling to 20 °C over a period of 3 h and ageing for 48 h. The DMF:MeOH content was varied from 10:90 to 40:60 *v/v* (Figure S5. 7). Transmission electron microscopy (TEM) analysis revealed that below 30% of DMF content, aggregated, long, and length-disperse nanofibers were obtained (L_n > 2 µm, Figure S5. 7B-D). At 40% DMF content morphologically pure long and length-disperse nanofibers with no evident aggregation were observed by TEM (Figure 5. 2B, S7E). Fragmentation of the length-disperse nanofibers via sonication (3 h at 0 °C) yielded seed nanofibers with an average length L_n = 54 nm ($Đ$ = 1.09, σ = 17 nm. Figure 5. 2C) by TEM.

Nanofibers of tunable lengths were prepared via living CDSA by adjusting the m_{unimer}/m_{seed} (equivalents) of $PFTMC_{18}$-*b*-PFr_{92} unimer supplemented to diluted seed nanofiber solutions (in DMF:MeOH 40:60), followed by a 48 h ageing period. By modulating the equivalents of unimer added from 0:1 to 20:1, nanofiber length control was achieved from $L_{n(seed)}$ = 54 nm ($Đ$ = 1.09, σ = 17 nm) to L_n = 1201 nm ($Đ$ = 1.08, σ = 335 nm), as observed by TEM (Figure 5. 2D-G, S8). All living CDSA experiments yielded low length dispersity $PFTMC_{18}$-*b*-PFr_{92} nanofibers ($Đ \leq 1.08$. Figure 5. 2H-I). In addition, a linear trend between the final length of the nanofibers vs m_{unimer}/m_{seed} ratio was observed (Figure 5. 2J). The resulting nanofiber length at a given mass of equivalents (m_{unimer}/m_{seed}) added was in good agreement with the theoretical length ($L_{n(theory)}$) and

experimental error associated with the addition of unimer to seeds of $L_{n(seed)}$ = 54 nm (σ = 17. Figure 5. 2J), given by the following equation:

$$L_{n(theory)} = (L_{n(seed)} \times {}^{m_{unimer}}/_{m_{seed}}) + L_{n(seed)} \quad (\boldsymbol{eq.1})$$

To assess if complete unimer consumption was reached after 48 h, TEM analysis of the PFTMC$_{18}$-*b*-PFr$_{92}$ nanofiber sample with 20 equivalents of unimer added was conducted after 4 months. Within error, the length and dispersity of the nanofibers remained unchanged for up to 4 months when compared to the data collected after 48 h as shown by TEM, consistent with complete unimer consumption within the initial 48 h (20 eqs; 48 h: L_n = 1201 nm, $Đ$ = 1.08, σ = 335 nm. 4 months: L_n = 1256 nm, $Đ$ = 1.06, σ = 313nm. Table S5. 2 and Figure S5. 9). A summary of the contour length analysis of the PFTMC$_{18}$-*b*-PFr$_{92}$ diBCP nanofibers is presented in Table S5. 2.

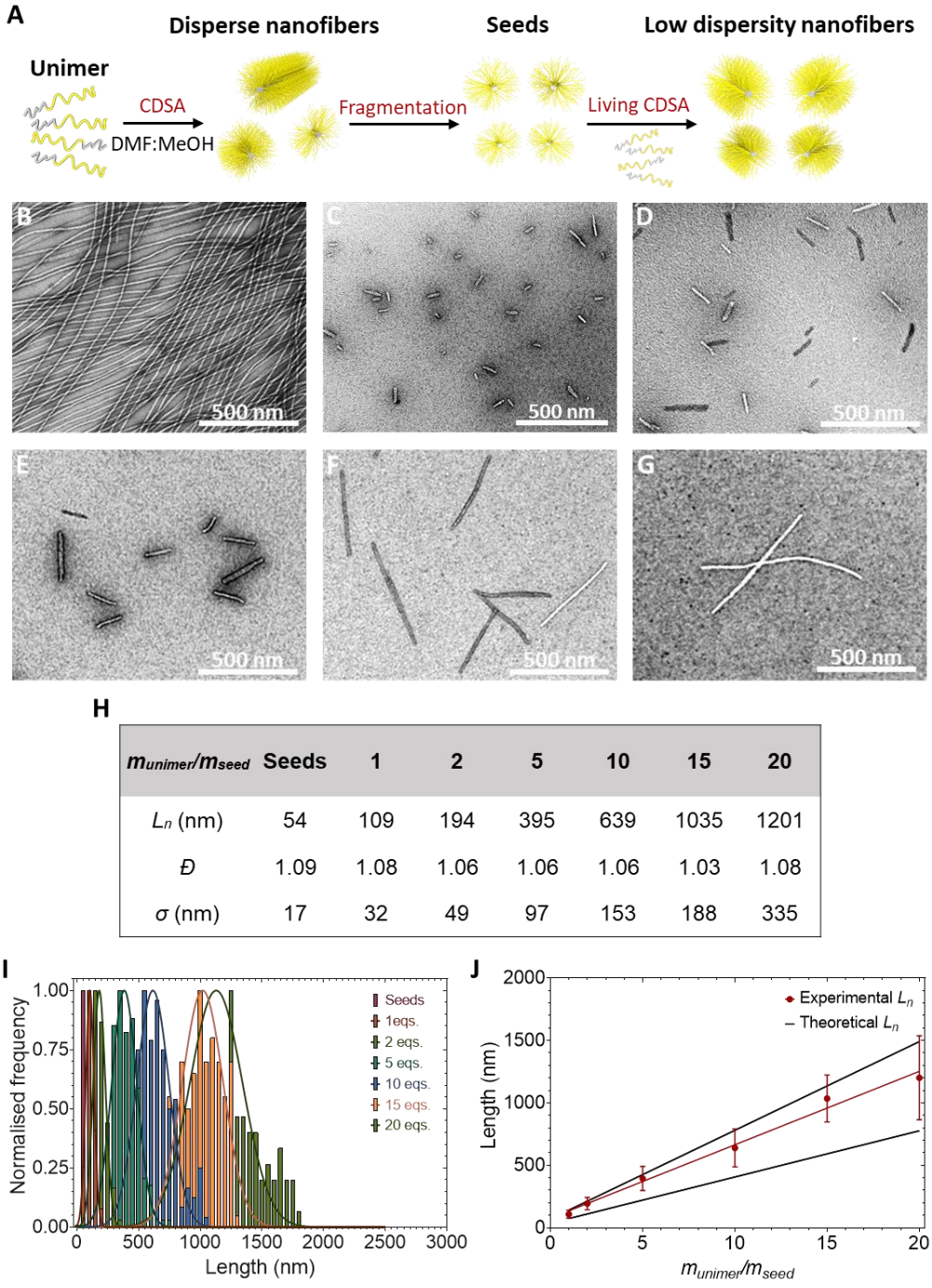

m_{unimer}/m_{seed}	Seeds	1	2	5	10	15	20
L_n (nm)	54	109	194	395	639	1035	1201
$Đ$	1.09	1.08	1.06	1.06	1.06	1.03	1.08
σ (nm)	17	32	49	97	153	188	335

Figure 5. 2. Preparation of low-dispersity nanofibers of controlled length. A) Schematic representation of the generation of low-dispersity PFTMC$_{18}$-*b*-PFr$_{92}$ nanofibers by sequential CDSA, sonication, and living CDSA methods. B) TEM micrograph of disperse PFTMC$_{18}$-*b*-PFr$_{92}$ nanofibers (0.5 mg/mL) prepared in DMF:MeOH (40:60 *v/v*), after annealing at 75 °C for 3 h, and ageing for 48 h. C) TEM micrograph of seed nanofibers (54 nm, $Đ$ = 1.09, σ = 17 nm) prepared through sonication of the disperse nanofibers (from B, in DMF:MeOH 40:60) for 3h at 0 °C. D-G) TEM images of low-dispersity nanofibers prepared through seeded-growth by addition of PFTMC$_{18}$-*b*-PFr$_{92}$ unimer in DMF to nanofiber seed solutions at: D) 1:1 E) 2:1 F) 5:1 and G) 10:1 m_{unimer}/m_{seed} ratios. H) Nanofiber length summary. I) Contour length histograms of seeds and low length dispersity nanofibers of controlled lengths J) Plot of m_{unimer}/m_{seed} against experimental and theoretical length (L_n), error bars indicate standard deviation ($n \geq 150$ number of nanofibers). TEM images were stained with uranyl acetate (3 wt % in MeOH).

5.3.3 Water Solubility of PFTMC$_{18}$-*b*-PFr$_{92}$ DiBCP Nanofibers

Both DMF and MeOH are known to be toxic solvents for humans.[62,63] Removal of DMF and MeOH from PFTMC$_{18}$-*b*-PFr$_{92}$ nanofibers is therefore required prior to be used for biomedical applications. Hence, to explore the colloidal stability of PFTMC$_{18}$-*b*-PFr$_{92}$ nanofibers in water and to remove DMF and MeOH, low-dispersity PFTMC$_{18}$-*b*-PFr$_{92}$ nanofibers L_n = 395 nm ($Đ$ = 1.06, σ = 97 nm, prepared via Living CDSA at 5 m_{unimer}/m_{seed}.. Figure 5. 2F) were transferred to water via dialysis. After dialysis and 2 weeks of aging, the nanofiber solution was clear and no obvious precipitation was observed, elucidating the good stability of the nanofibers in water. By TEM no change in nanofiber morphology was observed after dialysis and ageing of the sample (Figure S5. 10A-B). Furthermore, the lengths of the nanofibers measured before and after dialysis into water and subsequent 2 weeks of aging were similar (before L_n = 395 nm ($Đ$ = 1.06, σ = 97 nm), after L_n = 394 nm ($Đ$ = 1.07, σ = 107 nm. Figure S5. 10C). This evidence indicates the good colloidal solubility of the diBCP nanofibers in water and demonstrates that no significant nanofiber fragmentation occurs during the dialysis process.

5.3.4 Preparation of Segmented Nanofibers with Spatially Distinct Corona-Forming Blocks

After demonstrating the CDSA and living CDSA of PFTMC$_{18}$-*b*-PFr$_{92}$ diBCP nanofibers (Figure 5. 2), we sought to prepare segmented nanofibers containing fractions made from PFTMC$_{18}$-*b*-PFr$_{92}$. We aimed to accommodate the PFTMC$_{18}$-*b*-PFr$_{92}$ segments at the ends of triblock nanofibers (Figure 5. 3) since the terminal fractions of segmented nanofibers are likely more exposed to interact with the environment, consequently, this would allow better targeting efficiency. Three distinct preformed nanofibers were prepared

via the living CDSA method according to reported procedures,[54,61] and characterized by TEM (PFTMC$_{19}$-*b*-PEG$_{275}$ diBCP nanofibers: L_n = 127 nm, $Đ$ = 1.06, σ = 32 nm. Figure 5. 3A, S11. PFTMC$_{18}$-*b*-PNIPAM$_{425}$ diBCP nanofibers L_n = 127 nm, $Đ$ = 1.03, σ = 22 nm. Figure 5. 3B, S12. PFTMC$_{18}$-*b*-PBMA$_{44}$-*b*-PNIPAM$_{70}$ triBCP nanofibers L_n = 163 nm, $Đ$ = 1.05, σ = 38 nm. Figure 5. 3C, S13). To the three solutions of preformed nanofibers (diluted in DMF:MeOH 40:60) 1 or 0.5 equivalents of the PFTMC$_{18}$-*b*-PFr$_{92}$ unimer were added and the solutions were aged for 72 h at 20 ºC (Figure 5. 3). The resulting nanofiber solutions were analyzed by TEM (Figure 5. 3D-F). The segments of the three triblock nanofibers can be distinguished by TEM from the preformed nanofibers owing to the higher contrast provided by a higher concentration of staining agent at the PFr-corona block resulting on darker terminal segments (Figure 5. 3D-F). Contour length analysis revealed that the resulting lengths of the triblock nanofibers with flanking PFTMC$_{18}$-*b*-PFr$_{92}$ ends were in good agreement with the lengths predicted for a living CDSA process (*eq. 1*) considering that $L_{n(seed)} = L_n$ of the preformed nanofibers; PFTMC$_{18}$-*b*-PFr$_{92}$-***m***-PFTMC$_{19}$-*b*-PEG$_{275}$-***m***-PFTMC$_{18}$-*b*-PFr$_{92}$ nanofibers L_n = 249 nm ($Đ$ = 1.04, σ = 47 nm. Figure 5. 3D, S11), PFTMC$_{18}$-*b*-PFr$_{92}$-***m***-PFTMC$_{18}$-*b*-PNIPAM$_{425}$-***m***-PFTMC$_{18}$-*b*-PFr$_{92}$ nanofibers L_n = 297 nm ($Đ$ = 1.09, σ = 90 nm. Figure 5. 3E, S12), and PFTMC$_{18}$-*b*-PFr$_{92}$-***m***-PFTMC$_{18}$-*b*-PBMA$_{44}$-*b*-PNIPAM$_{70}$-***m***-PFTMC$_{18}$-*b*-PFr$_{92}$ nanofibers L_n = 225 nm ($Đ$ = 1.08, σ = 66 nm. Figure 5. 3F, S13). **'*m*'** is used to distinguish between different micellar nanofiber sections. Together, the TEM and contour length data confirm the preparation of segmented nanofibers with terminal PFr-segments for potential targeting of TNBC tissue.

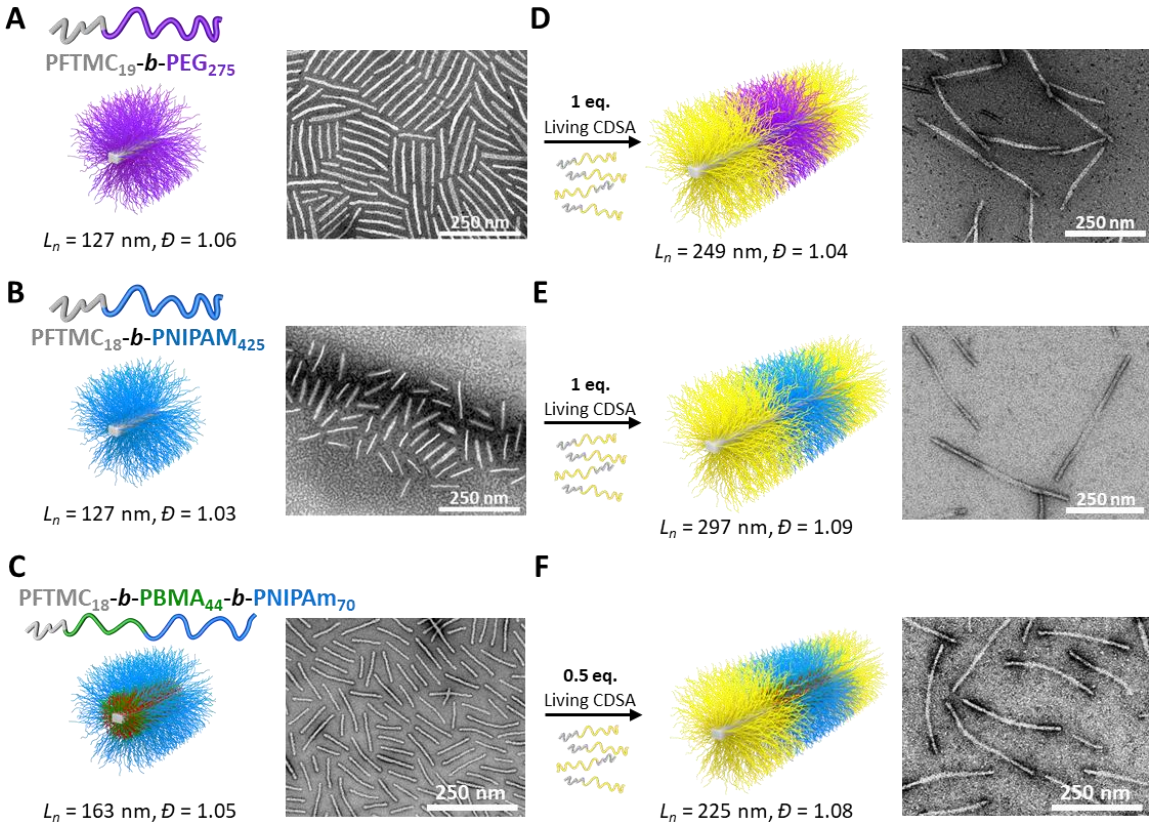

Figure 5. 3. Preparation of low-dispersity triblock nanofibers of controlled lengths. Schematic representation and TEM micrographs of preformed A) PFTMC$_{19}$-*b*-PEG$_{275}$ diBCP nanofibers L_n = 127 nm, $Đ$ = 1.06, σ = 32 nm, B) PFTMC$_{18}$-*b*-PNIPAM$_{425}$ diBCP nanofibers L_n = 127 nm, $Đ$ = 1.03, σ = 22 nm, and C) PFTMC$_{18}$-*b*-PBMA$_{44}$-*b*-PNIPAM$_{70}$ triBCP nanofibers L_n = 163 nm, $Đ$ = 1.05, σ = 38 nm, utilized for cargo loading (red dots) reported by ourselves.[61] Scheme and TEM micrographs of the preparation of triblock nanofibers (in DMF:MeOH 40:60) after the addition of PFTMC$_{18}$-*b*-PFr$_{92}$ unimer (10 mg/mL in DMF) to preformed nanofibers in A (1 m_{unimer}/m_{seed}), B (1 m_{unimer}/m_{seed}), C (0.5 m_{unimer}/m_{seed}) with 72 h ageing at 20 °C, D) PFTMC$_{18}$-*b*-PFr$_{92}$-*m*-PFTMC$_{19}$-*b*-PEG$_{275}$-*m*-PFTMC$_{18}$-*b*-PFr$_{92}$ nanofibers L_n = 349 nm, $Đ$ = 1.04, σ = 47 nm, E) PFTMC$_{18}$-*b*-PFr$_{92}$-*m*-PFTMC$_{18}$-*b*-PNIPAM$_{425}$-*m*-PFTMC$_{18}$-*b*-PFr$_{92}$ nanofibers L_n = 297 nm, $Đ$ = 1.09, σ = 90 nm, and F) PFTMC$_{18}$-*b*-PFr$_{92}$-*m*-PFTMC$_{18}$-*b*-PBMA$_{44}$-*b*-PNIPAM$_{70}$-*m*-PFTMC$_{18}$-*b*-PFr$_{92}$ nanofibers L_n = 225 nm, $Đ$ = 1.08, σ = 66 nm.

5.3.5 Preparation of Pentablock Nanofibers

A nanoparticle-based therapeutic must overcome several biological barriers prior to the successful delivery of payload to a specific site.[5,36] To increase the circulation time of the nanofibers with potential targeting capabilities, living CDSA can be used in sequence to add pegylated diBCP to the ends of the preformed triblock nanofibers to yield pentablock nanofibers (Figure 5. 4). PEG-containing vectors have been used to increase circulation times of nanoparticles, decrease immune recognition, enhance the overall efficacy of drug

delivery vehicles, is nontoxic, and is FDA approved.[64–66] Furthermore, we have also reported the low cytotoxicity of PFTMC-*b*-PEG diBCP nanofibers[54] making this diBCP an excellent candidate for such purpose. A solution of $PFTMC_{19}$-*b*-PEG_{275} unimers (10 mg/mL in THF) was therefore added to triblock $PFTMC_{18}$-*b*-PFr_{92}-***m***-$PFTMC_{18}$-*b*-$PBMA_{44}$-*b*-$PNIPAM_{70}$-***m***-$PFTMC_{18}$-*b*-PFr_{92} nanofibers (L_n = 225 nm, $Đ$ = 1.08, σ = 66 nm. Figure 5. 3F, 4A). Segmented nanofibers with newly grown segments were analyzed by TEM (Figure 5. 4B). Contour length analysis of the nanofibers indicated an increase of the length to L_n = 354 nm ($Đ$ = 1.08, σ = 98 nm. Figure S5. 13). Within error, the resulting length of the nanofibers was consistent with the addition of 0.36 equivalents of unimer to the triblock nanofibers given by *eq. 1* (Figure S5. 13). The TEM and contour length analysis indicated the successful preparation of pentablock nanofibers with the following arrangement: $PFTMC_{19}$-*b*-PEG_{275}-***m***-$PFTMC_{18}$-*b*-PFr_{92}-***m***-$PFTMC_{18}$-*b*-$PBMA_{44}$-*b*-$PNIPAM_{70}$-***m***-$PFTMC_{18}$-*b*-PFr_{92}-***m***-$PFTMC_{19}$-*b*-PEG_{275} (Figure 5. 4B, S13). The pentablock nanofiber is constituted by PEG terminal segments with stealth properties, two intermediate PFr targeting segments, and a middle triBCP segment dedicated for encapsulation of cargo[61] (Figure 5. 4C). The symmetric C-B-A-B-C pentablock nanofiber arrangement possesses three distinct corona forming-blocks that can be utilized at different stages of the drug delivery process (Figure 5. 4C). It is noteworthy to mention that different segmented nanofiber configurations and other corona-forming blocks can be incorporated via sequential living CDSA, however, the most efficient design must be experimentally determined.

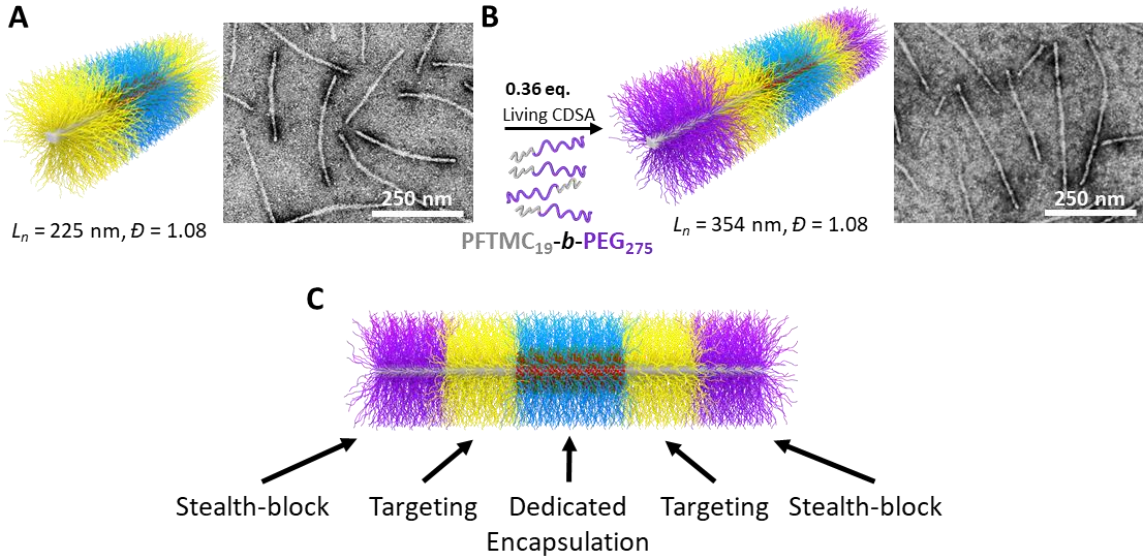

Figure 5. 4. Preparation of low-dispersity pentablock nanofibers of controlled length. A) Schematic representation and TEM micrograph of triblock PFTMC$_{18}$-*b*-PFr$_{92}$-*m*-PFTMC$_{18}$-*b*-PBMA$_{44}$-*b*-PNIPAM$_{70}$-*m*-PFTMC$_{18}$-*b*-PFr$_{92}$ nanofibers (L_n = 225 nm, $Đ$ = 1.08, σ = 66 nm), and B) pentablock PFTMC$_{19}$-*b*-PEG$_{275}$-*m*-PFTMC$_{18}$-*b*-PFr$_{92}$-*m*-PFTMC$_{18}$-*b*-PBMA$_{44}$-*b*-PNIPAM$_{70}$-*m*-PFTMC$_{18}$-*b*-PFr$_{92}$-*m*-PFTMC$_{19}$-*b*-PEG$_{275}$ nanofibers (L_n = 354 nm, $Đ$ = 1.08, σ = 98 nm). C) Side view of the schematic representation of the pentablock nanofibers with the function of each segment.

5.3.6 Preliminary Investigation of the Loading of Curcumin into PFTMC$_{18}$-*b*-PFr$_{92}$ Nanofibers

Finally, a preliminary exploration of the preparation of nanofiber-based therapeutics was performed through a study of the association of curcumin to PFTMC$_{18}$-*b*-PFr$_{92}$ nanofibers. Curcumin is a natural therapeutic compound,[55-57] is hydrophobic, and can hydrogen bond to fructose molecules.[58] The hydrogen bonding between curcumin to the PFr-corona was explored as a route to prepare loaded nanofibers (Figure 5. 5). The nanofibers and the curcumin were transferred to water via the preformed-nanoparticle solvent-switch loading (PNSL) method.[61] The PNSL procedure allows to control the solvent-switch transfer to water via a syringe-pump (flow rate = 100 µL/min) enabling hydrophobic cargo to accommodate near the hydrophobic core of crystalline-core nanofibers, and to potentially associate with the PFr corona-forming block, achieving nanofiber loading.

Curcumin (in MeOH) was added to preformed PFTMC$_{18}$-*b*-PFr$_{92}$ diBCP nanofibers (in DMF:MeOH 40:60. L_n = 395 nm, $Đ$ = 1.06, σ = 97 nm. Figure 5. 2F, 5B). The nanofiber (0.1 mg/mL) with curcumin (1 wt %) solution was transferred to water via the PNSL process (Figure 5. 5A-B). TEM analysis of the resulting nanofiber sample revealed colocalization of large curcumin aggregates along the axis of preformed PFTMC$_{18}$-*b*-PFr$_{92}$ nanofibers (Figure 5. 5C). Contour length analysis of the nanofibers after loading with curcumin revealed no significant change of the nanofiber length (L_n = 411 nm, $Đ$ = 1.08, σ = 117 nm. Figure 5. 5D). A purification step appears to be required as curcumin aggregates that are not associated with the nanofibers can be observed by TEM (Figure 5. 5E). Based on the TEM data, the reported hydrogen bonding association of curcumin with fructose,[58] and the evidence of hydrophobic cargo accumulation at the core-corona interface shown in Chapter 3, and in references [61,67], it is possible for curcumin to associate with the PFr corona forming-block at the edge of the hydrophobic PFTMC core-forming block. We hypothesize that the large-sized curcumin aggregates on the nanofiber axis may result from initial association of curcumin with the PFr-corona which provides nucleation sites for further curcumin accumulation. However, further work is required to prove the curcumin-PFr association and not random aggregation of curcumin on the nanofiber axis, as nonbonded aggregates were present (Figure 5. 5E). Future work will focus on optimization of the curcumin loading conditions, selection of an adequate purification method, proving the association of curcumin with the PFr corona, and quantification of curcumin uptake by PFTMC-*b*-PFr nanofibers. The results presented here may open the door to the facile preparation of curcumin loaded nanofiber-therapeutics with noncytotoxic, degradable, and FDA approved components.[44,54]

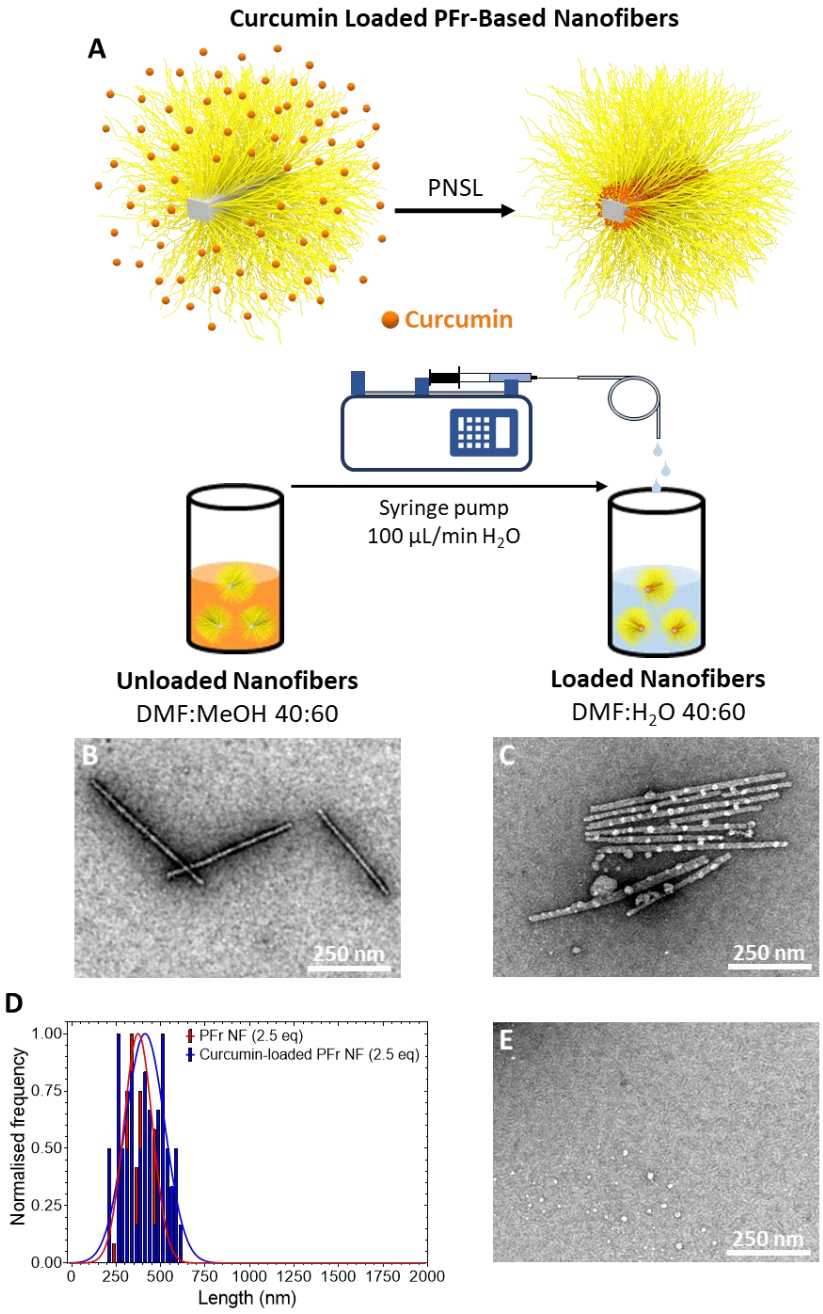

Figure 5. 5. A) Scheme of the association process of curcumin (1 wt %) with low-dispersity PFTMC$_{18}$-*b*-PFr$_{92}$ nanofibers (0.1 mg/mL in DMF:MeOH 40:60) by transfer to H_2O via the PNSL method. TEM micrographs of low-dispersity PFTMC$_{18}$-*b*-PFr$_{92}$ diBCP nanofibers; B) before (L_n = 395 nm, $Đ$ = 1.06, σ = 97 nm), and C) after curcumin association via the PNSL method (L_n = 411 nm, $Đ$ = 1.08, σ = 117 nm). D) Contour length histograms (from B and C) of PFTMC$_{18}$-*b*-PFr$_{92}$ nanofibers before (red) and after (blue) loading with curcumin. E) TEM micrograph of curcumin aggregates nonbounded to PFTMC$_{18}$-*b*-PFr$_{92}$ nanofibers.

5.4 Summary and Conclusions

Well-defined PFTMC$_{18}$-*b*-PFr$_{92}$ diBCP nanofibers with a crystalline core-forming block (PFTMC) and a water-soluble polyfructose (PFr) corona-forming block were prepared. Length-controlled and morphologically pure nanofibers were obtained via the living CDSA of PFTMC$_{18}$-*b*-PFr$_{92}$. The length of the nanofibers was controlled from ca. 50 – 1200 nm with low length dispersities ($Đ \leq 1.09$) as determined by TEM analysis. Both passive and active targeting were potentially attained in one nanoparticle system via the modulation of the PFTMC$_{18}$-*b*-PFr$_{92}$ diBCP nanofiber length and by incorporation of a GLUT5 targeting corona-forming block.

Addition of unimeric PFTMC$_{18}$-*b*-PFr$_{92}$ diBCP to three solutions of preformed PFTMC$_{19}$-*b*-PEG$_{275}$, PFTMC$_{18}$-*b*-PNIPAM$_{425}$, and PFTMC$_{18}$-*b*-PBMA$_{44}$-*b*-PNIPAM$_{70}$ nanofibers yielded triblock segmented nanofibers with terminal PFTMC$_{18}$-*b*-PFr$_{92}$ segments via living CDSA, as demonstrated by TEM. Addition of unimeric PFTMC$_{19}$-*b*-PEG$_{275}$ to a solution of triblock segmented nanofibers yielded pentablock segmented nanofibers with terminal PFTMC$_{19}$-*b*-PEG$_{275}$ segments, intermediate PFTMC$_{18}$-*b*-PFr$_{92}$ blocks, and a middle PFTMC$_{18}$-*b*-PBMA$_{44}$-*b*-PNIPAM$_{70}$ segment. Hence, living CDSA was used to prepare nanofibers with spatially defined segmented chemistries to build nanofibers with segments suited for the multiple stages of the drug delivery process. In this regard, the pentablock segmented nanofibers present terminal stealth blocks (PEG),[66] with intermediate targeting segments (PFr),[39,45] and a middle component dedicated to encapsulation (PBMA-*b*-PNIPAM).[61]

Proof-of-concept studies indicate that curcumin may associate with the PFr corona of PFTMC$_{18}$-*b*-PFr$_{92}$ nanofibers, as curcumin aggregates were observed along the

nanofiber axis and at the edge of the hydrophobic crystalline core-forming block. However, further evidence is required to demonstrate such association instead of random curcumin aggregation in the PFr corona along the nanofiber axis. Optimization of loading conditions, purification, and quantification of the amount of curcumin taken by the nanofibers is the focus of current work in our group. Cautious assessment on the effect of curcumin will be required as it has been identified as a pan-assay interreference compound.[70-72] In the future, we aim to experimentally study the targeting properties of PFTMC-*b*-PFr-containing nanofibers. We believe that this work paves the way for the development of PFr-containing nanofiber therapeutics that incorporate both passive and active targeting and may outperform traditional spherical nanoparticle vectors owing to the morphological, size-tunable, and segmented chemistries permitted by our self-assembly process.

5.5 Supporting Information

5.5.1 General Considerations and Instrumentation

FTMC was synthesized according to the procedure reported by Finnegan et al.[54] Synthesis of the fructose monomer (FrM, 1-*O*-acryloyl-2,3:4,5-di-*O*-isopropylidene-*β*-D-fructopyranose) was synthesized according to the procedure reported by Lu et al.[47] Synthesis of 2-cyano-5-hydroxypentan-2-yl ethyl carbonotrithioate (RAFT-CTA) was prepared according to the procedure reported by Arno et al.[68] Synthesis and characterization of PFTMC-CTA from reported procedure.[61] Synthesis, characterization and self-assembly of PFTMC-b-PNIPAM and PFTMC-b-PEG diblock copolymers (diBCP) were previously reported by our group.[61] All other reagents and solvents were purchased from Sigma-Aldrich (Canada), VWR (Canada), or Fisher Scientific (Canada) and used as received unless otherwise noted. DMF and MeOH for self-assembly were of HPLC grade and were filtered through nylon with a pore size of 200 nm before use. Ring-opening reactions were carried out in an MBraun 200B glove box under a nitrogen atmosphere or using standard Schlenk line techniques. RAFT polymerizations were performed in custom-made schlenk-vials to fit dry heating blocks. 1,8-diazabicyclo[5.4.0]undec-7-ene (DBU) was dried over CaH_2, and purified by distillation under reduced pressure. Anhydrous solvents were dried and purified using an MBraun Grubbs/Dow solvent purification system.[69]

Ultrasonication

Micelle sonication was carried out using a Fisherbrand 112xx series advanced ultrasonic cleaner (FB-11203). The instrument was operated in sweep mode at 80% power and 37 MHz at 10 °C.

NMR Spectroscopy

^{1}H NMR spectra were obtained using a Bruker 500 MHz spectrometer with CD_2Cl_2 (^{1}H NMR: δ = 5.32 ppm), or DMSO-d_6 (^{1}H NMR: δ = 2.50 ppm) as the solvents. Chemical shifts are quoted in parts per million, with spectra referenced to the residual solvent peak. Multiplicities are abbreviated as brs (broad singlet), s (singlet), d (doublet), t (triplet), q (quartet), p (pentet), m (multiplet) and *app.* (apparent) or combinations thereof.

Gel permeation chromatography (GPC)

GPC was conducted on a Malvern OMNISEC chromatograph equipped with a refractive index (RI), UV/Vis photodiode detector array, light scattering detector and viscometer. Triethylamine/THF (1% *v/v*) was used as the eluent, with the flow rate set at 1 mL/min. The columns used were grade T3000, followed by T5000 (Viscotek) at a constant temperature of 35 °C. The calibration (universal) of the RI detector was carried out using polystyrene standards (Viscotek). Samples were prepared at 1 mg/mL in eluent and filtered through a polytetrafluorethylene membrane filter, pore size = 0.2 µm.

Matrix-assisted laser desorption/ionization-time of flight mass spectrometry (MALDI-TOF MS)

MALDI-TOF MS measurements performed using a Bruker Ultraflextreme running in linear mode. Samples were prepared using a *trans*-2-[3-(4-*tert*-butylphenyl)-2-methyl-2-propenylidene]malononitrile matrix (20 mg/mL in THF) and the polymer sample (2 mg/mL in THF), mixed in a 10:1 (*v*/*v*) ratio. Approximately 3 μL of the mixed solution was deposited onto a stainless-steel sample plate and allowed to air dry.

Transmission electron microscopy (TEM)

TEM images were obtained on a JEOL 1011 microscope with an 11 Megapixel CCD camera, operated at 80 kV. Samples were prepared by drop-casting 7.5 μL of the micelle solution onto a carbon-coated copper grid, followed by drop-casting 10 μL of uranyl acetate in MeOH (3 wt %). The staining solution interacts well with the PFr_{92} corona-forming block, leaving the core-forming block unstained resulting in a bright core with a dark contrast. Sample concentrations for TEM analysis were either 0.5 or 0.1 mg/mL based on nanofiber concentration. Copper grids (400 mesh) were purchased from Ted Pella, and carbon films (ca. 6 nm) were prepared on mica sheets by carbon sputtering with a Leica ACE 600 carbon coater. The carbon films were deposited onto the copper grids by floatation on water and the carbon-coated grids were allowed to dry in air.

For micelle contour length analysis, a minimum of n = 150 nanofibers (unless otherwise indicated) in several images were traced manually using the ImageJ software package developed at the US National Institute of Health. The number average micelle length (L_n) or width (W_n) and weight average micelle length (L_w) were calculated using eq. S1-2 from measurements of the contour lengths (L_i) of individual micelles, where Ni is the

number of micelles of length Li, and n is the number of micelles examined in each sample. The distribution of micelle lengths is characterized by $Đ = L_w/L_n$.

$$L_n = \frac{\sum_{i=1}^{n} N_i L_i}{\sum_{i=1}^{n} Ni} \qquad L_w = \frac{\sum_{i=1}^{n} N_i L_i^2}{\sum_{i=1}^{n} NiLi} \qquad \text{(eq. S1-2)}$$

Dynamic Light Scattering (DLS)

Dynamic light scattering (DLS) experiments were carried out using a Zetasizer Pro. Samples of different polymer concentrations were prepared in filtered solvents by passing through a 0.45 μm nylon membrane filter into an optical quartz glass cuvette (PCS8501 type, 10.0 mm light path). The correlation function was acquired in real time and analyzed with a function capable of modelling multiple exponentials (Cumulant analysis). This process enabled the diffusion coefficients for the component particles to be extracted, and these were subsequently expressed as the intensity weighted mean hydrodynamic size ($R_{h,z}$) using the Stokes-Einstein relationship for coated spheres in DMF (Refractive Index = 1.43, Dispersant Viscosity = 0.92, Dispersant Dielectric Constant = 37.8), with core properties of polystyrene latex (Refractive Index = 1.590, Absorption = 0.010).

5.5.2 Synthetic Procedures

5.5.2.1 Synthesis of PFTMC$_{18}$-CTA

Scheme S5. 1. Synthesis of PFTMC$_{18}$-CTA by ring-opening polymerization of FTMC.

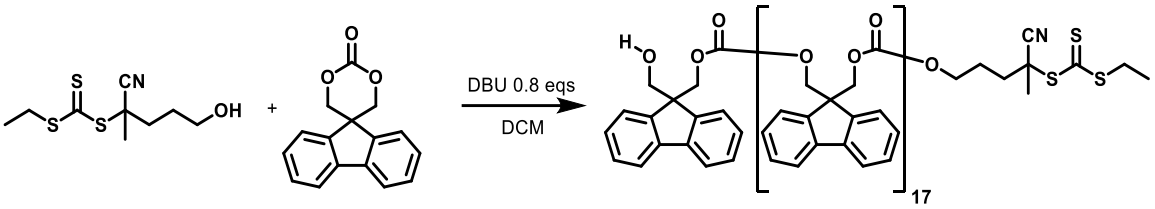

To a solution of 2-cyano-5-hydroxypentan-2-yl ethyl carbonotrithioate[68] in anhydrous CH_2Cl_2 (500 µL, 100 mg/mL, 0.2 mmol, 1.0 eq), DBU (24 µL, 24.4 mg, 0.16 mmol, 0.8 eq) was added in an oven-dried round bottom flask equipped with a magnetic stirring bar. To the stirring solution, FTMC (1.01 g, 4.0 mmol, 20 eq) in anhydrous CH_2Cl_2 (6 mL) was added, and the reaction mixture was stirred at room temperature for 1 h, before the reaction mixture was quenched by the addition of benzoic acid (100 mg). The crude product was purified by precipitation into 0 °C diethyl ether three times, followed by precipitation into methanol at 0 °C three times, and drying *in vacuo* to yield PFTMC$_{18}$-CTA as a yellow solid (1.0 g, 95%).[61]

MALDI-TOF MS $[M]^+$ found: 4729.3, DP_n: 18.

GPC: M_n = 4,800, $Đ_M$ = 1.17.

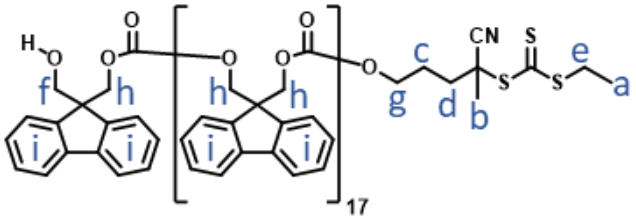

^{1}H NMR (500 MHz, CD_2Cl_2) δ 7.78 – 7.69 (36H, m, Hi), 7.61 – 7.47 (36H, m, Hi), 7.44 – 7.34 (36H, m, Hi), 7.32 – 7.19 (36H, m, Hi), 4.50 – 4.27 (70H, m, Hh), 4.07 (2H, t, *J* = 5.2 Hz, Hg), 3.70 (2H, d, *J* = 6.4 Hz, Hf), 3.31 (2H, dd, *J* = 7.4 Hz, He), 2.22 – 2.13

(1H, m, Hd), 2.06 – 1.98 (1H, m, Hd), 1.87 (2H, h, Hc), 1.80 (3H, s, Hb), 1.31 (3H, t, J = 7.4 Hz, Ha). The ^{1}H ratio of g/f indicates the CTA capping efficiency. ^{1}H integration is based on 'f' (HOCH_2).

5.5.2.2 Synthesis of protected PFTMC$_{18}$-*b*-PPFr$_{92}$

Scheme S5. 2. Synthesis of PFTMC$_{18}$-*b*-PPFr$_{92}$ by RAFT polymerization.

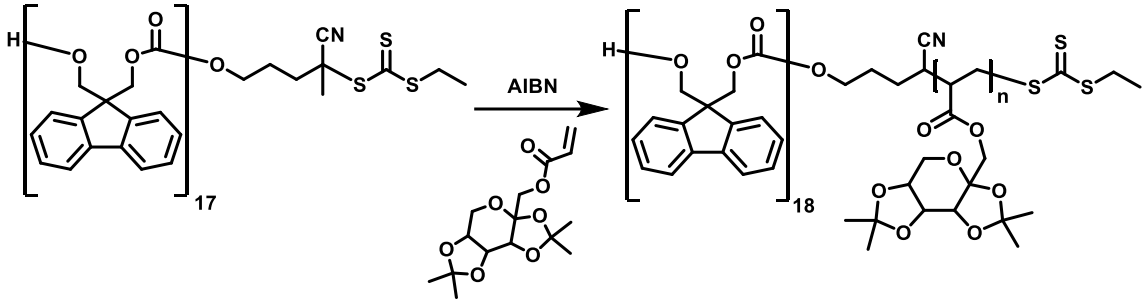

PFTMC$_{18}$-CTA (15 mg, 0.003 mmol, 1 eq), fructose monomer (FrM, 1-*O*-acryloyl-2,3:4,5-di-*O*-isopropylidene-*β*-D-fructopyranose, 249 mg, 0.8 mmol, 250 eq), and AIBN (0.1 mg, 0.6 µmol, 0.2 eq) were dissolved in dimethylacetamide (1.6 mL, DMAc) in a custom-made schlenk-vial followed by four freeze-pump-thaw cycles. The vial with the reaction mixture was placed in a preheated dry heating block and heated to 70 °C for 16 h. The reaction was quenched by submersion in liquid nitrogen. The product was precipitated three times in methanol at 0 °C. The product was dried *in vacuo* to yield the protected PFTMC$_{18}$-*b*-PPFr$_{92}$ as a pale yellow solid (111 mg, 42%).

GPC: M_n = 15,600, $Đ_M$ = 1.26.

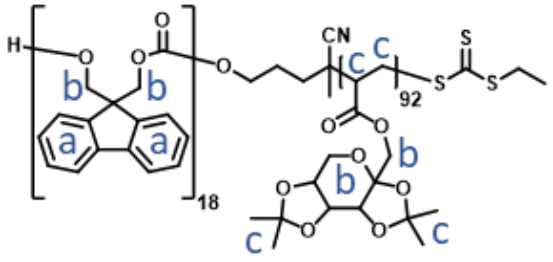

^{1}H NMR (500 MHz, CD_2Cl_2) δ 7.87 – 7.25 (144H, m, Ha), 4.80 – 3.58 (762H, m, Hb), 1.66 – 1.21 (1277H, m, Hc). The DP_n value of the PPFr block was determined by comparing the relative ^{1}H NMR integration of the $PFTMC_{18}$ block at 7.87 – 7.25 ppm (144H, Ha, OCH_2C) to the resonance of the PPFr block at 4.80 – 3.58 ppm, and 1.66 – 1.21 and corresponded to $PFTMC_{18}$-*b*-$PPFr_{92}$.

5.5.2.3 Synthesis of deprotected $PFTMC_{18}$-*b*-PFr_{92}

Scheme S5. 3. Synthesis of deprotected $PFTMC_{18}$-*b*-PFr_{92}.

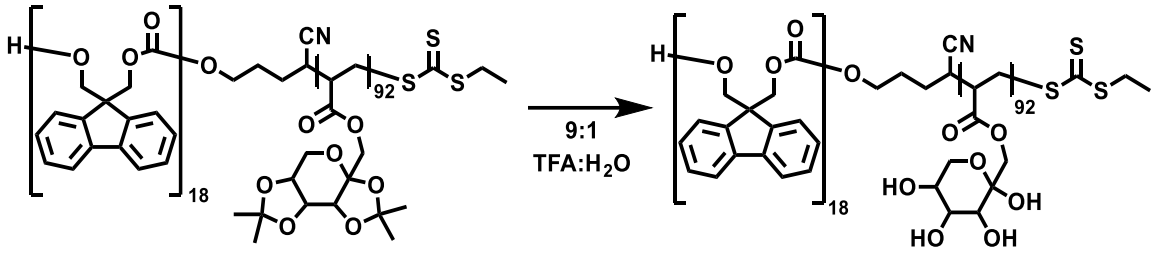

Deprotection of the $PFTMC_{18}$-$PPFr_{92}$ was conducted by according to a modified procedure reported by Ganda et al.[22] $PFTMC_{18}$-$PPFr_{92}$ (50 mg, 0.001 mmol) was dissolved in 3 mL of 9:1 trifluoroacetic acid:H_2O (TFA:H_2O) for 1 h. The reaction was quenched by addition of excess MeOH. The resultant solution was dialyzed against 1 L of Milli-Q water for 72 h (molecular weight cut-off (MWCO) = 3,500 Da. Spectra/Por). The Mili-Q water was replaced 5 times. The supernatant was collected and subsequently freeze dried to yield the deprotected $PFTMC_{18}$-*b*-PFr_{92} as a white solid (27 mg, 69%).

GPC analysis was not conducted as $PFTMC_{18}$-*b*-PFr_{92} is not soluble in THF.

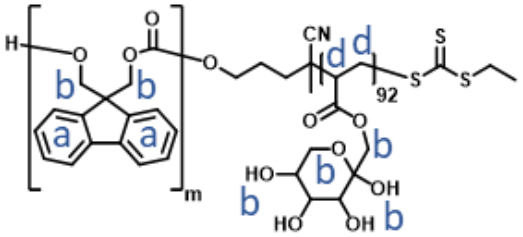

^{1}H NMR (500 MHz, DMSO-d_6) δ 7.95 – 7.06 (144H, m, Ha), 4.51 – 3.36 (1388H, m, Hb), 2.05 – 1.21 (284H, m, Hc). The DP_n value of the PFr block was determined by comparing the relative ^{1}H NMR integration of the $PFTMC_{18}$ block at 7.95 – 7.06 (144H, Ha, OCH_2C) to the resonance of the PFr block at 4.51 – 3.36 ppm, and 2.05 – 1.21 and corresponded to $PFTMC_{18}$-*b*-PFr_{92}.

5.5.3 Self-Assembly Procedures

Composition of all solvents given in *v/v*

Self-nucleation of PFTMC$_{18}$-*b*-PFr$_{92}$. PFTMC$_{18}$-*b*-PFr$_{92}$ (0.5 mg) were placed in a vial, followed by addition of a mixture of DMF:MeOH (10 – 40% DMF, 1 mL). The resulting solution (0.5 mg/mL) was manually shaken for ~15 s and heated to 75 °C for 3 h. The solution was cooled to 20 °C over 3 h, and aged for 48 h. The resulting solutions contained morphologically pure nanofibers with disperse lengths, as analyzed via TEM.

Preparation of PFTMC$_{18}$-*b*-PFr$_{92}$ seed nanofibers. PFTMC$_{18}$-*b*-PFr$_{92}$ disperse nanofibers (1 mL, 0.5 mg/mL, 40:60 DMF:MeOH) were fragmented by ultrasonication for 3 h at 0 °C. The resulting seed nanofibers were analyzed by TEM (L_n = 54 nm, $Đ$ = 1.09, σ = 17 nm).

Preparation PFTMC$_{18}$-*b*-PFr$_{92}$ nanofibers of controlled length and low dispersity by seeded growth (living CDSA). For seeded growth assemblies aliquots of PFTMC$_{18}$-*b*-PFr$_{92}$ unimer (10 mg/mL in DMF), equivalent to corresponding m_{unimer}/m_{seed} (1 – 20), were added to diluted seed nanofiber solutions in DMF:MeOH (40:60, 200 µL) at 20 °C. The self-assembly solutions in MeOH (0.1 mg/mL, DMF content: 40 – 50% in MeOH) were manually shaken for ~15 s and aged for 48 h at 20 ºC.

Preparation of triblock nanofibers

To prepare segmented nanofibers with spatially distinct coronal chemistries via the seeded growth method, aliquots of PFTMC$_{18}$-*b*-PFr$_{92}$ unimer (2 or 4 µL, 10 mg/mL in DMF), equivalent to 0.5 or 1 m_{unimer}/m_{seed} (equivalent), were added to diluted preformed nanofiber solutions in 40:60 DMF:MeOH (0.2 mg/mL, 200 µL) at 20 °C. The self-assembly solutions were manually shaken for ~15 s and aged for 48 h at 20 ºC. The resulting nanofibers were analyzed by TEM

The preformed nanofibers were made via the seeded growth method following reported procedures from $PFTMC_{19}$-*b*-PEG_{275} (L_n = 127 nm, $Đ$ = 1.06, σ = 32 nm),[54] $PFTMC_{18}$-*b*-$PNIPAm_{425}$ (L_n = 127 nm, $Đ$ = 1.03, σ = 22 nm, Chapter 3), and $PFTMC_{18}$-*b*-$PBMA_{44}$-*b*-$PNIPAm_{70}$ (L_n = 163 nm, $Đ$ = 1.06, σ = 38 nm).[61]

Preparation of pentablock nanofibers

To solution containing nanofibers with three distinct segments (i.e., $PFTMC_{18}$-*b*-PFr_{92}-*m*-$PFTMC_{18}$-*b*-$PBMA_{44}$-*b*-$PNIPAm_{70}$-*m*-$PFTMC_{18}$-*b*-PFr_{92}, L_n = 225 nm, $Đ$ = 1.08, σ = 66 nm) an aliquot of $PFTMC_{18}$-*b*-PFr_{92} unimer (4 µL, 10 mg/mL in DMF), equivalent to 0.36 m_{unimer}/m_{seed}, were added to the segmented nanofiber solution in 40:60 DMF:MeOH (0.2 mg/mL, 200 µL) at 20 °C. The self-assembly solutions were manually shaken for ~15 s and aged for 48 h at 20 ºC. The resulting nanofibers were analyzed by TEM.

5.5.4 Supplementary Tables

Table S5. 1. Summary of molecular weight data for $PFTMC_{18}$-CTA, and $PFTMC_{18}$-*b*-$PPFr_{92}$ polymers.

Polymer	M_n (g/mol) GPC	M_w (g/mol) GPC	$Đ_M$ GPC	DP_n NMR	DP_n MALDI-TOF
$PFTMC_m$	4,800	5,600	1.17	m =18	18
$PFTMC_{18}$-*b*-PFr_n	15,600	19,700	1.26	n = 92	-

Table S5. 2. Statistical analysis of contour length measurements for $PFTMC_{18}$-*b*-PFr_{92} diBCP nanofibers prepared via seeded growth at 20 °C, in DMF:MeOH solvent mixtures (DMF = 40 – 50%), measured via TEM. The number of nanofibers measured is represented by *n*, and *σ* represents the standard deviation of the measured length, and L_n/eq corresponds to the L_n of the nanofibers per mass equivalent of triBCP in the sample.

Length	m_{unimer}/m_{seed}								
	Seeds	1	2	5	5°	10	15	20	20*
n	152	158	173	172	150	161	165	159	150
L_n (nm)	54	109	194	395	394	639	1035	1201	1256
L_w (nm)	59	118	206	418	423	675	1069	1294	1334
Đ	1.09	1.08	1.06	1.06	1.07	1.06	1.03	1.08	1.06
L_n/eq (nm)	54	54	65	66	66	58	65	57	60
σ (nm)	17	32	49	97	107	153	188	335	313
σ / L_n	0.31	0.29	0.25	0.25	0.27	0.24	0.18	0.28	0.25

°Measured 2 weeks after transfer to H_2O. *Measured 4 months after the sample was originally prepared.

5.5.5 Supplementary Figures

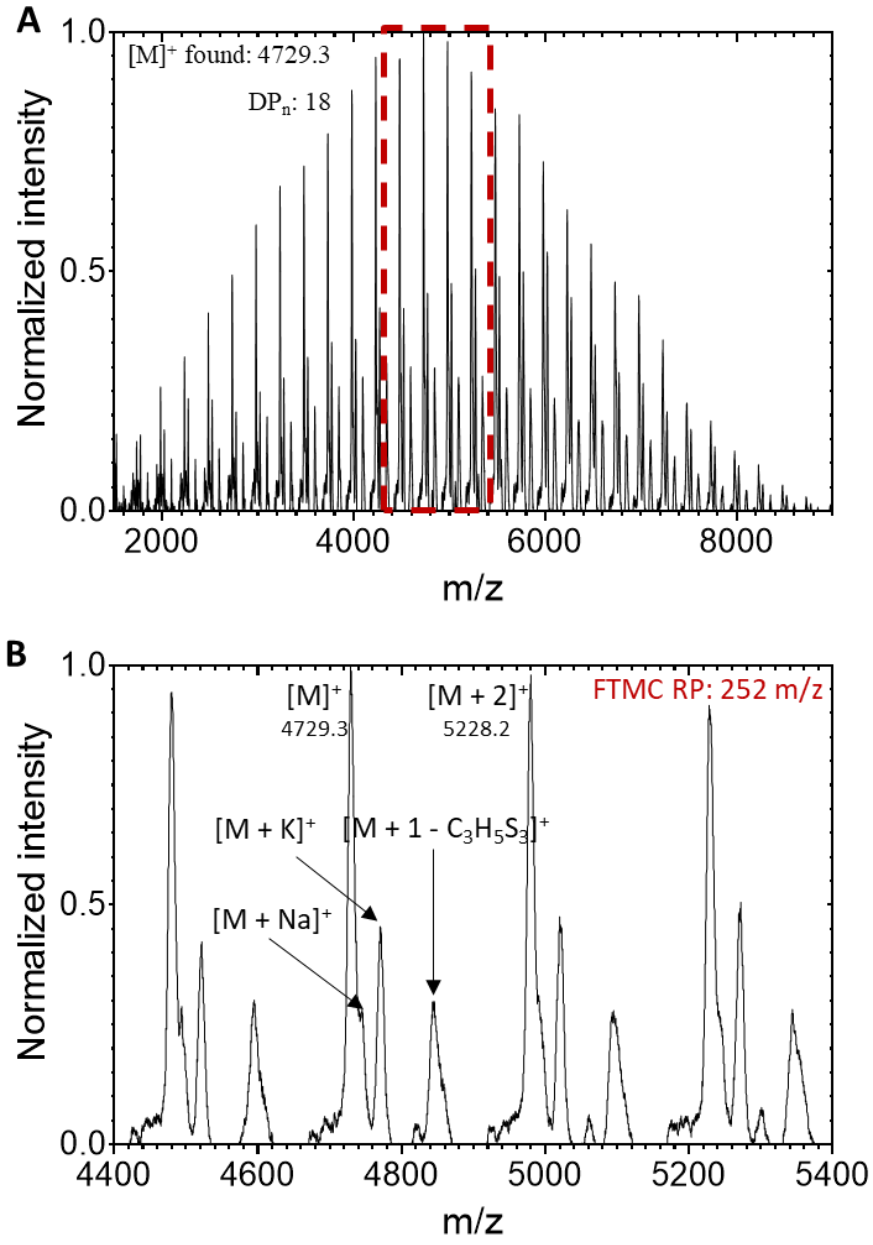

Figure S5. 1. MALDI-TOF MS spectra of $PFTMC_{18}$. The red square represents the area expanded in B. RP: repeating unit. Reproduced from ref [61].

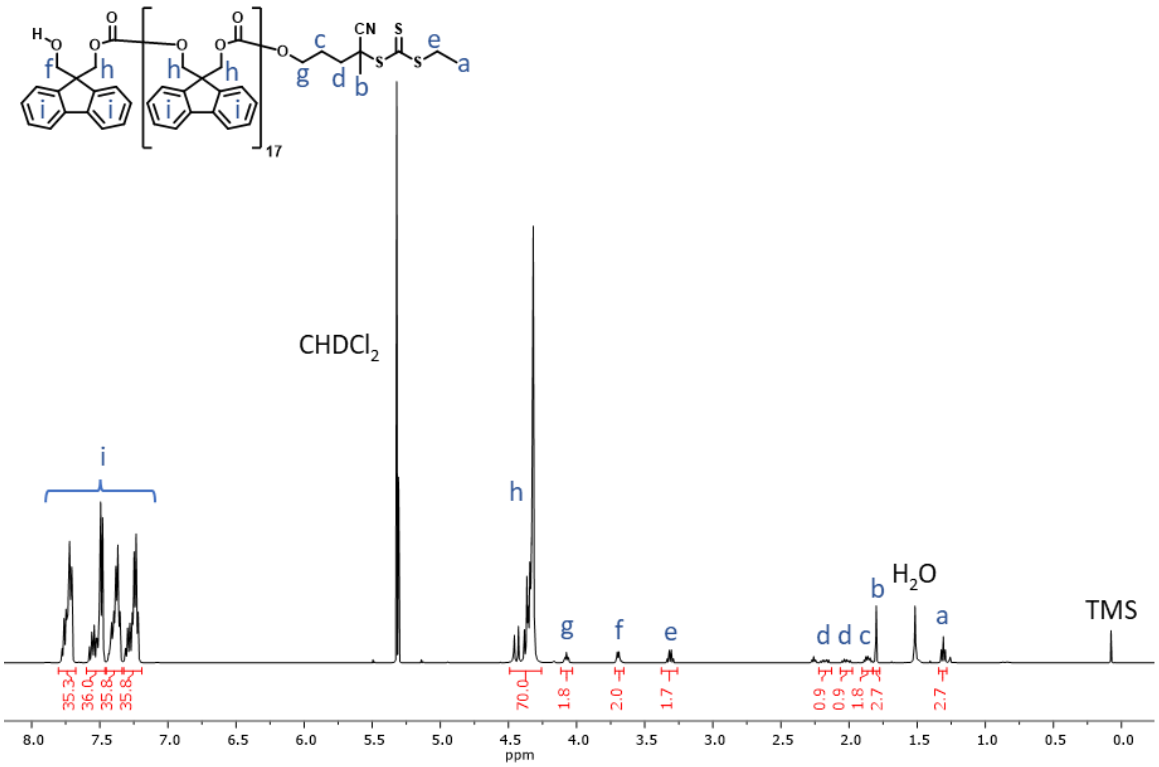

Figure S5. 2. ^{1}H NMR spectra (in CD_2Cl_2) of $PFTMC_{18}$-CTA. Reproduced from ref [61].

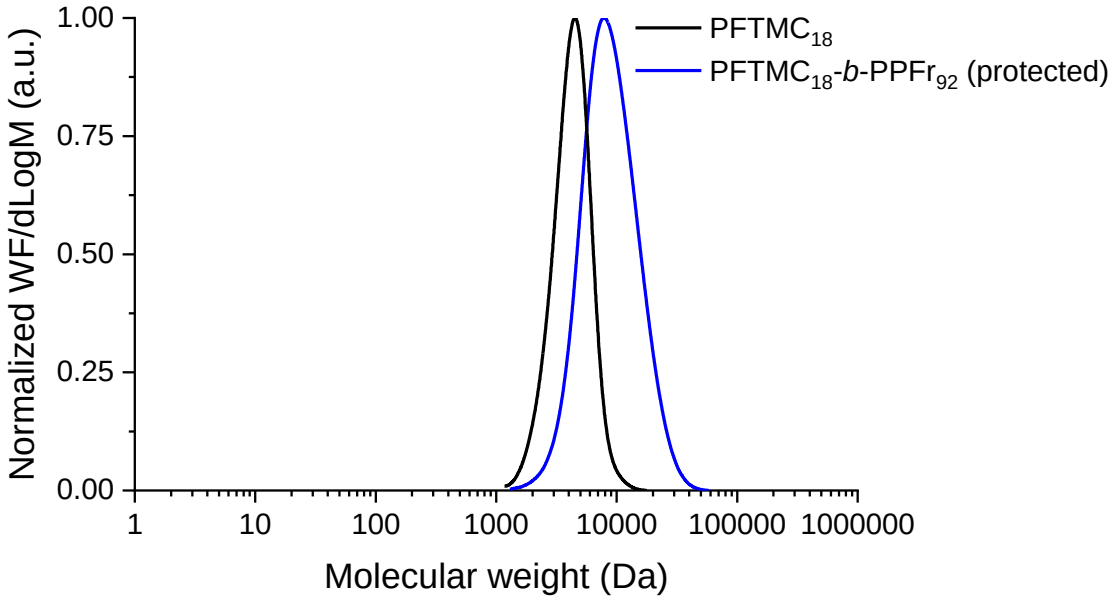

Figure S5. 3. GPC (refractive index) traces of in triethylamine/THF (1% *v/v*) 1 mL min^{-1}, at 35 °C of $PFTMC_{18}$ homopolymer capped with the CTA (black trace, 1 mg/mL), $PFTMC_{18}$-*b*-$PPFr_{92}$ protected diBCP (blue trace, 1 mg/mL). The y-axis reflects the distribution of weight fractions by molecular weight. Adapted from ref [61].

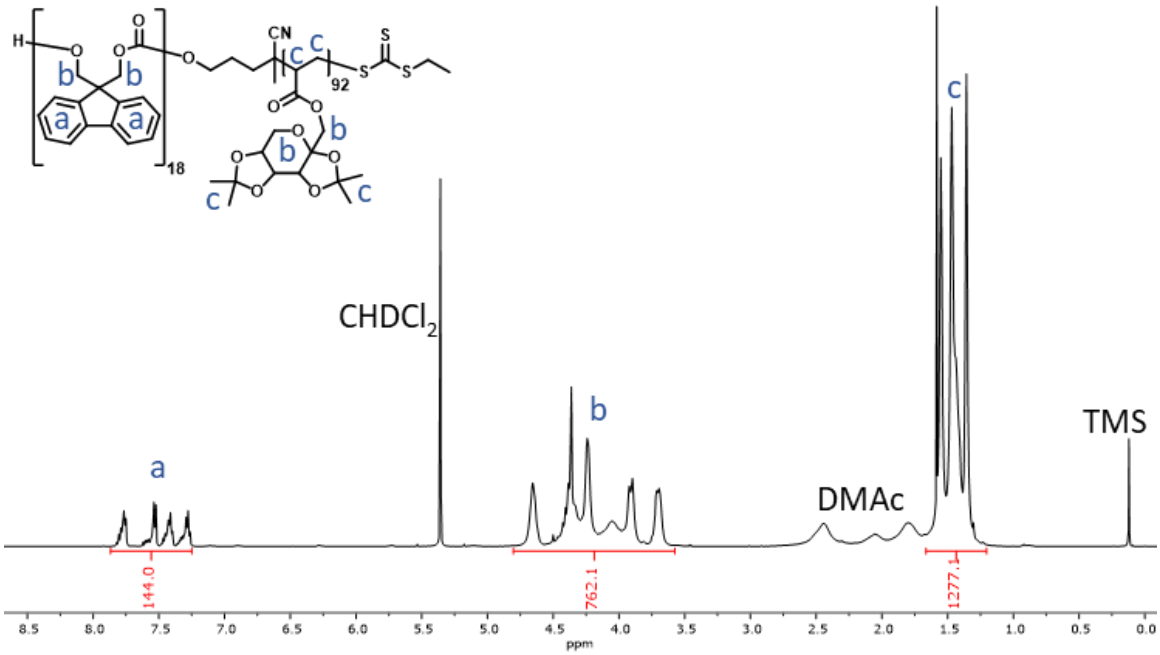

Figure S5. 4. ^{1}H NMR spectra (in CD_2Cl_2) of the fructose-protected $PFTMC_{18}$-*b*-$PPFr_{92}$.

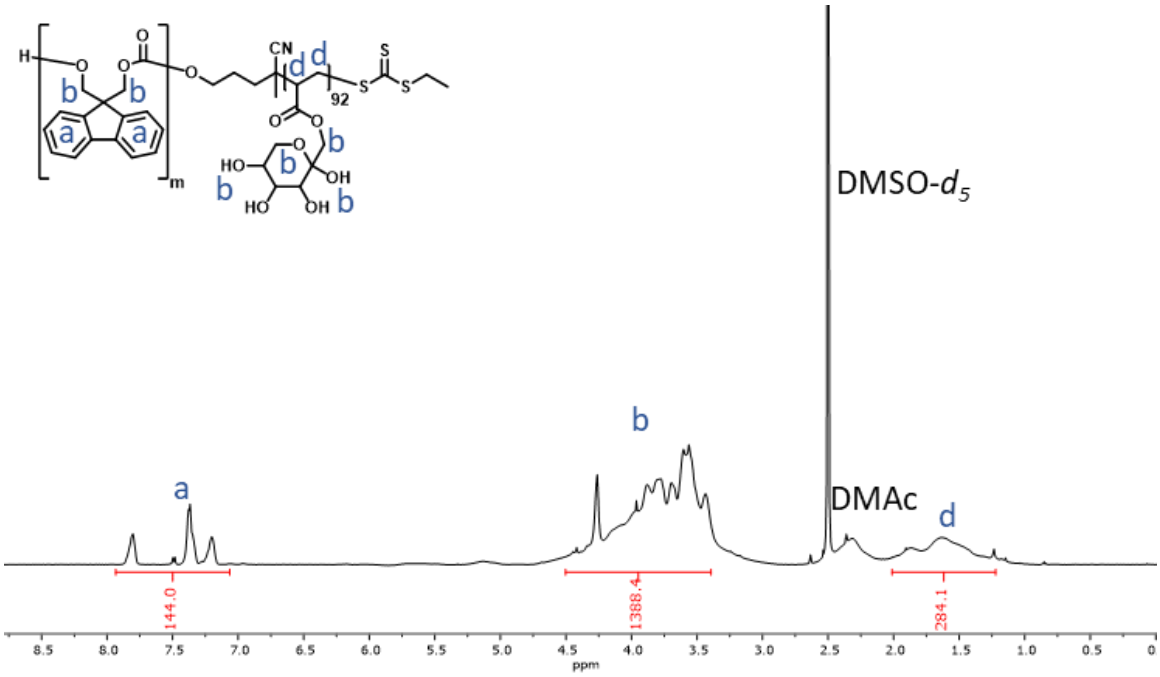

Figure S5. 5. ^{1}H NMR spectra (in DMSO-d_6) of fructose-deprotected $PFTMC_{18}$-*b*-PFr_{92}.

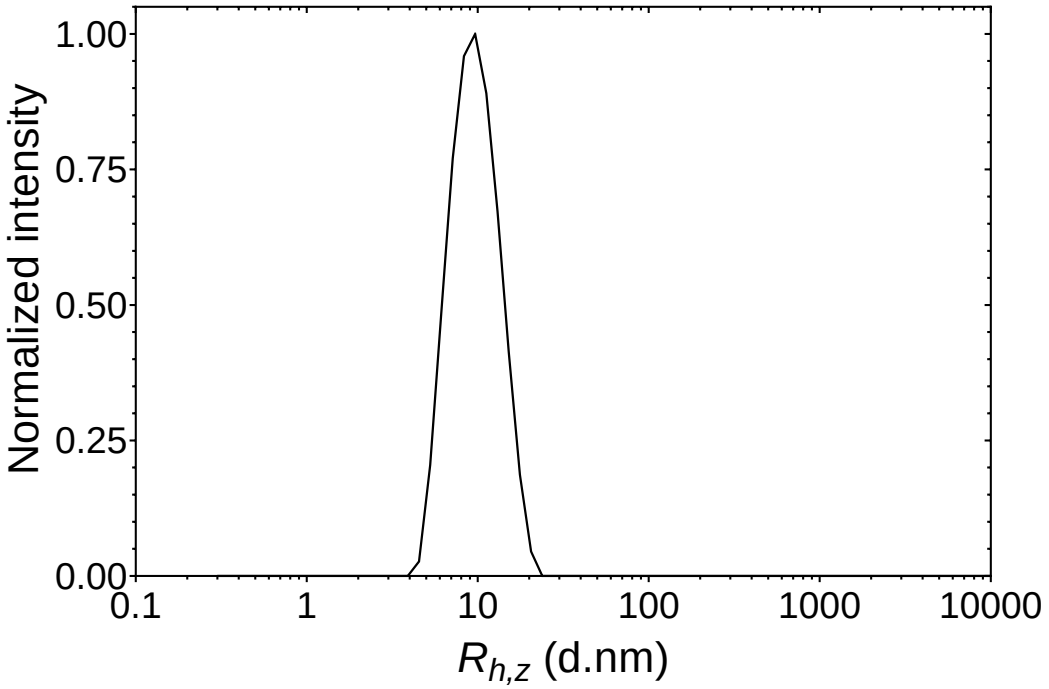

Figure S5. 6. DLS of the fructose-deprotected $PFTMC_{18}$-*b*-PFr_{92} diBCP in dimethylformamide (DMF); $R_{h,z}$ = 9.8 nm, σ = 3.34 nm.

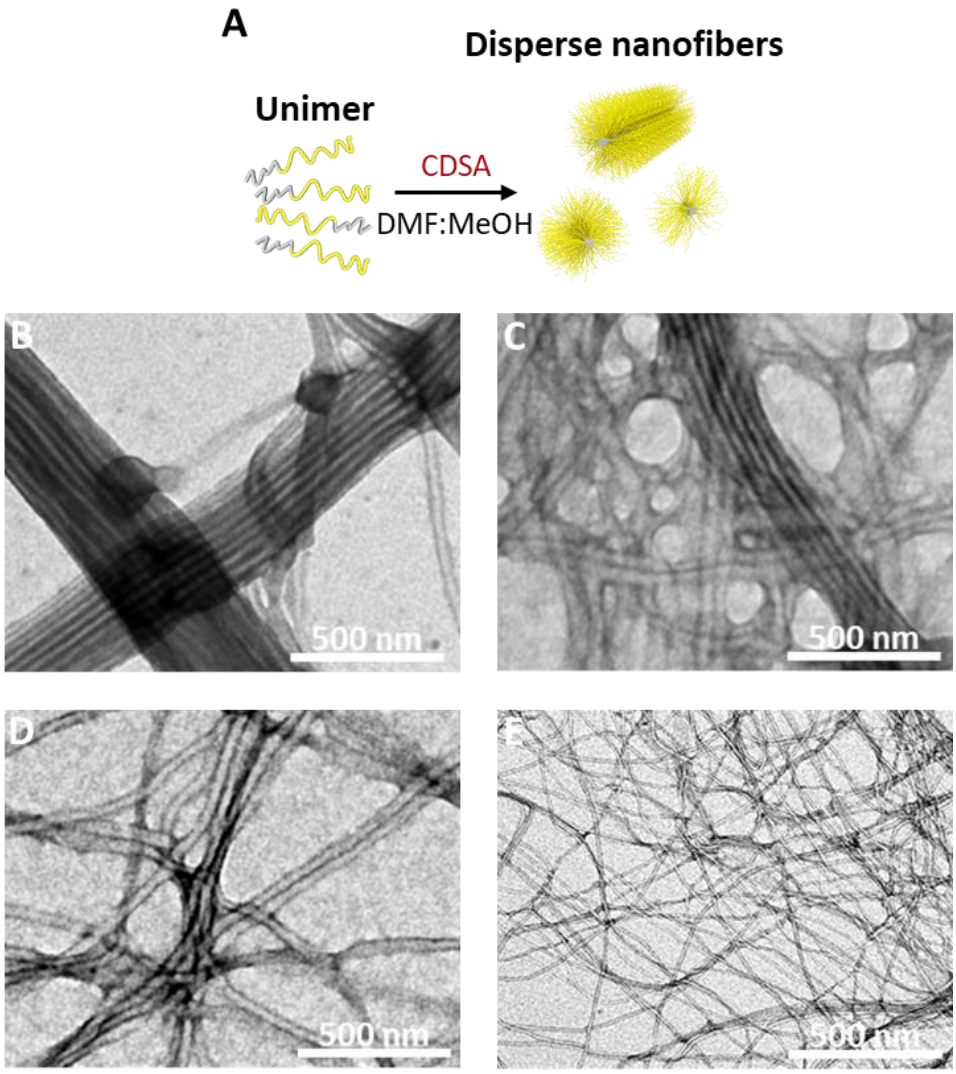

Figure S5. 7. Solvent screening conditions for the spontaneous self-nucleation of $PFTMC_{18}$-*b*-PFr_{92} to yield nanofibers via CDSA A) Schematic representation of spontaneous self-nucleation process. B-E) TEM micrographs of the resulting assemblies at different solvent mixtures in DMF:MeOH (*v/v*); B) 10:90. C) 20:80, D) 30:70, and E) 40:60.

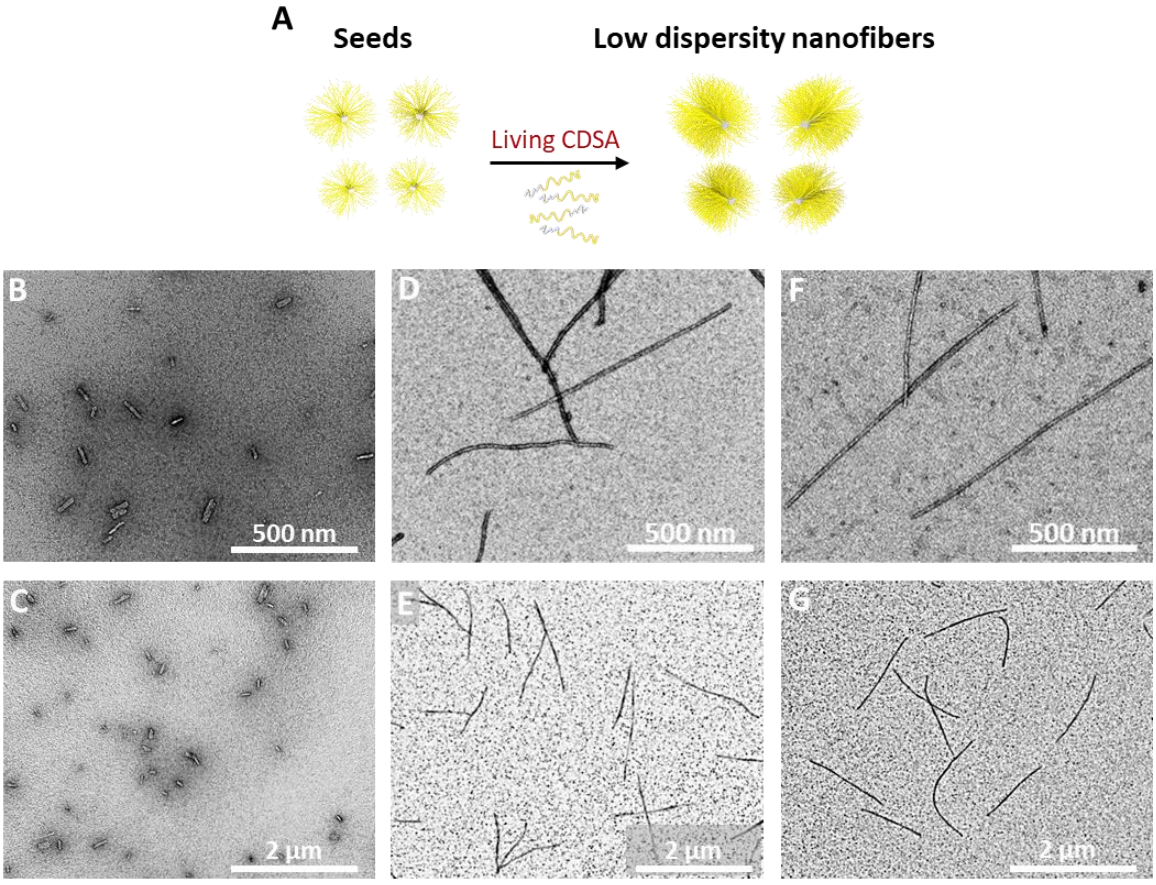

Figure S5. 8. A) Schematic representation of the generation of low-dispersity nanofibers made from $PFTMC_{18}$-*b*-PFr_{92}. B-C) TEM micrographs of seed nanofibers prepared by sonication for 3 h at 0 °C. TEM micrograph of low dispersity nanofibers of controlled length prepared via Living CDSA at m_{unimer}/m_{seed} ratios added to solutions of seed nanofibers. D-E) m_{unimer}/m_{seed} = 15:1 (L_n = 1035 nm, $Đ$ = 1.03, σ = 188 nm). F-G) m_{unimer}/m_{seed} = 20:1 (L_n = 1201 nm, $Đ$ = 1.08, σ = 335 nm).

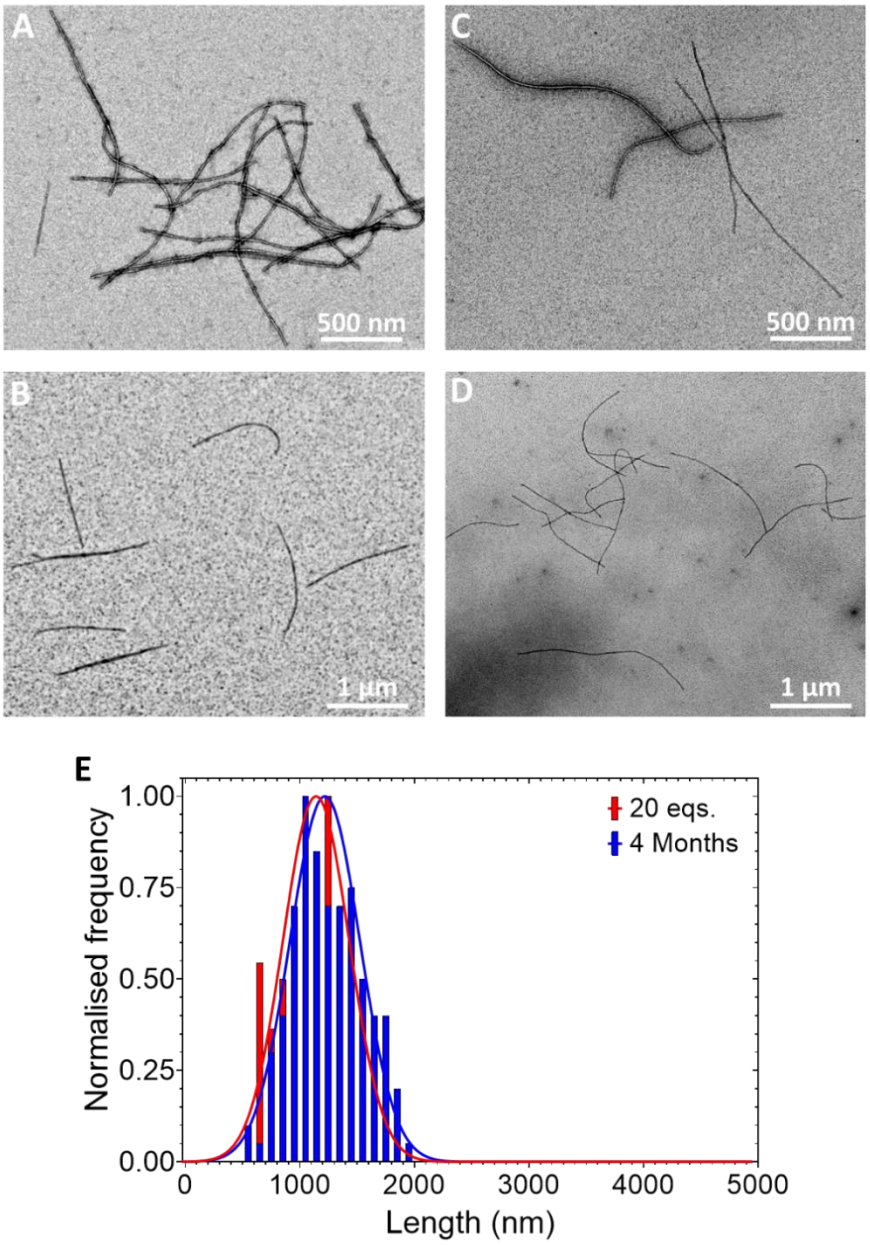

Figure S5. 9. TEM micrographs of PFTMC$_{18}$-*b*-PFr$_{92}$ nanofibers prepared via the seeded growth (living CDSA) after the addition of 20 m_{unimer}/m_{seed} (equivalent) of PFTMC$_{18}$-*b*-PFr$_{92}$ unimer: A-B) after 48 h; L_n = 1201 nm ($Đ$ = 1.08, σ = 335 nm. In DMF:MeOH 40:60), and C-D) after 4 months; L_n = 1256 nm ($Đ$ = 1.06, σ = 313 nm). E) Contour length histograms of the nanofibers in A and B.

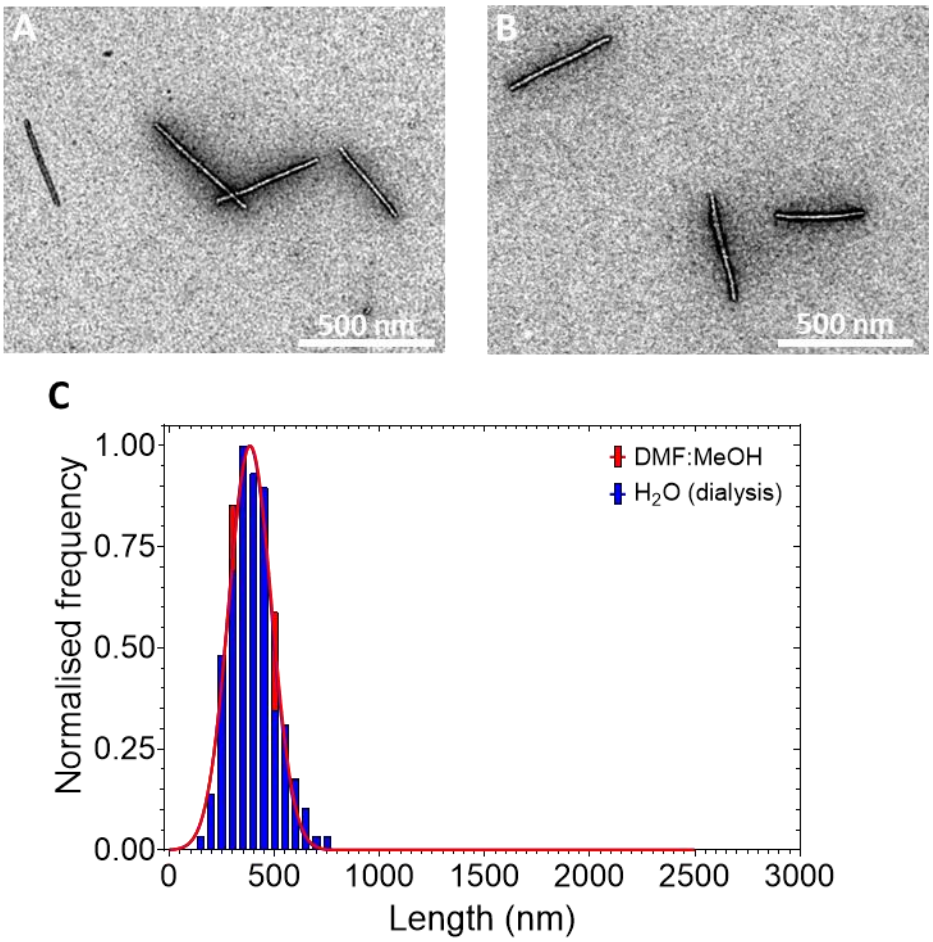

Figure S5. 10. TEM micrographs of $PFTMC_{18}$-*b*-PFr_{92} nanofibers prepared via the seeded growth (living CDSA) after the addition of 5 m_{unimer}/m_{seed} (equivalent) of $PFTMC_{18}$-*b*-PFr_{92} unimer: A) before L_n = 395 nm ($Đ$ = 1.06, σ = 97 nm. In DMF:MeOH 40:60), and B) after dialysis to water and 2 weeks of aging L_n = 394 nm ($Đ$ = 1.07, σ = 107 nm. 1 L, 5 water replacements, 72 h. MWCO: 3,500 Da). C) Contour length histograms of the nanofibers in A and B.

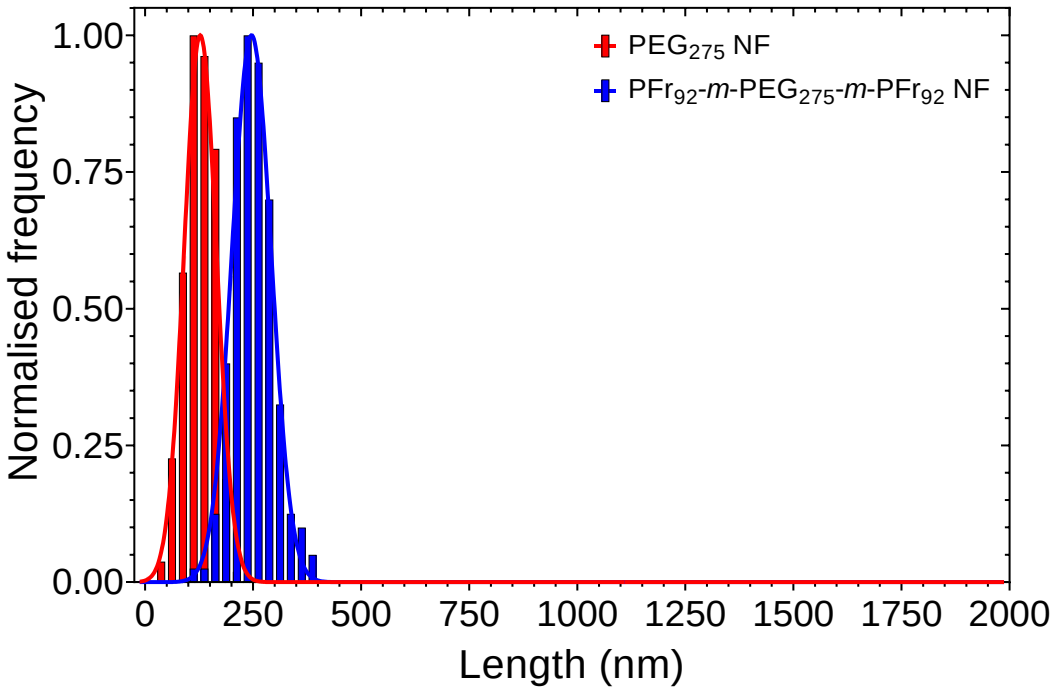

Figure S5. 11. Contour length histograms (from TEM micrographs, Figure 5. 3A) of the PFTMC$_{19}$-*b*-PEG$_{275}$ diBCP nanofibers (L_n = 127 nm, $Đ$ = 1.06, σ = 32 nm, red), and triblock PFTMC$_{18}$-*b*-PFr$_{92}$-*m*-PFTMC$_{19}$-*b*-PEG$_{275}$-*m*-PFTMC$_{18}$-*b*-PFr$_{92}$ nanofibers (L_n = 349 nm, $Đ$ = 1.04, σ = 47 nm, blue) after the addition of 1 m_{unimer}/m_{seed} (equivalent) of PFTMC$_{18}$-*b*-PFr$_{92}$ unimer (in DMF) to PFTMC$_{19}$-*b*-PEG$_{275}$ nanofibers (in DMF:MeOH 40:60). NF: nanofiber. '*m*' is used to indicate different segments of the nanofibers. Only the corona-forming blocks were used in the legends for clarity.

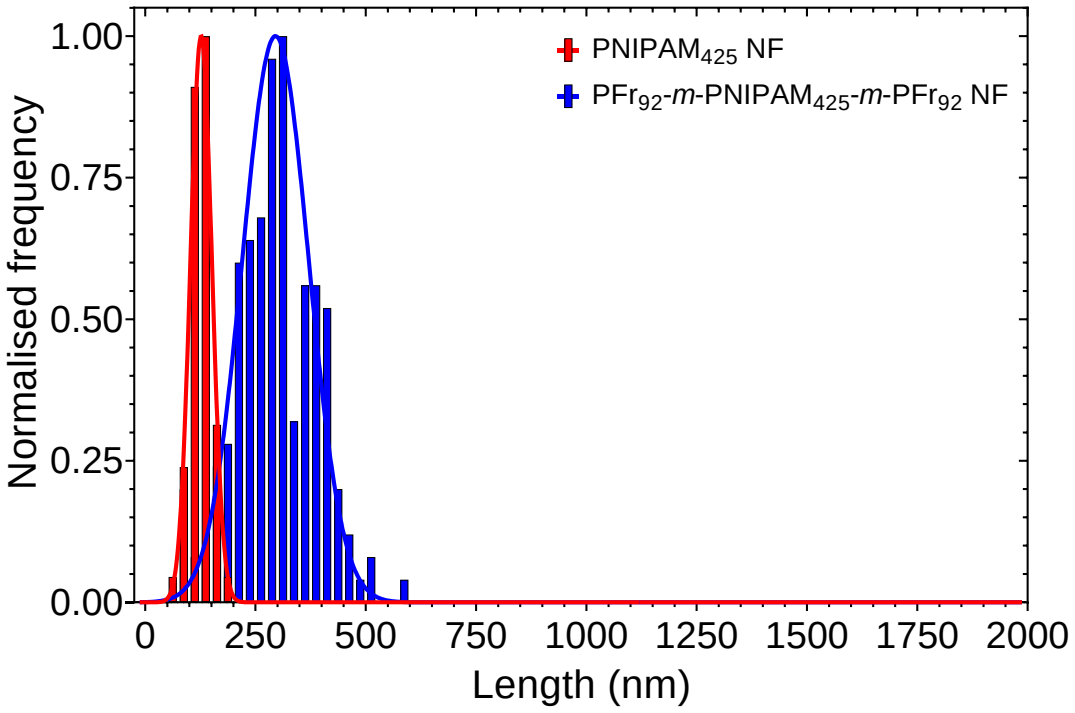

Figure S5. 12. Contour length histograms (from TEM micrographs, Figure 5. 3B) of the PFTMC$_{18}$-*b*-PNIPAM$_{425}$ diBCP nanofibers (L_n = 127 nm, $Đ$ = 1.03, σ = 22 nm, red), and triblock PFTMC$_{18}$-*b*-PFr$_{92}$-*m*-PFTMC$_{18}$-*b*-PNIPAM$_{425}$-*m*-PFTMC$_{18}$-*b*-PFr$_{92}$ nanofibers (L_n = 297 nm, $Đ$ = 1.09, σ = 90 nm, blue) after the addition of 1 m_{unimer}/m_{seed} (equivalent) of PFTMC$_{18}$-*b*-PFr$_{92}$ unimer (in DMF) to PFTMC$_{18}$-*b*-PNIPAM$_{425}$ nanofibers (in DMF:MeOH 40:60). NF: nanofiber. '*m*' is used to indicate different segments of the nanofibers. Only the corona-forming blocks were used in the legends for clarity.

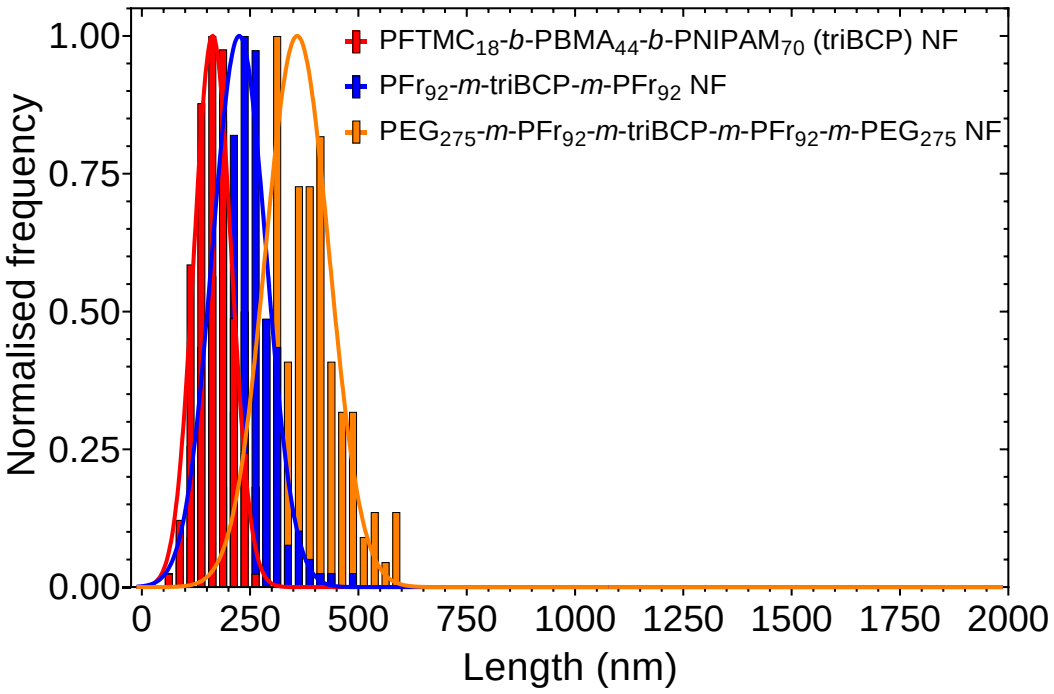

Figure S5. 13. Contour length histograms (from TEM micrographs, Figure 5. 3C and 4) of the PFTMC$_{18}$-*b*-PBMA$_{44}$-*b*-PNIPAM$_{70}$ triBCP nanofibers (L_n = 163 nm, $Đ$ = 1.05, σ = 38 nm, red). Triblock PFTMC$_{18}$-*b*-PFr$_{92}$-*m*-PFTMC$_{18}$-*b*-PBMA$_{44}$-*b*-PNIPAM$_{70}$-*m*-PFTMC$_{18}$-*b*-PFr$_{92}$ nanofibers (L_n = 225 nm, $Đ$ = 1.08, σ = 66 nm, blue) after the addition of 0.5 m_{unimer}/m_{seed} (equivalents) of PFTMC$_{18}$-*b*-PFr$_{92}$ unimer (in DMF) to PFTMC$_{18}$-*b*-PBMA$_{44}$-*b*-PNIPAM$_{70}$ nanofibers (in DMF:MeOH 40:60). Pentablock PFTMC$_{19}$-*b*-PEG$_{275}$-*m*-PFTMC$_{18}$-*b*-PFr$_{92}$-*m*-PFTMC$_{18}$-*b*-PBMA$_{44}$-*b*-PNIPAM$_{70}$-*m*-PFTMC$_{18}$-*b*-PFr$_{92}$-*m*-PFTMC$_{19}$-*b*-PEG$_{275}$ (L_n = 354 nm, $Đ$ = 1.08, σ = 98 nm, orange) after the addition of 0.36 m_{unimer}/m_{seed} (equivalents) of PFTMC$_{19}$-*b*-PEG$_{275}$ unimer (in THF) to PFTMC$_{18}$-*b*-PFr$_{92}$-*m*-PFTMC$_{18}$-*b*-PBMA$_{44}$-*b*-PNIPAM$_{70}$-*m*-PFTMC$_{18}$-*b*-PFr$_{92}$ triblock nanofibers (in DMF:MeOH 40:60). NF: nanofiber. '*m*' is used to indicate different segments of the nanofibers. Only the corona-forming blocks were used in the legends for clarity.

5.6 References

(1) Petros, R. A.; DeSimone, J. M. Strategies in the Design of Nanoparticles for Therapeutic Applications. *Nat. Rev. Drug Discov.* **2010**, *9* (8), 615–627.

(2) Hauert, S.; Bhatia, S. N. Mechanisms of Cooperation in Cancer Nanomedicine: Towards Systems Nanotechnology. *Trends Biotechnol.* **2014**, *32* (9), 448–455.

(3) Kisby, T.; Yilmazer, A.; Kostarelos, K. Reasons for Success and Lessons Learnt from Nanoscale Vaccines Against COVID-19. *Nat. Nanotechnol.* **2021**, *16* (8), 843–850.

(4) Cabral, H.; Miyata, K.; Osada, K.; Kataoka, K. Block Copolymer Micelles in Nanomedicine Applications. *Chem. Rev.* **2018**, *118* (14), 6844–6892.

(5) Blanco, E.; Shen, H.; Ferrari, M. Principles of Nanoparticle Design for Overcoming Biological Barriers to Drug Delivery. *Nat. Biotechnol.* **2015**, *33* (9), 941–951.

(6) Geng, Y.; Dalhaimer, P.; Cai, S.; Tsai, R.; Tewari, M.; Minko, T.; Discher, D. E. Shape Effects of Filaments versus Spherical Particles in Flow and Drug Delivery. *Nat. Nanotechnol.* **2007**, *2* (4), 249–255.

(7) Black, K. C. L.; Wang, Y.; Luehmann, H. P.; Cai, X.; Xing, W.; Pang, B.; Zhao, Y.; Cutler, C. S.; Wang, L. V.; Liu, Y.; Xia, Y. Radioactive 198Au-Doped Nanostructures with Different Shapes for in Vivo Analyses of Their Biodistribution, Tumor Uptake, and Intratumoral Distribution. *ACS Nano* **2014**, *8* (5), 4385–4394.

(8) Yu, Q.; Roberts, M. G.; Houdaihed, L.; Liu, Y.; Ho, K.; Walker, G.; Allen, C.; Reilly, R. M.; Manners, I.; Winnik, M. A. Investigating the Influence of Block Copolymer Micelle Length on Cellular Uptake and Penetration in a Multicellular Tumor Spheroid Model. *Nanoscale* **2021**, *13* (1), 280–291.

(9) Zhao, Y.; Wang, Y.; Ran, F.; Cui, Y.; Liu, C.; Zhao, Q.; Gao, Y.; Wang, D.; Wang, S. A Comparison between Sphere and Rod Nanoparticles Regarding Their in Vivo Biological Behavior and Pharmacokinetics. *Sci. Rep.* **2017**, *7* (1), 1–11.

(10) Champion, J. A.; Mitragotri, S. Shape Induced Inhibition of Phagocytosis of Polymer Particles. *Pharm. Res.* **2009**, *26* (1), 244–249.

(11) Li, Z.; Sun, L.; Zhang, Y.; Dove, A. P.; O'Reilly, R. K.; Chen, G. Shape Effect of Glyco-Nanoparticles on Macrophage Cellular Uptake and Immune Response. *ACS Macro Lett.* **2016**, *5* (9), 1059–1064.

(12) Pearce, A. K.; Wilks, T. R.; Arno, M. C.; O'Reilly, R. K. Synthesis and Applications of Anisotropic Nanoparticles with Precisely Defined Dimensions. *Nat. Rev. Chem.* **2021**, *5* (1), 21–45.

(13) Blanazs, A.; Ryan, A. J.; Armes, S. P. Predictive Phase Diagrams for RAFT Aqueous Dispersion Polymerization: Effect of Block Copolymer Composition, Molecular Weight, and Copolymer Concentration. *Macromolecules* **2012**, *45* (12), 5099–5107.

(14) Massey, J. A.; Temple, K.; Cao, L.; Rharbi, Y.; Raez, J.; Winnik, M. A.; Manners, I. Self-Assembly of Organometallic Block Copolymers: The Role of Crystallinity of the Core-Forming Polyferrocene Block in the Micellar Morphologies Formed by Poly(Ferrocenylsilane-b-Dimethylsiloxane) in n-Alkane Solvents. *J. Am. Chem. Soc.* **2000**, *122* (47), 11577–11584.

(15) Tritschler, U.; Pearce, S.; Gwyther, J.; Whittell, G. R.; Manners, I. 50th Anniversary Perspective: Functional Nanoparticles from the Solution Self-Assembly of Block Copolymers. *Macromolecules.* **2017**, *50* (9), 3439–3463.

(16) Jiang, N.; Yu, T.; Darvish, O. A.; Qian, S.; Mkam Tsengam, I. K.; John, V.; Zhang, D. Crystallization-Driven Self-Assembly of Coil-Comb-Shaped Polypeptoid Block Copolymers: Solution Morphology and Self-Assembly Pathways. *Macromolecules* **2019**, *52* (22), 8867–8877.

(17) Yin, R.; Sahoo, D.; Xu, F.; Huang, W.; Zhou, Y. Scalable Preparation of Crystalline Nanorods through Sequential Polymerization-Induced and Crystallization-Driven Self-Assembly of Alternating Copolymers. *Polym. Chem.* **2020**, *11* (13), 2312–2317.

(18) Nabiyan, A.; Biehl, P.; Schacher, F. H. Crystallization vs Metal Chelation: Solution Self-Assembly of Dual Responsive Block Copolymers. *Macromolecules* **2020**, *53* (13), 5056–5067.

(19) Gilroy, J. B.; Gädt, T.; Whittell, G. R.; Chabanne, L.; Mitchels, J. M.; Richardson, R. M.; Winnik, M. A.; Manners, I. Monodisperse Cylindrical Micelles by Crystallization-Driven Living Self-Assembly. *Nat. Chem.* **2010**, *2* (7), 566–570.

(20) Ganda, S.; Stenzel, M. H. Concepts, Fabrication Methods and Applications of Living Crystallization-Driven Self-Assembly of Block Copolymers. *Prog. Polym. Sci.* **2020**, *101* (101195), 1–33.

(21) Street, S. T. G.; He, Y.; Jin, X.-H.; Hodgson, L.; Verkade, P.; Manners, I. Cellular Uptake and Targeting of Low Dispersity, Dual Emissive, Segmented Block Copolymer Nanofibers. *Chem. Sci.* **2020**, *11* (32), 8394–8408.

(22) Ganda, S.; Wong, C. K.; Stenzel, M. H. Corona-Loading Strategies for Crystalline Particles Made by Living Crystallization-Driven Self-Assembly. *Macromolecules* **2021**, *54* (14), 6662–6669.

(23) Jin, X. H.; Price, M. B.; Finnegan, J. R.; Boott, C. E.; Richter, J. M.; Rao, A.; Matthew Menke, S.; Friend, R. H.; Whittell, G. R.; Manners, I. Long-Range Exciton Transport in Conjugated Polymer Nanofibers Prepared by Seeded Growth. *Science* **2018**, *360* (6391), 897–900.

(24) Shen, S.; Wu, Y.; Liu, Y.; Wu, D. High Drug-Loading Nanomedicines : Progress , Current Status , and Prospects. *Int. J. Nanomedicine* **2017**, *12*, 4085–4109.

(25) Kita, K.; Dittrich, C. Drug Delivery Vehicles with Improved Encapsulation Efficiency: Taking Advantage of Specific Drug-Carrier Interactions. *Expert Opin. Drug Deliv.* **2011**, *8* (3), 329–342.

(26) Tietjen, G. T.; Bracaglia, L. G.; Saltzman, W. M.; Pober, J. S. Focus on Fundamentals: Achieving Effective Nanoparticle Targeting. *Trends Mol. Med.* **2018**, *24*, 598.

(27) Clemons, T. D.; Singh, R.; Sorolla, A.; Chaudhari, N.; Hubbard, A.; Iyer, K. S. Distinction between Active and Passive Targeting of Nanoparticles Dictate Their Overall Therapeutic Efficacy. *Langmuir* **2018**, *34* (50), 15343–15349.

(28) Banerjee, A.; Qi, J.; Gogoi, R.; Wong, J.; Mitragotri, S. Role of Nanoparticle Size, Shape and Surface Chemistry in Oral Drug Delivery. *J. Control. Release* **2016**, *238* (1), 176–185.

(29) Zhao, J.; Stenzel, M. H. Entry of Nanoparticles into Cells: The Importance of Nanoparticle Properties. *Polym. Chem.* **2018**, *9* (3), 259–272.

(30) Gaumet, M.; Vargas, A.; Gurny, R.; Delie, F. Nanoparticles for Drug Delivery: The Need for Precision in Reporting Particle Size Parameters. *Eur. J. Pharm. Biopharm.* **2008**, *69* (1), 1–9.

(31) Doncom, K. E. B.; Blackman, L. D.; Wright, D. B.; Gibson Ab, M. I.; O'Reilly, R. K. Dispersity Effects in Polymer Self-Assemblies: A Matter of Hierarchical Control. *Chem. Soc. Rev* **2017**, *46* (14), 4119–4134.

(32) Yoo, J.; Park, C.; Yi, G.; Lee, D.; Koo, H. Active Targeting Strategies Using Biological Ligands for Nanoparticle Drug Delivery Systems. *Cancers (Basel).* **2019**, *11* (5), 640–653.

(33) Bazak, R.; Houri, M.; Samar, E. A.; Kamel, S.; Refaat, T. Cancer Active Targeting by Nanoparticles: A Comprehensive Review of Literature. *J Cancer Res Clin Oncol* **2015**, *141* (5), 769–784.

(34) Zhao, Z.; Ukidve, A.; Kim, J.; Mitragotri, S. Targeting Strategies for Tissue-Specific Drug Delivery. *Cell* **2020**, *181* (1), 151–167.

(35) Chan, D. P. Y.; Owen, S. C.; Shoichet, M. S. Double Click: Dual Functionalized Polymeric Micelles with Antibodies and Peptides. *Bioconjug. Chem.* **2013**, *24* (1), 105–113.

(36) Elsabahy, M.; Wooley, K. L. Design of Polymeric Nanoparticles for Biomedical Delivery Applications. *Chem. Soc. Rev.* **2012**, *41* (7), 2545–2561.

(37) Palomeras, S.; Ruiz-Martínez, S.; Puig, T. Targeting Breast Cancer Stem Cells to Overcome Treatment Resistance. *Molecules* **2018**, *23* (9), 2209.

(38) Lebert, J. M.; Lester, R.; Powell, E.; Seal, M.; Mccarthy, J. Advances in the Systemic Treatment of Triple-Negative Breast Cancer. *Curr. Oncol.* **2018**, *25* (1), S142–S150.

(39) Zamora-Leon, S. P.; Golde, D. W.; Conchat, I. I.; Rivas, C. I.; Delgado-Lopez, F.; Baselgat, J.; Nualart, F.; Vera, J. C. Expression of the Fructose Transporter GLUT5 in Human Breast Cancer. *PNAS* **1996**, *93* (5), 1847–1852.

(40) Niness, K. R. Inulin and Oligofructose: What Are They? *J. Nutr.* **1999**, *129* (7), 1402S-1406S.

(41) Ahmed, W.; Rashid, S. Functional and Therapeutic Potential of Inulin: A Comprehensive Review. *https://doi.org/10.1080/10408398.2017.1355775* **2019**, *59* (1), 1–13.

(42) Taylor, S. R.; Ramsamooj, S.; Liang, R. J.; Katti, A.; Pozovskiy, R.; Vasan, N.; Hwang, S.-K.; Nahiyaan, N.; Francoeur, N. J.; Schatoff, E. M.; Johnson, J. L.; Shah, M. A.; Dannenberg, A. J.; Sebra, R. P.; Dow, L. E.; Cantley, L. C.; Rhee, K. Y.; Goncalves, M. D. Dietary Fructose Improves Intestinal Cell Survival and Nutrient Absorption. *Nat. 2021* **2021**, 1–5.

(43) Nakagawa, T.; Lanaspa, M. A.; Millan, I. S.; Fini, M.; Rivard, C. J.; Sanchez-Lozada, L. G.; Andres-Hernando, A.; Tolan, D. R.; Johnson, R. J. Fructose Contributes to the Warburg Effect for Cancer Growth. *Cancer Metab.* **2020**, *8* (1), 1–12.

(44) Office of Nutrition and Food Labeling; Center for Food Safety and Applied Nutrition; Food and Drug Administration; U.S. Department of Health and Human Services. *Science Review of Isolated and Synthetic Non-Digestible Carbohydrates*; 2016.

(45) Zhao, J.; Babiuch, K.; Lu, H.; Dag, A.; Gottschaldt, M.; Stenzel, M. H. Fructose-Coated Nanoparticles: A Promising Drug Nanocarrier for Triple-Negative Breast Cancer Therapy. *Chem. Commun.* **2014**, *50* (100), 15928–15931.

(46) Lu, M.; Chen, F.; Cao, C.; Garvey, C. J.; Fletcher, N. L.; Houston, Z. H.; Lu, H.; Lord, M. S.; Thurecht, K. J.; Stenzel, M. H. Importance of Polymer Length in Fructose-Based Polymeric Micelles for an Enhanced Biological Activity. *Macromolecules* **2019**, *52* (2), 477–486.

(47) Lu, M.; Chen, F.; Noy, J.-M.; Lu, H.; Stenzel, M. H. Enhanced Antimetastatic Activity of the Ruthenium Anticancer Drug RAPTA-C Delivered in Fructose-Coated Micelles. *Macromol. Biosci.* **2017**, *17* (10), 1600513.

(48) Yu, D.; Zhang, N.; Liu, S.; Hu, W.; Nie, J. J.; Zhang, K.; Yu, B.; Wang, Z. G.; Xu, F. J. Self-Assembled Nucleotide/Saccharide-Tethering Polycation-Based Nanoparticle for Targeted Tumor Therapy. *ACS Mater. Lett.* **2020**, *2* (5), 550–556.

(49) Ganda, S.; Dulle, M.; Drechsler, M.; Förster, B.; Förster, S.; Stenzel, M. H. Two-Dimensional Self-Assembled Structures of Highly Ordered Bioactive Crystalline-Based Block Copolymers. *Macromolecules* **2017**, *50* (21), 8544–8553.

(50) Zhao, J.; Lu, H.; Wong, S.; Lu, M.; Xiao, P.; Stenzel, M. H. Influence of Nanoparticle Shapes on Cellular Uptake of Paclitaxel Loaded Nanoparticles in 2D and 3D Cancer Models. *Polym. Chem.* **2017**, *8* (21), 3317–3326.

(51) Zhao, J.; Lu, H.; Xiao, P.; Stenzel, M. H. Cellular Uptake and Movement in 2D and 3D Multicellular Breast Cancer Models of Fructose-Based Cylindrical Micelles That Is Dependent on the Rod Length. *ACS Appl. Mater. Interfaces* **2016**, *8* (26), 16622–16630.

(52) Li, Z.; Zhang, Y.; Wu, L.; Yu, W.; Wilks, T. R.; Dove, A. P.; Ding, H. M.; O'Reilly, R. K.; Chen, G.; Jiang, M. Glyco-Platelets with Controlled Morphologies via Crystallization-Driven Self-Assembly and Their Shape-Dependent Interplay with Macrophages. *ACS Macro Lett.* **2019**, *8* (5), 596–602.

(53) Song, Y.; Elsabahy, M.; Collins, C. A.; Khan, S.; Li, R.; Hreha, T. N.; Shen, Y.; Lin, Y. N.; Letteri, R. A.; Su, L.; Dong, M.; Zhang, F.; Hunstad, D. A.; Wooley, K. L. Morphologic Design of Silver-Bearing Sugar-Based Polymer Nanoparticles for Uroepithelial Cell Binding and Antimicrobial Delivery. *Nano Lett.* **2021**, *21* (12), 4990–4998.

(54) Finnegan, J. R.; He, X.; Street, S. T. G.; Garcia-Hernandez, J. D.; Hayward, D. W.; Harniman, R. L.; Richardson, R. M.; Whittell, G. R.; Manners, I. Extending the Scope of "Living" Crystallization-Driven Self-Assembly: Well-Defined 1D Micelles and Block Comicelles from Crystallizable Polycarbonate Block Copolymers. *J. Am. Chem. Soc.* **2018**, *140* (49), 17127–17140.

(55) Zahedipour, F.; Hosseini, S. A.; Sathyapalan, T.; Majeed, M.; Jamialahmadi, T.; Al-Rasadi, K.; Banach, M.; Sahebkar, A. Potential Effects of Curcumin in the Treatment of COVID-19 Infection. *Phyther. Res.* **2020**, *34* (11), 2911–2920.

(56) Salehi, B.; Stojanović-Radić, Z.; Matejić, J.; Sharifi-Rad, M.; Anil Kumar, N. V.; Martins, N.; Sharifi-Rad, J. The Therapeutic Potential of Curcumin: A Review of Clinical Trials. *Eur. J. Med. Chem.* **2019**, *163* (1), 527–545.

(57) Giordano, A.; Tommonaro, G. Curcumin and Cancer. *Nutrients* **2019**, *11* (10), 2396.

(58) Wong, S.; Zhao, J.; Cao, C.; Wong, C. K.; Kuchel, R. P.; De Luca, S.; Hook, J. M.; Garvey, C. J.; Smith, S.; Ho, J.; Stenzel, M. H. Just Add Sugar for Carbohydrate Induced Self-Assembly of Curcumin. *Nat. Commun.* **2019**, *10* (1), 1–9.

(59) Cao, L.; Manners, I.; Winnik, M. A. Influence of the Interplay of Crystallization and Chain Stretching on Micellar Morphologies: Solution Self-Assembly of Coil−Crystalline Poly(Isoprene-Block-Ferrocenylsilane). *Macromolecules* **2002**, *35* (22), 8258–8260.

(60) Hudson, Z. M.; Boott, C. E.; Robinson, M. E.; Rupar, P. A.; Winnik, M. A.; Manners, I. Tailored Hierarchical Micelle Architectures Using Living

Crystallization-Driven Self-Assembly in Two Dimensions. *Nat. Chem.* **2014**, *6* (10), 893–898.

(61) Garcia-Hernandez, J. D.; Street, S. T. G.; Kang, Y.; Zhang, Y.; Manners, I. Cargo Encapsulation in Uniform, Length-Tunable Aqueous Nanofibers with a Coaxial Crystalline and Amorphous Core. *Macromolecules* **2021**, *54* (12), 5784–5796.

(62) Gescher, A. Metabolism of N,N-Dimethylformamide: Key to the Understanding of Its Toxicity. *Chem. Res. Toxicol.* **2002**, *6* (3), 245–251.

(63) Tephly, T. R. The Toxicity of Methanol. *Life Sci.* **1991**, *48* (11), 1031–1041.

(64) Dai, J.; Dong, X.; Wang, Q.; Lou, X.; Xia, F.; Wang, S. PEG-Polymer Encapsulated Aggregation-Induced Emission Nanoparticles for Tumor Theranostics. *Adv. Healthc. Mater.* **2021**, *10* (24), 2101036.

(65) Veronese, F. M.; Pasut, G. PEGylation, Succesful Approach to Drug Delivery. *Drug Discov. Today* **2005**, *10* (21), 1451–1458.

(66) Milton Harris, J.; Chess, R. B. Effect of Pegylation on Pharmaceuticals. *Nat. Rev. Drug Discov.* **2003**, *2* (3), 214–221.

(67) Cao, C.; Zhao, J.; Lu, M.; Garvey, C. J.; Stenzel, M. H. Correlation between Drug Loading Content and Biological Activity: The Complexity Demonstrated in Paclitaxel-Loaded Glycopolymer Micelle System. *Biomacromolecules* **2019**, *20* (4), 1545–1554.

(68) Arno, M. C.; Inam, M.; Coe, Z.; Cambridge, G.; Macdougall, L. J.; Keogh, R.; Dove, A. P.; O'Reilly, R. K. Precision Epitaxy for Aqueous 1D and 2D Poly(ϵ-Caprolactone) Assemblies. *J. Am. Chem. Soc.* **2017**, *139* (46), 16980–16985.

(69) Pangborn, A. B.; Giardello, M. A.; Grubbs, R. H.; Rosen, R. K.; Timmers, F. J. Safe and Convenient Procedure for Solvent Purification. *Organometallics* **1996**, *15* (5), 1518–1520.

(70) Bahadori, F.; Demiray, M. A Realistic View on "the Essential Medicinal Chemistry of Curcumin." *ACS Med. Chem.* Lett. **2017**, 8 (9), 893–896.

(71) Baell, J.; Walters, M. A. Chemical Con Artists Foil Drug Discovery. *Nature* **2014**, 513 (7519), 481–483.

(72) Nelson, K. M.; Dahlin, J. L.; Bisson, J.; Graham, J.; Pauli, G. F.; Walters, M. A. The Essential Medicinal Chemistry of Curcumin. *J. Med. Chem.* **2017**, 60 (5), 1620–1637.

Chapter 6

Summary and Future Work

The work presented in this thesis demonstrates the versatility of living CDSA to yield morphologically pure, length-controlled, and low length dispersity nanofibers from PFTMC-based BCPs. The general aim of this work is to contribute to the development of high aspect ratio polymeric micelles prepared via living CDSA methods for biomedical applications. This work lays the foundation for the development of crystalline core-forming BCP nanofibers for drug delivery applications, medical treatments, and material composites with previously inaccessible cargo loaded nanofibers and fiber-like networks.

6.1 Loading of Coaxial Core Nanofibers

One of the largest unresolved challenges for nanoparticles with crystalline core is the inability to load cargo in the micelle interior.[1,2] **Chapter 2** demonstrates how nanofibers with a crystalline core-forming block can be loaded with hydrophobic cargo. The aim of this project was to combine the features of BCP nanofibers with a crystalline core prepared via living CDSA (uniform morphology and controlled size) with the ability to load cargo of amorphous core-forming nanoparticles.[3] For this purpose, triBCP nanofibers were designed to comprise a crystalline inner core (PFTMC), an amorphous outer core (PBMA), and a solubilizing corona-forming block (PNIPAM), i.e., $PFTMC_{18}$-*b*-$PBMA_{44}$-*b*-$PNIPAM_{70}$. In selective solvent mixtures, nanofibers of precise lengths with low dispersities were prepared via the living CDSA method. The PBMA block was initially soluble in the selective solvent mixture but became insoluble upon transfer to water. Preformed triBCP nanofibers in the presence of hydrophobic cargo were slowly transferred

from the selective solvent mixture to water via a syringe pump, resulting in encapsulation of the hydrophobic fluorescent dye NR in the PBMA outer core. Slow transfer to water minimized nanofiber fragmentation and facilitated cargo uptake by low dispersity nanofibers with lengths relevant for drug delivery (~125 nm).[4] Optimal conditions for cargo loading were found at a ratio of 1 wt % hydrophobic cargo to polymer with ca. 600 – 667 ng of NR loaded per mg of nanofiber.

Future work will focus on optimization of the triBCP polymer blocks to increase the amount of cargo that can be loaded by coaxial core nanofibers. For instance, the DP_n of the PFTMC could be reduced from 18 to 8. Preliminary results have shown that $PFTMC_8$ is sufficiently long to undergo CDSA which would minimize the volume occupied by the crystalline core, thereby increasing the volume fraction of the outer core and the loading capacity. Additionally, the DP_n of the PBMA could be maximized to allow for a larger encapsulation volume. Assessment of the release kinetics for in vitro or in vivo cargo delivery is also an important future direction. For this to be enabled, collaborations with experts in the field will need to be set up. Broadening the scope of hydrophobic drug molecules that can be loaded onto coaxial core nanofibers is vital. Loading of hydrophobic anticancer molecules such as paclitaxel, doxorubicin, docetaxel, vincristine, and curcumin, to name a few, are interesting avenues with great potential.[5] So far, NR was loaded into the PBMA outer-core based on hydrophobic interactions. However, assessment of the Hildebrand solubility parameter between the outer-core polymer and the drug ($\chi_{polymer\text{-}drug}$) has not been considered. This may lead to the selection of optimal outer-core polymer blocks for a particular drug, thereby maximizing the loading of coaxial-core nanofibers by increasing its miscibility.[6]

6.2 Loading of DiBCP Nanofibers

In Chapter 2, comparative studies of hydrophobic cargo loading at the core-corona interface by diBCP nanofibers indicated that cargo uptake was possible without an amorphous outer core. Recently, amorphous core-forming BCP spherical micelles were reported to load cargo at the core-corona interface.[7] The work described in **Chapter 3** involves an investigation of cargo loading at the core-corona interface by diBCP nanofibers with a crystalline core. Three PFTMC-based diBCP nanofiber systems with corona-forming blocks of different compositions and lengths were studied (i.e., $PNIPAM_{425}$, PEG_{275}, PEG_{530}). Fluorescence spectroscopy analysis of length-controlled and low dispersity nanofibers indicated that cargo uptake takes place at the core-corona interface and is independent of the chemical identity and DP_n of the corona-forming block. Cargo loading analysis indicated no statistically significant differences among the means of NR loaded by the three diBCP nanofiber systems studied (ca. 250 ng of NR per mg of polymer). The crystalline core radii of the three nanofiber systems were found to be similar (ca. 4.5 nm), consistent with the near-identical values of DP_n (18 – 19) for the PFTMC core-forming block. The similar quantities loaded by the three nanofiber systems and the matching core radii dimensions suggest a loading mechanism where cargo accumulates at the core-corona interface and is directly influenced by the surface area of the crystalline core of diBCP nanofibers. Although the loading by diBCP nanofibers is 2 – 3 times less efficient than coaxial core nanofibers, the design is considerably simpler, making them more accessible.

The polymer design of the three nanofiber systems studied in this chapter is unoptimized. Therefore, future work will focus on improving the loading capacity of

nanofibers by increasing the DP_n of the PFTMC block to enhance the surface area of the crystalline core of diBCP nanofibers. Initially, similar drug molecules suggested for loading as future work for Chapter 2 can also be used for loading diBCP nanofibers. This would allow to investigate and compare loading differences based on the substrate and the nanofiber system used (diBCP or coaxial core nanofibers). Further work may involve loading potent hydrophobic drugs where high cargo uptake is not required. The release kinetic profiles of drugs from diBCP nanofibers are also important to investigate in future. The biodistribution of nanofibers based on their length (i.e., passive targeting) is an interesting avenue to explore. This can be performed by labelling the nanofibers with Cy5 dye and assessing its distribution in mouse models. An alternative would be to analyze the distribution profiles of nanofibers in body-on-a-chip devices prior to moving to in vivo models.[8] Collaboration with experts on the field would be needed to conduct such research. The degradability of nanofibers with a crystalline core could be tuned for enhanced delivery (i.e., in tumor environments) and for clearance (after delivery). If nanofiber accumulation in particular tissues is dictated by the nanofiber length, then nanofibers functionalized with organic contrast agents could be used for enhanced length-based targeted imaging of organs, with fewer side effects than traditional metal-based contrast agents.[9]

6.3 Fiber-Like Micellar Networks

In general, the majority of associative triBCPs self-assemble into spherical flower-like micelles, except at high concentrations where micellar networks of spherical micelles are formed.[10] **Chapter 4** describes the CDSA and living CDSA of B-A-B triBCPs with crystallizable terminal PFTMC segments (i.e., $PEFTMC_{14}$-*b*-PEG_{900}-*b*-$PFTMC_{14}$). At low

triBCP concentrations (>5 mg/mL) and low common solvent fractions (10%), discrete crystalline core flower-like micelles were formed via CDSA. TriBCP unimer addition to micelle seeds yielded length-controlled and low length-dispersity flower-like micelles (up to 806 nm, $Đ \leq 1.10$). Fiber-like micelle networks/bundles were obtained at high triBCP concentrations (>5 mg/mL) and high common solvent fractions (~20%) via CDSA. Addition of triBCP to preformed diBCP nanofibers at low concentration (0.9 mg/mL) yielded segmented triBCP-***m***-diBCP-***m***-triBCP nanofibers. Conversely, at high concentrations (9 mg/mL) of both diBCP nanofibers and triBCP, fiber-like micellar networks were achieved. The intermicellar network formation was facilitated when the solutions were warmed to ~ 50 °C. A competitive mechanism between crystallization-driven nanofiber growth and intermicellar network formation was postulated. To our knowledge, this is the first report of nanofibers with a crystalline core being linked by a triBCP.

Future work will involve the development of multigram synthesis of the triBCP, as some applications can demand high quantities of material. Fiber-like networks can be investigated for materials reinforcement in resins or nylon fibers. Successful transfer of the fiber networks to water in sufficient quantity is a topic for future work. Similarly, the rheological characterization of the fiber-like networks at different concentrations in organic solvents and in water is required. Tuning the degree of micellar network formation may lead to distinct mechanical properties suited for different applications. Fiber-like networks may be blended with hydrogels to mimic the inherent fiber-like nature of the extracellular matrix to promote cell growth and differentiation.[11] Tuning the degree of fiber-like micellar networks may allow stem cells to differentiate into different kinds of cells. At present, in

collaboration with the Willerth group at the University of Victoria, we are investigating the effect of diBCP length-tuned nanofibers blended with fibrin-based bioink for printing pluripotent stem cells to prepare constructs for tissue engineering.[12] The fiber-like micelle networks could further enhance the mechanical properties of the constructs compared to diBCP nanofibers. Furthermore, a mixture of diBCP nanofibers and fiber-like networks can be used to prepare the constructs.

6.4 Polyfructose-Containing and Segmented Nanofibers

Chapters 2 and 3 of this thesis explored loading of hydrophobic cargo into crystalline core nanofibers. In **Chapter 5** the work described addresses how to target nanofibers to a particular tissue by incorporating functional corona-forming blocks. **Chapter 5** also describes the preparation of segmented nanofibers that may be suited for multistep applications. A polyfructose (PFr) corona-forming block was employed owing to its potential to target the GLUT5 receptors that are overexpressed in triple negative breast cancer (TNBC) cells.[13,14] Via the living CDSA method, the length of $PFTMC_{18}$-*b*-PFR_{92} diBCPs nanofibers was controlled from 50 – 1200 nm with low length dispersities ($Đ < 1.09$). The nanofibers may display passive targeting properties based on their length, and active targeting capabilities based on the PFr corona. Additionally, pentablock nanofibers with a middle block dedicated to drug encapsulation, with flanking targeting segments, and terminal stealth-blocks were prepared. The segmented nanofiber was prepared bearing in mind the multiple barriers a nanoparticle delivery vehicle must overcome prior to the delivery of cargo.[15] Finally, preliminary studies regarding the association between curcumin, a known anticancer, anti-inflammatory, and antiviral

drug,[16–18] and the PFr corona suggest possible association. However, further studies to prove the association of curcumin with the PFr corona are required.

Future work will involve the assessment of the targeting capabilities of the PFr-containing diBCP nanofibers towards TNBC cells, and the performance of segmented nanofibers compared to non-segmented nanofibers to deliver cargo. To investigate active targeting, dye-labelled PFr-containing nanofibers can be added to cocultures of healthy cells and of those overexpressing the GLUT5 receptor. Immunocytochemistry or flow-cytometry could be used for measuring the targeting efficiency of the nanofibers. Body-on-a-chip or microfluidic devices can be utilized for assessing the targeting properties of the nanofibers in flow and in more complex systems, although mice models could also be used. The aforementioned studies could be complemented with nanofibers of different lengths to assess the influence of this variable on the targeting and uptake of nanofibers by the cells (passive targeting). The efficiency of the segmented nanofibers could be evaluated in microfluidic devices. For example, epithelial models in microfluidic devices[19] could be used to assess the extravasation performance of segmented nanofibers against non-segmented nanofibers. Collaborations to conduct the aforementioned research will need to be established. Realization of CDSA and living CDSA in biological relevant aqueous media with suitable BCPs is currently challenging and limited examples exist.[20,21] CDSA of PFr-based BCPs has yielded promising results in aqueous solutions, but further optimization is required.

6.5 Outlook

Living CDSA is a versatile method to gain access to high aspect ratio nanofiber morphologies in pure form with exquisite dimensional control. The nanoparticles fabricated via living CDSA present inherent morphological advantages compared to spherical analogues that may help to address current challenges in the biomedical field. This proof-of-concept work lays the foundation for the development of nanofiber therapeutics, a very promising and young field. Nanofiber engineering and optimization is required in order to achieve cargo loadings above 0.1 wt %. However, common loading quantities (> 10 wt %) may not be required if the nanofiber vector has higher performance and specificity for the delivery of cargo. In future, the length of nanofiber-based formulations may be tuned to target a specific tissue, and the nanofiber design (diBCP or coaxial core) may be tailored to the potency of a particular drug. The ability to incorporate distinct nanofiber segments suited for multistep applications such as drug delivery may enhance the overall performance of nanoparticle vectors. Incorporation of nanofiber networks into composites or hydrogels could lead to stronger and better properties for tissue engineering and materials reinforcement applications. An interesting area of research to explore in the future would be to replace the crystalline PFTMC core-forming block by polymeric forms of crystalline drugs approved for cancer treatment.[22] Nanoparticles with low curvature of the core-corona interface accessed via living CDSA are also advantageous for a range of applications including catalysis,[23] light harvesting devices,[24] and for information storage,[25] among others.[26] Drug delivery and light responsive properties may be incorporated on nanofibers to provide photothermal, photodynamic, and synergistic approaches for the treatment of pathologies via π-conjugated BCP nanofibers.[27] To further

advance these areas and also the biomedical field, and to address some of the emerging challenges of our modern world, there is a need for further expansion of the range of crystallizable materials that are capable of undergoing living CDSA.[28]

6.6 References

(1) Bains, A.; Cao, Y.; Moffitt, M. G. Multiscale Control of Hierarchical Structure in Crystalline Block Copolymer Nanoparticles Using Microfluidics. *Macromol. Rapid Commun.* **2015**, *36* (22), 2000–2005.

(2) Gou, J.; Feng, S.; Xu, H.; Fang, G.; Chao, Y.; Zhang, Y.; Xu, H.; Tang, X. Decreased Core Crystallinity Facilitated Drug Loading in Polymeric Micelles without Affecting Their Biological Performances. *Biomacromolecules* **2015**, *16* (9), 2920–2929.

(3) Cabral, H.; Miyata, K.; Osada, K.; Kataoka, K. Block Copolymer Micelles in Nanomedicine Applications. *Chem. Rev.* **2018**, *118* (14), 6844–6892.

(4) Elsabahy, M.; Wooley, K. L. Design of Polymeric Nanoparticles for Biomedical Delivery Applications. *Chem. Soc. Rev.* **2012**, *41* (7), 2545–2561.

(5) Patra, J. K.; Das, G.; Fraceto, L. F.; Campos, E. V. R.; Rodriguez-Torres, M. D. P.; Acosta-Torres, L. S.; Diaz-Torres, L. A.; Grillo, R.; Swamy, M. K.; Sharma, S.; Habtemariam, S.; Shin, H. S. Nano Based Drug Delivery Systems: Recent Developments and Future Prospects. *J. Nanobiotechnology* **2018**, *16* (71), 1–33.

(6) Kim, S.; Shi, Y.; Kim, J. Y.; Park, K.; Cheng, J. X. Overcoming the Barriers in Micellar Drug Delivery: Loading Efficiency, in Vivo Stability, and Micelle–Cell Interaction. *Expert Opin. Drug Deliv.* **2009**, *7* (1), 49–62.

(7) Cao, C.; Zhao, J.; Lu, M.; Garvey, C. J.; Stenzel, M. H. Correlation between Drug Loading Content and Biological Activity: The Complexity Demonstrated in Paclitaxel-Loaded Glycopolymer Micelle System. *Biomacromolecules* **2019**, *20* (4), 1545–1554.

(8) Sung, J. H.; Wang, Y. I.; Narasimhan Sriram, N.; Jackson, M.; Long, C.; Hickman, J. J.; Shuler, M. L. Recent Advances in Body-on-a-Chip Systems. *Anal. Chem.* **2019**, *91* (1), 330–351.

(9) Akakuru, O. U.; Iqbal, M. Z.; Saeed, M.; Liu, C.; Paunesku, T.; Woloschak, G.; Hosmane, N. S.; Wu, A. The Transition from Metal-Based to Metal-Free Contrast

Agents for T1 Magnetic Resonance Imaging Enhancement. *Bioconjug. Chem.* **2019**, *30* (9), 2264–2286.

(10) Winnik, M. A.; Yekta, A. Associative Polymers in Aqueous Solution. *Curr. Opin. Colloid Interface Sci.* **1997**, *2* (4), 424–436.

(11) Smith, L. R.; Cho, S.; Discher, D. E. Stem Cell Differentiation Is Regulated by Extracellular Matrix Mechanics. *Physiology* **2018**, *33* (1), 16–25.

(12) Smits, I. P. M.; Blaschuk, O. W.; Willerth, S. M. Novel N-Cadherin Antagonist Causes Glioblastoma Cell Death in a 3D Bioprinted Co-Culture Model. *Biochem. Biophys. Res. Commun.* **2020**, *529* (2), 162–168.

(13) Zamora-Leon, S. P.; Golde, D. W.; Conchat, I. I.; Rivas, C. I.; Delgado-Lopez, F.; Baselgat, J.; Nualart, F.; Vera, J. C. Expression of the Fructose Transporter GLUT5 in Human Breast Cancer. *PNAS* **1996**, *93* (5), 1847–1852.

(14) Zhao, J.; Babiuch, K.; Lu, H.; Dag, A.; Gottschaldt, M.; Stenzel, M. H. Fructose-Coated Nanoparticles: A Promising Drug Nanocarrier for Triple-Negative Breast Cancer Therapy. *Chem. Commun.* **2014**, *50* (100), 15928–15931.

(15) Blanco, E.; Shen, H.; Ferrari, M. Principles of Nanoparticle Design for Overcoming Biological Barriers to Drug Delivery. *Nat. Biotechnol.* **2015**, *33* (9), 941–951.

(16) Zahedipour, F.; Hosseini, S. A.; Sathyapalan, T.; Majeed, M.; Jamialahmadi, T.; Al-Rasadi, K.; Banach, M.; Sahebkar, A. Potential Effects of Curcumin in the Treatment of COVID-19 Infection. *Phyther. Res.* **2020**, *34* (11), 2911–2920.

(17) Salehi, B.; Stojanović-Radić, Z.; Matejić, J.; Sharifi-Rad, M.; Anil Kumar, N. V.; Martins, N.; Sharifi-Rad, J. The Therapeutic Potential of Curcumin: A Review of Clinical Trials. *Eur. J. Med. Chem.* **2019**, *163* (1), 527–545.

(18) Giordano, A.; Tommonaro, G. Curcumin and Cancer. *Nutrients* **2019**, *11* (10), 2396.

(19) Thuenauer, R.; Rodriguez-Boulan, E.; Rümer, W. Microfluidic Approaches for Epithelial Cell Layer Culture and Characterisation. *Analyst* **2014**, *139* (13), 3206–3218.

(20) Arno, M. C.; Inam, M.; Coe, Z.; Cambridge, G.; Macdougall, L. J.; Keogh, R.; Dove, A. P.; O'Reilly, R. K. Precision Epitaxy for Aqueous 1D and 2D Poly(ϵ-Caprolactone) Assemblies. *J. Am. Chem. Soc.* **2017**, *139* (46), 16980–16985.

(21) Yu, W.; Foster, J. C.; Dove, A. P.; O'Reilly, R. K. Length Control of Biodegradable Fiber-Like Micelles via Tuning Solubility: A Self-Seeding Crystallization-Driven Self-Assembly of Poly(ε-Caprolactone)-Containing Triblock Copolymers. *Macromolecules* **2020**, *53* (4), 1514–1521.

(22) Hughes, D. L. Review of Synthetic Routes and Crystalline Forms of the Oncology Drugs Capmatinib, Selpercatinib, and Pralsetinib. *Org. Process Res. Dev.* **2021**, *25* (10), 2192–2204.

(23) Tian, J.; Zhang, Y.; Du, L.; He, Y.; Jin, X.-H.; Pearce, S.; Eloi, J.-C.; Harniman, R. L.; Alibhai, D.; Ye, R.; Phillips, D. L.; Manners, I. Tailored Self-Assembled Photocatalytic Nanofibres for Visible-Light-Driven Hydrogen Production. *Nat. Chem.* **2020**, *12* (12), 1150–1156.

(24) Jin, X. H.; Price, M. B.; Finnegan, J. R.; Boott, C. E.; Richter, J. M.; Rao, A.; Matthew Menke, S.; Friend, R. H.; Whittell, G. R.; Manners, I. Long-Range Exciton Transport in Conjugated Polymer Nanofibers Prepared by Seeded Growth. *Science* **2018**, *360* (6391), 897–900.

(25) Hudson, Z. M.; Lunn, D. J.; Winnik, M. A.; Manners, I. Colour-Tunable Fluorescent Multiblock Micelles. *Nat. Commun.* **2014**, *5*, 1–8.

(26) Macfarlane, L.; Zhao, C.; Cai, J.; Qiu, H.; Manners, I. Emerging Applications for Living Crystallization-Driven Self-Assembly. *Chem. Sci.* **2021**, *12* (13), 4661–4682.

(27) MacFarlane, L. R.; Shaikh, H.; Garcia-Hernandez, J. D.; Vespa, M.; Fukui, T.; Manners, I. Functional Nanoparticles through π-Conjugated Polymer Self-Assembly. *Nat. Rev. Mater.* **2021**, *6* (1), 7–26.

(28) Hai, T.; Feng, Z.; Sun, Y.; Wong, W.-Y.; Liang, Y.; Zhang, Q.; Lei, Y. Vapor-Phase Living Assembly of π-Conjugated Organic Semiconductors. *ACS Nano* **2022**, *16* (2) 3290-3299.